A Viscoelastic Analysis Approach to the Energy Dissipation in Fatigue of Fibre Reinforced Polymer Composites

Master of Science Thesis

Lennart Laurens Krieg | 4862120

TU Delft
Faculty of Aerospace Engineering
Aerospace Structures & Materials

Date of defence
Friday September 19th 2025

A Viscoelastic Analysis Approach to the Energy Dissipation in Fatigue of Fibre Reinforced Polymer Composites

Master of Science Thesis

by

Lennart Laurens Krieg

4862120

To obtain the degree of Master of Science at the Delft University of Technology,
this thesis is to be defended on Friday September 19, 2025 at 09:30 AM.

Project duration:
December 9, 2024 – September 3, 2025

Graduation committee:

Chair:	Prof.dr.ir. R. Benedictus
Examiner:	Dr. S.J. Garcia Espallargas
Responsible supervisor:	Prof.dr.ir. R.C. Alderliesten
Advisory member:	S.F. Sartorio, M.Sc.

TU Delft

Faculty of Aerospace Engineering
Department of Aerospace Structures & Materials

Preface

This thesis is the result of my research carried out as part of obtaining the Master's degree in Aerospace Structures and Materials at the Aerospace Engineering faculty of the Delft University of Technology. It marks the end of my seven year journey at this faculty, where in parallel to the BSc and MSc programs I have been fortunate enough to further develop myself as an engineer though participation in the Formula Student team and a number of exciting internship opportunities. Now that this phase in time is coming to a close, I reflect with fond memories on all the interactions, lessons learnt and challenges overcome that have ultimately provided me the skills to be set free into the wider field as an aerospace engineer.

The motivation for this particular thesis work originates from both a scientific and a practical perspective. Fibre-reinforced polymer composites play an ever increasingly important role in the engineering of modern structures, yet their fatigue behaviour remains complex and time-intensive to fully characterise. With this research my aim was to contribute to the development of more efficient energy dissipation-based approaches to fatigue analysis and prediction, with the ultimate goal of reducing the dependence on extensive empirical testing. I hope that this thesis' results can be a meaningful piece in the overall wider puzzle of the ongoing efforts in the energy dissipation centred composite fatigue, and that it will serve as a useful proof of concept of the currently undertaken modified linear viscoelastic analysis approach.

This project has been challenging at times, but ultimately a very rewarding process. I would like to express a deep thank you to my supervisor René Alderliesten for his great guidance, expertise and passion for his field. Our regular discussions were always a triggering motivation to dig deeper into the topic. I furthermore would like to thank PhD candidates Sofia Sartorio and Valentin Perruchoud as well as all DASML staff, whose discussions, guidance and assistance in the laboratory made this thesis possible.

Lastly, I would like to thank my friends and family for all their continuous encouragement and support over these last seven years. Without them, I would not be who and where I am today.

Lennart Laurens Krieg
Rotterdam, September 2025

Abstract

The fatigue behaviour of fibre-reinforced polymer composites is traditionally characterised through extensive empirical-phenomenological stress–life (S–N) testing, which is both time-consuming and costly. Recent studies have suggested that energy dissipation trends may provide a more consistent basis for fatigue life prediction. This thesis contributes to these efforts by developing and applying a modified linear viscoelastic framework to describe cyclic energy dissipation in continuous fibre-reinforced composites under tensile–tensile fatigue loading. The main research question that guided this work was defined as follows:

How can linear viscoelastic theory be adapted to define a consistent energy dissipation formulation for fibre-reinforced polymer composites under tensile-tensile fatigue, and how can these be used in conjunction with a critical dissipated energy criteria to predict fatigue lives across varying stress levels and R-ratios?

The considered approach adapts classical complex modulus-based linear viscoelastic theory by introducing energy-based R-ratio correction factors that compensate for the otherwise unaccounted dependencies in strain energy input. These corrections enable cyclic hysteresis energy, cyclic and total dissipation ratios, and total or critical dissipated energies to be consistently defined across stress levels and load ratios as relation to a common viscoelastic loss factor definition at an equivalent $R = -1$ cycle. Using this proposed analysis approach, datasets for a literature reference $\pm 45^{\circ}$ and experimentally tested $[0/90]_{4s}$ laminates were analysed, being able to compare and combine these fatigue hysteresis measurements with dynamic mechanical analysis (DMA).

These results showed that energy-weighted effective loss factors ($\sin(\phi_{eff})$) measured in fatigue collapsed across R–ratios when expressed through the proposed correction factors, and correlated strongly with DMA-derived loss factor measurements of the pristine materials. The intersection of such fatigue-derived $\sin(\phi_{eff})$ curves with pristine DMA values provided consistent estimates of the high-cycle fatigue strength (HCFS) for both reference and experimental datasets, further supported by the inherent similarity to commonly documented infrared thermography trends in literature. Additionally, the ratio of total dissipated energy to total work done in the specimen's fatigue lives (TDE/TW) was concluded to be a direct product of such $\sin(\phi_{eff})$ vs maximum stress relations and therefore was shown to exhibit a similar two-domain trend: near constant below the HCFS and increasing linearly with stress beyond it.

Furthermore, critical dissipated energy (CDE), defined as the energy dissipated up to the onset of final failure, was identified as a promising fatigue failure criteria. For the $[0/90]_{4s}$ laminate, such CDE–stress relations were shown to be independent of R in the intermediate to high-cycle regimes. Combined with the collapsed $\sin(\phi_{eff})$ trends, this enabled accurate fatigue life predictions at alternative R–ratios from only a limited input dataset. Failure strain vs maximum stress analysis further supported the energy-based framework, with trends also collapsing across different R-ratios when normalised for the ratio of cyclicly applied strain energy to the peak strain potential.

The findings of this thesis thus demonstrate that the concept of a modified viscoelastic energy approach can provide a physically consistent and reliable framework for describing fatigue in fibre-dominated laminates. The work allowed for the formation of strong links between fatigue hysteresis energy dissipation, dynamic mechanical analysis and the already common infrared thermography methods. The observed consistency and apparent linearities in the current work further highlight the potential of energy-based frameworks to reduce the experimental burden of composite fatigue characterisation while improving predictive capability.

Nomenclature

Abbreviations

Abbreviation	Definition
3PB	Three-Point Bending
C-C	Compressive-Compressive Fatigue
CDE	Critical Dissipated Energy
CLD	Constant Life Diagram
DASML	Delft Aerospace Structures & Materials Laboratory
DCB	Dual Cantilever Bending
DIC	Digital Image Correlation
DMA	Dynamic Mechanical Analysis
E-glass	Electrical grade glass fibre
FEA	Finite Element Analysis
FRP	Fibre Reinforced Polymer
FVF	Fibre Volume Fraction
GFRP	Glass Fibre Reinforced Polymer
HCFL	High-Cycle Fatigue Life
HCFS	High-Cycle Fatigue Strength
IR	Infrared (thermography)
LVE	Linear Viscoelastic (theory)
SDC	Specific Damping Capacity
SLERA	Strength-Life Equal Rank Assumption
S–N	Stress–Number of cycles relation
T-C	Tensile-Compressive Fatigue
T-T	Tensile-Tensile Fatigue
TDE	Total Dissipated Energy
TW	Total Work
UD	Unidirectional

Symbols

Symbol	Definition	Unit
E	Young's modulus	[Pa]
G	Shear modulus	[Pa]
ν	Poisson's ratio	[-]
X	Longitudinal strength	[Pa]
Y	Transverse strength	[Pa]
S	Shear strength	[Pa]
$\|E^*\|$	Complex modulus	[Pa]
E_{dyn}	Dynamic modulus	[Pa]
E'	Storage modulus	[Pa]
E''	Loss modulus	[Pa]
f	Frequency	[Hz]
ω	Radial frequency	[Rad]
v	Velocity	[m/s]
ρ	Density	[kg/m^3]
μ	Viscosity	[$mPa \cdot s$]
t	Time	[s]
t_{peak}	Time spent near cycle peak	[s]
T	Temperature	[$^\circ C$]
ΔT	Temperature change	[$^\circ C$]
N_f	Number of cycles to failure	[-]
R	Stress ratio ($\sigma_{\min}/\sigma_{\max}$)	[-]
W_a	Applied work per cycle	[MJ/m^3]
W_h	Hysteresis dissipated energy per cycle	[MJ/m^3]
$\dot{W}_h$	Hysteresis dissipation rate	[$MJ/(m^3 \cdot s)$]
W_{ref}	Equivalent work done at $R = -1$	[MJ/m^3]
ΔW	LVE dissipated energy per cycle	[MJ/m^3]
W	Maximum strain potential	[MJ/m^3]
TW	Total work over fatigue life	[MJ/m^3]
TDE	Total dissipated energy	[MJ/m^3]
CDE	Critical dissipated energy	[MJ/m^3]
ϵ	Strain	[-]
ϵ_a	Strain amplitude	[-]
ϵ_{max}	Maximum cyclic strain	[-]
ϵ_{min}	Minimum cyclic strain	[-]
ϵ_{mean}	Mean cyclic strain	[-]
ϵ_f	Failure strain	[-]
$\dot{\epsilon}$	Strain rate	[$1/s$]
$\dot{\epsilon}_{peak}$	Cyclic peak strain rate	[$1/s$]
$\dot{\epsilon}_{avg}$	Cyclic average strain rate	[$1/s$]
σ	Stress	[Pa]
σ_a	Stress amplitude	[Pa]
σ_{max}	Maximum cyclic stress	[Pa]
σ_{min}	Minimum cyclic stress	[Pa]
σ_{mean}	Mean cyclic stress	[Pa]
P	Applied force	[N]
$\dot{P}$	Loading rate	[N/s]
A_{gauge}	Gauge cross-sectional area	[m^2]
w	Specimen width	[m]
ϕ	Phase lag between stress and strain	[rad]
$\sin(\phi)$, $\tan(\phi)$	Loss factor (per-cycle)	[-]
$\sin(\phi_{\text{eff}})$	Effective loss factor (lifetime)	[-]

List of Figures

2.1 Schematic representation of a hysteresis loop under cyclic loading [16] 5
2.2 Dominant damage mechanisms in unidirectional laminate fatigue [29] 8
2.3 Generalised fatigue damage evolution stages [1] 9
2.4 Comparison of cycle time spent above 90% of σ_{max} for varying R-ratios under constant frequency. 15
2.5 Change in cyclicly applied strain energy as result of increasing R-ratio. 15
2.6 Thermography based high cycle fatigue strength determinations by a) Colombo et al. [67] and b) Han et al. [8] 19
2.7 Total dissipated energy vs total work done on different glass/epoxy laminates, graph provided by [1] 20
2.8 Visualisation of revised two-domain TDE/TW hypothesis 21

3.1 Visual representation of A) exaggerated creep considered as part of hysteresis behaviour B) creep strain shifts represented as independent from hysteresis. 25
3.2 Polar plot representation of relation between the complex, storage and loss moduli with the phase lag angle. 26
3.3 Definition of complex moduli components within a hysteresis loop [17]. 27
3.4 Phase shift between cyclic input stress and strain response of (a) pure elastic, (b) perfectly viscous and (c) viscoelastic material types [17]. 28
3.5 Visual representation of differences in cyclic work done on the material at constant stress amplitude for A) fully reversed cycles, B) tensile-compressive cycles and C) tensile-tensile cycles. 30
3.6 Cyclic energy dissipation correction factor vs R-ratio. 34

4.1 Avarage laminate modulus degradation and energy dissipation per cycle over normalised fatigue life as reconstructed from [15]. 38
4.2 Quasi-static test results at 5 mm/min and 30.5 kN/s [15]. 39
4.3 Calculated applied strain energy per cycle (W_a) over normalised life. 40
4.4 Calculated ratio W_h/W_a per cycle (W_a) over normalised life. 40
4.5 Fatigue derived viscoelastic loss factor $\sin(\phi)$ over normalised life, including DMA reference. 42
4.6 Fatigue derived loss moduli (E'') vs normalised life, indluding DMA reference. 43
4.7 HCFS determination using effective loss factor vs the applied maximum stress. 45
4.8 Bi-linear energy dissipation rate trends for a) current prediction and b) reference data by Colombo et al. [67] for $\pm 45^\circ$ woven glass/epoxy. 46
4.9 Predicted two-domain TDE/TW ratio vs maximum stress trend. 46
4.10 Log-linear trend of total dissipated energy (TDE) and max stress at R=0.1. 47

5.1 Puck-based quasi-static tensile test simulation of the various laminate options. 52
5.2 Puck-based quasi-static tensile test simulation of the [0/90] laminate at two strain rates of 10^{-4} and 10^{-1} s^{-1}. 55
5.3 Evaluated dogbone fatigue specimen geometries: A) linear, B) double radius and C) single curve reduction without constant gauge section. 57
5.4 Maximum S_{12} shear stresses along clamp-to-clamp distance comparison between optimised iterations of type A, B and C dogbone geometries for 15 mm gauge width and 20 mm tab width. 59
5.5 Maximum Tsai-Wu failure index along clamp-to-clamp distance comparison between optimised iterations of type A, B and C dogbone geometries for 15 mm gauge width and 20 mm tab width. 60

5.6 Final iteration dimensions of the tensile and fatigue specimen geometry. 61
5.7 Maximum τ_{12} shear stresses along clamp-to-clamp distance for the final selected geometry. 61
5.8 Maximum Tsai-Wu failure index along clamp-to-clamp distance for the final selected geometry. 62
5.9 Maximum S_{12} shear stress based mesh convergence for the final selected specimen geometry. 62
5.10 Comparison of strain rates for constant frequency, constant stress rate and constant strain rate conditions. 65
5.11 Required testing frequency vs maximum stress for constant strain rates at $R = 0.1$, 0.3 and 0.5. 65
5.12 Comparison of applied energy rate for constant frequency, constant stress rate and constant strain rate conditions. 66
5.13 Time spent above 90% of σ_{max} per cycle vs R-ratio for four constant strain rate conditions. 67
5.14 Experimental set-up used for high-rate monotonic tensile and fatigue testing. 67
5.15 TA Instruments RSA-G2 solids analyser used for the DMA measurements. 70
5.16 Two used DMA bending set-ups: a) 3-Point Bending (3PB), b) Dual Cantilever Bending (DCB). 71

6.1 Flowchart representing the flow of data and processing steps. 72
6.2 Flowchart representing the DIC processing procedures. 73
6.3 Example of the DIC processing scheme output for first recording of test F-21 at R0.3 325 MPa. 74
6.4 μDIC implementation relative error w.r.t. 2D-VIC for first DIC batch of each test. 75
6.5 Example of DIC-based maximum strain correction function for test F21 at R0.3 325 MPa. 76
6.6 Example of DIC-based minimum strain correction function for test F21 at R0.3 325 MPa. 76

7.1 Monotonic tensile test results at quasi-static 5 mm/min and dynamic 25.5 mm/s displacement rates. 80
7.2 Maximum stress vs fatigue life ($S - N$) curves for the performed fatigue tests at $R = 0.1$ and $R = 0.3$. 81
7.3 Stress amplitude vs fatigue life ($S_a - N$) curves for the performed fatigue tests at $R = 0.1$ and $R = 0.3$. 82
7.4 Complex modulus degradations over normalised fatigue lives for $R = 0.1$ (solid) and $R = 0.3$ (dashed) tests. 82
7.5 Comparison of fatigue life average complex moduli across the tested maximum stresses and R-ratios. 83
7.6 Average cycle strain rate over normalised fatigue lives for $R = 0.1$ (solid) and $R = 0.3$ (dashed) fatigue tests. 84
7.7 Fatigue failure strains vs cyclic maximum gauge stress. 84
7.8 Fatigue failure strains vs cyclic maximum gauge stress collapsed to an equivalent $R = 0$ case. 85
7.9 Infrared temperature measurements during tests F-4 and F-5. 86
7.10 Hysteresis energy dissipation W_h over the normalised fatigue lives for $R = 0.1$ (solid) and $R = 0.3$ (dashed) tests. 86
7.11 Example of hysteresis loop shape change throughout fatigue life for F-2 at 400 MPa $R = 0.1$. 87
7.12 Modified viscoelastic loss factor $\sin(\phi_i)$ progression over normalised fatigue lives for intermediate to low stresses at $R = 0.1$ (solid) and $R = 0.3$ (dashed). 88
7.13 Comparison of final failure damage at increasing maximum fatigue stress (350, 450 and 650 MPa) at $R = 0.3$. 89
7.14 Log-linear critical dissipated energy (CDE) vs σ_{max} curves for $R = 0.1$ and $R = 0.3$ fatigue datasets, including overlapping 95% confidence intervals. 89
7.15 DMA measured storage modulus and loss factor vs temperature for the 3PB and DCB mode tests. 90
7.16 Reduced DMA measured storage modulus and loss factor vs temperature plot, focussed on the more representative $25 - 100°C$ temperature range. 91

7.17 Effective loss factors $\sin(\phi_{eff})$ vs maximum cyclic gauge stress and their intersection with the DMA measured loss factors for HCFS estimation. 92
7.18 Energy dissipation of the first cycle in each fatigue test vs the maximum cyclic gauge stress. 92
7.19 Comparison of DMA and $\sin(\phi_{eff})$ based dissipation rate prediction $\dot{W}_h$ and stabilised infrared temperature measurements. 93
7.20 Critical dissipated energy (CDE) vs cycles to failure (N_f) for the $R = 0.1$ and $R = 0.3$ fatigue datasets. 94
7.21 R-ratio normalised critical dissipated energy (CDE) vs cycles to failure (N_f) for the $R = 0.1$ and $R = 0.3$ fatigue datasets. 95
7.22 Predicted stress amplitude vs fatigue life ($S_a - N$) curves using the $R = 0.1$ dataset as model input and $R = 0.3$ as validation data. 95

A.1 Maximum S_{12} shear stresses along clamp-to-clamp distance comparison between iterations of type A dogbone geometries. 118
A.2 Tsai-Wu failure indices along clamp-to-clamp distance comparison between iterations of type A dogbone geometries. 118
A.3 Maximum S_{12} shear stresses along clamp-to-clamp distance comparison between iterations of type B dogbone geometries. 119
A.4 Tsai-Wu failure indices along clamp-to-clamp distance comparison between iterations of type B dogbone geometries. 119
A.5 Maximum S_{12} shear stresses along clamp-to-clamp distance comparison between iterations of type C dogbone geometries. 120
A.6 Tsai-Wu failure indices along clamp-to-clamp distance comparison between iterations of type C dogbone geometries. 120

B.1 Laminated specimen and tab material plates vacuum bagged ready for curing. 122
B.2 Initial pre-cut $0/90$ specimen strips. 123
B.3 Post-machined monotonic tensile and fatigue specimen. 124
B.4 3D-printed tool for tapering of the composite tabs to a consistent angle. 124
B.5 Tapered $\pm 45^\circ$ glass/epoxy tabs ready for bonding. 125
B.6 Clamping arrangement for tab bonding. 125
B.7 Example of a number of testing-ready dogbone specimen including DIC speckle pattern. 126

C.1 Overview of failed specimen: Part A (F-1 to F-4). 134
C.2 Overview of failed specimen: Part B (F-5 to F-8). 134
C.3 Overview of failed specimen: Part C (F-9 to F-12). 135
C.4 Overview of failed specimen: Part D (F-13 to F-16). 135
C.5 Overview of failed specimen: Part E (F-17 to F-20). 135
C.6 Hysteresis energy dissipation W_h over the normalised fatigue lives for high stresses ($\sigma_{max} \geq 600$ MPa) at $R = 0.1$ (solid) and $R = 0.3$ (dashed). 136
C.7 Modified viscoelastic loss factor $\sin(\phi_i)$ progression over normalised fatigue lives for high stresses ($\sigma_{max} \geq 600$ MPa) at $R = 0.1$ (solid) and $R = 0.3$ (dashed). 136
C.8 Cyclic dissipation ratios $\frac{W_h}{W_a}$ over normalised fatigue lives at $R = 0.1$ (solid) and $R = 0.3$ (dashed). 137

List of Tables

4.1 Fatigue test maximum stresses and corresponding average frequency, fatigue life and failure strain as obtained from [15]. . . . 38
4.2 Calculated initial moduli for the various stress levels. . . . 39

5.1 Glass fibre UD prepreg material details. . . . 50
5.2 Assumed UD glass-fibre epoxy mechanical properties [72]–[75]. . . . 51
5.3 Progressive failure knockdown factors [78], [79]. . . . 51
5.4 Comparison of moduli and failure stresses across the laminate options. . . . 52
5.5 Laminate selection trade-off table. . . . 53
5.6 Percentage in mechanical property increase of E-glass/epoxy UD between quasi-static strain rate and $1 \cdot 10^{-1} s^{-1}$ as reported in [48]. . . . 54
5.7 Expected quasi-static vs equivalent rate dynamic tensile test parameters. . . . 54
5.8 Produced specimen allocation and dimensions. . . . 63
5.9 Overview of fatigue testing parameters. . . . 69

7.1 Overview measured laminate tensile properties. . . . 79
7.2 Overview of maximum stress, average gauge stress, cycles to failure and failure strains for the $R = 0.3$ fatigue tests. . . . 80
7.3 Overview of maximum stress, average gauge stress, cycles to failure and failure strains for the $R = 0.1$ fatigue tests. . . . 81
7.4 Overview of critical dynamic mechanical analysis testing parameters. . . . 90

B.1 Glass fibre UD prepreg material details. . . . 121
B.2 Recommended curing cycle for laminates up to 5 mm thickness. . . . 123

Contents

Preface i

Abstract ii

Nomenclature iii

1 Introduction 1

2 Literature Review 4
2.1 Stress-strain hysteresis . . . 4
2.2 Application of hysteresis loops . . . 5
2.3 Sources of viscoelastic damping . . . 6
2.4 Composite fatigue damage mechanisms . . . 7
2.5 Effects of frequency, strain-rate, R-ratio and temperature . . . 10
2.6 Strain energy dissipation based fatigue analysis methods . . . 16
2.7 Reflection on initial TDE/TW hypothesis . . . 20
2.8 Adjusted hypothesis and objectives . . . 21
2.9 Research questions . . . 23

3 Viscoelastic Theory 24
3.1 Linear viscoelastic approach . . . 24
3.2 Viscoelastic loss factor . . . 27
3.3 Linear viscoelastic hysteresis energy dissipation . . . 28
3.4 Limitations of linear hysteresis dissipation . . . 30
3.5 Energy based correction factors . . . 31
3.6 Cyclic dissipation ratio $\frac{W_h}{W_a}$ . . . 34
3.7 Total dissipated energy, total work done and TDE/TW ratio . . . 35
3.8 Extension to fatigue life prediction . . . 35
3.9 Conclusion of approach . . . 36

4 Preliminary Analysis 37
4.1 Reference fatigue dataset . . . 37
4.2 Modulus degradation and hysteresis energy . . . 38
4.3 Cyclic dissipation ratio W_h/W_a . . . 39
4.4 Conversion to viscoelastic characteristics . . . 41
4.5 Estimating high cycle fatigue strength . . . 44
4.6 Relation to TDE/TW vs maximum stress . . . 46
4.7 Total dissipated energy . . . 47
4.8 Preliminary analysis conclusions . . . 48

5 Experiment Design and Execution 49
5.1 Testing objectives . . . 49
5.2 Choice of material . . . 50
5.3 Composite layup selection . . . 51
5.4 Dynamic property prediction . . . 54
5.5 Specimen design . . . 55
5.6 Produced specimen overview . . . 62
5.7 Fatigue loading parameter evaluation . . . 64
5.8 Tensile and fatigue testing experimental set-up and procedure . . . 67
5.9 Dynamic mechanical analysis . . . 70

6 Data Processing **72**
6.1 DIC processing . . . 73
6.2 DIC-based strain correction . . . 75
6.3 Calculation of fatigue metrics . . . 77
6.4 DMA data processing . . . 78

7 Results **79**
7.1 Monotonic tensile tests . . . 79
7.2 Overview of general fatigue performance . . . 80
7.3 Hysteresis dissipation and loss factor progression . . . 85
7.4 Total and critical dissipated energies . . . 88
7.5 Dynamic mechanical analysis . . . 90
7.6 Effective loss factor and HCFS . . . 91
7.7 Fatigue life predictions . . . 93

8 Discussion **97**
8.1 Evaluation of changing loss factors throughout fatigue life . . . 97
8.2 Effective loss factor, DMA correlation and HCFS estimates . . . 98
8.3 Application of TDE and CDE and their dependence on R-ratio . . . 101
8.4 TDE/TW-ratio and its hypothesised two-domain trend . . . 102
8.5 Fatigue failure strains . . . 103
8.6 Limitations of the current work . . . 103

9 Conclusions **106**
9.1 Answers to sub-questions . . . 106
9.2 Main research question and overall conclusion . . . 108

10 Recommendations **109**

References **111**

A Additional specimen geometry FEA results **117**
A.1 Geometry type A . . . 117
A.2 Geometry type B . . . 119
A.3 Geometry type C . . . 120

B Specimen production overview **121**
B.1 UD prepreg material . . . 121
B.2 Cutting of prepreg material . . . 122
B.3 Material lamination and curing . . . 122
B.4 Specimen cutting and machining . . . 123
B.5 Tab preparation and bonding . . . 124
B.6 DIC speckle pattern . . . 126
B.7 Deltapreg BT080 datasheet . . . 126

C Additional experimental results **134**
C.1 Failed specimen overview . . . 134
C.2 High stress level dissipation plots . . . 136
C.3 Cyclic dissipation ratios . . . 137

1

Introduction

It's been over 150 years since fatigue phenomena were first studied and incorporated into engineering applications, pioneered by August Wöhler's investigation into failing train axles. As worded well by Bhangale in [1], the development of fundamental theories in these early days of fatigue analysis greatly outpaced their ability to perform precise experimental observations. However, due to the progressive evolution of sophisticated testing capabilities and computer aided data analysis, particularly in recent decades, this trend has slowly reversed itself to a situation where detailed experimental fatigue observations can now be made with relative ease. Nevertheless, despite this wealth of test data, the development of further fundamental theories that support the continuous influx of observations made on new material types has lacked behind in pace [1].

This particularly holds for the fatigue analysis of fibre reinforced composites, which are inherently sensitive to small alterations in constituent material, laminate configurations and internal defects, not yet to speak about the varying effects of environmental and loading conditions. Unlike in metals, their crack initiation and propagation processes are furthermore often not dominated by a single instance or mechanism. Instead, depending on the material, loading and external conditions, a variety of damage mechanisms may (simultaneously) occur and interact with one-another such as matrix cracking, fibre-matrix debonding, delamination, fibre breakage or void growth [2]. This variation and especially the interaction of these modes combined with their dependence on external factors makes it difficult to predict which of their progressions of will lead to the dominant cause of failure under dynamic loading. Because of this, there exists no single standardized methodology for fatigue testing and analysis of composite materials that can cover all conditions and extrapolate lab controlled measurements to service life predictions across most alternative loading scenarios [3]–[5].

Therefore, in most practical applications the fatigue performance of fibre reinforced composites is still evaluated following a time and cost intensive empirical-phenomenological framework similar to those originating for isotropic metals, where many fatigue tests are performed with varying loading and environmental conditions [1], [5]. Subsequent descriptions of the failure life remain commonly expressed in terms of Wöhler S-N curves [6] and Haigh constant life diagrams [7], with predictions on non-tested intermediate conditions made based on the interpolation of the existing data. In many cases however, such sole expressions of fatigue life in terms of (log scale) number of cycles without direct connection with their underlying governing physics and failure mode interactions only further supports the knowledge gap between experiments and theory [1]. As described in Vassilopoulos' historic review of fibre-reinforced composite fatigue research [5], the abundance of scientific experimental data and documentation has allowed for a description of almost all fatigue failure mechanisms, damage evolution styles, loading and environmental effects, being able to rationalise shifts in the aforementioned S-N or CLD curves as results of individual deviations from tested conditions. However, on smaller quantity datasets such predictions are rarely deterministic outside of the tested variable ranges and do struggle with combined effects, for example creep-fatigue interaction, which limits their direct engineering application.

More recent efforts in literature aim to improve this through an understanding of the micromechanics level behaviour of composite materials under cyclic loading based on the principles of irreversible thermodynamic and continuum damage mechanics models [1], [5], [8]. Here the aim is typically to associate an irreversible portion of the cyclic dissipation of strain energy to quantify the damage energy and damage entropy accumulation in order to link this to a subsequent measure of damage growth. Although such methods do provide a greater understanding of the underlying physical principles that lead to the formation and propagation of fatigue damage in polymer-based fibre-reinforced composite materials, for laminate (or greater) scale applications these methods thus far still require interpolation or parameter determination based on substantial material and laminate fatigue testing datasets in order to come to predictions of fatigue failure life or material property residuals [1], [8].

The thesis outlined in this document aims to contribute to new work within ASM department with the goal to significantly reduce the dependence on extensive and time-consuming fatigue testing projects of FRP material across many different loading and environmental conditions, whilst still yielding acceptable physics based predictions on material fatigue characteristics. This is particularly relevant within the context the aviation sustainability transition plans [9], which sets the ambitious goal of a net-zero pollution of the industry by 2050. To meet this, the development and mechanical characterisation of fibre-reinforced composite materials would benefit greatly from accelerated understanding of macro-level energy-based composite fatigue phenomena and prediction methods. Here, the potential of improvement in consistency and predictive capability of strain energy dissipation trends over the typical fatigue life expressions in terms cycles to failure combined with alternative and more simplistic means of measuring material damping characteristics are recognised.

Early observations regarding this matter seemed to suggest that the total dissipated strain energy (TDE) divided by the accumulated work done (TW) in all fatigue load cycles to failure would yield a fixed ratio for a given composite, related to a specific failure mechanism [10]. Furthermore, it was hypothesized that such TDE/TW ratio of the composite laminate could potentially be estimated through simpler and more time effective material measurements, for example through the energy dissipation in monotonic tensile tests. The understanding of such hypothesized ratio could be a powerful tool in a strain energy dissipation based fatigue analysis framework, particularly if combined with an understanding of the accumulation of cyclic strain energy dissipation up to a critical level. Even if such dissipation ratio is proven to be not be a constant, it would remain of great potential as long as one is able to describe its progression through a predictable and physics based trend. However, currently most common fatigue testing methodologies for composites remain largely focused on expressing material failure or degradation in terms of number of cycles at fixed testing frequencies, rather than accumulated strain, dissipated strain energy or work done, and thus such potential correlations remain largely uncovered.

To evaluate the TDE/TW ratio hypothesis and to further identify related energy dissipation trends, this thesis will follow an approach of modelling the dissipated strain energy per cycle as a linear viscoelastic damping problem where new correcting terms are introduced that account for non-linear energy-based effects. Here, pure viscoelastic and plastic (damage) energy dissipation components are combined into a single effective loss factor, whose development throughout fatigue tests at varying stress levels and R-ratio combinations will be evaluated. Although on the surface simplistic, such approach can focus on the direct effects of stress levels, loading ratios and stiffness degradation without the need for extensive and continuous evaluation of non-linear viscoelastic parameters. This furthermore allows for valuable comparisons to be made to viscoelastic damping loss factors derived from methods such as dynamic mechanical analysis. To limit the scope of this thesis, the experimental focus will be kept to the analysis of continuous fibre reinforced thermoset matrix composites under tensile-tensile fatigue loading.

This thesis starts with a literature study in chapter 2, covering the fundamental principles of fatigue hysteresis, internal damping sources, fatigue damage mechanisms as well as a discussion on existing energy dissipation based fatigue analysis methods. At the end of chapter 2, the initial hypothesis is evaluated and research questions are formulated. Following this in chapter 3, the linear viscoelastic theory that forms the basis of this thesis' analysis is introduced and modified in order to derive formulations for total dissipated energy, total work applied and their ratio with explicit inclusions of the effects of R-ratio, loss factor and stiffness degradation. In chapter 4 these findings are then applied to a preliminary analysis on a $\pm 45^{\circ}$ glassfibre-epoxy dataset obtained from literature as a first proof of concept of the developed method. Based on the outcomes of this preliminary analysis, the test objectives are refined, for which a specific fatigue specimen geometry and experimental procedure are designed in chapter 5. The experimental results rely heavily on the measurements taken through high speed DIC for which an analysis pipeline was self-developed. Thererfore chapter 6 is dedicated to the DIC processing methods and their validation using the well-regarded 2D-VIC software. The experimental results are then finally presented and discussed in chapter 7 and chapter 8, respectively. Lastly, the thesis conclusions and further research recommendations are presented in chapter 9 and chapter 10.

2
Literature Review

In this chapter, an extensive review is provided on the existing literature related to the fatigue behaviour of continuous fibre-reinforced polymer composites, with particular focus on energy dissipation mechanisms and viscoelastic theory. The review aims to give the reader an overview of the concepts and causes of cyclic energy dissipation by viscoelastic composites as well as its relation to damage mechanisms and sensitivities of the inherent time-dependent characteristics. Through an evaluation of existing methods, assumptions and limitations of prior work, a research gap is identified that drives the work presented in this thesis.

First, section 2.1 introduces the concept of stress–strain hysteresis in cyclic loading, which is followed by section 2.2 that outlines some of the weaknesses in classical fatigue assessment methods in which cyclic energy dissipation evaluations play a critical augmentive role. After a giving an overview of the various damping sources in composite materials in section 2.3, after which section 2.4 discusses the different types and progressions of damage mechanisms and how these relate to energy dissipation. Section 2.5 then gives a comprehensive overview of the effects of loading frequency, strain rate, loading ratio and temperature on both material properties as fatigue damage accumulation characteristics. This is followed by section 2.6 where a selection of particularly relevant prior work is discussed. The conclusions from this discussion have lead to a reflection on the initial hypothesis in section 2.7, which paved the way for the revised hypothesis and research objectives presented in section 2.8. To finally close off this chapter, section 2.9 formulates the research questions that emerge from this literature foundation.

2.1. Stress-strain hysteresis

The cyclic energy dissipation observed in fatigue testing of fibre-reinforced polymer composite materials has its roots in the stress-strain hysteresis effect caused by internal damping [11]. When a linear elastic material is exposed to an applied stress, elastic strain energy is stored in the material. This stored strain energy equals the amount of work done by the stress to attain the corresponding strain, as shown in Equation 2.1.

$$W_a = \frac{\sigma_{max} \cdot \epsilon_{max}}{2} = \frac{\sigma_{max}^2}{2E} \tag{2.1}$$

Here, σ represents the applied stress, ϵ the resulting material strain and E the material's Young's modulus. For applied stresses below the material's elastic limit, unloading of such perfect linear elastic materials leads to all of the applied strain energy being recovered.

However, among many other material types, fibre-reinforced polymer composites do often not behave in such perfectly elastic fashion under cyclic loading. Instead, due to the viscoelastic nature of primarily the polymer matrix and the fibre-matrix interface combined with internal friction caused by fibre disbonds and crack surfaces [12], [13], the mechanical response of these materials includes a time-dependent damping component, which manifests itself as cyclic hardening and softening [5], [14], [15]. This means that under acceleration and deceleration of the applied stress in a sinusoidal cyclic load case, the material follows an unequal loading and unloading strain response, resulting in a stress-strain hysteresis loop as depicted in Figure 2.1 below.

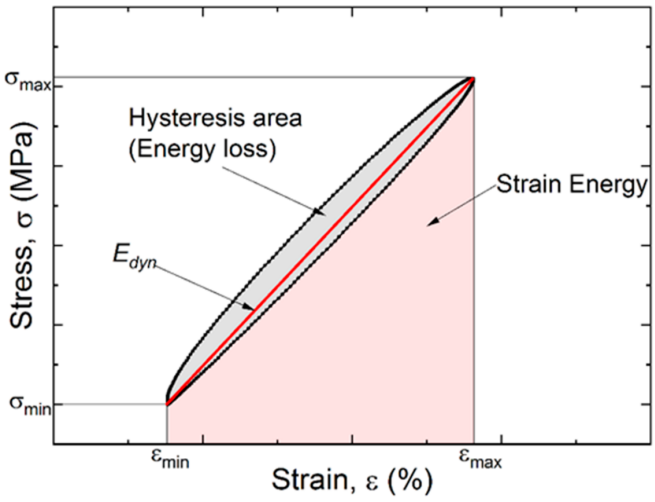

Figure 2.1: Schematic representation of a hysteresis loop under cyclic loading [16]

The area enclosed by such hysteresis loop represents this portion of the applied strain energy that is irreversibly lost during the cycle and converted into heat [17], [18]. If the cyclic stress level in the material is large enough for the formation or propagation of damage, then additional plastic strain energy is dissipated within the hysteresis loop. However, for high cycle fatigue this plastic component of dissipated strain energy is considered comparatively small to that of the viscoelastic and friction based internal damping, as reported in literature on polymer-based composite laminate fatigue [1], [8], [11].

2.2. Application of hysteresis loops

The most common fibre-reinforced polymer composite fatigue damage quantification methods are based on either residual strength, stiffness degradation or in more specific cases quantification of damage growth by crack or delamination length [19]. Bogdanov et al. [20] gave an overview of direct and indirect fatigue damage assessment methods. Here, direct measurements are classified as those that directly aim to measure the quantity or size of the fatigue damage. This includes non-destructive methods such as CT scans, ultrasound or visual inspection as well as destructive approaches in the likes of tensile testing the material for residual strength after a certain number of cycles [20]. However, as these techniques are either destructive or in most cases require the tests to paused or even aborted, they do not lend well to a continuous and uninterrupted evaluation of the fatigue damage progression up to the point of failure. Such test interruptions can have significant effect on the fatigue behaviour. This was for example shown by Vassilopoulos et al. [21] who for interrupted tests on $\pm 45^{\circ}$ glass/epoxy laminates reported increases in cycles to failure between 34 to 126% of those measured on uninterrupted laminates. One of the major contributors to this effect was the distinct creep relaxation during the the unloaded phase.

To avoid such additional variables, uninterrupted tests are typically much favoured unless the viscoelastic creep relieve behaviour is the primary research objective. However, the difficulty of specimen access without the interruptions limits the direct measurements that can be taken. Therefore, continuous fatigue monitoring and damage assessment methods are often distinguished as indirect [20]. Here, the most widely used indirect damage quantification method is by evaluating the degradation of the dynamic modulus of the material, shown as E_{dyn} in Figure 2.1 [1], [5], [20]. This can be considered as the effective stiffness of the material between the two extremes of the hysteresis loop. As damage in the composite laminate accumulates, the fatigue modulus generally decreases, tilting (and stretching) the hysteresis loop. The progression of this decrease in stiffness throughout a fatigue test compared to its initial value, described by the ratio E_i/E_0, is the most commonly accepted parameter in literature to indirectly describe the state of damage in the composite [1], [5], [11]. However, for different materials, testing styles and failure mechanisms, such stiffness degradation rules can show vastly different progressions. Some largely continuous fibre dominated laminates may not even show a well traceable

stiffness degradation at all until very shortly before failure [1], [20], [22]. This does however not mean that no damage is forming in the material, only that it is effecting the stiffness in a reduced manner. Because of this variance in relation of stiffness degradation to actual internal damage formation, there can be a disconnect between the indirect fatigue damage parameter and the actual state of damage in the laminate.

Considering the limitations of a pure stiffness degradation approach, the analysis of the energy dissipation within the hysteresis loops can offer an additional insight into the behaviour of fibre-reinforced composites under cyclic loading. Here the particular link of interest is that of an internal damping factor, which can relate the magnitude of dissipated hysteresis energy to the applied energy/work done in the cycle as a measure of relative energy loss. Such damping factors, which are conceptually closely related to the hypothesised TDE/TW ratio, can be expected to increase throughout a fatigue tests due to increasing damage-based friction [13]. Because of this relation to damage-based dissipation, hysteresis loops are an increasingly resorted tool in fatigue analysis to augment classical stiffness degradation based approaches [5].

In addition to stiffness degradation and energy dissipation, the the hysteresis loops of cyclicly loaded fibre-reinforced polymers also tend to shift on the positive strain axis as indication of progressive accumulation of strain [16], [23]. This strain shift of the hysteresis loops towards an final fatigue failure strain is referred to as fatigue ratcheting and is most commonly associated with fatigue creep in stress cycles with a non-zero mean stress [5].

2.3. Sources of viscoelastic damping

The stress-strain hysteresis in fibre-reinforced polymer composites involves a number of simultaneous damping mechanisms, making their response slightly different to those of conventional viscoelastic materials. According to reviews on damping characteristics by Chandra et al. [13] and Tang et al. [24], the primary damping mechanisms in fibre-reinforced polymer composites can be categorised as follows:

- **Viscoelastic characteristics of the constituent materials:** As the name suggests, this means the characteristics of the materials that make up the composite itself, in which the major contributor is the viscoelastic polymer matrix with its chain structure. Upon deformation, these polymer chains re-align and slide past one another creating friction and thus internal damping, of which the magnitude is dependent on the rate of the applied strain (i.e. the velocity of the sliding) [13], [24]. Generally, the direct individual viscoelastic contribution of the volume of fibres is comparatively much less than that of the matrix [13], [25]. Across different fibre types, their degree of viscoelasticity varies depending on their material structure. Apart from their own damping characteristics, the modulus of the fibres effects the overall damping of the laminate. Low modulus fibres generally result in larger strains on the matrix, which amplifies the relative viscoelastic contribution that the matrix has on the overall composite laminate damping characteristics.
- **Fibre-matrix interface damping:** The second viscoelastic contribution to damping in fibre-reinforced composite is related to the interface between fibre and matrix. This so called 'interphase' is the distinct transition region between the chemical treatment layer on the fibre (so called sizing) and the bulk matrix [13], [26]. Despite this interphase region being typically a number of magnitudes smaller than the fibre diameter, it still has a critical role in the mechanical performance of the fibre-matrix bond [13]. Differences in sizing diffusion, degrees of cross-linking and residual stresses effect the damping characteristics of the interphase region relative to the bulk matrix. However, both Chandra et al. [13] and Tang et al. [24] noted in their reviews that the primary damping contribution of the fibre-matrix interface is related to its strength. Here, weaker interfaces have been shown to increase damping characteristics of the composite through fibre-matrix slip initiation with consequent increase of internal friction in the laminate [13], [24], [27].

- **Internal friction due to damage:** As eluded to in the previous bullet-point, the damping characteristics and energy dissipation in fibre-reinforced composites change due to the formation and propagation of internal damage. Is is predominantly in the form of friction caused by fibre-matrix slip as well as that between crack and delamination surfaces. This mechanism of damping has been described in literature as being more sensitive to the state of fatigue damage in the composite than evaluating solely the degradation of the laminate stiffness as per common practice [13], [27]. Like discussed in section 2.2 makes a strong point for the need to continuously evaluate the damping through energy dissipation during a fatigue test for an improved understanding of the damage progression.
- **Viscoplastic damping:** Finally, viscoplastic damping is related to the strain energy dissipation by local yielding of matrix material in stress-concentrated regions around fibres or at the crack tips [28]. For thermoset polymers, like epoxy based matrices, the mobility of the polymer chains is very limited due to dense cross-linking. This results in minimal local plastic deformation before final failure, which gives epoxy-based thermoset matrices their brittle nature. As result of this the viscoplastic damping effects can be assumed to be small in comparison to viscoelastic and friction based damping contributions [13], [24]. On thermoplastic matrices however, plasticity and yielding are not restrained by cross-linking, resulting in a more ductile behaviour instead. Regarding this, Kenny and Marchetti [28] for example showed a clear increase in hysteresis energy of angle-ply carbon/PEEK laminates at maximum stress levels above the matrix yielding threshold. This would suggest that for thermoplastic matrix based composites, the contribution of viscoplastic damping cannot simply be ignored.

2.4. Composite fatigue damage mechanisms

In the previous sections, the change in hysteresis stiffness and dissipated energy through damping were associated with viscoelastic material properties, but also damage accumulation. However, as mentioned in the introduction of this thesis, the damage initiation and propagation mechanisms in fibre-reinforced polymer composites are not dominated by a single damage type or process. Therefore, to further understand what fatigue damage in such laminate means, this section aims to establish a brief overview of the typical types of fatigue damage mechanisms observed in various configurations of fibre reinforced composite laminates.

Damage in composite materials is mostly associated by the creation of discontinuities in either the constituent materials or their interface, which can be categorised by matrix cracking, fibre breakage, matrix-fibre debonding and ply delamination [1], [22], [29]. Talreja [22] reviewed the basic damage mechanisms and their interaction of various laminate configurations, which for tensile-tensile fatigue loading are summarised here below:

- **On-axis unidirectional laminate:** In unidirectional laminates the load acts parallel to the fibre directions. Due to statistical distribution in strength of the fibres, combined with surrounding material defects, first fibre breakages may occur well below the static failure strength of the laminate [29]. As result of a fibre break, a shear stress concentration is formed in the nearby fibre-matrix interface. Depending on the interface strength, this can lead to debonding of the fibre from its neighbouring matrix [22]. Consequently, a longitudinal stress concentration in the debonded matrix area acts as a nucleation site for transverse matrix cracks. In case of sufficiently low cyclic stress or strain levels, such transverse cracks may be halted from any further propagation by the next fibre encounter. This crack arresting is shown in the so called 'fatigue life diagram' of Figure 2.2 below a suggested high cycle fatigue limit. At high stress levels however, the stress concentration at the matrix crack tip can be enough to induce a new debonding with the encountered fibre and again propagate as matrix crack on the other side of the fibre creating fibre bridging. Ultimately when the density of such transverse matrix cracks, fibre-matrix debonds and/or fibre bringing become great enough, a chain reaction of fibre failure is set off [22].

- **Off-axis unidirectional laminate:** Such laminates have a fibre orientation at $0° < \theta < 90°$ relative to the load. As a result of this angle, the dominant fatigue fracture mechanism will be a combined mode between crack opening normal to the fibres and shear component in parallel [22]. For increasing off-axis angle, the opening mode is said to become increasingly dominant to the extreme case at $\theta = 90°$, which is limited purely by the transverse fibre-matrix interface strength [22], [29]. Once a transverse interface crack has initiated, it quickly propagates both along the length of the fibre as well as being able to jump to and chain up with those on tightly packed neighbouring fibres [30].
- **Angle-ply laminate:** These contain alternating layers at fibre orientations of $\pm\theta$, where again $0° < \theta < 90°$. Common types of angle-ply laminates are at $\pm 30°$, $\pm 45°$ or $\pm 60°$. Here, the damage mechanisms are essentially as discussed for the off-axis UD laminates, however with the further influence of delamination growth in between the alternating layers due to interlaminar stresses [22].
- **Cross-ply and quasi-isotropic laminates:** Finally, these laminate options consist of respectively $[0/90]_s$ and $[0/\pm 45/90]_s$ stacking arrangements. The sequence of their dominant damage mechanisms in both cases is reported to be initiated by the transverse fibre-matrix debonding in the $90°$ layers [22]. For quasi-isotropic laminates, this is then followed by debonding along the $\pm 45°$ fibres, which at this angle is dominated by shear. These debonds then accumulate and grow as cracks towards the interfaces with the adjacent plies in the laminate, leading to the formation and propagation of delamination [22]. As such delaminations greatly reduces the load distribution and load-sharing between the layers, the main load carrying $0°$ fibre layers are quickly overloaded until final failure.

For these last two categories in particular, Pipes and Reifsnider [31] introduced a general 3-stage description of fatigue damage development as shown in Figure 2.3.

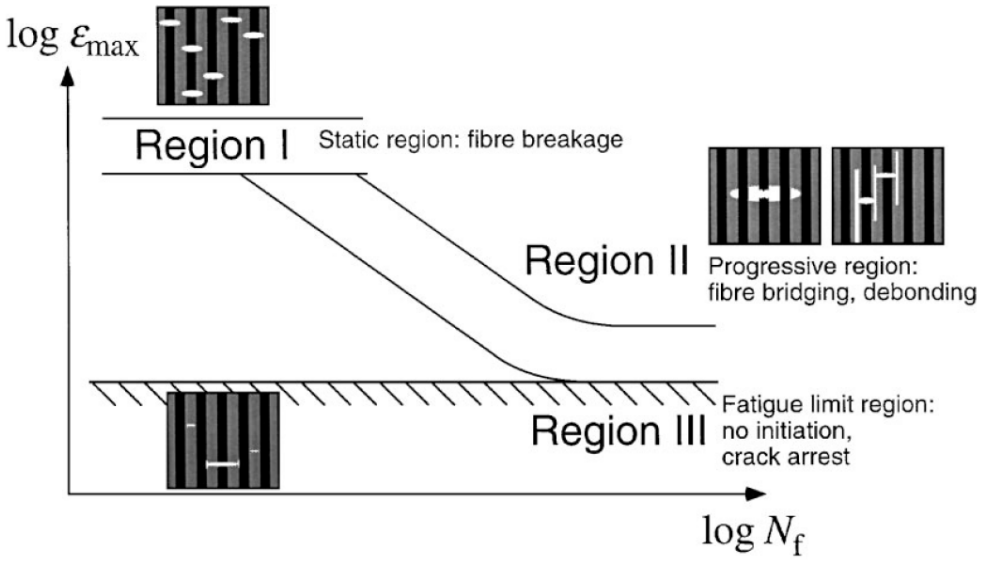

Figure 2.2: Dominant damage mechanisms in unidirectional laminate fatigue [29]

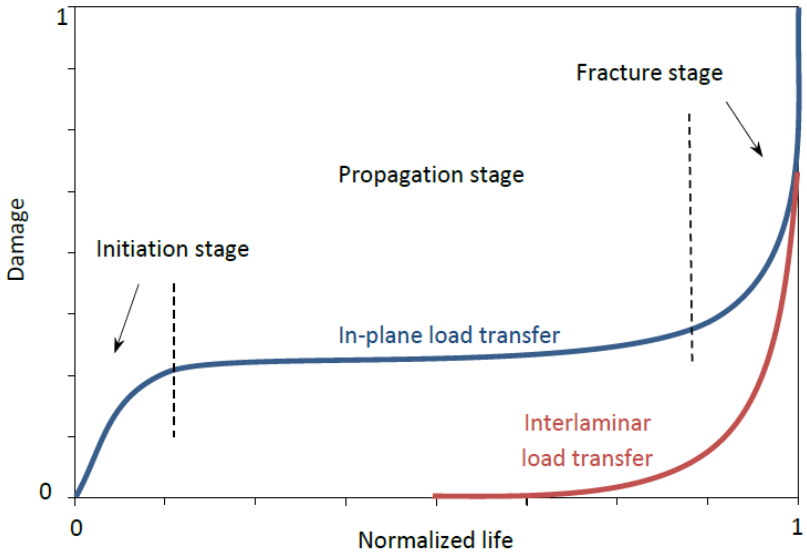

Figure 2.3: Generalised fatigue damage evolution stages [1]

The first stage of fibre-reinforced polymer composite fatigue damage is called the initiation stage and typically lasts less than 15-20% of the total fatigue life [1]. Here, the matrix microcracks and fibre-matrix debonds as described before are rapidly initiated, resulting in reduced load transfer to and between fibres, and therefore a swift initial reduction in mechanical properties of the laminate [29]. The second phase in the fatigue damage evolution is the propagation stage. For low to medium cyclic stress levels, the damage growth rate usually stabilises for the majority portion of the fatigue life, as the matrix cracks and fibre-matrix debonds slowly saturate [1]. As described for the cross-ply and quasi-isotropic laminates, this propagation reaches the adjacent plies, causing a delayed initiation of interlaminar fracture in the ply interfaces. This ultimately leads to rapid delamination growth pushing the laminate into its final fracture stage, where main load carrying 0° layers are overloaded to fibre fracture.

From this generalised failure progression, it be concluded that the matrix material and particularly the fibre-matrix interface strength play a critical role in the fatigue damage initiation and propagation. In composite systems with a high fibre-matrix bond strength such as carbon/epoxy systems, matrix cracks running perpendicular to the fibre direction have a greater likelihood in either being arrested from further propagation by a fibre encounter [29]. Furthermore, a higher interface strength reduces the transverse debond initiation in off-axis layers which was identified as one of the critical damage initiation mechanisms in multi-direction laminates. The progression such damage formation effects the magnitude of the dissipated hysteresis energy in two primary ways. First off, under constant stress amplitude fatigue loading, a decrease in laminate stiffness proportionally increases the strain amplitude and therefore the amount of work done on the laminate each cycle. Next to this, the increase in internal friction as result of the formed damages is expected to raises the effective damping factor [13]. Thus the combination of both a larger energy input with a higher damping factor means an overall increasing magnitude of hysteresis energy dissipation.

As final remarks to this section, both fibre modulus (E_f) and fibre volume fraction (FVF) are widely reported in literature to have a great effect on the fatigue resistance of the composite [25], [29], [32]–[35]. Lower reinforcing fibre moduli and/or fibre content reduce the overall laminate stiffness, hence again a larger amount of work being done on the matrix and fibre-matrix interface each cycle. The combination of these consequently leads to fibre-matrix interface debonding at lower stresses than in higher modulus fibre systems [25]. Increasing the fibre volume fraction initially contributes to a similar effect by reducing the strain on the matrix, however at too high FVF the presence increasing void content is detrimental to the initiation stage of the fatigue life [33], [34].

2.5. Effects of frequency, strain-rate, R-ratio and temperature

As has become clear from the preceding sections, the varying degrees of viscoelasticity and friction based damping in fibre-reinforced polymer composites give these materials time-dependent characteristics. As Reifsnider [36] put it well already in the 1980's, one must be cautious to not fully detach such time-dependent characteristics of the material in the pursuit of fatigue descriptions as a pure cycle dependent process. Thus, when aiming to express the fatigue performance of a material in a cycle-based phenomenological framework using S-N curves and constant life diagrams, the intrinsic material sensitivities to standard fatigue loading and environmental parameters such as frequency, applied strain rates, stress ratio and temperatures should first be carefully understood and aimed to be isolated from pure cyclic phenomena. One particular material system under specific conditions may be more sensitive to creep, where so called 'time at load' could be the critical fatigue criteria rather than cycles to failure [19]. For another, the effects of loading rate, critical energy dissipation, or perhaps temperature have greater consequences on its fatigue life [37], [38]. Each of these effects have been widely reported upon in literature for a plethora of fibre and matrix combinations as discussed in Vassilopoulos' review [5]. However, these findings are often contradictory depending on the tested material or are very much intertwined. This section therefore aims to, as best as possible, set a general overview of the individual effects of these fatigue loading parameters within the current context of viscoelastic fibre-reinforced polymer composites. This shall then be an important reference for the design of the experimental phase of this thesis.

2.5.1. Frequency effects

The most straightforward to adjust fatigue loading parameter is arguably the cyclic frequency, i.e. the amount of load cycles exerted each second. For intermediate to high cycle fatigue testing, the chosen frequency mandates the test duration and therefore a high frequency is favourable from an experiment time and cost standpoint. The ASTM D3479/D3479M standard for tension-tension fatigue testing of polymer composite materials [39] suggests that all fatigue tests under varying stress levels and load ratios should be performed under constant and equal frequency, unless there are specific research purposes to not do so. The upper limit of acceptable testing frequency according to both ASTM D3479 as well as most common literature is one before which hysteresis heating takes a dominant effect on the fatigue behaviour [1], [5], [39]. This form of self-heating is the result of the now well discussed cyclic energy dissipation through internal damping, whose heating power is proportional to the cyclic frequency. As this is thus very dependent on the damping properties the particular material is, the ASTM D3479 standard does not recommend any universal testing frequency limit. However, across studies in literature between 5 to 10 Hz is most commonly used [1], [5], [38], [40], [41].

Although self-heating is the common criteria for frequency selection in literature, it is not the only dominant frequency effect. For example, Perreux and Joseph [42] evaluated the frequency effects on tensile-tensile fatigue life of pressurised $\pm 55^{\circ}$ filament wound E-glass/epoxy composite pipe samples. These authors showed that for varying stress levels, increasing testing frequencies between 0.2 and 1 Hz consistently improved the amount of cycles to failure. However, for load cycles at 1 to 5 Hz the fatigue life was shown to remain almost constant. When additionally comparing the maximum and minimum strains for each cycle at 0.2 and 1 Hz, Perreux and Joseph showed that despite similar strain amplitudes, both minimum and maximum strains were higher for the lower of the two frequencies. These authors therefore contributed this frequency effect to a matrix creep dominant process, where at low frequencies the material is exposed to load near its cyclic peak for a longer duration each cycle. Under this longer exposure, viscoelastic and viscoplastic creep is given more time to accumulate per cycle towards a critical value, therefore decreasing the fatigue life expressed in cycles.

Crowther et al. [43] made similar observations on mixed chopped-mat and woven-layer glass/polyester laminates exposed to trapezoidal loading cycles. Here, the loading and unloaded rates were kept constant, such that the frequency changes only effected the holding time at the peak stress. They showed that for low frequencies up to 0.25 Hz, the fatigue life followed an accumulated 'time under load' criteria for creep-dominated failure. At frequencies beyond this 0.25 Hz, the fatigue life would again best be described in cycles to failure irrespective of time. Crowther et al. therefore suggested the existence of a 'boundary frequency' that separates these creep and cycle dominated frequency regimes. For

similar trapezoidal constant loading rate waveforms, Mandell and Meier [44] also showed extended lives of $[0/90]_s$ E-glass/epoxy laminates at increasing frequencies as result to reduced time at load. Epaarachchi and Clausen [19] confirmed a similar a creep dominated regime between 0.1 to 1 for the typical sinusoidal waveform loaded triaxial glass/epoxy laminates.

Eftekhari and Fatemi [45] showed that for short glass-reinforced polypropylene, increasing testing frequencies between 0.25 to 4 Hz also increased the fatigue life. However, unlike the previous sources, Eftekhari and Fatemi contributed this increased life to a stern reduction of hysteresis energy dissipation each cycle. Instead of the creep based 'time at load' being the critical factor, this suggested a fatigue failure criteria related to the total cyclic energy dissipation. Here in particular, the material's sensitivity of viscoelastic damping to the increase in strain rate by means of frequency would have played a pivotal role in lowering the energy dissipation per cycle, thus increasing the fatigue life at higher frequencies. This particular effect will be explored further in subsection 2.5.2.

Baere et al. [46] on the other hand presented results showing that for carbon/PPS unidirectional composite, frequency changes up to 5 Hz did not result in any significant effect on fatigue performance. This was contributed to the near negligible time-dependent characteristics of such fibre dominated unidirectional carbon laminate. Hence, creep nor strain rate sensitivities were suggested to have any significant effect here.

From the above selection of sources, it is concluded that testing frequency has a wider possible set of effects on the fatigue performance of fibre-reinforced polymer composites than just self-heating alone. For both thermoset and thermoplast matrix dominated laminates at frequencies below 1 Hz creep effects must be particularly considered. At higher frequencies typically self-heating does become a limiting factor. However, of particular importance for this thesis are the noted changes in viscoelastic damping as result of increased strain rates at higher frequencies. This is generally an under-represented phenomenon in testing frequency justification in literature.

2.5.2. Strain rate sensitivity

For viscoelastic polymer materials with their combined elastic and viscous characteristics, the apparent stiffness of the material will vary depending on the rate of deformation [17]. This also holds for most fibre-reinforced polymer composites, with the general exception of heavily zero degree unidirectional layer dominated carbon fibre laminates [46], [47] However, literature has shown that other characteristics of fibre reinforced polymer composites, such as their ultimate strength, failure strain and damping factor are also a function of the applied the strain rate [47].

The effect of strain rate on the mechanical properties of a composite material can be tested reasonably well in isolation using a high speed material testing machine or through the use of a Hopkinson bar device [47], [48]. For example, Kwon et al. [49] performed an extensive study on the effects of strain rate on the tensile properties of $[0]$, $[90]$, $[0/90]_s$, $[\pm 45]$ and $[0/\pm 45/90]_T$ carbon/epoxy laminates. Here, strain rates were varied between a large range of 0.001 s^{-1} to 100 s^{-1} using such high speed material testing machine. In line with the already discussed carbon/PPS results by Baere et al. [46], Kwon et al. concluded negligible changes in elastic modulus, failure strength and failure strain for pure 0 degree unidirectional carbon/epoxy. Here the authors argued that the carbon fibres themselves are strain rate insensitive and so dominant on the 0° tensile properties that the strain rate sensitivity of the matrix does not result in any measurable distinction of properties. However, for the same tests on the matrix-dominated 90° specimen the elastic modulus was shown to increase significantly by 53%, the strength by 80% and the failure strain by 65%. Combined, the $[0/90]_s$ still retained a reasonable rate dependent gains of 16%, 27% and 10% for stiffness, strength and failure strain respectively. For a $\pm 45^\circ$ configuration the laminate stiffness attained only a minor stiffness increase of 6%. But, most noticeably the elastic limit, ultimate strength and failure strain all increased by about 100% when comparing 0.001 s^{-1} to 100 s^{-1} results.

These results by Kwon et al. would thus suggest that even for strain rate insensitive fibres such as carbon, the rate dependence of the polymer matrix and fibre-matrix interface still shows its hand in combined orientation layups. Here, matrix tension in 90° unidirectional layers has the most effect on the change in modulus. Increases in ultimate strength on the other hand were assumed related to a delayed fibre-matrix debond initiation under high strain rates [49].

Although it is experimentally interesting to evaluate changes in tensile properties between two (or more) distinct strain rates, from an engineering and application point of view a common means of strain rate sensitivity description is of much more practical importance. Regarding this, literature has repeatability suggested that for a range of different FRP material systems the changes in tensile properties are largely proportional with the log of strain rate [37], [47], [48]. This then forms a more universal rate sensitivity description in terms of percentages of property change per so called 'decade' (factor 10x) in applied strain rate. As most materials lend themselves well to such log-linear trends, the strain rate sensitivities of different material systems can be easily compared. Most relevant comparison for this thesis was that of carbon vs glass reinforced epoxies. Here, Kwon et al [49], Daniel et al. [37] and Harding and Welsh [50] all agreed on negligible strain rate sensitivities of carbon/epoxy UD along the fibre direction. For E-Glass/epoxy UD on the other hand Barré et al. [48] reported a stiffness sensitivity of 2-3% per decade strain rate and strength sensitivity of around 8% per decade. Both these authors as well as Jacob et al. [47] in their review on the rate effects on polymer composite materials attributed this to a small natural rate sensitivity of the bare glass fibres in combination with their lower fibre modulus and strength, such that the relative contribution of the matrix is amplified.

As will be discussed more extensively in chapter 5, ASTM standard quasi-static and fatigue testing strain rates can easily be separated by 2 to 3 orders of magnitude [41]. In the case of the above mentioned glass/epoxy material this would equate to an estimated strength increase of 16 to 25 percent. However, the beneficial effects of such relative strength increase on the fatigue performance are typically under-represented in literature [5], [19], [38]. It is common practice to include the material's quasi-static strength into S-N curve representations with either fatigue stresses expressed as a fraction of this static strength or the static data is directly included as a $\frac{1}{2}$ or 1 cycle to failure entry in the S-N curve. For a material known to be strain rate sensitive, this artificially flattens off the low cycle fatigue portion of such S-N curves in order to forcefully include the mismatching static data point. Authors such as Epaarachchi and Clausen [19] and D'Amore et al. [38] have therefore argued that material ultimate strengths and failure strains should be only be considered as part of the fatigue dataset when obtained at equivalent strain rates to those of the cyclicly loaded specimen. Under these conditions, the inclusions of the high-rate monotonic strengths into the S-N curves were also shown to agree much better with extrapolations of cyclic data towards a single cycle to failure.

As continuation of this reasoning D'Amore et al. [38] expanded on the 'stress life equal rank assumption' (SLERA) by Hann and Kim [51] and proposed a method for adjusting the residual strength degradation function derived from fatigue tests at one specific testing frequency to that of another based on the change in two-parameter Weibull distribution functions of tensile strengths under the original and desired effective strain rates. This method was shown to be effective in the fatigue life prediction of angle-ply carbon/epoxy laminates exposed to two distinct frequency loading blocks. Lee et al. [52] in earlier work also studied the damage accumulation on fibre reinforced epoxy matrix composite under tensile fatigue loading in order to construct a strain rate dependent residual strength model. These authors suggested that both stress intensity factor and damage growth rate are dependent on the cyclic maximum stress, the existing state of damage as well as the direct inclusion of strain-rate sensitive damage growth parameters. Lee et al. concluded from their experiments that with both material stiffness increasing as well as a reduction in damage growth rate at higher strain rates, the residual strength degradation was reduced and the observed cycles to failure increased. Both D'Amore et al. and Lee et al. thus associate the fatigue strain rate with the strength degradation rate, which although not discussed by these authors, could very well be related to delayed and reduced fibre-matrix debonding as concluded by Kwon et al. for high-rate monotonic tensile tests. This would be further supported by Ma et al. [53] who concluded in their review of FRP strain rate effects that the dynamic energy dissipation in the highly stressed matrix zone directly around the fibre inhibits the propagation of matrix cracks, effectively raising the damage threshold in dynamic loading compared to quasi-static.

Thus, the effective fibre-matrix interface strength increases with higher strain rate as result of delayed debond initiation and reduced propagation rates [38], [52], [53]. From an energy dissipation perspective, this has an important side effect. In section 2.3 the fibre-matrix interface strength was identified by Chandra et al. [13] and Tang et al. [24] as contributor to damping characteristics due to the onset of fibre-matrix slip and consequent friction based damping. Therefore a stronger interface strength with a slower propagation rate would suggest a decrease of this component to hysteresis energy dissipation at higher strain rates. To further effect the cyclic energy dissipation, also the viscoelastic damping factor of the polymer matrix is likely to decrease with growing strain rate. The reason for this is the reduced time available for matrix polymer chain mobility and re-alignment, limiting viscous relaxation and its associated damping as result [24]. This would match the results by Eftekhari and Fatemi [45] who observed lower hysteresis energy when increasing fatigue frequency from 0.25 to 4 Hz. Such reasoning would furthermore be consistent with observation from so called dynamic mechanical analysis measurements showing general decreasing damping factors (loss factor) at increasing test frequency [17], [25], [54]. Then finally, the last loading rate effect on energy dissipation is related to the the sensitivity of the increasing laminate modulus. At a constant maximum stress, a higher stiffness reduces the strain amplitude and thus the strain energy applied each cycle. The combination of a reduced input energy with a lower total damping factor from the first two points leads to an overall reduction hysteresis dissipated energy per cycle.

Despite there being good conceptual understanding of different strain rate effects on composites as those discussed in this section, concrete quantification of consequences on fatigue performance of in terms of explicit cycles to failure or total energy dissipation remain scarce in literature as strain rate is not an easy to isolate variable. As shown by equations 2.2 and 2.3, the peak and average strain rates of each fatigue cycle depend on the maximum stress, R-ratio, frequency and current laminate modulus.

$$\dot{\epsilon}_{peak} = \frac{\pi \sigma_{max}(1-R)f}{E} \qquad (2.2)$$

$$\dot{\epsilon}_{avg} = \frac{2 \cdot \sigma_{max}(1-R)f}{E} \qquad (2.3)$$

Assuming a constant R-ratio and maximum stress as primary fatigue variable, then the only means of controlling the strain rate is by altering the frequency. As the materials most effected by strain rate are also likely to be more sensitive to viscoelastic creep and self-heating, such variable frequency in order to keep the strain rate constant would inevitably introduce further side effects as those discussed in subsection 2.5.1. Still for this thesis with the purpose of evaluating composite fatigue from an energy dissipation ratio perspective, it is believed that the rate-dominated effects on stiffness, strength, damage propagation and viscoelastic characteristics of the material itself are non-negligible. Therefore the aim is to keep strain rates equivalent across stress levels and R-ratios such that material damage and damping characteristics remain similar in order to suppress their related variances. Consequent effects of varying frequency such as creep and self-heating should be considered and minimised in the specimen and experiment design.

2.5.3. Stress ratio

The stress ratio, often referred to as R-ratio, is the fraction of cyclic maximum stress over the minium stress, like shown by Equation 2.4.

$$R = \frac{\sigma_{max}}{\sigma_{min}} \qquad (2.4)$$

The value of the R-ratio can be used to split up the types of loading cycles into three categories:

- $0 \leq R < 1$ represents tensile-tensile (T-T) load cycles where both minimum and maximum stress levels are positive.
- $-1 \leq R < 0$ gives tensile-compressive (T-C) loading, where as the name suggests the maximum stress level is positive with a negative (compressive) stress as minimum.
- $R > 1$ is referred to as compression-compression (C-C) loading, where both minimum and maximum stresses have a negative value.

In the fatigue of metals, the R-ratio effect is mostly associated with the change in mean stress and crack closure. In composites however, the consequences of changing R-ratio are more complicated and tie in heavily with the aforementioned effects of time at load and strain rate [5], [53]. Additionally, for a constant maximum stress level, a change in R-ratio also alters the magnitude of cyclic strain energy applied to the material. The sensitivity of damage formation and growth to any (combination of) these effects is therefore dependent on the composition and characteristics of each individual composite material and laminate configuration, as has become apparent from the preceding literature study sections on frequency and strain rate effects. Therefore for composite materials there exists no universal rule that dictates whether R-ratio will have a positive or negative effect on fatigue life expressed in cycles [52].

Furthermore, fatigue damage mechanisms of continuous fibre reinforced composites differ greatly between tensile and compressive loading [1], [18]. Under tensile loads, damage formation is centred around fibre-matrix debonding, matrix cracking and delamination growth [22]. Damage under compressive loading however is much different with stability phenomena such as fibre kinking and (local) buckling playing a dominant role as well [1], [11]. For comparatively low compressive minimum stresses authors such as El-Kadi and Ellyin [18] and Cadavid et al. [11] even argue that the compression part of T-C cycles have negligible contribution to damage formation. As discussed in the introduction of this thesis however, the scope for this project would remained focussed on energy dissipation related effects under positive R-ratios. Therefore C-C and T-C fatigue will not be further considered in this section.

For tensile-tensile loading (T-T) at $0 \leq R < 1$, the effect of R-ratio on the strain rate was already shown by equations 2.2 and 2.3. As well as the discussion regarding strain rate related changes in damping of subsection 2.5.2. This R-ratio specific section does not have any more specific details to add to that. For creep sensitive viscoelastic composite laminates on the otherhand, subsection 2.5.1 already introduced the concept of a critical time at load under low frequency fatigue loading. However, the R-ratio brings a further significant contribution to this, which will be briefly discussed here. Namely, for high R-ratios where you approach $R \approx 1$, the the argument can be made that the loading is not considered cyclic any more, but instead is a near constant hold at the mean stress level with increasingly negligible oscillation between the maximum and minimum stress. In that case, the life would be dictated purely by viscoelastic and viscoplastic creep. Therefore, as you go up in R-ratio from 0 to 1, progressively the increasing mean stress as calculated by Equation 2.5 becomes a more controlling factor as the cyclic stress amplitude decreases.

$$\sigma_{mean} = \frac{\sigma_{min} + \sigma_{max}}{2} = \frac{\sigma_{max}(1+R)}{2} \tag{2.5}$$

Furthermore, under the typical case of fatigue testing at a constant stress amplitude and constant frequency, the R-ratio directly effects the time per cycle that the stress is above a given fraction p of the maximum cyclic stress. For a sinusoidal waveform, such relation of time spent above this maximum stress fraction can be derived as shown by Equation 2.6, which is also visualised in Figure 2.4 for three typical frequencies.

$$t_{\text{peak}} = \frac{1}{\pi f}\left(\pi - 2\sin^{-1}\left(\frac{2p-(1+R)}{1-R}\right)\right) \tag{2.6}$$

where:

- t_{peak}: time spent above the threshold stress per cycle [s]
- f: frequency of loading [Hz]
- p: fraction of peak stress (e.g. 0.9 for 90%) [-]
- R: stress-ratio [-]

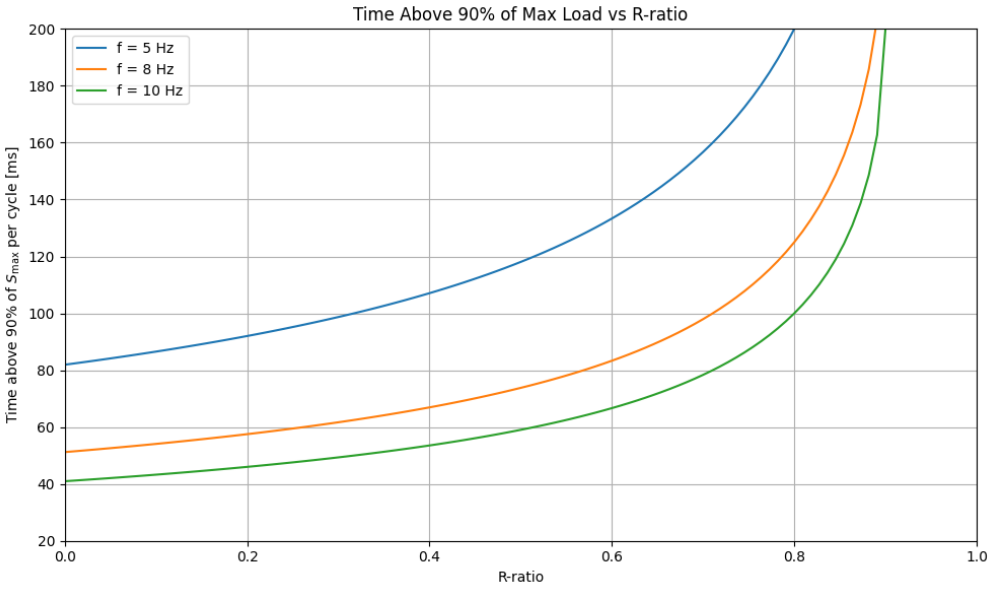

Figure 2.4: Comparison of cycle time spent above 90% of σ_{max} for varying R-ratios under constant frequency.

Figure 2.4 highlights clearly how under constant amplitude loading, the time spent above 90% of the maximum stress is proportional to the frequency and increases with R-ratio. For low R-ratio changes, say between 0.1 to 0.3, the effect on the time at load criteria remains somewhat marginal. However, by its heavily non-linear nature this grows very quickly as high R-ratios are approached. This this figure thus confirms that for creep sensitive fibre-reinforced polymer composites, particularly a low frequency with high R-ratio cycle combination should be approached from a creep time at load criteria.

From an energy perspective on more fibre-dominated laminates however, increasing the positive R-ratio at a fixed maximum stress decreases the stress amplitude and thus the applied energy or work done on the specimen per cycle. Under the assumption of an equivalent material viscoelastic damping factor irrespective of the R-ratio, this would then result in an expected reduction of the magnitude of dissipated hysteresis energy for such cycle. If then furthermore the magnitude of such dissipated energy is considered related to the damage growth as done by a number of authors [18], [28], [55], [56], then an increase in R-ratio for equal maximum stress would most likely result in a longer fatigue life and thus a reduced slope of the S-N curve. A representation of the change in considered applied strain energy and consequent size of the hysteresis loop is given by Figure 2.5.

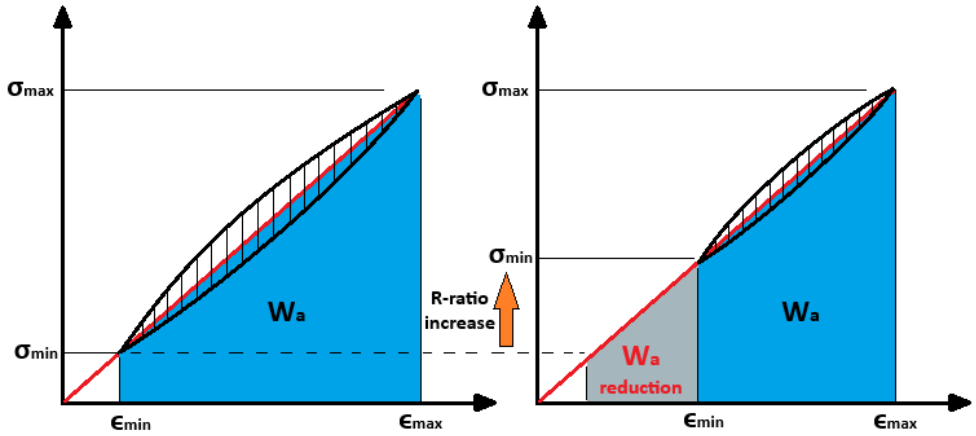

Figure 2.5: Change in cyclicly applied strain energy as result of increasing R-ratio.

2.5.4. Temperature

Temperature, either as external environment or internally generated, has a significant impact on the fatigue behaviour of fibre-reinforced polymer composites. Mechanical properties such as elastic modulus, strength, and fracture toughness are all temperature-dependent, with significant reductions observed as it approach the glass transition temperature [53]. Compared to the polymer matrices, most common reinforcing fibres themselves are not very sensitive to rising temperature [34]. It is therefore the changing ductility of the matrix and greater polymer chain mobility as well as reduced interface strength that are the driving factor behind the temperature sensitivity of the composite laminates [53]. Furthermore, the viscoelasticity of the composite is directly related to that of the matrix and the fibre-matrix interface. As the mobility of the polymer chains increase with rising temperature, the viscoelastic contribution of the matrix thus increases. This can set off a snowball effect where viscoelastic and friction based energy dissipation locally heat up the material mostly where the initial fatigue damage is formed. As the matrix in the damage zone softens, it dissipates even more energy, leading to a further temperature rise and degradation of laminate strength. These reductions are typically more pronounced in matrix-dominated failure modes or when in off-axis fibre orientations the contribution of the fibres to the load-carrying capacity of the laminate is reduced due to matrix softening.

Increased sensitivity to creep under elevated temperatures further aggravates the fatigue degradation. Conversely, reduced (negative) temperatures where the matrix becomes more linearly elastic can enhance fatigue life by increasing matrix stiffness and delaying the onset of viscoelastic damage mechanisms. For example, Flore et al. [34] discussed substantial increases in fatigue life for a GFRP composites tested at sub-zero temperatures (down to -150°C). However most interestingly from their study, Flore et al. showed that when the maximum stresses on the S-N curves of tests performed at temperatures ranging between -150 and 150 C$^\circ$ were normalized by their static strengths at the corresponding temperatures, the distinct S-N curves all mostly collapsed. This would suggest that despite the material static strengths being effected by temperatures, the relative strength degradation per cycle remains equivalent.

2.5.5. Parameter selection conclusions

Based on preceding chapter sections, it is thus believed that for good evaluation of isolated effects, such as that of the R-ratio on strain energy dissipation vs applied strain energy, testing parameters should be chosen such as to minimise the side-effects of frequency, strain rates, time at peak load as well as temperature. With a particular focus on energy dissipation, this would mean stepping away of standard fixed frequency testing as most often performed in literature, optimising in favour of consistent viscoelastic material behaviour under equivalent strain rates or alternatively for very creep sensitive materials frequencies such that time near peak load each cycle remain constant over the test variables. However, despite a wide spectra of available literature on this topic, the selection of testing frequency in most published studies can be considered to be under-justified by sole reference to such 'standard' 5-10 Hz frequencies as a convenience factor combined with a common remark claiming no significant heating effects. As result, further frequency effects dominated by creep or variances in strain rate are often overlooked. In this regard, the ASTM D3479 standard is also lacking in recommendations as it suggests constant frequency testing only.

2.6. Strain energy dissipation based fatigue analysis methods

Having established the prerequisite general knowledge on fibre-reinforced polymer composite energy dissipation, damping sources, damage mechanisms and the effects of the different fatigue loading parameters, this section will now discuss some of the energy dissipation based fatigue analysis approaches already undertaken in literature. Through this discussion, the aim is to further put the initially hypothesized constant TDE/TW ratio into the context of the existing experimental knowledge on the topic. This then leads into the re-evaluation of the initial hypothesis at the end of this chapter, from which the research gaps and research questions of this thesis will be formulated.

As discussed in section 2.3, the hysteresis energy dissipation in fibre-reinforced polymer composite fatigue has viscoelastic, friction and viscoplastic damping components. This dissipated strain energy comprises of an irreversible change of internal energy (dU) as well as heat energy (dQ) [57]. The challenging factor in a detailed analysis of the energy dissipation however is the difficulty to predict

and/or measure the relative split between these two hysteresis energy components [8]. This means that based on purely a measurement of the dissipated energy in a cycle, one can not simply isolate the change of internal energy (dU) which actually contributed to the formation and propagation of fatigue related damage. This limits the direct application of continuum damage mechanics and irreversible thermodynamic approaches without substantial additional material data and assumptions [1].

Therefore instead, the current author sees that most fatigue hysteresis energy or damping related studies in literature are effectively split up into two main alternative categories. Here the first are predictive methods that generally aims to improve the empirical-phenomenological stress-life predictions by considering trends with either applied or dissipated strain energy as driving factor rather than solely the stress level. The second category on the other hand rather uses the a description of cyclic energy dissipation or damping as another means of analysing and understanding the composites material fatigue resistance, particularly in relation to factors such as a high cycle fatigue strength. For each of these two catagorical distinctions, a selection of existing literature will be discussed which is considered relevant to the initial hypothesis and formation of the research questions.

2.6.1. Predictive methods

Some of the early literature published that applied a strain energy concept to fibre-reinforced polymer composite fatigue prediction was by the authors El-Kadi and Ellyin [18], [58] in the early 90's. Following a similar approach to that what these authors considered for metals, they tried to relate the cyclic applied strain energy to damage formation. More specifically, El-Kadi and Ellyin suggested that instead of a typical S-N curve, the fatigue life of angle-ply unidirectional composites could be expressed as power-law relation between the magnitude of applied strain energy and consequent cycles to failure. As the heat loss (dQ) at the time was considered a difficult measurement, which it still is today, these authors assumed that the change in thermal dissipation was negligible such that $dW_{supplied} \propto dU_{damage}$. I.e. a twofold of the applied strain energy directly doubles the damage related dissipation. Mandegarian and Taheri-Behrooz [59] followed up on this concept and suggested that the applied strain energy should be normalised by the maximum strain energy stored in a quasi-static test. Such normalisation was then argued to collapse the normalised strain energy vs cycles to failure into a single power-law trend irrespective of off-axis fibre angle. However, both methods by El-Kadi and Ellyin as well as Mandegarian and Taheri-Behrooz indirectly assumed that the applied strain energy per cycle is a constant and does not change throughout the fatigue life as result stiffness degradation. Such approach has therefore only shown to give reasonable results for a limited selection of off-axis unidirectional composites.

Movahedi-Rad et al. [41], [57], [60] are authors that have been more recently developing and further pushing the predictive application of hysteresis energy dissipation methods. As part of a continual work, Movahedi-Rad et al. proposed the concept of a total dissipated energy criteria, which takes the form of a power-law relation between the total dissipated energy and the maximum cyclic stress. Their fatigue life prediction approach is based on the evaluation of the dissipated energy only. Based on a geometrical approach by Hahn et al. [61], which simplifies the hysteresis loop geometry into a two-triangle formation, a scaling factor is proposed on the hysteresis loop area based on the stress amplitude, hysteresis loop width and R-ratio. Using this so called dissipated energy 'shift factor', the mean dissipated energy per cycle measured at fatigue stress level on a reference R-ratio can be 'shifted' to a predicted mean dissipation on a target R-ratio. Although not explicitly stated by the original authors, the TDE vs σ_{max} power-law relation is assumed as effectively constant, irrespective of R-ratio. Therefore by the adjusted mean dissipation value, a fatigue life at a different R-ratio and stress level combination can be estimated as the amount of cycles it takes to reach the critical TDE value for that stress level. This is further compensated by a power-law based pure creep dissipation factor, although for the shown reference cases this contribution remains negligible until a high R-ratio of 0.7.

The concept of a seemingly fixed TDE vs maximum stress level seems promising, however Movahedi-Rad et al. do not further discuss nor prove this using the validation data. Also in literature not much concrete evidence has been come across yet to fully support this well. This is especially questionable in the light of section 2.5 where the effects of frequency, loading rate and temperature were discussed on the composite strength and damage propagation rates. Therefore as part of this thesis' work it would be of interest to evaluate the consistency of such TDE vs σ_{max} trends with respect to the R-ratio.

El-Kadi and Ellyin, Mandegarian and Taheri-Behrooz and finally Movahedi-Rad et al. thus take completely different approaches to the same goal. One with energy input as sole parameter, whilst the other only considered the hysteresis energy 'output' until a critical TDE value. In both cases however, the methods by these authors inevitably assumed that either input energy or energy dissipation per cycle is an effective constant. Both thus only consider one side of a damping balance, not a damping ratio of energy loss over the energy input. Particularly the dual-triangle based energy dissipation shifting factor by Movahedi-Rad et at. is seen by the current author to loose the critical connection to the underlying damping mechanisms and their sensitivities to existing damage, loading rates or thermal effects as extensively discussed already in this literature review. Here, the current author believes that the hysteresis energy should be seen as the output of the combined damping mechanisms with the critical input being the applied strain energy. Effects of R-ratio should thus be considered through the input energy and the effects of heat or damage throughout life as changes to the overall damping factor of the material. Particularly the latter is unlikely to remain constant throughout a fatigue test as damage progresses and stiffness decreases, yet the above discussed methods assume this to be a constant. An understanding of the progression of an effective damping ratio throughout the fatigue life, as well as how this is changes for different stress levels and R-ratios is the considered as the missing key.

2.6.2. Analytical methods

As discussed in section 2.2, energy dissipation analysis methods find a strong purpose in literature to augment otherwise stiffness degradation based damage progression evaluations. For example, Khoshmanesh et al. [62] used acoustic decay and infrared thermographic methods to calculate the relative change of damping in order to evaluate the damage accumulation process of adhesively bonded composites. These authors concluded that the measured changes in specimen damping properties were more sensitive to the damage formation than the degradation of stiffness. They therefore argued that damping property evaluation would be an effective means of condition monitoring of adhesively bonded blade structures. Similarly, Mandegarian et al. [63] calculated the hysteresis based strain energy dissipation on $\pm 45^{\circ}$ carbon/epoxy laminates to distinguish the initiation of in-plane shear failure.

Other energy dissipation related analysis methods in literature aim to establish a high cycle fatigue limit (HCFL) or high cycle fatigue stress (HCFS), based on the 'thermographic methodology' originally introduced by La Rosa and Risitano [64]. Here, the stabilised or average temperatures of the samples during the fatigue test are plotted against their respective maximum stress values. This will then usually form a double-linear trend, where the stress level at the infliction point identifies the high cycle fatigue stress. As the measured temperature is proportional to the heat dissipation rate, the identified HCFS thus is a stress level beyond which the energy dissipation per cycle starts to rapidly increases as indication of the onset of a critical fatigue damage mechanism [65], [66]. This phenomenon is typically associated with a critical saturation of matrix cracks [66], [67]. Such high cycle fatigue strengths can be found documented in literature for fibre-reinforced composite laminates such as $\pm 45^{\circ}$, cross-ply and quasi-isotropic, and occurs most often in the range of $10^6 - 10^7$ cycles [65]. However, this does not imply that no failure occurs below this limit. Instead, it behaves much more like a high cycle fatigue endurance limit, where thus the slope of the S-N curve is said to rapidly decrease.

Colombo et al. [67] performed such infrared thermography, where a so called 'D-mode' method was used to estimate the local infrared energy dissipation on what appears as $\pm 45^{\circ}$ woven glass/epoxy laminates. These authors plotted the average D-mode dissipation power value against the maximum cyclic stress levels and obtained a very similar dual-linear trend as by La Rosa et al. [64]. This is shown in Figure 2.6a below. Both Colombo et al. as well as a later discussion by Cadavid et al. [11] interpreted such plot as strong evidence for the existence of a high cycle fatigue threshold, below which the damage saturation may not be great enough to trigger the onset of the fatigue failure mechanism.

Within the context of this current thesis and the performed literature study this could indicate that below such high cycle fatigue strength, the viscoelastic damping of the material dominates the energy dissipation such that the contributions of friction and viscoplastic based damping under minor internal damage can be considered negligible. Above this HCFS threshold however, the internal damage progressively accumulates, such that the overall damping factor of the laminate starts to divert from the pure viscoelastic damping. As the stress level increases, damage-based friction and plastic damping components then become more and more dominant.

When searching further in literature with the above reasoning, one can find more energy dissipation related trends to support of such dual-domain damping behaviour. Bledzki and Gassan [56] for example studied the accumulative energy dissipation under tensile-tensile fatigue tests of woven-layer glass fibre reinforced epoxy foams. For specimen with fatigue lives well over 1 million cycles, the energy dissipation per cycle reaches a near constant value. For increased stresses beyond this, the accumulation of dissipated energy vs number of cycles took the form of an increasingly exponential-like function. This means an increasing rate of energy dissipation per cycle after a distinct onset.

Along similar lines Kenny and Marchetti [28] calculated a so called 'the specific damping capacity' (SDC) of angle-ply thermoplastic composites. This viscoelastic parameter, of which the meaning will be discussed in more detail in chapter 3, is effectively a normalisation of the dissipated energy by the total strain potential. Kenny and Marchetti plotted the mean SDCs against the maximum fatigue stresses, which also followed a near identical bi-linear trend as those from the thermography method. Kenny and Marchetti used the inflection point to identify the stress at which local matrix yielding occurred. Consistent with the current discussion, this inflection point as onset of local matrix yielding in the fatigue cycles can alternatively considered as the onset of viscoplastic damping on top of the pure viscoelastic damping.

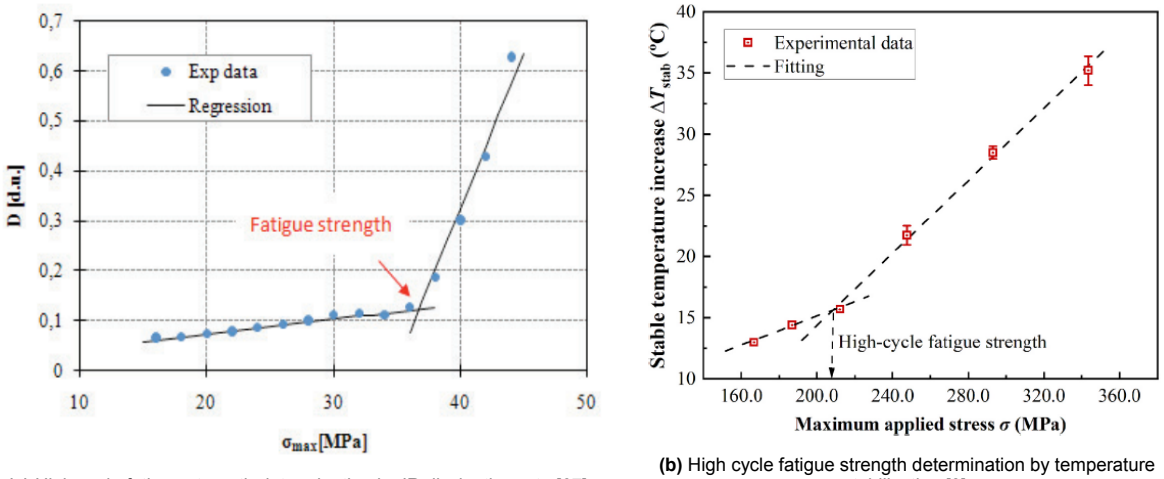

(a) High cycle fatigue strength determination by IR dissipation rate [67].

(b) High cycle fatigue strength determination by temperature stabilisation [8].

Figure 2.6: Thermography based high cycle fatigue strength determinations by a) Colombo et al. [67] and b) Han et al. [8]

As the final literature source to discuss here, Han et al. [8] very recently proposed a critical damage entropy accumulation approach based on cyclic energy dissipation and heat build-up of quasi-isotropic E-glass/epoxy laminates under R=0.1 tensile-tensile fatigue loading. These authors used a rather comprehensive thermal approach that combines infrared measurements with thermal model to predict the heat dissipation rate using convection, radiation and external cooling through clamping interfaces. This allowed for the splitting of thermal energy dissipation from from the viscoelastic and damage (internal) energy components.

These authors also estimated the high cycle fatigue strength through the dual-line stress vs stabilised temperature method. In line with the discussion so far, the assumption by Han et al. here was that below this HCFS, the dissipation of plastic strain energy is negligible compared to its viscoelastic counterpart. Below the HCFS, it is thus assumed that only viscoelastic damping occurs. This assumed pure viscoelastic damping contribution below the HCFS is then extrapolated and removed for stresses above the HCFS, such that using their thermal dissipation model the remaining damage energy could be isolated and converted into a damage entropy accumulation. Here, Han et al. showed that for fatigue lives of $1.5 \cdot 10^4$ cycles and above, the accumulated damage entropy up to failure is constant and independent of the stress level. Such demonstration of a constant damage entropy could be fundamentally linked to the assumed fixed TDE vs stress power-law relation by Movahedi-Rad et al.[55].

2.7. Reflection on initial TDE/TW hypothesis

As was introduced in chapter 1, previous work in the ASM department spiked interest in the analysis of the ratio between total dissipated energy until fatigue failure (TDE) over the corresponding total amount of cyclic work done on the specimen (TW). As Alderliesten [10] (personal communication) initially described it, such ratio could potentially be seen as a composite material's natural resistance to the amount of work done to it under fatigue loading. In practical terms a higher TDE/TW ratio dissipates more of the total applied energy, which when related to damage formation would suggest faster damage growth and thus a lower natural fatigue resistance.

This TDE/TW hypothesis by Alderliesten and Movahedi-Rad originated from data provided by Bhangale [1] for a verity of glass/epoxy laminate types. This is shown in Figure 2.7, where the TDE is given as ΔW_p and the TW as ΔW_T. Here it appears that the total dissipated energy and total work done follow a seemingly linear relationship, albeit with a fair amount of scatter. Despite fatigue tests performed under different maximum stresses and stress amplitudes, such linear trends would indicate a rather fixed ratio between the TDE and TW.

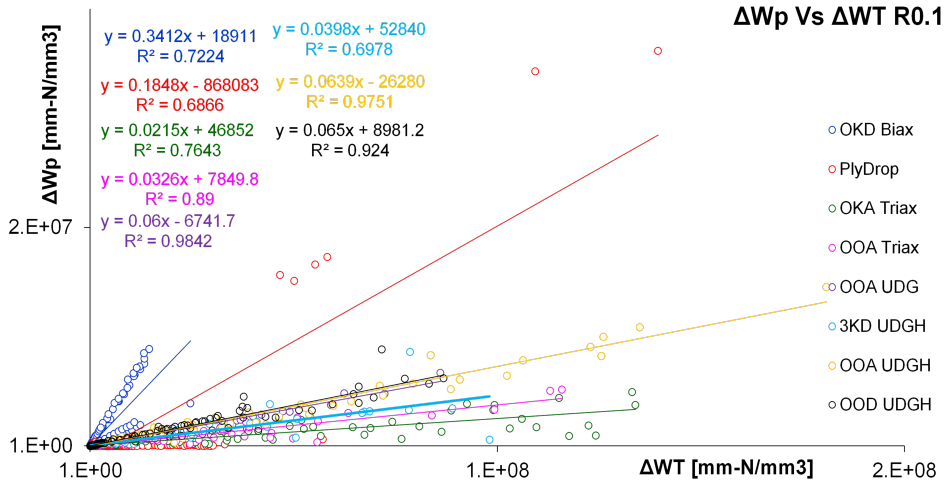

Figure 2.7: Total dissipated energy vs total work done on different glass/epoxy laminates, graph provided by [1]

However, based on the discussion of subsection 2.6.2 the current author believes that there is diverse enough evidence in literature to suggest that below a certain stress threshold, referred to as a high cycle fatigue strength, the cyclic energy dissipation is dominated by pure viscoelastic damping characteristics of the composite material. Aside from this, the current author sees the TDE/TW ratio more in the form of an effective or average energy dissipation ratio over the whole fatigue life, rather than a fatigue resistance factor. Therefore, by extension of the assumed constant viscoelastic damping factor with negligible friction and and plastic damping contributions at stress levels below a HCFS threshold, one could argue that a constant TDE/TW ratio is to only be expected for very high cycle fatigue life. For increasing stresses beyond the HCFS however, the different observations from literature suggest a steady increase in friction and plastic deformation damping contributions on top of the fixed viscoelastic, which is believed to then also logically translate to an increasing TDE/TW effective damping ratio. This thus argues against the initial hypothesis of a fixed ratio.

The reason that this has not become initially apparent from Bhangale's TDE vs TW plot of Figure 2.7 is believed to be the result of the linear axis scales. As Movahedi-Rad et al. [57], [60] have shown, the relation between total dissipated energy and cyclic maximum stress takes the form of a decaying power-law. In other words, the amount of total dissipated energy is drastically larger for lower fatigue stresses. For Bhangale's plot this means that the most prominently displayed data points represent fairly high cycle fatigue tests, thus low stresses, which by the reasoning of the previous paragraph are most likely to have a (near) constant TDE/TW ratio. However, as a lot of the higher stress level data is thus clustered and suppressed close to the origin, the non-linearities of the TDE/TW vs σ_{max} trends do not appear.

2.8. Adjusted hypothesis and objectives

Following the discussion of the previous section, it is thus believed that the initial hypothesis should be adjusted. Considering all the discussed factors, the revised hypothesis for this thesis is formulated as:

Under the condition of equivalent strain rates, the ratio of total dissipated energy (TDE) over total work done (TW) of a continuous fibre-reinforced polymer composite material under fatigue loading to failure follows a two-domain trend with the cyclic maximum stress, where below a high cycle fatigue strength the ratio is constant and driven by the viscoelastic damping properties of the material.

A visualisation of this revised TDE/TW ratio hypothesis is sketched in Figure 2.8.

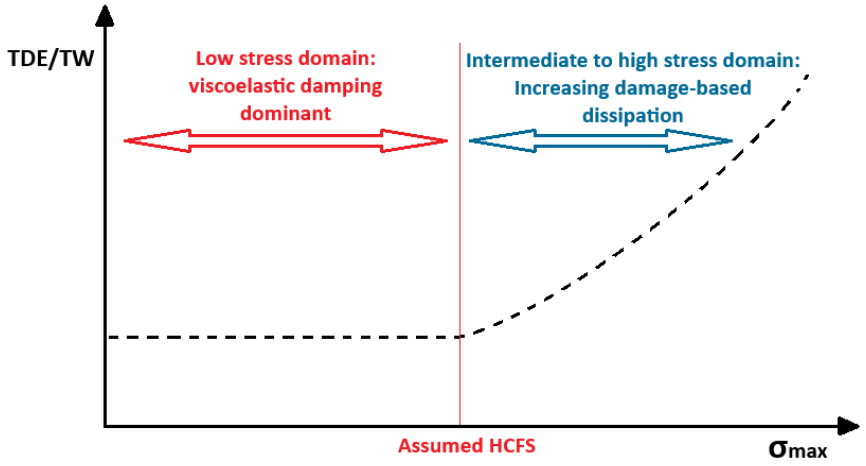

Figure 2.8: Visualisation of revised two-domain TDE/TW hypothesis

As mentioned in the introduction, part of the goal of energy dissipation based fatigue analysis work in the ASM department is to find simpler and or quicker methods to evaluate critical fatigue material characteristics that can be used to reduce the amount of fatigue testing required for confident predictions. For the revised hypothesis, particular relevance here would be the alternative measurement of the assumed constant viscoelastic damping below the HCFS. As fatigue lives for stresses below such high cycle fatigue strength are most often documented to be in the $10^6 - 10^7$ cycles range or even higher, the evaluation both the HCFS value itself as well as the assumed constant damping properties require very extensive test durations. Therefore, if the fibre-reinforced composite material damping properties can be alternatively measured and directly compared/implemented into fatigue derived damping ratios, it could save a lot of extremely time intensive high cycle fatigue testing.

To the best knowledge of the current author however, there is no mainstream experimental literature that directly evaluates the hypothesized trend or similar energy dissipation ratios based on a viscoelastic theory damping factor, i.e. one that removes all the additional parameters and looks purely at a damping factor that relates the changing energy input energy through σ, E and R to dissipated output. If assumed in literature that below a HCFS threshold, pure viscoelastic damping dominates, then a means of comparison should be set up such that pure viscoelastic damping factor measurements can be compared to their equivalents in fatigue. For the damping properties of polymer materials, so called Dynamic Mechanical Analysis (DMA) is the standard method [17]. This is a method where small material samples are cyclicly loaded at very low forces and the phase shift between applied stress wave and resulting strain wave is measured to derive a viscoelastic loss factor. Typically this is measured through a temperature sweep to give the sensitivity of the material's viscoelastic damping to temperature.

In literature, DMA testing of fibre-reinforced polymer composite materials is not uncommon. Most often it is applied as a means to determine the glass transition temperature of the material, or evaluate the effects of various material parameters such fibre volume fraction on the material's structural/vibrational damping performance. The classical viscoelastic theory loss factor calculation, which will be shown and

discussed further in chapter 3, also finds its way into a number of composite fatigue related studies. For example the aforementioned work by Khoshmanesh et al. [62] on the evaluation of damage progression of adhesively bonded composites or work by Movahedi-Rad et al. [21] where a loss factor was calculated to evaluate the effects of fatigue test interruptions. However, the problem that the current author has with this and other alike literature is that classical viscoelastic literature is originally based on damping of acoustics/vibrations, under fully reversed cycles [17]. A fundamental assumption there is that only positive strain energy contributes to damping [17]. Therefore, for a fully reversed cycle only half the stress range, the stress amplitude, is used for the calculation of the loss factor. Most fatigue related literature that considers the viscoelastic loss factor directly applies this definition without further consideration or corrections for the actual applied strain energy in a fatigue cycle and in particular its relation to the R-ratio. This then gives a fatigue damping loss factor for which the relative changes can be evaluated within the context of the fatigue analysis, but their exact values cannot be directly compared to those obtained at different R-ratios or even other methods such as the well established DMA tests.

In order to evaluate the revised hypothesis as well as being able to consistently compare hysteresis damping measurements across stress levels and R-ratios, it will be attempted in this thesis to define the hysteresis energy and applied energies in such a way that they are most consistent with linear viscoelastic theory and described as explicit functions of maximum stress, R-ratio and stiffness. If a consistent definition of damping with respect of R-ratio can indeed be formulated and shown to be consistently applicable, then the energy dissipation in fatigue tests at different R-ratios can be compared through a uniform loss factor definition. Furthermore, the effect on the average damping ratio and by extension TDE/TW would have its use for not only establishing and justifying the widely assumed existence of a HCFS and constant viscoelastic damping below it, but could also be a critical link in fatigue life predictions. If a trend between the fatigue stress level and mean dissipation factor or TDE/TW is well understood and predictable for different R-ratios, then the average energy dissipated per fatigue cycle could be straightforward to estimate. If this is combined with a fixed trend for total dissipated energy until failure as considered by Movahedi-Rad et al., then this can lead to a physics based strain energy dissipation fatigue prediction framework. However, the literature review for this thesis was not able to find any concrete data on how the TDE failure criteria changes with R-ratio. Especially the discussed strain rate effects are assumed to possibly play a role here due to its consequences on strength and damage growth rates. Hence TDE vs σ_{max} should also be experimentally evaluated for different R-ratios.

This thesis will thus have the following research objectives:

1. To define definitions of the applied strain energy in a fatigue cycle, the consequent hysteresis dissipated strain energy as well as the summations to a total dissipated over total applied energy ratio, with consistency to classical linear viscoelastic theory.
2. To evaluate the progression of the linear viscoelastic loss factor throughout the fatigue lives of fibre-reinforced polymer composites at varying cyclic maximum stresses and different R-ratios.
3. To measure the pristine material viscoelastic loss factors through dynamic mechanical analysis and compare these to the (weighted) average loss factors measured in fatigue tests to conclude on the viscoelastic damping based high cycle fatigue limit.
4. To relate the measured pristine material viscoelastic loss factors and (weighted) average loss factors from fatigue to their respective TDE/TW ratio in order to evaluate the hypothesized two-domain TDE/TW vs σ_{max} trend.
5. To evaluate the relation between total dissipated energy and cyclic maximum stress for its consistency with respect varying R-ratio and its ability to be combined with loss factor trends for the prediction of fatigue lives at alternative R-ratios.
6. To evaluate how the fatigue failure strains relate to the cyclic maximum stress, R-ratio and total work done.

2.9. Research questions

Based on the revised hypothesis and definition of the research objectives, the main research question for this thesis is formulated as follows:

How can linear viscoelastic theory be adapted to define a consistent energy dissipation formulation for fibre-reinforced polymer composites under tensile-tensile fatigue, and how can these be used in conjunction with a critical dissipated energy criteria to predict fatigue lives across varying stress levels and R-ratios?

In support of this main research question, the following research sub-questions are defined:

- How can the applied and dissipated strain energies per cycle as well the TDE/TW ratio be defined as explicit functions of viscoelastic loss factor, R-ratio and laminate stiffness whilst being consistent with classic linear viscoelastic theory?
- How does the viscoelastic loss factor progress during fatigue life for different cyclic maximum stresses and R-ratios and how can be this be related to the occurring damping and damage mechanisms?
- How do viscoelastic loss factors measured via dynamic mechanical analysis compare to the (weighted) average loss factors obtained from fatigue tests, and what does this imply about the viscoelastic damping-based high cycle fatigue limit?
- How do the DMA- and fatigue-derived loss factors relate to the corresponding TDE/TW ratios, and do these relations support the hypothesized two-domain trend of TDE/TW vs σ_{max}?
- How is the total dissipated energy (TDE) vs maximum stress (σ_{max}) relation effected by the R-ratio, and how can these be combined with loss factor trends to predict the fatigue lives at alternative maximum stresses and R-ratios?
- How do the fatigue failure strains correlate with cyclic maximum stress, R-ratio, and total work done?

3

Viscoelastic Theory

In the literature study of the previous chapter, the close relation between cyclic energy dissipation in fibre-reinforced polymer composite fatigue and viscoelastic damping characteristics of these material types was established. To build upon this and addresses the first of the research sub-questions, this chapter outlines the physical principle based theoretical approach taken to directly quantify the identified critical fatigue dissipation terms as functions of viscoelastic material properties.

This chapter starts with an introduction of the general principles and assumptions of the linear viscoelastic approach in section 3.1 that forms the basis of this thesis' theory. This is followed by section 3.2 with a broader discussion on the meaning and application of the viscoelastic loss factor in particular. Then, section 3.3 describes how such approach results in a linear dissipation function, whose shortcoming that prevent it from general application in fatigue analysis are discussed in section 3.4. Then, in section 3.5 energy based correction factors are established that based on physical principles are believed to circumvent these limitations and should make the otherwise linear viscoelastic approach applicable to a wider range of fatigue stress ratios. Sections 3.6 and 3.7 then take these modified cyclic energy dissipation functions to establish explicit formulations for the cyclic and total dissipation ratios respectively. Finally, section 3.8 extends this modified linear viscoelastic theory into a fatigue life prediction concept.

3.1. Linear viscoelastic approach

Most engineering materials are assumed to behave in a linear elastic manner until an elastic limit is reached. In such cases the stress is considered proportional to the applied strain through the elastic Young's modulus as shown in Equation 3.1 below.

$$\sigma = E\epsilon \tag{3.1}$$

Here, all the applied strain energy is stored in the material and released upon unloading. On the opposite side of the material mechanical response spectrum are the pure viscous materials, where all energy is dissipated through viscous damping due to the lack of an elastic component in their strain response. The stresses in such viscous materials are therefore only time-dependent through the applied strain rate and the viscosity, μ as shown in Equation 3.2.

$$\sigma(t) = \mu\frac{d\epsilon}{dt} \tag{3.2}$$

Viscoelastic materials on the other hand have mechanical characteristics that are somewhere in between these two extremes. As discussed extensively in chapter 2, most fibre-reinforced polymer composites can be considered as part of this material class, with the majority of the applied strain energy being elastically stored and recovered when unloading, while the remaining portion of strain energy is lost through viscous dissipation. This therefore results in the strain response comprising of both linear elastic as well as time-dependent viscous components as shown in Equation 3.3.

$$\sigma(t) = E\epsilon + \mu\frac{d\epsilon}{dt} \tag{3.3}$$

There are a number of mathematical approaches that can be taken to model the behaviour of such viscoelastic materials. Common practice is to consider the apparent stiffness of the material as an arrangement of linear springs and viscous dampers (dashpots). Which is done using so called Kevin-Voigt and Maxwell units, which consist of a spring and damper in parallel and series respectively [17]. Their corresponding formulations are given by Equation 3.4 and 3.5 below.

$$\epsilon(t) = \left(\frac{1}{E_1 + \eta_1 \frac{d}{dt}} \right) \sigma(t) \tag{3.4}$$

$$\epsilon(t) = \left(\frac{1}{E} + \frac{1}{\eta \frac{d}{dt}} \right) \sigma(t) \tag{3.5}$$

Vassilopoulos et at. [41] showed for example how a combination of a linear spring, multiple Kevin-Voigt units and a final dashpot could be combined in series to model the elastic, viscoelastic and permanent strain components of an off-axis glass fibre composite laminate under interrupted tensile-tensile fatigue loading. Their time-dependent strain function following from this is shown by Equation 3.6.

$$\varepsilon(t) = \left(\frac{1}{E} + \frac{1}{E_1 + \eta_1 \frac{\partial}{\partial t}} + \frac{1}{E_2 + \eta_2 \frac{\partial}{\partial t}} + \cdots + \frac{1}{E_i + \eta_i \frac{\partial}{\partial t}} + \frac{1}{\eta \frac{\partial}{\partial t}} \right) \sigma(t) \tag{3.6}$$

However, each of the elastic moduli (E_i) and viscosities (η_i) used for such formulations require fitting to existing experimental data and as also shown by Vassilopoulos et at., the values of these parameters continuously change throughout a fatigue test as the damping characteristics of the composite are sensitive to damage formation and stiffness degradation. Furthermore, due to its differential nature equations such as 3.6 do not pose well for an easily understandable closed-form solution. Therefore, the application of such modelling approach where all elastic, cyclic viscous and permanent strain components are aimed to be included in a single expression remains limited to interrupted fatigue data where cyclic strain, creep build-up as well as creep relaxation during the interruptions can be captured and used to re-fit and update the model parameters. This in combination with the dependence on a large number of continuously varying parameters makes such extensive series of individual spring and dashpot units impractical for the general application of analysing the variation of damping characteristics and strain energy dissipation trends in continuous fatigue tests.

Therefore, for this thesis a simplified, yet arguably more practical approach is considered where the the cyclic viscoelastic strain that forms the hysteresis loops is explicitly decoupled from the build-up of creep strain. This is based on the assumption that for continuous fibre-reinforced polymer composites, particularly the more fibre-dominated ones, the build-up of creep strain within each cycle is small enough such that the hysteresis cycles can be considered and modelled as closed loops [60]. Creep strain is then instead regarded as a separate time-dependent function, which only represents the 'rigid' shifts of the now closed hysteresis loops between cycles. A visual representation of this is shown by Figure 3.1 for an exaggerated case, for which the total strain strain is then written as in Equation 3.7.

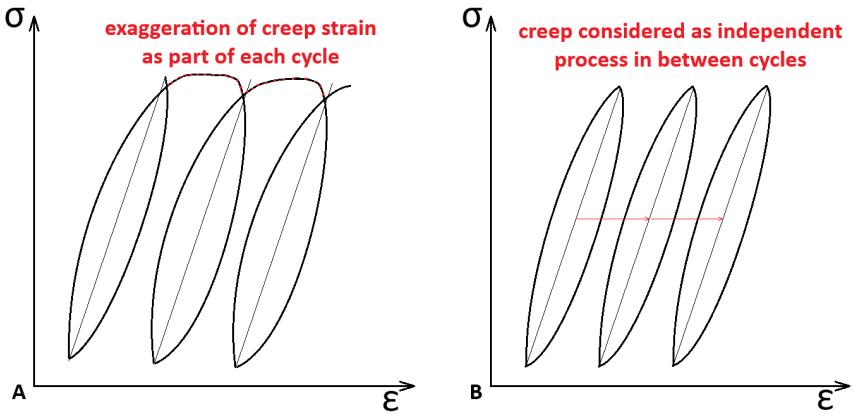

Figure 3.1: Visual representation of A) exaggerated creep considered as part of hysteresis behaviour B) creep strain shifts represented as independent from hysteresis.

$$\epsilon_{total}(t) = \epsilon_{hysteresis}(t) + \epsilon_{creep}(t) \tag{3.7}$$

As extension to the above, the energy dissipation during the fatigue life can then also be separated into individual viscoelastic hysteresis and creep components. This is consistent with the approach taken by Movehedi-Rad et al. [57], [60] as discussed in subsection 2.6.1.

As result of the decoupling of the (permanent) creep strain from the pure cyclic hysteresis, the now independent cyclic strain response of the material can be modelled as a spring-mass system with only a single complex stiffness spring, following the general principle of linear viscoelastic theory [17]. Here, the complex spring stiffness $k = k' + jk''$ has both a real (elastic) and an imaginary (viscous) component. When instead of force-displacement, this is expressed as stress-strain relation where inertial effects are furthermore assumed to be negligible under constrained cyclic loading in fatigue, then the general relation between stress and strain can be written as in Equation 3.8 [17]. Please note that from here on, the cyclic hysteresis strain component will be denoted using a shortened subscript (ϵ_h).

$$\epsilon_h(t) = \left(\frac{1}{E' + iE''}\right)\sigma(t) \tag{3.8}$$

In the above equation, E' is the so called storage modulus, representative of the elastic energy stored by the material. E'' on the other hand is the loss modulus which is associated with the viscous dissipation. For a sine wave stress input with the amplitude σ_a and radial frequency ω, this is then written as in Equation 3.9 for which the general solution is given by Equation 3.10 [17].

$$\epsilon_h(t) = \left(\frac{1}{E' + iE''}\right)\sigma_a \sin(\omega t) \tag{3.9}$$

$$\epsilon_h(t) = \frac{\sigma_a}{|E^*|}\sin(\omega t - \phi) \tag{3.10}$$

Here, $|E^*|$ represents the magnitude of the so called complex modulus, whilst ϕ is the viscous phase angle with which the damped strain response lags behind the stress input. The relation between these viscoelastic loss, storage and complex moduli as well as that of the phase angle best shown through a simple polar plot like Figure 3.2.

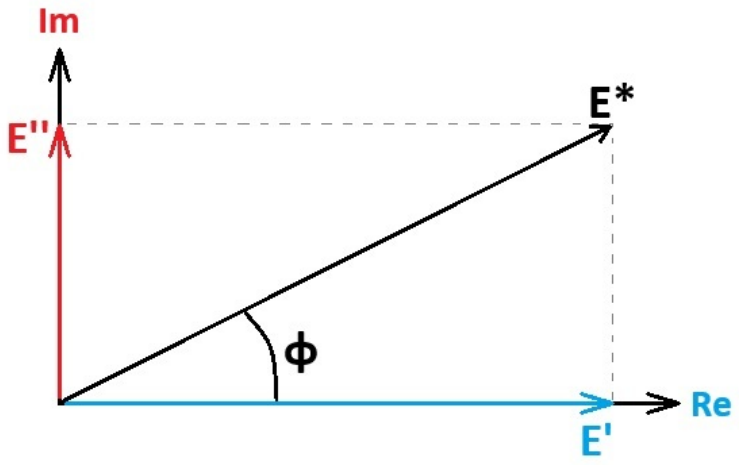

Figure 3.2: Polar plot representation of relation between the complex, storage and loss moduli with the phase lag angle.

As shown above, the vector E^* is thus formed in polar coordinates by vector addition of the real (elastic) storage modulus and the imaginary (viscous) loss modulus. The parameter ϕ is therefore the angle

between vector E^* and the real axis. By trigonometry, the angle ϕ is thus equal to the inverse tangent of the viscous over elastic moduli ratio as also shown by Equation 3.11. The length of the complex modulus vector $|E^*|$ on the other hand is calculated by Equation 3.12 and describes the total apparent apparent stiffness of the material, which in more practical terms is the average stress-strain slope between the two extremes of the hysteresis loop. This matches the description of the more commonly used term 'dynamic modulus' [16].

$$\phi = \tan^{-1}(\frac{E''}{E'}) \tag{3.11}$$

$$\begin{aligned} |E^*| &= \sqrt{(E')^2 + (E'')^2} \\ &= E'\sqrt{1 + \tan^2(\phi)} \end{aligned} \tag{3.12}$$

A representation of how these three moduli definitions relate themselves to a typical hysteresis cycle is shown in the following Figure 3.3.

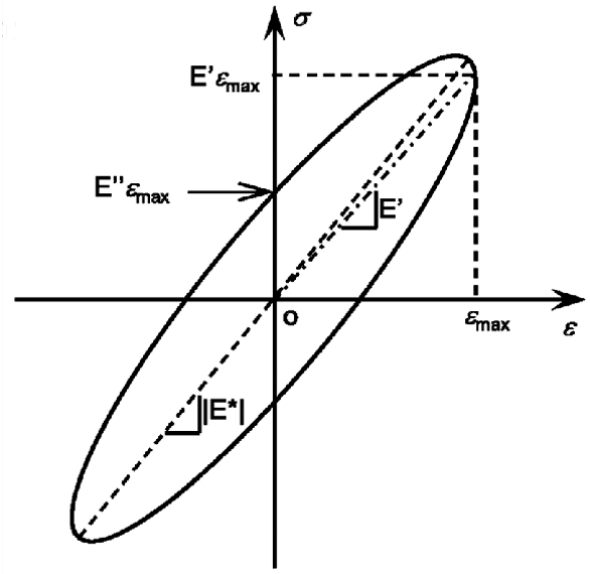

Figure 3.3: Definition of complex moduli components within a hysteresis loop [17].

3.2. Viscoelastic loss factor

The phase angle ϕ is thus identified as a critical viscoelastic characteristic that through $tan(\phi) = \frac{E''}{E'}$ is also a direct description of how well the material dissipates the applied mechanical strain energy. Because of this, $tan(\phi)$ is referred to as the viscoelastic loss factor [17].

As Figure 3.4 by Koruk and Rajagopal [17] shows below, the phase lag angle ϕ between the sinusoidal stress input and the complex modulus based strain response is ultimately responsible for the formation of the elliptical hysteresis loops. The enclosed area of the hysteresis loop and thus the amount of energy dissipation within it is therefore heavily associated with the phase angle ϕ and by extension the loss factor $tan(\phi)$.

For a perfectly elastic material, the loss modulus E'' in the polar plot of Figure 3.2 equates to zero, also resulting in a phase angle of zero and instantaneous strain reaction under cyclic stress. For a phase angle of $\phi = \frac{\pi}{4}$, the loss factor $tan(\phi) = \frac{E''}{E'}$ is equal to 1 which implies that 50% of the applied cyclic strain energy is elastically recovered whilst the other half is dissipated. Following the same process, Figure 3.2 thus implies that for an imaginary pure viscous material where the elastic storage modulus

$E' = 0$, the strain must always lags behind by exactly a quarter cycle at $\phi = \frac{\pi}{2}$, for which the loss factor goes to infinity. Consequently, for viscoelastic materials such as fibre-reinforced polymer composites, the phase shift must be in between these extremes such that $0 < \phi < \frac{\pi}{2}$.

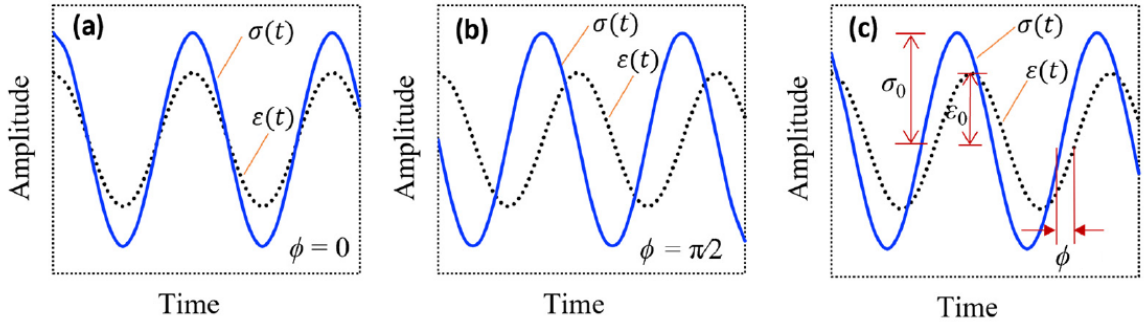

Figure 3.4: Phase shift between cyclic input stress and strain response of (a) pure elastic, (b) perfectly viscous and (c) viscoelastic material types [17].

As discussed in section 2.3 of the literature study, the total viscoelastic response of a fibre-reinforced composite is attributed to the combined contributions of the constituent materials, fibre-matrix interface and friction based damping. As given by Equation 3.13, for a composite material these factor can therefore be combined in the description of a total loss factor [12].

$$\tan(\phi_{total}) = \tan(\phi_{constutuents}) + \tan(\phi_{interface}) + \tan(\phi_{friction}) \tag{3.13}$$

The contributions of the individual constituent materials that make up the composite are determined by a modulus-weighed rule of mixtures between fibre and matrix in the loading direction as per Equation 3.14. By weighing the summation with their relative volume fraction and modulus, the contribution to the overall loss factor is dependent on the portion of the total applied mechanical strain energy stored by these individual material components.

$$\tan(\phi_{constituents}) = \frac{v_f \tan(\phi) E_f + v_m \tan(\phi) E_m}{v_f E_f + v_m E_m} \tag{3.14}$$

Therefore, if one has a very stiff fibre with negligible viscoelastic loss factor, which is then combined with an equal volume of a comparatively low stiffness polymer matrix, the viscoelastic loss factor of the combined unidirectional material will still be dominated by that of the fibres as those get to contain the vast majority of the applied energy. This then makes the progression of the fibre-matrix interfaces and internal friction more noticeable in comparison through Equation 3.13.

3.3. Linear viscoelastic hysteresis energy dissipation

With descriptions of the viscoelastic phase lag angle and loss factor defined, the aim now is to relate these to the quantity of strain energy dissipated for a given sinusoidal stress cycle, which is universally defined as Equation 3.15.

$$\sigma(t) = \sigma_a \sin(\omega t) + \sigma_{mean} \tag{3.15}$$

For such stress input, the general complex stiffness strain solution as first presented in Equation 3.10 is written as Equation 3.16 below.

$$\epsilon_h(t) = \frac{\sigma_a}{|E^*|} \sin(\omega t - \phi) + \frac{\sigma_{mean}}{|E^*|} \tag{3.16}$$

Following Green's Theorem, the area within a closed parametric function can be calculated as the line integral along its boundary, which for this case of the area enclosed within the stress-strain hysteresis loop of a single cycle with period $T = \frac{2\pi}{\omega}$ is defined as Equation 3.17.

$$\Delta W = \frac{1}{2} \int_0^T \left(\sigma(t) \frac{d\epsilon}{dt} - \epsilon(t) \frac{d\sigma}{dt} \right) dt \tag{3.17}$$

Here, the required derivatives of $\frac{d\sigma}{dt}$ and $\frac{d\epsilon}{dt}$ are given as follows:

$$\frac{d\sigma}{dt} = \sigma_a \omega \cos(\omega t) \tag{3.18}$$

$$\frac{d\epsilon}{dt} = \frac{\sigma_a}{|E^*|} \omega \cos(\omega t - \phi) \tag{3.19}$$

When substituting the functions for $\sigma(t)$, $\epsilon(t)$ and their derivatives as well as already eliminating all terms that cancel each other out or average to zero over the full cycle, the integral for the hysteresis area simplifies to Equation 3.20.

$$\Delta W = \frac{1}{2} \cdot \frac{\sigma_a^2 \omega}{|E^*|} \int_0^T \left[\sin(\omega t) \cos(\omega t - \phi) - \sin(\omega t - \phi) \cos(\omega t) \right] dt \tag{3.20}$$

This then conveniently matches with the trigonometric identity of Equation 3.21.

$$\sin(a)\cos(b) - \sin(b)\cos(a) = \sin(a - b) \tag{3.21}$$

This identity allows Equation 3.20 to further reduce to Equation 3.22 where the line integral contains only a single constant sine term of the phase lag angle. This then finally leads to a description of the hysteresis dissipated energy as function of the stress amplitude, the sine of the phase lag angle and the complex modulus of the cycle as given by Equation 3.23.

$$\Delta W = \frac{1}{2} \cdot \frac{\sigma_a^2 \omega}{|E^*|} \int_0^T \sin(\phi) dt \tag{3.22}$$

$$\Delta W = \frac{1}{2} \cdot \frac{\sigma_a^2 \omega}{|E^*|} \sin(\phi) \frac{2\pi}{\omega}$$

$$\boxed{\Delta W = \pi \sigma_a^2 \frac{\sin(\phi)}{|E^*|}} \tag{3.23}$$

Following Figure 3.2 again, here it should be that $\sin(\phi) = \frac{E''}{|E^*|}$ and thus equals the ratio of viscous loss modulus over the total apparent complex modulus. This can be substituted directly to form Equation 3.24.

$$\Delta W = \pi \sigma_a^2 \frac{E''}{|E^*|^2} \tag{3.24}$$

This shows that the hysteresis dissipated energy is inversely proportional to the square of the complex modulus, and therefore very sensitive to the laminate stiffness degradation in fatigue. However, the loss modulus E'' on its own remains somewhat of an artificial parameter, as it is typically not a measured factor unlike the phase angle or complex modulus. Furthermore, E'' will also not be a constant and is separately dependent on the damage accumulation in fatigue. Therefore, the ratio between E'' and

the complex modulus $|E^*|$ as given by $\sin(\phi)$ remains the most direct and descriptive factor to evaluate the viscoelastic and damage friction based damping.

For most continuous fibre-reinforced polymer composites materials the viscoelastic loss factor small and typically between $0.005 < tan(\phi) < 0.05$ [68], [69]. In such cases $|E^*| = E'\sqrt{1+\tan^2(\phi)} \approx E'$ which means that the complex and elastic moduli can be considered to be (near) equal. This would imply that $\frac{E''}{E'} \approx \frac{E''}{|E^*|}$, from which it can be said that for these materials the terms $\sin(\phi)$ and $\tan(\phi)$ can be used interchangeably. Therefore the current author argues that the term of viscoelastic loss factor itself, associated in viscoelastic polymer literature as only $\tan(\phi)$ [17], can in the context of continuous fibre reinforced polymer fatigue also be used to directly address $\sin(\phi)$ terms. Therefore, for the sake mathematical consistency the $\sin(\phi)$ term will be kept in the formulations to come, however in in-text descriptions it will be referred to as the viscoelastic loss factor as well.

3.4. Limitations of linear hysteresis dissipation

Although Equation 3.23 is able to describe the hysteresis dissipated energy as function of the stress amplitude, the viscoelastic loss factor and the apparent (complex) modulus, the current author believes that there remain a few fundamental limitations to the considered linear viscoelastic approach that restrict the direct implementation of Equation 3.23 into general fatigue analysis. These limitations are with regards to changes in the amount of mechanical work done on the material within a cycle as function of the mean stress and loading ratio. The derivation of ΔW of section 3.3 was explicitly started with stress and strain functions that included mean stress and and strain terms respectively, but as shown, these did not translate themselves to the final form Equation 3.23.

Ultimately, this independence of ΔW to mean stress and R-ratio based input energy changes is what makes it an inherently linear viscoelastic dissipation formula. Namely, the magnitude of energy dissipation for a cycle is only dependent on the stress amplitude (i.e. the magnitude of the input), and not its starting position (the mean stress). Linear viscoelastic dissipation descriptions thus assume a fixed relation between the stress amplitude and the consequent cyclic input energy (or work done). However, as Figure 3.5 below aims to demonstrate for three distinct R-ratio scenarios at a constant stress amplitude, this is not the case in practice.

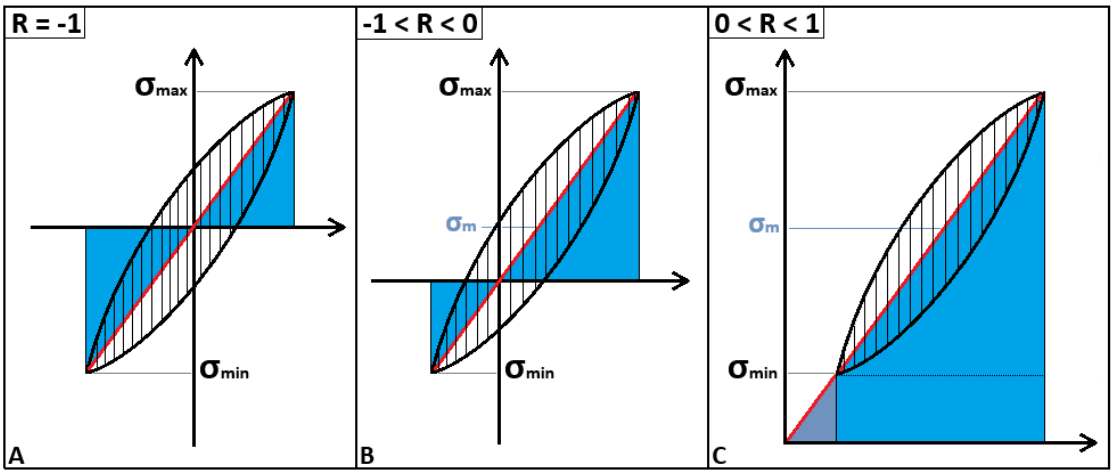

Figure 3.5: Visual representation of differences in cyclic work done on the material at constant stress amplitude for A) fully reversed cycles, B) tensile-compressive cycles and C) tensile-tensile cycles.

Here, the area of the blue highlighted regions represent the input energy or work done during a single cycle. As the R-ratio increases from -1 up to a positive value, this input energy per cycle also increases. If one assumes that the cyclic viscoelastic hysteresis dissipation should be proportional to the amount of input energy, then for a fixed stress amplitude like shown above, one could expect an increase in dissipation for an increased R-ratio. However, as discussed above, the linear viscoelastic dissipation formula of Equation 3.23 does not account for this.

Additionally, at R-ratios greater than zero there is a second unaccounted effect coming into play. As result of a cycle at $R > 0$ not having any distinct point in time where the material is fully unloaded, there will be a portion of the total strain energy stored by the material that is disconnected from the load cycle. This constant portion of the strain energy below the minimum stress acts instead as an effective energy 'preload', independent of the amount of work done on the material throughout the cycle.

Furthermore, as highlighted by the dotted line on right-most example of Figure 3.5, the input strain energy of the cycle in blue can be split up into two regions. Here the upper half is directly associated with the triangle formed underneath the hysteresis loop and is equal to that of an equivalent cycle at $R = 0$. For a constant stress amplitude however, the bottom (rectangular) segment is purely proportional to the value of the minimum stress and therefore a direct function of the R-ratio.

The problem of this mentioned preload energy and the bottom segments of the input energy below the minium stress at R-ratios greater than zero is that these are not directly accounted for by the definition of the viscoelastic loss factor. As result, if no additional compensating factors are introduced, then the direct use of loss factor terms like $\tan(\phi) = \frac{E''}{E'}$ or $\sin(\phi) = \frac{E''}{|E^*|}$ will result in an over-estimate of the hysteresis energy dissipation. This matches observations made by Cortazar-Noguerol et al. [70] who have for example shown that for increasing values positive minimum stress on polyurethane samples at constant stress amplitude, the dynamic mechanical analysis (DMA) measured loss factors decreased. Although these authors have not explicitly related this to energy effects as described in this section, their results are in agreement with the current argument for a decreasing compensation term for the loss factor at increasing R-ratios greater than zero.

Because of these limitations, linear viscoelastic theory in literature remains mostly associated with vibrational damping analysis where the experienced cycles are naturally fully reversed such that these mentioned energy based limitations do not play a role [17]. Authors such as Khoshmanesh et al. [62] and Kenny and Marchetti [28] have aimed to directly apply similar linear viscoelastic dissipation to tensile-tensile fatigue data. However, without implementation of energy based correction factors to such an approach, the magnitudes of the inversely derived damping characteristics and loss factors through measurement of the hysteresis energy are mostly arbitrary. This severely limits the application of such viscoelastic approach to only the analysis of relative changes within a single fatigue test and do not allow for comparisons across different maximum stress and R-ratio combinations.

Therefore, in line with the objectives of this thesis as discussed in section 2.8, the next section aims to introduce energy based correction factors to the linear viscoelastic dissipation formula of Equation 3.23 in order to make the relation between hysteresis dissipation and the viscoelastic loss factor applicable to, and comparable between, a wider range of fatigue testing R-ratios. With such improved relation established, this can then be extended to direct formulations of TDE and TDE over TW ratio as function of the aforementioned correction factors and the viscoelastic loss factor of the material. To the current authors best knowledge, such energy based correction factors to an otherwise linear viscoelastic approach have not yet been presented or applied in literature.

3.5. Energy based correction factors

Despite the limitations discussed in section 3.4 there is still a great benefit to fibre-reinforced composite fatigue energy dissipation analysis through linear viscoelasticity based on the concept of the complex modulus. This primarily due to its simplicity through only the dependence on the two material properties, namely the apparent material stiffness in the form of the complex modulus and a single parameter describing the viscous damping characteristic of the material through the viscoelastic loss factor. This leaves the loss factor as an easy to evaluate single variable which can be solved for as a means to describe the change in damping characteristics during a fatigue test and associate this with damage formation and incremental dissipation of energy towards a total or critical dissipation level.

This section therefore aims to derive stress-ratio based correction factors that account for the varying input energies and pre-load effects through the range of $R = -1$ to $R = 1$ in order to come to a formulation that allows direct comparison of loss factors measured under these different conditions. Hence a non-linear model is aimed to be approached through R-ratio correction factors applied to the otherwise linear viscoelastic model of section 3.3. These will be split up into two the distinct regimes of tensile-compressive loading at $-1 \leq R \leq 0$ and tensile-tensile loading with $0 \leq R \leq 1$.

3.5.1. Dissipation function for $-1 \leq R \leq 0$

As discussed in section 3.4, it is believed that for tensile-compressive loading where $-1 \leq R \leq 0$ only a single correction term is required to compensate for the increasing amount of cyclic input energy when raising the R-ratio at constant stress amplitude. The corrected hysteresis energy dissipation W_h is defined as Equation 3.25 and equals the linear viscoelastic dissipation ΔW times the ratio of the actual applied work W_a over a reference amount work done W_{ref} in an equivalent amplitude cycle at $R = -1$.

$$W_h = \Delta W \cdot \frac{W_a}{W_{ref}} \tag{3.25}$$

Here, W_a is the sum of the work done in both tension and compression and is given by Equation 3.26. When the relation $\sigma_{max} = \frac{2\sigma_a}{1-R}$ is substituted into this, then the applied work can instead be expressed directly as a function of the stress amplitude, as shown by Equation 3.27

$$W_a = \frac{\sigma_{max}^2}{2 \cdot |E^*|} + \frac{\sigma_{min}^2}{2 \cdot |E^*|} = \frac{\sigma_{max}^2(1+R^2)}{2 \cdot |E^*|} \tag{3.26}$$

$$W_a = \frac{2\sigma_a^2}{|E^*|} \frac{(1+R^2)}{(1-R)^2} \tag{3.27}$$

The reference energy is then simply obtained by filling in $R = -1$ into Equation 3.27, which gives $W_{ref} = \frac{\sigma_a^2}{|E^*|}$. Therefore, the compensating term $\frac{W_a}{W_{ref}}$ as shown by Equation 3.28 becomes independent of the stress amplitude and material stiffness and is a factor based on solely the cycle's R-ratio.

$$\frac{W_a}{W_{ref}} = 2\frac{1+R^2}{(1-R)^2} \tag{3.28}$$

With this, the total formulation of the hysteresis dissipated energy for cycles between $R = -1$ and $R = 0$ is then finally given by Equation 3.29.

$$W_h = 2\pi\sigma_a^2 \frac{1+R^2}{(1-R)^2} \frac{\sin(\phi)}{|E^*|} \quad \text{for } -1 \leq R \leq 0 \tag{3.29}$$

The above relation thus implies that as the R-ratio changes from the reference case of $R = -1$ to an equal amplitude cycle at $R = 0$, the amount of work done on the material doubles and therefore the expected dissipation should double as well. Then filling in $R- = 1$ directly, Equation 3.29 simply reduces to the direct formulation of the linear viscoelastic ΔW.

However, as in composite fatigue analysis the load cycles are more commonly expressed using their maximum stress and the R-ratio, Equation 3.29 can more practically be written in the alternatively form given by Equation 3.30.

$$\boxed{W_h = \frac{\pi\sigma_{max}^2(1+R^2)}{2} \frac{\sin(\phi)}{|E^*|} \quad \text{for } -1 \leq R \leq 0} \tag{3.30}$$

3.5.2. Dissipation function for $0 \leq R \leq 1$

For the case of positive R-ratios in the range of $0 \leq R \leq 1$, still an applied energy correction factor is considered alike to the one for the negative R-ratios. However, next to this an additional term of $\left(\frac{\sigma_a}{\sigma_m}\right)^2$ is incorporated to compensate for the energy segments that are naturally not accounted for in the definition of the viscoelastic loss factor. This effectively reduces to the ratio of energy associated with the stress amplitude and mean stress. Furthermore, by being equal to 1 for at $R = 0$, this term still ensures critical continuity with the W_h formulation for $-1 \leq R \leq 0$ as given in subsection 3.5.1.

The hysteresis dissipated energy W_h for this stress ratio range is therefore defined as Equation 3.31.

$$W_h = \Delta W \cdot \frac{W_a}{W_{ref}} \cdot \left(\frac{\sigma_a}{\sigma_m}\right)^2 \tag{3.31}$$

Here, for R-ratios between 0 and 1, the applied work per cycle is equal to the maximum strain potential of the cycle minus the the constant strain energy. Following a similar steps as taken in the previous section, the applied work per cycle for this R-ratio range is again given as function of the stress amplitude and R-ratio itself by Equation 3.32.

$$W_a = \frac{\sigma_{max}^2}{2 \cdot |E^*|} - \frac{\sigma_{min}^2}{2 \cdot |E^*|} = \frac{\sigma_{max}^2(1 - R^2)}{2 \cdot |E^*|}$$

$$W_a = \frac{2\sigma_a^2(1 - R^2)}{|E^*|(1 - R)^2} \tag{3.32}$$

As the reference energy W_{ref} still remains that of an equivalent cycle at $R = -1$. The ratio of $\frac{W_a}{W_{ref}}$ is thus calculated as Equation 3.33.

$$\frac{W_a}{W_{ref}} = 2\frac{1 - R^2}{(1 - R)^2} \tag{3.33}$$

If the above $\frac{Wa}{W_{ref}}$ ratio is substituted into Equation 3.31 and furthermore the relation of $\sigma_m = \sigma_a \frac{1+R}{1-R}$ is used, then the full expression for the hysteresis dissipated energy W_h in cycles with loading ratio's between 0 and 1 is given by Equation 3.34.

$$W_h = 2\pi\sigma_a^2 \frac{1 - R}{1 + R} \frac{\sin(\phi)}{|E^*|} \quad \text{for } 0 \leq R \leq 1 \tag{3.34}$$

And again, this can instead be more conveniently expressed in terms of the maximum stress as given by Equation 3.35.

$$\boxed{W_h = \frac{\pi\sigma_{max}^2}{2} \frac{(1 - R)^3}{1 + R} \frac{\sin(\phi)}{|E^*|} \quad \text{for } 0 \leq R \leq 1} \tag{3.35}$$

3.5.3. Correction factor vs R-ratio overview

Following the outcomes of the previous two sections, Figure 3.6 below finally gives an overview of the total dissipation correction factor values over the wider stress ratio range between $R = -1$ and $R = 1$. This plot is split up into individual curves for both cases of a hypothetical constant stress amplitude as well as that for a constant maximum stress. Here, both corrections equal 1 for stress ratio of $R = -1$, as there the linear viscoelastic dissipation formulation is naturally applicable without correction. At a stress ratio of $R = 1$ on the other hand, the loading type reduces to a pure preload creep case where no cyclic energy is dissipated. The R-ratio correction factor then reduces to zero.

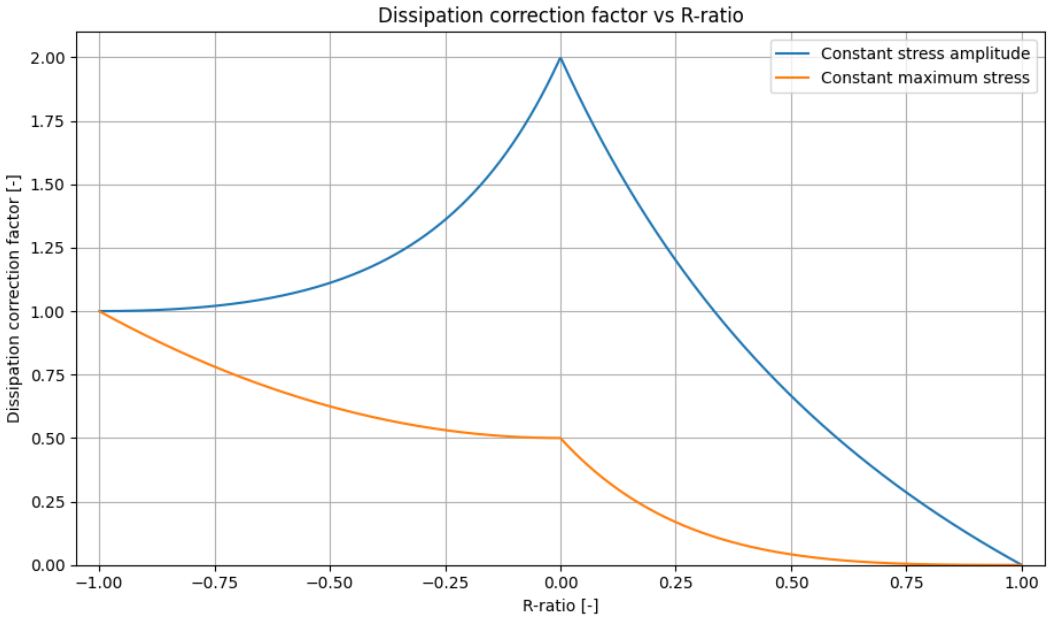

Figure 3.6: Cyclic energy dissipation correction factor vs R-ratio.

3.6. Cyclic dissipation ratio $\frac{W_h}{W_a}$

Now having come to expressions for the hysteresis dissipated energies W_h as well as knowing the amount of input energy or work done in a cycle W_a, the cyclic dissipation ratio can be established. This ratio, as given by Equation 3.36, effectively quantifies as what fraction of the amount of cyclicly applied energy is lost through viscous dissipation as well as internal friction resulting from damage.

$$\frac{W_h}{W_a} = \pi \left(\frac{1-R}{1+R}\right)^2 \sin(\phi) \quad \text{for } 0 \leq R \leq 1 \tag{3.36}$$

Here, any direct contributions of the maximum stress and laminate stiffness cancel each other out, leaving an expression with solely the viscoelastic loss factor in the form of $\sin(\phi)$ and the R-ratio. The particular R-ratio correction remaining would suggest that for fatigue cycles with increasing R-ratio between 0 and 1, the ratio between dissipated and applied energy per cycle will decrease, assuming a constant viscoelastic loss factor term $\sin(\phi)$ under the condition of equivalent strain rate. However, it remains to be seen experimentally how the stress level of the cycle indirectly influences Equation 3.36 through damage related changes of this loss factor for increasing cyclic maximum stresses, as well as its average loss factor value over its the fatigue life.

In fatigue testing at a high enough data sampling rate, the dissipated hysteresis energy of a fatigue cycle can be measured with relative ease by integration of the area of each hysteresis loop formed in the stress-strain data [1], [63]. Furthermore, the applied energy can also be estimated using the measured complex modulus and minimum and maximum cycle stress. Therefore using such experimental measurements, inverting Equation 3.36 such that it written as Equation 3.37 gives a convenient and clean method to determine the viscoelastic loss factor $\sin(\phi)$ of each cycle.

$$\sin(\phi) = \frac{1}{\pi}\frac{W_h}{W_a}\left(\frac{1+R}{1-R}\right)^2 \quad \text{for } 0 \leq R \leq 1 \tag{3.37}$$

3.7. Total dissipated energy, total work done and TDE/TW ratio

So far, the derived expressions for hysteresis dissipated energy and cyclic dissipation ratio addressed only individual load cycles. However, as part of the objectives of this thesis the aim is to further exploit these established relations into direct functions for the total dissipated energy (TDE), total work done (TW) and their ratio ($\frac{TDE}{TW}$). These are focussed on drawing out the per-cycle viscoelastic and damage based damping trends to weighted averages over the whole fatigue life as direct single-term comparisons of overall tests at different R-ratio and maximum stress combinations.

The TDE, TW and the ratio $\frac{TDE}{TW}$ can be obtained by summation of the corresponding per-cycle values W_h and W_a over the number of cycles to failure N_f. Under constant amplitude fatigue loading, the maximum stress and R-ratio remain constant and can therefore be taken out of the summations. This then gives the following expression of equations 3.38-3.40.

$$TDE = \frac{\pi\sigma_{max}^2}{2}\frac{(1-R)^3}{1+R}\sum_{i=1}^{N_f}\frac{\sin(\phi_i)}{|E_i^*|} \quad \text{for } 0 \leq R \leq 1 \tag{3.38}$$

$$TW = \frac{\sigma_{max}^2(1-R^2)}{2}\sum_{i=1}^{N_f}\frac{1}{|E_i^*|} \quad \text{for } 0 \leq R \leq 1 \tag{3.39}$$

$$\frac{TDE}{TW} = \pi\left(\frac{1-R}{1+R}\right)^2\frac{\sum_{i=1}^{N_f}\frac{\sin(\phi_i)}{|E_i^*|}}{\sum_{i=1}^{N_f}\frac{1}{|E_i^*|}} \quad \text{for } 0 \leq R \leq 1 \tag{3.40}$$

Following from this, the total dissipated energy and the $\frac{TDE}{TW}$ ratio are more conveniently expressed by the average loss factor over complex modulus ratio and the effective loss factor $\sin(\phi)_{eff}$, respectively.

$$TDE \approx N_f \cdot \frac{\pi\sigma_{max}^2}{2}\frac{(1-R)^3}{1+R}\cdot\left(\frac{\sin(\phi)}{|E^*|}\right)_{avg} \tag{3.41}$$

$$\frac{TDE}{TW} \approx \pi\left(\frac{1-R}{1+R}\right)^2\sin(\phi_{eff}) \tag{3.42}$$

Here, the effective loss factor $\sin(\phi_{eff})$ is essentially the energy weighted average of the individual cycle loss factor values of each cycle. Compared to just a simple average, this directly accounts for the fact that not all load cycles contribute equally to the total dissipated energy and $\frac{TDE}{TW}$ ratio.

Therefore, Equation 3.42 critically confirms the at the end of the literature study hypothesized direct relation between an average or effective loss factor of a fatigue tests and the total dissipated over total work ratio. Although the direct effect of σ_{max} in the $\frac{TDE}{TW}$ ratio cancels out, it is believed that $\sin(\phi_{eff})$ will still remain strongly effected by the applied stress as this is a driving factor in the damage generation and consequent increases in friction. What remains to be experimentally shown is thus how the effective loss factor relates itself to varying maximum stresses and whether or not below a certain stress level such trend would flatten off towards a pure pristine material viscoelastic value.

3.8. Extension to fatigue life prediction

If indeed the total dissipated energy of fibre-reinforced polymer composites in fatigue follows a constant power-law relation with the maximum stress, independent of the R-ratio as was suggested by Movahedi-Rad et al. [57], then the $\frac{TDE}{TW}$ ratio as described in section 3.7 can be used as the basis of a fatigue life prediction method. Here, the assumption is that one has performed a fatigue test at a specific maximum stress and R-ratio (R_1), such that the measured total dissipated over total work ratio equals $\left(\frac{TDE}{TW}\right)_{R_1}$. Then, the equivalent ratio at the same stress level but alternative R-ratio (R_2) is related to the first test by Equation 3.43

$$\frac{\left(\frac{TDE}{TW}\right)_{R_1}}{\left(\frac{TDE}{TW}\right)_{R_2}} = \frac{\left(\frac{1-R_1}{1+R_1}\right)^2 \sin(\phi_{eff})_{R_1}}{\left(\frac{1-R_2}{1+R_2}\right)^2 \sin(\phi_{eff})_{R_2}} \tag{3.43}$$

Following the assumption of a constant TDE for equal maximum stress, this must then equal Equation 3.44:

$$\frac{\left(\frac{TDE}{TW}\right)_{R_1}}{\left(\frac{TDE}{TW}\right)_{R_1}} = \frac{TW_{R_2}}{TW_{R_1}} \tag{3.44}$$

Here, the rightmost part of Equation 3.44 can be further expanded into Equation 3.45, which in term can be set equal to Equation 3.43 in order to form Equation 3.8.

$$\frac{TW_{R_2}}{TW_{R_1}} = \frac{(1-R_2^2)}{(1-R_1^2)} \frac{N_{f_{R_2}}}{N_{f_{R_1}}} \frac{|E^*|_{avg,R_1}}{|E^*|_{avg,R_2}} \tag{3.45}$$

$$\frac{(1-R_2^2)}{(1-R_1^2)} \frac{N_{f_{R_2}}}{N_{f_{R_1}}} \frac{|E^*|_{avg,R_1}}{|E^*|_{avg,R_2}} = \frac{\left(\frac{1-R_1}{1+R_1}\right)^2 \sin(\phi_{eff})_{R_1}}{\left(\frac{1-R_2}{1+R_2}\right)^2 \sin(\phi_{eff})_{R_2}}$$

Finally, the above can be rearranged into Equation 3.46 to give a direct expression of the fatigue life of a specimen tested at a stress ratio R_2 based on a reference fatigue life obtained at the same maximum stress, but alternative R-ratio R_1.

$$N_{f_{R_2}} = N_{f_{R_1}} \cdot \frac{\left(\frac{1-R_1}{1+R_1}\right)^2}{\left(\frac{1-R_2}{1+R_2}\right)^2} \frac{(1-R_1^2)}{(1-R_2^2)} \frac{|E^*|_{avg,R_2}}{|E^*|_{avg,R_1}} \frac{\sin(\phi_{eff})_{R_1}}{\sin(\phi_{eff})_{R_2}} \tag{3.46}$$

This means that if the average specimen stiffness and effective loss factor over a fatigue test can be estimated or predicted for a non-tested R-ratio, then under the assumption of a constant TDE this can directly lead into a prediction of the associated fatigue life in number of cycles at such non-tested R-ratio.

3.9. Conclusion of approach

In this chapter, a linear viscoelastic approach was introduced and followed to come to a description of the cyclic viscoelastic hysteresis dissipated energy based on the stress amplitude, complex modulus and the viscoelastic loss factor. However, energy based limitations were identified that are believed to restrict the application of such approach to just fully reversed cycles at $R = -1$. To account for this, correction factors were established that based on physical principles circumvent these limitations and should make the linear viscoelastic approach applicable to all load cycles between $-1 \leq R \leq 1$. These should also aid and make possible the comparison of fatigue derived viscoelastic loss factor values to those of alternative measurement techniques such as dynamic mechanical analysis.

Through this, new definitions for fibre-reinforced polymer composite fatigue parameters such as the cyclic dissipation energy, cyclic dissipation ratio, total dissipated energy and TDE/TW ratio could be defined as explicit functions of the viscoelastic loss factor and these energy based correction factors. Therefore, for the experimental part of this thesis, one of the primary interest will be to aim to understand how this viscoelastic loss factor $\sin(\phi)$ changes throughout the fatigue life at different maximum stresses and R-ratios, as well as how this relates to the weighted average value over the complete fatigue life. If the latter can be shown to be consistent across different R-ratios or at least follow a predictable trend, then with a potential constant total dissipated energy, this can directly lead to fatigue life predictions.

4

Preliminary Analysis

In order to get an initial feel for the applicability of the proposed modified linear viscoelastic approach and the derived formulations of cyclic and total energy dissipation metrics, datasets obtainable from available literature were resorted to for preliminary analysis. Apart from gathering initial results that directly lead into the specific objectives of the experiment design in chapter 5, this chapter also serves the reader as introduction to the overall fatigue analysis framework enabled by the theory introduced in chapter 3. A very similar approach will be used to establish the later presented experimental results in chapter 7.

Section 4.1 will first briefly introduce the origins and loading conditions of the reference fibre-reinforced composite fatigue dataset. Following this, section 4.2 then shows the trends of laminate stiffness degradation and hysteresis energy dissipation over the normalised fatigue lives, which form the primary input data for the analysis throughout the remainder of the chapter. Then, in section 4.3 these trends are used to establish the progressions of the cyclic dissipation ratios over the fatigue lives and how these lead to the overall total dissipation ratios. Section 4.4 is then able to convert these trends to the progression of the viscoelastic material characteristics such as the loss factor and loss moduli and relate these to a pristine material reference measured through dynamic mechanical analysis. Having established the correlation with such DMA measurements, section 4.5 and section 4.6 aim to relay this back to the literature study and introduce an alternative method to come to a viscoelastic theory based the high cycle fatigue strength estimation. To close of the preliminary analysis, section 4.7 briefly discusses the observed trend in the total dissipated energy versus cyclic maximum stress. Then finally, this is followed by section 4.8 which concludes on the overall findings and limitations of the preliminary analysis which direly led into the experimental objectives of the upcoming chapter 5.

4.1. Reference fatigue dataset

The data for the preliminary analysis presented in this chapter was derived from a study by Movahedi-rad et al. [15] on the fatigue damage of $\pm 45^{\circ}$ woven glass/epoxy laminates under $R = 0.1$ tensile-tensile fatigue testing. This source data was particularly useful, as not only was it mostly presented in easily convertible linear scales over normalised life, but also importantly contained information on dissipated hysteresis energy per cycle, stiffness degradation throughout the fatigue life as well quasi-static and dynamic tensile test results. These form the minimum measurements required for the aimed type of analysis.

In their original paper, Mohavedi-rad et al. chose to perform fatigue tests at different stresses not using a fixed frequency, but rather at a constant loading rate of 30.5 kN/s. The authors proposed this constant loading rate over the usually standard practice of a fixed testing frequency with the goal of minimising the effects of hysteresis heating at higher applied stresses. Of particular interest for this thesis however, such constant loading rate has the added benefit of significantly reducing the disparity of experienced strain rates across the tested stress levels. As concluded in subsection 2.5.2 this aids the consistency of the material's viscoelastic properties, matrix stiffness and fibre-matrix interface strength.

This reference dataset consists of the average results of four tests per maximum stress level ranging from 47 to 64 MPa, or 38.5% to 52.5% of the ultimate strength. The corresponding test frequencies were not provided in the original publication by Mohavedi-rad et al. [15], but given the fixed loading rate of 30.5 kN/s these could be estimated using Equation 4.1. Finally, the average fatigue life and failure strains according to the original authors are presented in Table 4.1.

$$f = \frac{\dot{P}}{2A_{gauge}\sigma_{max}(1-R)} \tag{4.1}$$

Table 4.1: Fatigue test maximum stresses and corresponding average frequency, fatigue life and failure strain as obtained from [15].

Nominal σ_{max} [MPa]	Avg. σ_{max} [Mpa]	Test frequency [Hz]	Avg. fatigue life [cycles]	Failure strain [-]
47	48.00	6.33	677040	0.0184
49	49.36	6.10	305264	0.0198
53	54.36	5.53	45297	0.0205
58	59.22	5.06	17251	0.0256
64	64.34	4.68	2543	0.0313

4.2. Modulus degradation and hysteresis energy

Throughout their tests, Movahedi-Rad et al. measured the stress-strain hysteresis loops in order to derive the dynamic (complex) modulus and dissipated energy per cycle. Figure 4.1 below shows these measurements over the normalised fatigue life for the five usable stress levels respectively. More stress levels were tested by the original authors of this dataset, but for these the required input data for this preliminary analysis was not of sufficient resolution.

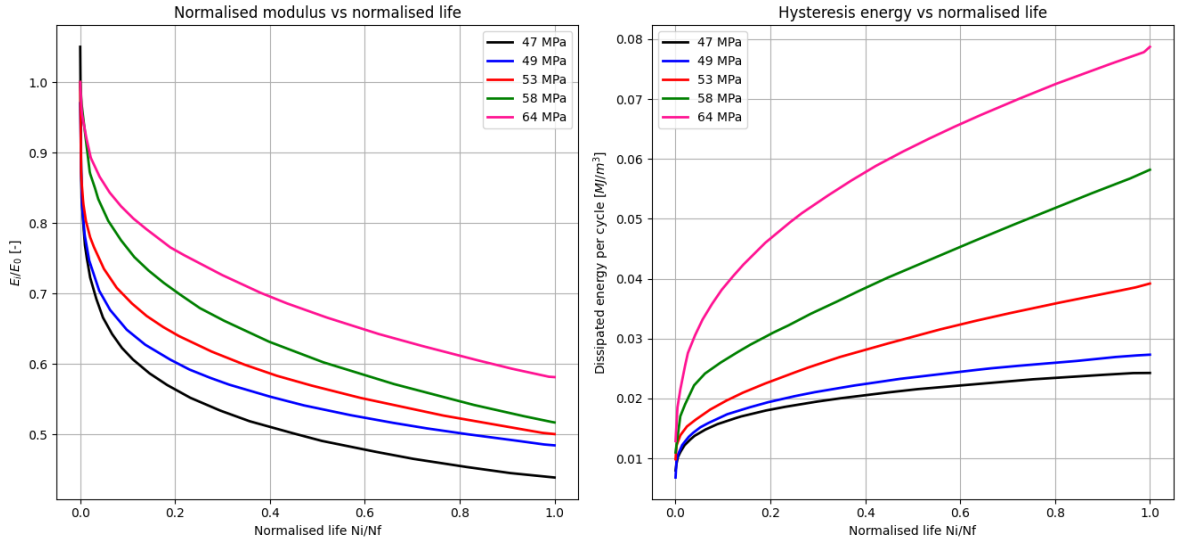

Figure 4.1: Avarage laminate modulus degradation and energy dissipation per cycle over normalised fatigue life as reconstructed from [15].

From the above figure one can clearly see how in the initial few fatigue cycles, sharp decreases in laminate stiffnesses occurred as matrix cracks and fibre-matrix debonds initiated, followed by a more stable propagation phase.

Somewhat counter-intuitively, at the lower maximum stresses a larger percentage of laminate stiffness is lost throughout the fatigue tests. However, this can be explained through a lower rate of modulus degradation per cycle over exponentially more cycles ultimately leading to an overall larger stiffness loss. This is supported by the rate of energy dissipation, which is considerably lower for reduced stress levels. As the maximum stress increases, the energy dissipation per cycle increases much more substantially over the specimen's lifetime.

However, as stiffness degradation is quite severe in this $\pm 45^\circ$ matrix dominated case, solely evaluating the damage propagation characteristics through the energy dissipation paints a skewed picture. Therefore, over the next sections the energy dissipation will be normalised by the applied energy in to be able to relate the cyclic dissipation ratio $\frac{W_h}{W_a}$ to the progression of the viscoelastic loss factor following the theory introduced in chapter 3.

4.3. Cyclic dissipation ratio W_h/W_a

The applied energy per load cycle is calculated using Equation 3.32 as originally shown in subsection 3.5.2. However, Figure 4.1 from the source data only gives the hysteresis stiffness degradation normalised by its initial value. Thus, to be able to evaluate the progression of the energy applied per cycle, the initial cycle moduli had to be estimated using the quasi-static test data at the equivalent loading rate shown in Figure 4.2. The resulting initial moduli estimates are given in Table 4.2.

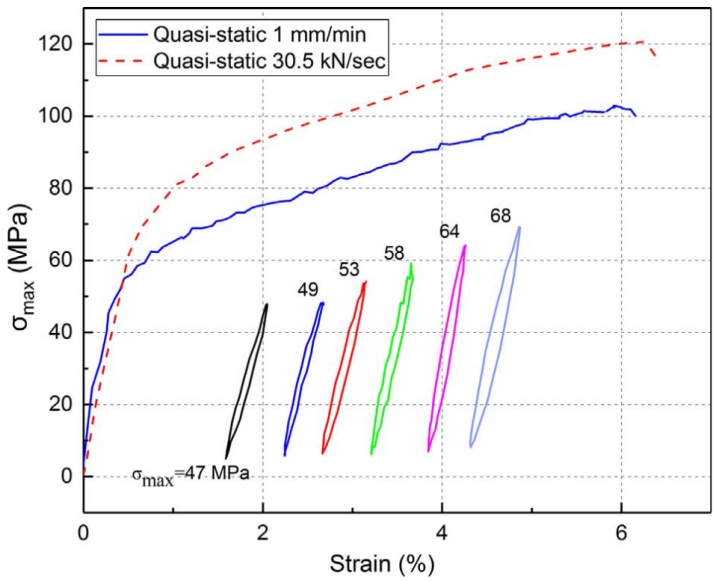

Figure 4.2: Quasi-static test results at 5 mm/min and 30.5 kN/s [15].

Table 4.2: Calculated initial moduli for the various stress levels.

Nominal σ_{max} [MPa]	Initial modulus [Mpa]
47	12322
49	12327
53	12336
58	12203
64	11721

The progression of the applied energy per cycle was calculated and plotted in Figure 4.3. As expected, this value is significantly greater for the highest stress levels and its increase throughout life proportional to the stiffness degradation. Unlike the energy dissipation however, the applied energy per cycle graphs appear similar in nature across the stress levels, predominantly being shifted up with increasing σ_{max} with a combined slight increases in final slopes.

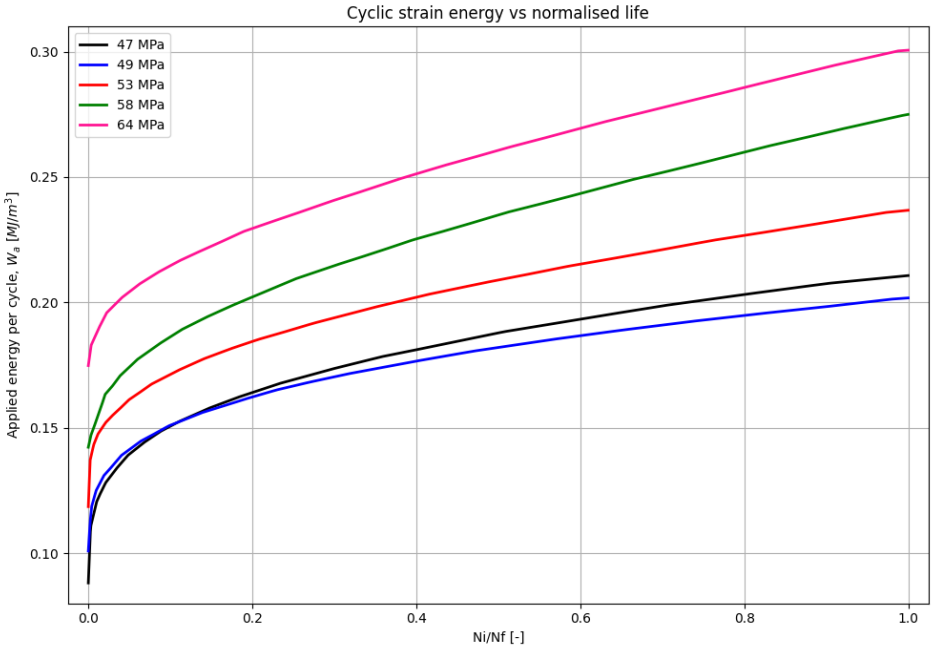

Figure 4.3: Calculated applied strain energy per cycle (W_a) over normalised life.

Now finally, the dissipated energy per cycle can be normalised by the respective cyclicly applied energy, forming the by now well discussed cyclic dissipation ratio $\frac{W_h}{W_a}$, as shown in Figure 4.4.

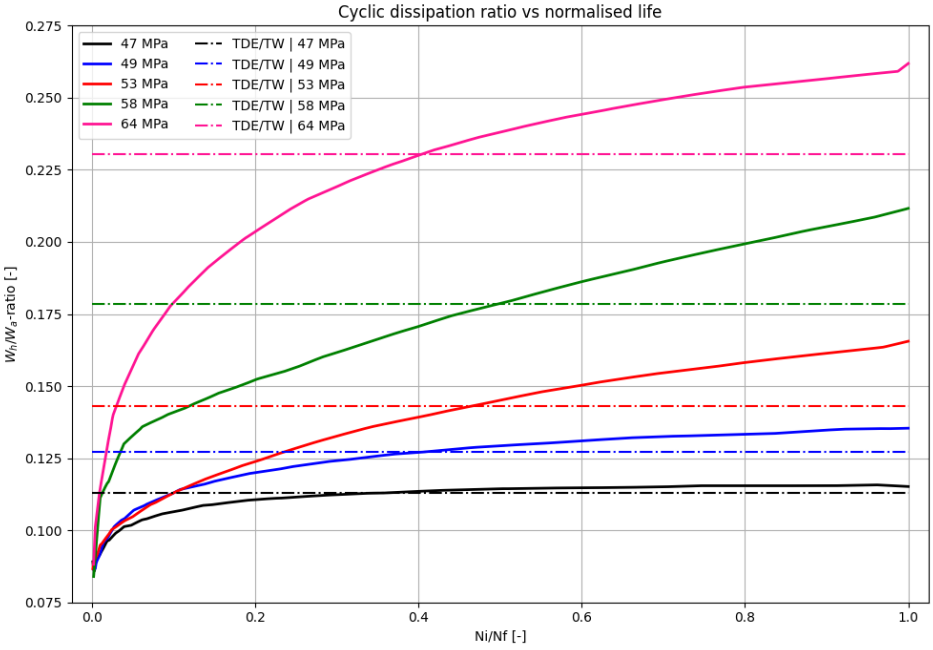

Figure 4.4: Calculated ratio W_h/W_a per cycle (W_a) over normalised life.

Here, the solid graphs represent the progression of the $\frac{W_h}{W_a}$-ratio per load cycle at the varying maximum stress levels, whist the dashed horizontal lines show the $\frac{TDE}{TW}$-ratio calculated over the complete fatigue life using Equation 3.40.

Unlike the dissipated and applied energy trends of figures 4.1 and 4.3 individually, the cyclic dissipation ratios shown in Figure 4.4 above give an arguably much better representation of the overall damage progression. At low stresses, there is a distinguished initiation phase in the first 15-20% of life where the cyclic dissipation ratio progressively increases. At the lowest maximum stress level it then tends to stabilise and remain near constant for most of the remaining fatigue life. This steady-state damping phase also coincides well with the total dissipation ratio of $\frac{TDE}{TW}$. This would indicate that at this low maximum stress level, the loss factor reaches a 'saturated value' after the initiation phase where the ratio of dissipated over applied energy per cycle remains near constant until failure. The ratio of total dissipated energy over total applied energy over the complete fatigue life is therefore closely matched to this stabilised phase of the cyclic dissipation ratio.

As the maximum stress is raised however, the cyclic dissipation ratio increases more drastically over the fatigue life and shows less clearly separated initiation and propagation phases. Particularly for the highest stress level of 64 MPa with a fatigue life of only 2500 cycles, one can argue based on Figure 4.4 that there is no stable propagation phase at all. Instead, the damage accumulation acts one continuous and aggressive process up to final failure.

Figure 4.4 also highlights that unlike initially hypothesised at the start of this thesis based on data by Bhangale [1], such great difference in behaviour of cyclic dissipation ratios also translates itself to the total dissipation ratio $\frac{TDE}{TW}$ clearly being a function of the applied stress, rather than a material constant. Despite both derived expressions for $\frac{W_h}{W_a}$ and $\frac{TDE}{TW}$ in equations 3.36 and 3.40 respectively being independent of the applied stress, the indirect effect of σ_{max} remains strong through the damage sensitivity of the viscoelastic loss factor term $\sin(\phi)$ appearing in both definitions.

4.4. Conversion to viscoelastic characteristics

To get a first opportunity to validate the modified linear viscoelastic dissipation theory introduced in chapter 3, the aim of this section is to compare the loss factor and loss modulus values derived for the fatigue dataset by Movahedi-Rad et al. to those of a similar material in an undamaged state. As shown on the cyclic energy dissipation ratio plot of Figure 4.4, for most of the lower stresses, the $\frac{W_h}{W_a}$ ratios appear to start from roughly the same value after which they diverge. This would indicate that in such first cycles where the fatigue damage is still at a minimum, the dissipation ratio remains dictated by the viscoelastic characteristics of the undamaged laminate. As proposed by Equation 3.37, which is repeated here below for reference, the value of the loss factor in a cycle is directly related to the cyclic dissipation ratio $\frac{W_h}{W_a}$ and an energy-based R-ratio correction factor.

$$\sin(\phi) = \frac{1}{\pi}\frac{W_h}{W_a}\left(\frac{1+R}{1-R}\right)^2 \quad \text{for } 0 \leq R \leq 1 \tag{3.37}$$

Therefore, if Figure 4.4 is converted to a $\sin(\phi_i)$ vs $\frac{N_i}{N_f}$ plot instead, one should expect the dynamic mechanical analysis (DMA) measured loss factor of the undamaged material to line up roughly with the starting values. A similar trend should hold when evaluating the progression of the viscoelastic loss modulus E''. However, unfortunately Movahedi-Rad et al. did not perform such DMA test on their material, as the viscoelastic loss factor is generally not a commonly applied material property to fatigue analysis. Other sources in literature were thus resorted in order to get a reasonable loss factor estimate to compare to.

4.4.1. DMA reference

As reference for this section, Karvanis et al. [68] performed such DMA study on various carbon and glass fibre composites. One of these tests was on quite similar woven $\pm 45^\circ$ glass/epoxy composite as tested by Movahedi-Rad et al., which also had comparable fibre contents at 63% and 62% respectively. Therefore, the loss factor measurement by Karvanis et al. will be used here to evaluate the correlation of the fatigue data to such DMA.

The loss factor reported by Karvanis et al. [68] for the $\pm 45^\circ$ woven glass/epoxy specimen equalled about 0.027, and was measured using a 3-point bending DMA test fixture with a 30 mm span. Their specimen had thicknesses between 2.35-2.45 mm and widths of 7 mm. To create the cyclic loading,

the specimen were preloaded with a 1N force, on top of which a 20μm displacement amplitude was applied. Given their specimen geometry, measured stiffness and 3-point bending span, the current author estimated a mean displacement of 65μm onto which the $\pm$20μm was added. With the linear relation between bending stress and displacement, the DMA load cycles by Karvanis et al. are thus estimated to have had a stress ratio of $R \approx 0.53$.

This DMA measurement stress ratio is import, as in chapter 3 it was established that the viscoelastic loss factor would only be directly applicable to hysteresis energy dissipation for load cases with stress ratio of $R = -1$. At alternative R-ratios, it was argued that energy-based correction factors would have to be applied in order to retain a consistent definition of the viscoelastic loss factor. These stress correction factors ensured that the loss factors measured at different stress ratios would remain a directly comparable material property as effectively collapsed values to an equivalent load cycle at $R = -1$.

Therefore, also in dynamic mechanical analysis the loss factor values measured at one particular R-ratio should not be equivalent those measured at another, unless the same energy effects are accounted for. Based Equation 3.34, this DMA loss factor correction to an equivalent $R = -1$ cycle is then given by Equation 4.2.

$$\sin(\phi) = \frac{\sin(\phi_{DMA})}{2} \frac{1 + R_{DMA}}{1 - R_{DMA}} \quad \text{for } 0 \leq R \leq 1 \tag{4.2}$$

Using the above, the actual material loss factor by Karvanis et al. is estimated at $\sin(\phi) \approx 0.043$, which is significantly different from the direct measurement at $R = 0.53$ of 0.027. Like discussed in section 3.4 of the previous chapter, the current author believes that his has so far been the main hindrance in being able to compare viscoelastic property measurements between dynamic mechanical analysis and fatigue load cycles.

4.4.2. Loss factor vs normalised life

Now with a reasonable pristine loss factor value estimated for a similar $\pm 45°$ woven glass/epoxy material, this value is highlighted for reference on the loss factor vs normalised fatigue life plots shown in Figure 4.5 below.

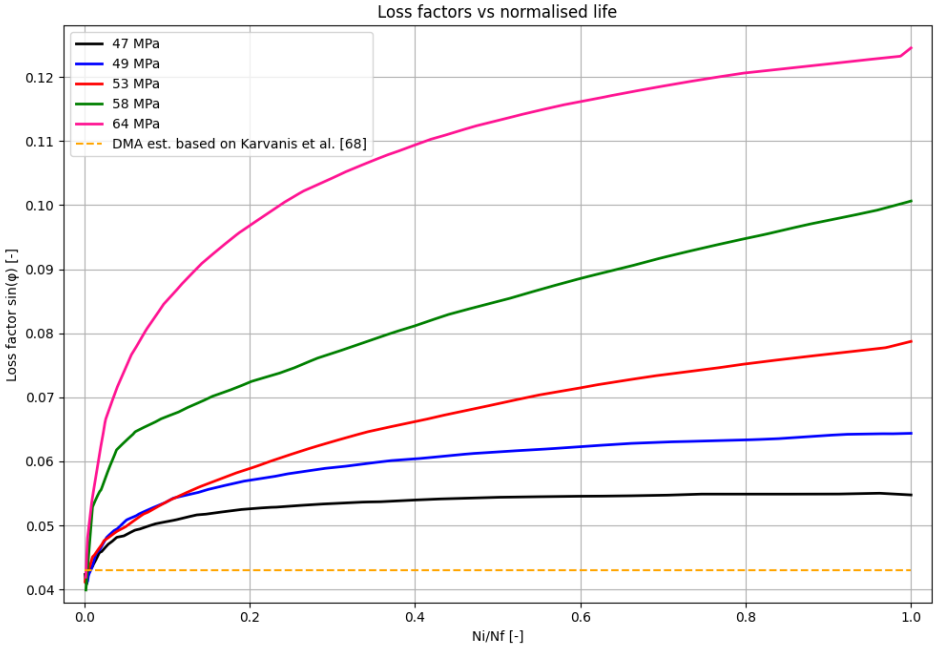

Figure 4.5: Fatigue derived viscoelastic loss factor $\sin(\phi)$ over normalised life, including DMA reference.

As the cyclic dissipation ratio was described as effectively only scaling of the loss factor by an R-ratio term and a factor π, the overall trends shown in the above figure are identical to those observed and already discussed for Figure 4.4. However, most importantly for the current comparison, the estimated pristine loss factor of a similar material does indeed appear to correlate well with the loss factors derived from the early cycle hysteresis.

To be critical, the DMA reference loss factor is slightly on the higher end. Nonetheless, this is to be somewhat expected as the strain rates in Movahedi-Rad's fatigue tests are higher than the DMA measurements, which which given the discussion of subsection 2.5.2 are bound to reduce the overall loss factor. All things considered, the shown correlation gave good initial confidence in the proposed energy corrected linear viscoelastic analysis approach.

4.4.3. Loss modulus vs normalised life

With the progression of the loss factor $\sin(\phi_i)$ determined, the analysis of changing laminate damping properties can take one step further. Namely, using the definition of the viscoelastic loss factor as the ratio of loss modulus E'' over the complex (dynamic) modulus $|E^*|$, the value of the loss moduli over the normalised fatigue lives can thus be estimated through $E''_i = |E^*_i| \cdot \sin(\phi_i)$. For the current reference dataset, the results from this are plotted in Figure 4.6. Also here, a reference value is shown based on the R-ratio corrected DMA measurement by Karvanis et al., which is calculated as $E''_{DMA} = |E^*_{DMA}| \cdot \sin(\phi_{DMA,corrected})$.

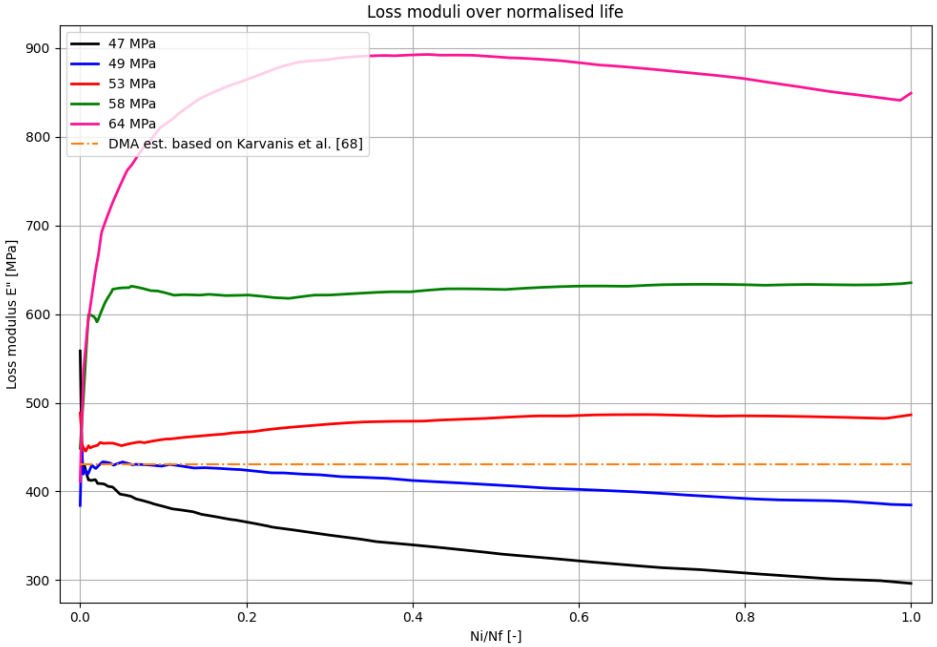

Figure 4.6: Fatigue derived loss moduli (E'') vs normalised life, indluding DMA reference.

Similar to the loss factor, the magnitudes of the early cycle loss moduli are again quite comparable to those derived from the DMA tests by Karvanis et al. [68].

Furthermore, it is observed that despite the fact that the loss factors shown in Figure 4.5 increased for all stress levels throughout the fatigue life, the calculated loss moduli for the two lowest stress levels of 47 and 49 MPa continuously decrease. For the slightly higer maximum stress level of 53, the loss moduli slowly increased throughout life at a seemingly constant rate. For the highest stress level of 64 MPa on the other hand, the loss moduli quickly increase in the first 20% of fatigue life. At around 40%, it start decreasing again which tends to line up well with the onset of necking at these high stresses reported by Movahedi-Rad et al. Particularly the latter here is interesting to note, as the observed necking at this high fatigue stress does has not become not apparent in any of the other fatigue metrics shown so far.

From the perspective of $\sin(\phi) = \frac{E"}{|E^*|}$, the observed loss moduli behaviour make sense with respect to the progression of loss factors shown in Figure 4.5. Namely that the loss factor for $\sigma_{max} = 47$ MPa stabilises to an almost constant value whist the complex modulus continuously decreases, which implies that the loss modulus must decreases proportionally along with it to keep their ratio constant. The decreasing loss modulus therefore effectively slows down the influence of the laminate stiffness degradation on the overall loss factor and cyclic dissipation ratio growths. For high stresses on the other hand, the increasing loss modulus accelerates the effect of complex modulus degradation.

4.4.4. Contribution of loss vs complex moduli on overall loss factor

Based on the discussion of section 2.3 on the sources of viscoelastic damping in fibre-reinforced polymer composites, one might have expected that with increasing fatigue damage in the form of matrix cracks, fibre-matrix debonds etc., that the internal friction would rise and thus always increase the overall loss modulus. However, based on this preliminary analysis exercise, this appears to not always be the case depending on stress level and damage mechanism.

As was discussed in section 3.2 of the previous chapter, the contribution of the matrix material to the overall viscoelastic damping characteristics of the laminate is dependent on the how much this matrix adds to the total laminate stiffness relative to the fibres. After all, if the modulus of a constituent material is low compared to the others, it will only store and be able to dissipate a small portion of the total applied mechanical energy. Following that reasoning, as fibre-matrix debonding and matrix cracking initiate, this stiffness contribution of the matrix decreases rapidly. This leads to an overall decrease of laminate complex modulus, but should also yield a roughly proportional decrease in viscoelastic loss modulus. Therefore, if the fatigue stress is low enough such that the friction based damping components remain negligible or at the very least stable, then the overall loss factor of $\sin(\phi) = \frac{E''}{|E^*|}$ shall remain reasonably constant as the numerator and denominator decrease roughly proportionally.

Nevertheless, such discussed behaviour may again be very different in more fibre dominated composites in the form of bi-axial or quasi-isotropic laminates. For those, the stiffness degradation in fatigue is generally much lower than in angle-ply laminates like currently discussed $\pm 45^\circ$ due to the inherently smaller reliance on the polymer matrix for stiffness [14]. In such alternative cases where the complex modulus $|E^*|$ remains more stable through to the fibres along the load direction, the $\frac{E''}{|E^*|}$-ratio should become inherently more sensitive to changes in net loss modulus E'' by the matrix and/or increased internal friction.

Alternatively, the fibres along the loading direction may even be so dominant on the overall damping characteristics that neither changes in matrix damping contribution or friction have have any significant effect on the overall cyclic damping ratio and thus by extension the total dissipation ratio. However, as such data is generally lacking in current literature, this remained to be shown through testing of such more fibre-dominated laminates in the experimental phase of this thesis.

4.5. Estimating high cycle fatigue strength

As discussed in subsection 2.6.2 of the literature study, authors such as La Rosa and Risitano [64], Montesano et al. [65] and Colombo et al. [67] have related the high cycle fatigue strength (HCFS) to the stress level at which a pronounced infliction point shows in the slope of infrared thermography measured average or stabilised energy dissipation rate. Beyond this stress level, the energy dissipation rate and measured temperature rapidly increase as result of the onset of a significant increase in internal damping. This was then linked with a critical damage mechanism initiation or critical damage density, which from that stress level onward would dominate the intermediate to high cycle fatigue life [65]–[67].

It was hypothesized towards the end of the literature study that if through a consistent viscoelastic analysis approach, a fatigue hysteresis loss factor measurement could be directly compared to that of a pristine material sample in dynamic mechanical analysis, then such thermography based HCFS may be seen as the stress at which the damping properties of the laminate start to significantly diverge from that of the pristine material. The previous section 4.4 has shown some initial supporting results for this, where both early fatigue cycle loss factors and loss moduli from the fatigue dataset by Movahedi-Rad et al. compared themselves well to those of a similarly R-ratio corrected DMA reference measurement by Karvanis et al.

Furthermore, the brief discussion that followed also reasoned that although damage may initiate at a lower stress than the HCFS, as long as the relative contribution of the matrix material to both loss and complex modulus decrease roughly proportionally then the overall loss factor would not change considerably. This would imply that the material's cyclic dissipation ratio will only significantly start to diverge from a pristine DMA measurement when such even degradation balance is disturbed by increasing levels of internal friction or plastic dissipation beyond the HCFS.

Within the current analysis framework, such high cycle fatigue strength estimate is considered to be best made by plotting the effective loss factors, which were defined in section 3.7 as the energy-weighted average loss factor value over the whole fatigue life, against maximum stress levels. The HCFS is then given by the intersection point between a constant horizontal line representing the DMA reference loss factor and the trend fitted through the $\sin(\phi_{eff})$ vs σ_{max} fatigue data. Here, the effective loss factor for each stress level is calculated by inverting Equation 3.42, which yields Equation 4.3.

$$\sin(\phi_{eff}) = \frac{1}{\pi}\left(\frac{1+R}{1-R}\right)^2 \frac{TDE}{TW} \tag{4.3}$$

The $\frac{TDE}{TW}$ ratios for each stress level are taken as those first shown in Figure 4.4. Using the above relation, the effective loss factors for each fatigue stress and their linear and power-law style extrapolations are shown below in Figure 4.7.

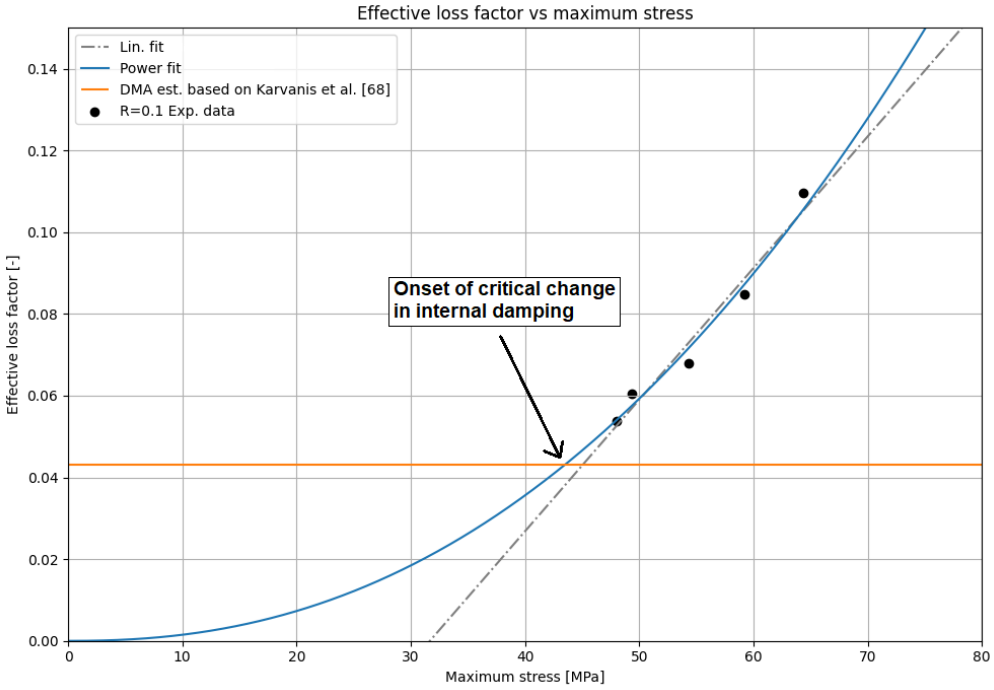

Figure 4.7: HCFS determination using effective loss factor vs the applied maximum stress.

Depending on whether a power-law or linear fit is drawn through this data, a high cycle fatigue strength estimate is made between 43 and 45 MPa. Based on the original S-N curve by Movahedi-Rad et al. [41] this result in a fatigue life between 10^6 and 10^7 cycles. For comparison, similar woven $\pm 45°$ glass/epoxy composite fatigue tests by Liang et al. [71] suggested an endurance limit of 45-50 MPa. Colombo et al. [67] on the other hand predicted a high cycle fatigue strength 37 MPa using the thermography method.

Finally, Figure 4.8 shows how the predicted dissipation rate ($\dot{W}_h = f \cdot W_h$) versus maximum stress based on the combined DMA and fatigue curves of Figure 4.7 relates itself to the thermography results by Colombo et al.

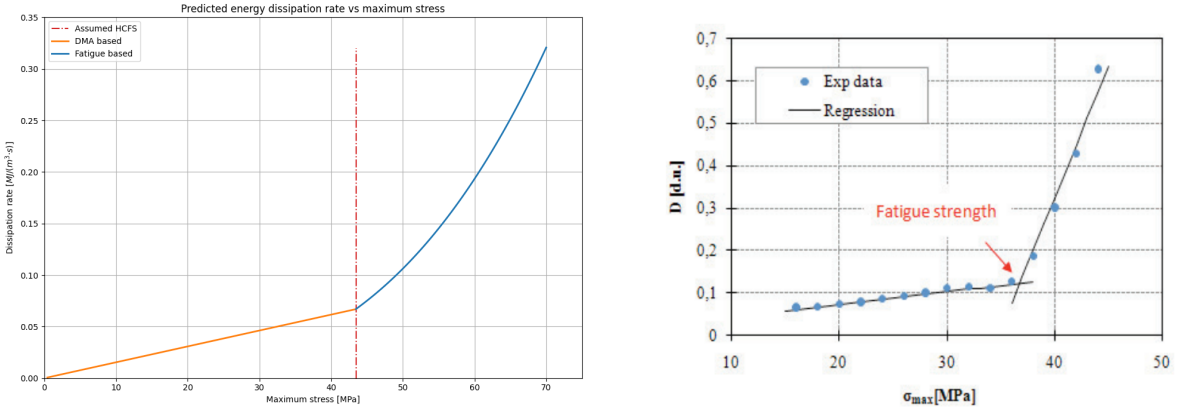

(a) Current predicted dissipation rate vs maximum stress trend.

(b) Reference dissipation rate vs stress results [67].

Figure 4.8: Bi-linear energy dissipation rate trends for a) current prediction and b) reference data by Colombo et al. [67] for $\pm 45°$ woven glass/epoxy.

The above figures show a clear similarity between the currently proposed DMA-intersection loss factor based high cycle fatigue limit determination method and a classic example of the well-established thermography method. Although this preliminary analysis is a rather small and limited dataset, this again gave early confidence in the overall modified linear viscoelastic approach before proceeding to with further experiments.

4.6. Relation to TDE/TW vs maximum stress

Following the DMA based effective loss factor up to the HCFS, the $\frac{TDE}{TW}$-ratio can be predicted using the R-ratio factor of Equation 3.42. How the changing R-ratio would effect the loss factor progression through life, the consequent effective loss factor over the whole fatigue life and finally the prediction of HCFS cannot be evaluated for this current dataset due to lack of such data. However, if this were still to be loosely predicted by simply assuming a fixed $\sin(\phi_{eff})$ vs σ_{max} trend independent of R, then the $\frac{TDE}{TW}$ ratios at increased R-ratios of 0.3 and 0.5 should be downwards shifts like shown in Figure 4.9.

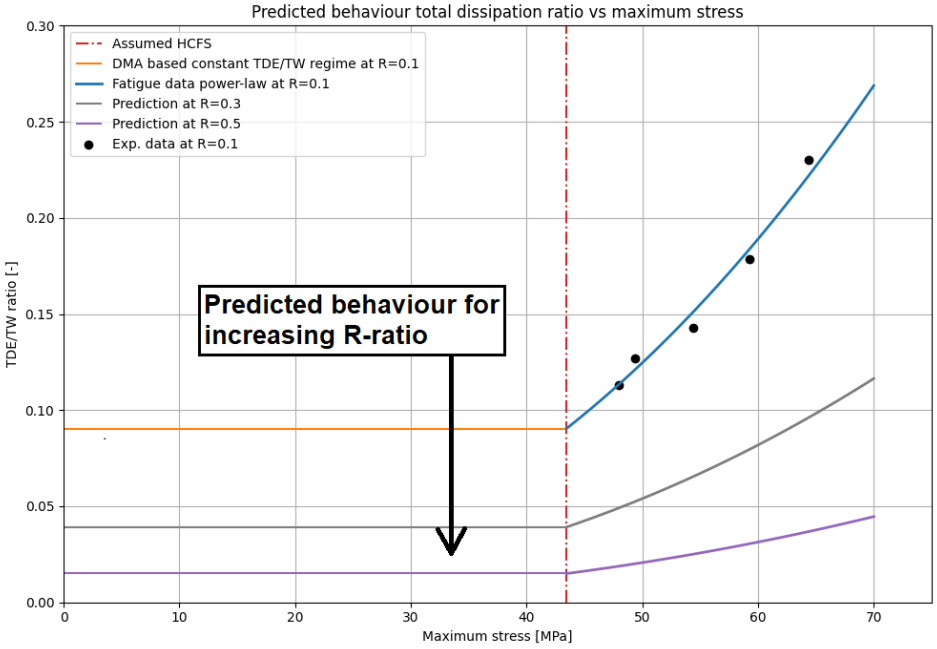

Figure 4.9: Predicted two-domain TDE/TW ratio vs maximum stress trend.

As shown in this figure, following the modified viscoelastic theory the $\frac{TDE}{TW}$ ratios are expected to decrease for increasing stress ratios. However, with the lack of data at alternative R-ratios this and the effect of changing R-ratio on the $\sin(\phi_{eff})$ vs σ_{max} trend remain to be further evaluated the experimental phase.

4.7. Total dissipated energy

Finally, to round up the preliminary analysis the total dissipated energy (TDE) for the current dataset is plotted against the maximum stress level in Figure 4.10.

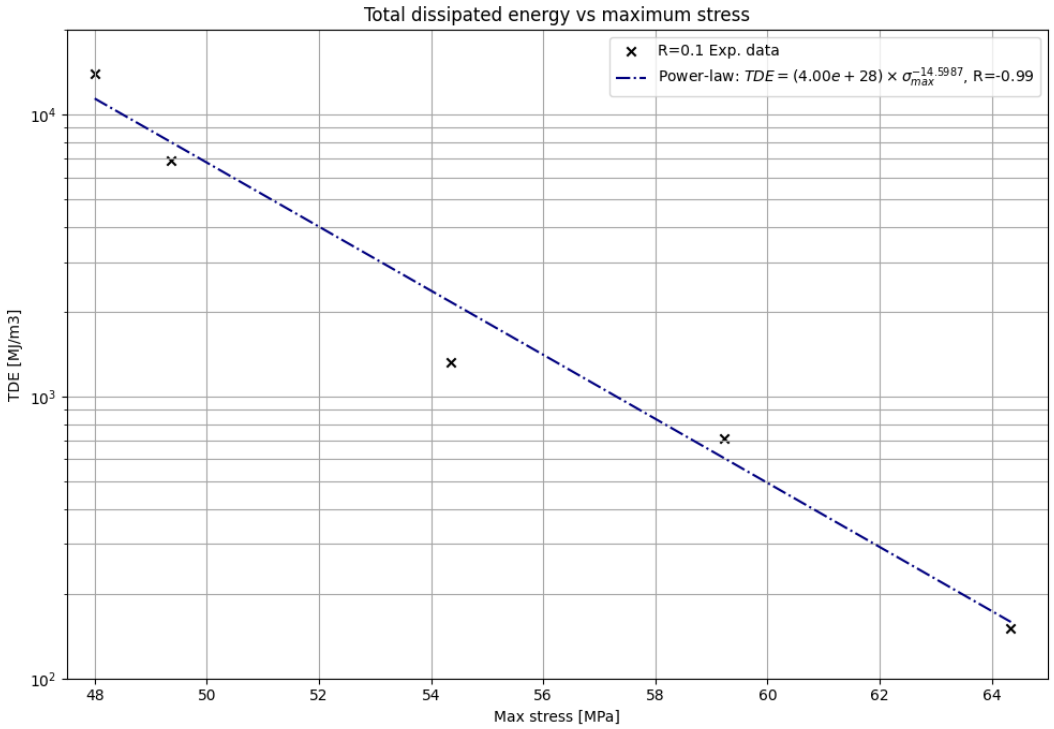

Figure 4.10: Log-linear trend of total dissipated energy (TDE) and max stress at R=0.1.

Despite the TDE as derived in Equation 3.38 appearing to be proportional to σ_{max}^2, the above figure tells a different story. Namely that with decreasing stress, the total energy dissipated over the specimen's life increases drastically. This thus means that the summation over the number of cycles in Equation 3.38, which was $\sum_{i=1}^{N_f} \frac{\sin(\phi_i)}{|E_i^*|}$, must thus have a much stronger negative exponential relationship with σ_{max} such that combined with the direct inclusion of σ_{max}^2, overall still more total energy is dissipated over the fatigue life at lower stresses.

4.8. Preliminary analysis conclusions

This preliminary analysis applied the proposed modified linear viscoelastic framework to a literature dataset of $\pm 45^\circ$ woven glass/epoxy fatigue tests, with the aim of evaluating the applicability of the derived cyclic and total energy dissipation metrics, and their link to viscoelastic material parameters such as loss factor and loss modulus. The exercise served as an early verification of the approach, revealed several behavioural trends of interest, and provided guidance for designing the experimental programme in chapter 5. The key conclusions from this preliminary analysis are given below.

- The cyclic dissipation ratio $\frac{W_h}{W_a}$ and viscoelastic loss factor $\sin(\phi_i)$ gave a clearer representation of damage progression than modulus or dissipated energy trends alone, particularly in identifying initiation and steady-state phases at lower stresses.
- Both $\frac{W_h}{W_a}$ and $\frac{TDE}{TW}$ were found to vary significantly with σ_{max}. At low enough stresses where both $\frac{W_h}{W_a}$ and $\sin(\phi_i)$ clearly stabilise, the $\frac{TDE}{TW}$ ratio was closely matched to this stabilised value. At higher stresses, there was a clear diversion from such stabilisation to where ultimately the whole fatigue life at high stress could be considered one large continuous damage phase to failure.
- Early-cycle loss factors derived from hysteresis data compared well with R-ratio corrected DMA values for a similar pristine material, supporting the proposed energy-based R-ratio correction factors.
- Loss modulus evolution was shown to be strongly stress-dependent. At low enough stresses, the matrix's contribution to the loss modulus tends to degrade with roughly the same proportional rate as that of the complex (dynamic) modulus. Only at increasing stresses where presumably friction based damping offsets this balance does the overall loss factor of the composite material significantly increase.
- Based on the diversion point of the effective loss factors over the whole fatigue life from the DMA reference value, a high cycle fatigue strength estimate of 43-45 MPa could be made that agreed reasonably well with literature based references and thermography measurements.
- The total dissipated energy (TDE) up to fatigue failure appears as a strong negative exponent power-law with the applied stress. This means that at low stresses, an exponentially larger amount of total hysteresis energy is dissipated up to failure.

Limitations

- No comparison to other R-ratios was possible. Although the link between cyclic dissipation ratio and loss factor was established for $R = 0.1$, it remains unknown whether the $\sin(\phi_{eff})$–σ_{max} trend is on itself independent of the R-ratio.
- Without such R-ratio variation, it cannot be determined whether hysteresis dissipation at alternative R-ratios is a pure scaling with R, or whether there are further underlying effects at play.
- Stiffness degradation plays a large role in this $\pm 45^\circ$ dataset. Between stress levels, the average stiffnesses differ considerably. It is suspected that R-ratio variation will amplify these differences, further influencing damping trends. Variation in (average) stiffness in between stress and R-ratio combination should therefore be minimised in further testing.
- The strong stiffness differences also imply variation in strain rates between stresses and R-ratios, introducing further uncertainty in loss factor comparisons.
- Testing must ensure that the fatigue specimens fail via a consistent dominant mechanism across all stress levels and R-ratios, to ensure comparability of damping and dissipation behaviour.

5

Experiment Design and Execution

The previous chapter on the preliminary analysis not only gathered some critical early insights, but most importantly acted as an initial proof of concept for the modified linear viscoelastic approach. This chapter follows up on this by documenting the design and execution of the experiments that together with the conclusions of the preliminary analysis of chapter 4 were aimed towards finally answering the research main and sub-questions stated in section 2.9. This process included an evaluation of the remaining primary test objectives, material and laminate selection, a specific and optimised specimen design as well as experiment parameters and procedures.

This chapter starts with establishing the experimental objectives in section 5.1. Then, the justification for the selected material type and laminate configurations will be given in sections 5.2 and 5.3, respectively. After that, section 5.4 discusses how the simulated laminate properties are expected to change under the high strain rate conditions of fatigue loading. This feeds right into section 5.5, where the dogbone specimen design optimisation will be covered. Section 5.6 then very briefly provides an overview of the critical production steps and final specimen testing allocation, after which section 5.7 explains the concept and justification of the fatigue loading parameter evaluation. The equipment set-up and test procedure used in the designed monotonic tensile and fatigue test experiments will then be covered in section 5.8. This is then finally followed up by section 5.9 where the procedures for the dynamic mechanical analysis experiments are provided.

5.1. Testing objectives

Based on the research questions combined with the early conclusions from the preliminary analysis, the objectives for the experimental phase of this thesis project were as defined below:

- To measure and evaluate the progression of the cyclic dissipation ratio $\frac{W_h}{W_a}$ and the viscoelastic loss factor $\sin(\phi_i)$ throughout fatigue life of a more fibre dominated laminate with a justified balance between well measurable viscoelastic hysteresis, limited influence of creep and consistent degradation of laminate stiffness throughout fatigue life. In such case where the laminate stiffness is expected to on average remain similar across a wider range of stress levels, the influence of the relative change in loss modulus over complex modulus in the formulation of the loss factor, loss modulus and their underlying relation to damage mechanisms should be more distinguished than in the preliminary analysed $\pm 45^\circ$ glass/epoxy dataset. Furthermore, such reduced spread in average laminate stiffness in the fatigue dataset implies more even strain rates throughout the specimens fatigue life.
- To perform fatigue tests as described above for a range of applied maximum stresses on at least two R-ratios. This aims to further evaluate the effect of cyclic maximum stress and stress ratio on the loss factor progression, magnitudes of total dissipated energies, overall $\frac{TDE}{TW}$-ratio, and finally the degree to which the $\frac{TDE}{TW}$ vs σ_{max} curve collapses onto a possibly single trend of $\sin(\phi_{eff})$ vs σ_{max}. These tests at different maximum stress and R-ratio combinations are to be performed under varying frequencies, such that the disparities in strain rates are minimised. As thoroughly discussed in the literature study, testing using the standard practice at a fixed 5-10 Hz frequency leads to a significant discrepancy in strain rate. Due to the rate-sensitivity of viscoelastic materials, this acts as unintended variable which reduces the value of the comparison of viscoelastic characteristics across stress levels and R-ratios.

- To perform monotonic tensile test at standard and fatigue-equivalent strain rates. Through this, the static and dynamic laminate strengths and failure strains are aimed to be measured and compared. The derived strain rate sensitivity aids in the calculation of the required fatigue testing frequencies. Furthermore, such equivalent rate strength and failure strain data provides a more consistent comparison of monotonic material properties to fatigue measurements, such as the inclusion of the dynamic strength into the S-N curve.
- To measure the pristine laminates loss factor through dynamic mechanical analysis. This will serve as baseline to compare the cyclic and effective loss factor values and aim to enable a prediction of the high cycle fatigue strength.

5.2. Choice of material

For this thesis project, two unidirectional thermoset composite material types were available. The first of these was M30S carbon fibre with a DeltaPreg DT120 epoxy matrix. The second option comprised of E-glass fibres with the DeltaPreg BT080 epoxy matrix. Both resin systems are generally quite comparable and both have a comparable glass transition temperatures in the range of $120 - 140°C$, with the main difference being that the BT080 is focussed towards out-of-autoclave processing.

Assuming that the two prepregs have a comparable matrix material, their difference in damping characteristics will be heavily depended on the viscoelastic nature of the reinforcing fibre as well as the strength of the fibre-matrix interface [13], [24]. As discussed in section 2.5 of the literature review, unidirectional carbon fibre oriented along the loading direction has been shown by multiple studies to have near negligible strain rate sensitivity [46], [49]. This directly implies an insignificant viscous component to the overall stiffness. As the testing objectives defined in section 5.1 stated that the aim is to test a fibre-dominated laminate configuration for more consistent stiffness degradation reasons, such negligible viscoelastic characteristics of the dominating $0°$-oriented carbon fibre unidirectional layers would have likely resulted in a rather small hysteresis energy dissipation measurement in fatigue.

Glass fibre on the other hand has a more amorphous structure compared to the quite crystalline layers of carbon fibre, and thus glass' molecular mobility under stress is larger [53]. As a result, it is more viscoelastic in terms of both strain rate sensitivity and damping under cyclic loading. It should thus naturally result in more pronounced and measurable cyclic hysteresis under fatigue loading. The inherent additional sensitivity to creep and the effects of variances in strain rates between tests are believed to be compensable with a well taught out loading parameter selection process. As additional benefit, the experimental results obtained for such glass/epoxy composites remain more directly comparable to those of the preliminary analysis.

Following the above reasoning, the DeltaPreg E-Glass/BT080 unidirectional composite material was selected as the best fit for the current objectives.

5.2.1. Estimated material properties

At the time of this thesis, no previous experiments had been performed using this material, nor was the supplier able to provide tested material properties. The only known material details beforehand are given in Table 5.1, combined with the processing data sheet given in Appendix B. Therefore, the further experiment design was based on material property estimates obtained through literature. Here, fairly generic mechanical properties for E-glass/epoxy unidirectional were assumed as given by Table 5.2, which were based on the combination of various sources [72]–[75].

Table 5.1: Glass fibre UD prepreg material details.

Material storage name	Deltapreg glass UD EGL-200-BT080-34 EF
Fibre type	E-glass
Matrix type	BT080 OoA epoxy based resin system
Fibre areal weight	200 g/m^2
Resin content by weight	34%
Cured fibre volume fraction	0.49
Cured layer thickness	0.157 mm

Table 5.2: Assumed UD glass-fibre epoxy mechanical properties [72]–[75].

Property	Value
Material name	E-Glass/Epoxy
E_1 [MPa]	39000
E_2 [MPa]	8600
G_{12} [MPa]	3800
ν_{12} [-]	0.28
X_t [MPa]	1080
X_c [MPa]	620
Y_t [MPa]	39
Y_c [MPa]	128
S [MPa]	50
E_{1f} [MPa]	73500
ν_{12f} [-]	0.22
m_{sig} [-]	1.3
p_{12}^{+} [-]	0.3
p_{12}^{-} [-]	0.25

5.3. Composite layup selection

With a base glass/epoxy composite material chosen, the decision remained on what laminate configuration or layup to test. The objectives outlined in section 5.1 aimed to evaluate the progression of the loss factor throughout the fatigue life at varying maximum stresses as well as the trends in the total effective loss factor, $\frac{TDE}{TW}$ ratio and the quantity of total dissipated energy over the whole fatigue life. For this, a fibre-dominated laminate was considered as desirable as the stiffness degradation could be expected to remain fairly stable for a considerable portion of the fatigue life compared to the preliminarily analysed matrix dominated $\pm 45^{\circ}$ data [49].

This meant that the ideal laminate to test was a trade-off between a sufficiently fibre dominant one, whilst still retaining a large enough matrix loading to create measurable hysteresis loops and evaluate the changing contribution of the matrix to the viscoelastic loss factor. For these reasons, pure unidirectional specimen at 0° and 90° orientations individually were not regarded as suitable options for these testing objectives. Additionally, further work on a $\pm 45^{\circ}$ laminate was also not considered favourable.

Therefore, the laminate layup options further considered for the fatigue tests were $[0/90]_{8s}$, $[0/45/\text{-}45/90]_{4s}$ and $[0/45/\text{-}45/0]_{4s}$. To get a sense of their their relative stiffnesses and dependencies on matrix failure, a progressive damage analysis code was written using classical laminate theory [76] and the Puck 2D unidirectional composite failure criteria [77]. This distinguished between fibre compressive and tensile failure and the three different matrix failure types: A, B and C. These correspond to tensile, longitudinal shear and transverse shear driven modes respectively. Upon the occurrence of a failure criteria trigger, a knockdown was applied to the associated material properties following Table 5.3 below, which is based the combination of knockdown factors proposed by McCarthy et al. [78] as well as by Camanho and Matthews [79]. The simulation results in the form of stress-strain plots to failure are shown in Figure 5.1.

Table 5.3: Progressive failure knockdown factors [78], [79].

Property	KD FFT	KD FFC	KD MFA	KD MFB	KD MFC
E_1	0.1	0.1	-	-	-
E_2	-	-	0.2	0.4	0.1
G_{12}	0.1	0.1	0.2	0.4	0.1
v_{12}	0.1	0.1	0.2	0.4	0.1

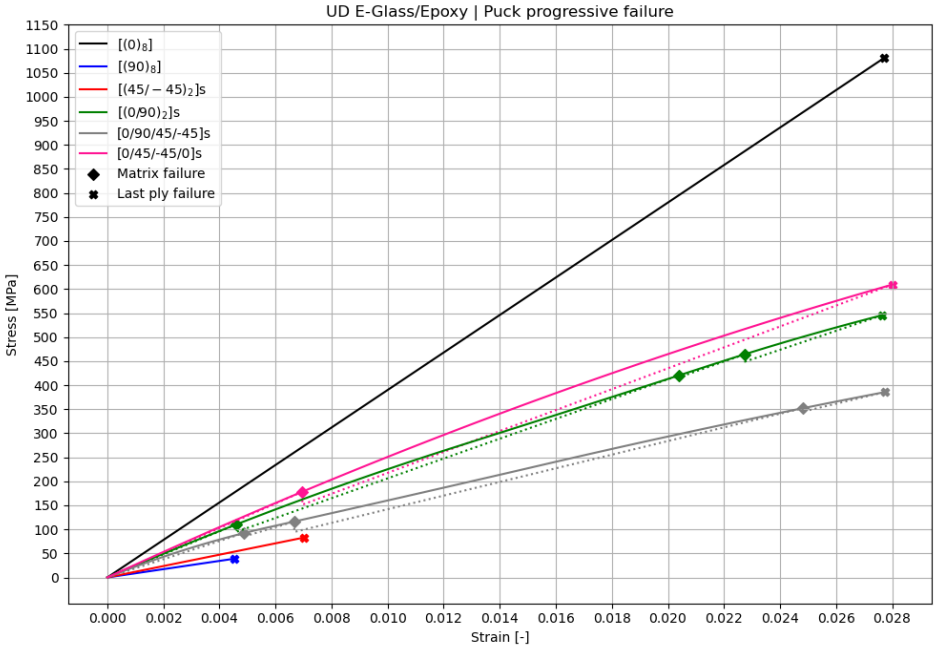

Figure 5.1: Puck-based quasi-static tensile test simulation of the various laminate options.

In the above figure, the simulation results for a $0°$, $90°$ and $\pm 45°$ laminate are still included for reference purposes. Each marker indicates a Puck failure criteria trigger and thus application of the failing ply knockdowns. The consequent drops in laminate stiffness are shown by the dotted lines. However, in reality the matrix failures will be more progressive and do not happen everywhere in the material at once. Therefore, a quadratic curve was fit through the failure points to approach a more gradual and progressive failure profile. For each of these laminates, the initial and final moduli estimates as well as first and last ply failure stresses are given in Table 5.4 below.

Table 5.4: Comparison of moduli and failure stresses across the laminate options.

Layup	Initial moduli [GPa]	Avg. moduli final 15% [GPa]	E_0/E_f [-]	FPF [MPa]	UTS [MPa]
$[0/90]_{8s}$	23.97	16.31	0.681	110	546
$[0/45/\text{-}45/90]_{4s}$	18.94	11.58	0.612	92	609
$[0/45/\text{-}45/0]_{4s}$	25.64	17.37	0.678	178	385

The advantages and disadvantages of each of these three laminate options are as follows:

- $[0/90]_{8s}$ **Cross-ply**: The stiffness of this laminate is dictated prominently by the $0°$-layers. Despite making up the other the other 50% of the thickness, the $90°$-layers only account for about 18% of total laminate stiffness. Yet, by half of the layers in the laminate thickness being along the $90°$ orientation, there should be sufficient matrix loading for measurable hysteresis energy.

  In the initiation phase, transverse matrix cracks will form in the $90°$-layers as result of fibre-matrix debonds, which will propagate to the $0°$ ply interfaces [22]. Carraro et al. [80] reported that for low stress levels, the propagation of the transverse cracks occur at near constant rate. However, this early onset of deterioration of the $90°$-layers, shown in Figure 5.1 to already start failing statically at around 110 MPa, should have limited influence on the overall laminate stiffness degradation. One can thus expect an initial drop in stiffness in the early fatigue cycles associated with transverse crack initiation and propagation in the $90°$-layers, followed by a stabilised phase where the transverse cracks are halted by the $0°$ ply interfaces.

Fatigue tests results by Han et al. [14] are in line with this reasoning by reporting how for $[0/90]$ glass/epoxy, the hysteresis energy remained mostly stable throughout the fatigue life, with an increase near the end of life by the onset of interlaminar and $0°$ fibres failure.

For such layup it would thus be of particular interest to see at which stress level the effective loss factor diverges from the pristine reference measurements, indicating the high cycle fatigue strength. This may occur directly at fatigue stresses near the onset of $90°$ matrix cracking, or as seen on the $\pm 45°$ data from the preliminary analysis there could be a delay in this due to the matrix' contribution to both loss and complex moduli first degrading proportionally without much additional friction. The quite limited number of distinct damage and failure mechanism possible in such simple cross-ply laminate should further aid this experimental distinction.

Finally, compared to the other two options, the $[0/90]$ cross-ply should be the least sensitive to creep due to its low stiffness dependence on the viscoelastic matrix, particularly in shear dominated creep in the absence of $\pm 45°$-layers. Such a reduced sensitivity to creep is beneficial for the aimed comparison between loss factor progression across different R-ratios.

- $[0/45/\text{-}45/90]_{4s}$ **Quasi-isotropic**: Damping in fibre-reinforced polymers is considered most influential under shear stress on the matrix due to the contribution of the fibre-matrix interface and fibre-matrix slip [25]. Therefore, compared to the cross-ply alternative, one can expect to measure a larger initial loss factor which throughout the fatigue life is also more sensitive to the state of damage in these $+45°$ and $-45°$ off-axis layers.

  However, due to this increased dependence on these off-axis layers, the progressive failure simulation results in Table 5.4 also showed that such quasi-isotropic laminate configuration would result in the largest relative stiffness loss. Therefore the stabilisation of stiffness degradation and dissipated energy can be expected to be less pronounced than that for the cross-ply alternative. For similar reasons, such quasi-isotropic laminate will also naturally be more sensitive to creep.

- $[0/45/\text{-}45/0]_{4s}$ **Tri-axial**: Compared to the quasi-isotropic laminate, this final option is more fibre dominated by having more unidirectional layers along the loading direction. Combined with the $\pm 45°$-layers, this leads to a higher stiffness and first ply failure strength than both cross-ply and quasi-isotropic laminates. However, the progression of overall stiffness degradation remains highly dependent on the state of damage in the $\pm 45°$-layers.

  Furthermore, due to the lack of any $90°$ fibres the laminate will experience greater transverse/Poisson's contraction. This tends to concentrate most critically around the constraints of the clamped specimen end tabs as well as interlaminar stress concentrations at the free edges [40]. On top of varying stiffness degradation at different stress levels and R-ratios, this may add additional variability to the damping measurements.

The above discussion points are summarised in the trade of table presented in Table 5.5, below.

Table 5.5: Laminate selection trade-off table.

Layup	Loss factor	Stiffness stabilisation	Creep sensitivity	Applicability DMA measurement	Manufacturing and test complexity
$[(0/90)_2]_s$	Lowest	Expected initial step, followed by stabilised phase.	Least	Combined individual 0 and 90 tests as suggested in literature [12].	Simplest to produce. Least failure variability.
$[0/45/\text{-}45/90]_s$	Largest	Expected more progression stiffness decreas	Worst	Interlaminar loss effects not well captured.	Increased layer and failure mode variability.
$[0/45/\text{-}45/0]_s$	Intermediate.	Intermediate.	Intermediate	Interlaminar loss effects not well captured.	Intermediate.

Based on the above table, it was believed that although a $0/90$ cross-ply laminate is most likely to result in a smaller hysteresis energy measurement per cycle than the two alternatives, overall it suits the outlined testing objectives best.

5.4. Dynamic property prediction

To improve specimen geometry design and the selection of the testing parameters, the so far assumed mechanical properties of the E-glass/epoxy material were adjusted for the discrepancy between quasi-static and the expected fatigue strain rates. Here, the American Society for Testing and Materials specifies a standard quasi-static cross-head speed of 2 mm/min in ASTM D3039/D3039M for the testing of tensile properties of polymer matrix composite materials [81]. For a further standard specimen geometry with a gauge length of around 150 mm, this is equivalent to a strain rate of $2.2 \cdot 10^{-4} s^{-1}$. In fatigue testing however, the average strain rate in a cycle is expected to be multiple orders of magnitude larger than this. According to the subsection 2.5.2 of the literature study, particularly for glass/epoxy composites this will have a quite significant effect on the stiffness and strength.

For comparison, the preliminary analysed $\pm 45^{\circ}$ data of chapter 4 showed fatigue strain rates in the range of about $1 \cdot 10^{-1}$ to $2 \cdot 10^{-1}\ s^{-1}$. As will be shown and discussed in more detail in section 5.8, the initially expected fatigue strain rates for the tests on the selected E-glass/epoxy cross-ply specimen would also be within this order of magnitude. This means that the expected average fatigue strain rates were about a factor 1000 larger than the testing quasi-static conditions that the initially assumed material properties of Table 5.2 and the progressive failure simulation of Figure 5.1 were based on. As no previous static or fatigue testing data was available for the calculation, evaluation and selection of the required testing parameters, the so far simulated tensile stress-strain behaviour was aimed to be further improved for this purpose by compensating for the known strain rate effects.

As reference for this strain strate correction, Barré et al. [48] showed that for unidirectional E-glass/epoxy the mechanical properties at a dynamic rate of $1 \cdot 10^{-1} s^{-1}$ increased by the percentages as shown in Table 5.6 compared to a quasi-static reference.

Table 5.6: Percentage in mechanical property increase of E-glass/epoxy UD between quasi-static strain rate and $1 \cdot 10^{-1} s^{-1}$ as reported in [48].

Property	Percentage increase compared to quasi-static
E_1	+5%
E_2	+15%
X_t	+20%
Y_t	+0%
S	+0%

When these sensitivity values were assumed and used to update the Puck-based progressive failure model, the effects on the simulated tensile stress-strain response are as shown in Figure 5.2. Here, the blue curves represents the quasi-static baseline, whist the red curve represents the modified properties of the high (dynamic) strain rate more comparable to those in a fatigue tests. The differences between the two are summarised in Table 5.7. All further calculations and predictions in the remainder of this chapter were based on these strain rate adjusted results.

Table 5.7: Expected quasi-static vs equivalent rate dynamic tensile test parameters.

Parameter	2 mm/min quasi-static	$0.1\ s^{-1}$ dynamic
Initial modulus, [GPa]	23.97	25.61
Ultimate strength, [MPa]	546	655
Failure strain, [%]	2.76	3.16

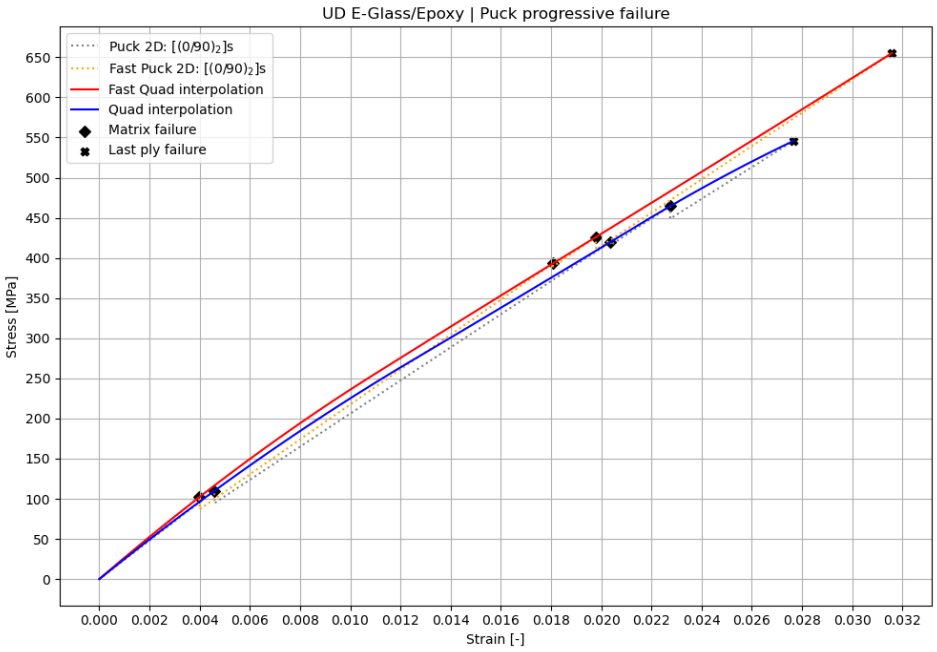

Figure 5.2: Puck-based quasi-static tensile test simulation of the [0/90] laminate at two strain rates of 10^{-4} and 10^{-1} s^{-1}.

5.5. Specimen design

For a balanced and symmetric laminate like the selected 0/90, ASTM D3479/D3479M for tensile-tensile fatigue testing of polymer matrix composites [39] refers to the previously mentioned ASTM D3039/D3039M for a standard recommended specimen geometry of 25 by 250 mm, with a thickness of 2.5 mm [81]. For such fibre dominated laminates the ASTM standard strongly recommends the use of tabs to prevent premature damage by the serrated machine clamp surfaces under the high clamping pressure required to reach the high stress levels. This is of particularly relevance for UD-based composites, whose layers can more easily split along the fibre direction as result of the low transverse strength [40]. However, such tabs create problems of themselves again in the form of stress concentrations as result of geometrical and stiffness discontinuities [40], [82]. Therefore, the topic tab material, tab thickness, taper angle and adhesive for the reduction of such stress concentrations is well discussed in literature and will be further covered in subsection 5.5.1.

Depending on the fibre and matrix material types and layup, the stress concentration at the tab ends may or may not pose a problem. For example, off-axis laminates such as $\pm 45°$ have lower transverse stiffness and a more shear driven deformation and are thus less stress sensitive to the constrainment of the natural Poisson contraction at the clamped tabs [40]. Furthermore, the contraction/necking at the centre of such specimen beyond a certain stress level naturally concentrates the failure towards the centre gauge section [83]. However, despite there being methods of reducing the tab stress concentration, rectangular specimen with constant cross section as recommended by ASTM D3479 and D3039 remain particularly problematic for fatigue testing of on-axis unidirectional and cross-ply laminates as discussed by Fazlali et al. [40] in their review of tabbing methods and specimen geometry with the aim of reducing these stress concentrations.

As neither ASTM and ISO standards for fatigue testing of fibre reinforced polymer composites consider fatigue failure at/in the tabbed region as valid data points, different specimen geometries than the standard 25 x 250 mm strip type should be considered in order to promote the likelihood of consistent and comparable gauge section failure. This was of particular relevance in this study due to the dependence of the energy dissipation and loss factor change on the local failure mechanisms. Therefore to suit the outlined testing objectives best, a specific combination of specimen and tab geometry was designed with the primary aim of consistent and localised central gauge section failure. Over the course of the following subsections, this specimen design process and its outcomes will be further elaborated upon.

5.5.1. Tab material and geometry

The ASTM D3039 standard recommends E-glass reinforced composite tabs at $\pm 45^{\circ}$ orientation to the load direction as default tab material, which is also widely supported in literature as it poses a good balance between strength and flexibility [40], [84], [85]. Particularly as the material for this thesis' fatigue tests was a glass-fibre composite itself, $\pm 45^{\circ}$ glass/epoxy tabs minimised the stiffness mismatch between tab and specimen.

For tab thickness, ASTM D3039 recommends a nominal value of 1.5 mm [81]. Fazlali et al. [40] reviewed various studies on the effect of tab thickness and concluded that there is a general agreement in literature that a smaller tab thickness leads to a more even stress distribution and reduced heat generation. However, for UD-based composites less than 1 mm tab thickness was reported to have a high likelihood of causing premature failure due to surface damage and fibre-splitting by the serrated gripping surfaces. Fazlali et al. thus recommend a 1 to 2 mm tab thickness range. As this ultimately aligned well with the ASTM D3039 standard, a nominal tab thickness of 1.5 mm was selected for this thesis.

Regarding tab tapers, the ASTM D3039 standard suggests that for hydraulic non-wedge grips with the tabs fully clamped, 90° straight edges can often be used successfully. However, for wedge-operated grip types and tabs sticking out of the grips, it is recommended to taper the tab ends by 7-10°. As the servo-hydraulic fatigue testing machines at the Delft Aerospace Composite and Materials Lab (DASML) where the fatigue tests were performed were all outfitted with hydraulic wedge grips, this recommendation of tapered tab ends was followed. Given the selected tab thickness of 1.5 mm, the most convenient taper to consistently produce was found to be 8.5°.

For the length of the tabs, considerations were made based on the maximum grip length of the aforementioned hydraulic wedge clamps as well as a minimum length to prevent uneven clamping pressure. From a stress perspective, larger tabs would be beneficial as the increased surface area allows for both lower grip pressure, as well as a larger adhesive area to reduce the chance of adhesive failure. With all these effects in mind, an overall tab length of 60 mm was selected. This meant that with the taper angle of 8.5°, an effective clamping length of 50 mm remained.

Finally, in their review on tabbing methods, Fazlali et al. [40] also concluded that a high modulus tab adhesive would amplify the longitudinal and transverse stresses at the tabs compared to lower modulus alternative which smoothen out the stiffness transition more. However, the consequently lower strengths of most low modulus adhesives are inherently more sensitive to adhesive related failures such as specimen pull-out or tab delamination and particular heat generation due to the increased mobility and friction. Ultimately, Loctite AE 3430 was selected as best available adhesive, with an overlap shear strength of 22 MPa and a modulus of 3.2 MPa [86].

5.5.2. Geometry concepts

For fibre-reinforced polymer composite monotonic tensile and fatigue tests, alternative geometries in literature mostly converge to so called 'dogbone' or 'dumbbell' shaped specimen [40], [46]. Such geometry concepts are centred around a reduced gauge section width compared to that of the clamped/tabbed region. The consequent reduction in cross-sectional area results in a lower net-section stress at the tabs for equal gauge stress and thus effectively delays the onset of tab and clamping induced failure modes. Although such shaped specimen are typically not recommended in ISO or ASTM composite material testing standards due to the shear stresses introduced as result of the transition curvature, De Baere et al. [83] raised an arguably valid reasoning that consistent gauge section failure in a slightly curved specimen with a well known stress state is still preferable over repeated and unpredictable failure at the clamped region due to various tab-related failure modes.

Following this reasoning, the three dogbone geometry concepts as shown in Figure 5.3 were considered for further evaluation. These three dogbone concepts will be referred to as Type A, B and C respectively.

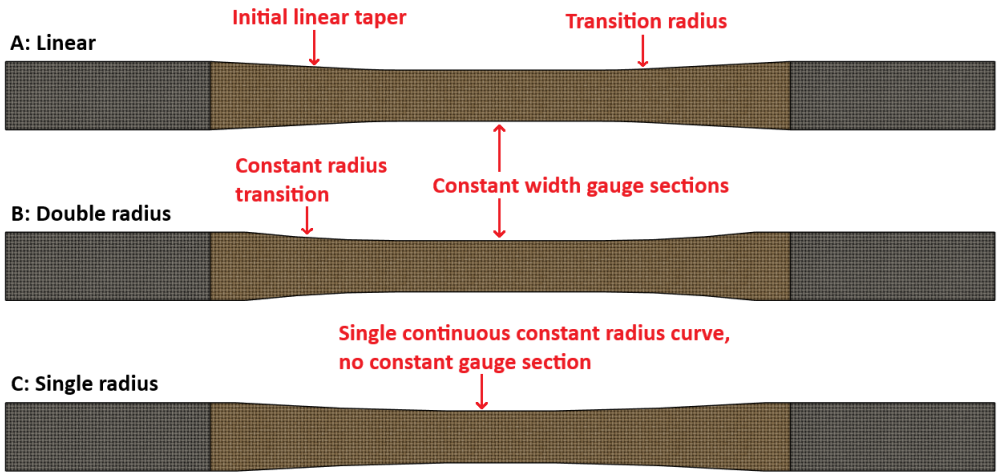

Figure 5.3: Evaluated dogbone fatigue specimen geometries: A) linear, B) double radius and C) single curve reduction without constant gauge section.

Here, geometry type A was recommended to the current author by Perruchoud (personal communication) [87] and consisted of a central constant width gauge section of variable length with a linear transition towards the tabbed region. Dogbone type B on the other hand was based loosely the ASTM 638-14 recommended geometry for tensile tensing of plastics [88]. This also consisted of a constant width gauge section, but this had constant radius transitions towards the tabbed region. Finally, the last evaluated geometry, type C, was based on work by De Baere et al. [83]. This last geometry trades-in the constant width gauge section of the two alternatives for a much larger and continuous single radius, which was aimed towards smoothening out local stress concentrations naturally induced at the transition zones. Each of these three geometry types was extensively evaluated using fully parametric Abaqus finite element models, the results of which will be discussed in subsection 5.5.5.

5.5.3. Gauge narrowing ratio

Before addressing the performed finite element based dogbone transition geometry optimisation, a common criteria had to be established that would determine the required tab to gauge width ratio in order to confidently prevent tab related failures. Regarding this, De Baere et al. [46], [82], [83] studied the effective stress concentration of straight 0/90 carbon/PPS laminate tensile and fatigue specimen with various tab materials and configurations. From their finite element study, these authors reported an effective net-section stress concentrations of 1.11 and 1.26 for straight samples with respectively $\pm 45^{\circ}$ and $0/90$ tapered tabs of the same material with 2.4 mm thickness and a 10 mm stick-out from the clamps. Glass-epoxy tabs at $\pm 45^{\circ}$ were shown to result in a similar concentration factor, namely 1.12. In later work [83], the same authors tested dogbone shaped specimen of type C in Figure 5.3. Here, the continuous radii curvature was sized such that the tab-to-gauge widths ratio was greater or equal to the rounded up concentration factor of 1.3 for the $0/90$ tabs. For this specimen design, Baere et al. reported consistent failure in this reduced centre section during both tensile and fatigue tests.

As little alternative sources were found on similar studies on particular glass/epoxy laminates, a tab stress concentration factor of at least 1.25 was assumed necessary for the current geometry selection. This was considered to remain on the conservative side, as the tabs by De Baerre et al. were fairly thick compared to standard and reduced tab thickness was documented by Fazlali et al. [40] to reduce the stress concentration. On top of this, the lower stiffness of the selected E-glass compared to the carbon fibre used by De Baerre et al. should further reduce the tab stress concentration effects. Therefore, in the design iterations of the various dogbone specimen geometries, the minimum gauge over tab width ratio as defined by Equation 5.1 was maintained.

$$\frac{w_{gauge}}{w_{tab}} < 0.8 \tag{5.1}$$

5.5.4. Fixed geometric parameters

For each geometry iteration a 16-ply $[0/90]_{4s}$ laminate was used with a total thickness of 2.4 mm. With the available E-glass/BT080 unidirectional prepreg having an estimated cured layer thickness of about 0.15 mm, this ensured a fully balanced and symmetric laminate, whilst remaining close to the recommended ASTM D3039 thickness of 2.5 mm. Furthermore, the clamp-to-clamp distances on all iterations were set at a fixed 190 mm. With the selected tab lengths of 60 mm and 10 mm taper, this corresponded to an overall specimen length of 290 mm. Given the 600 mm widths of the material prepreg rolls as well as required cutting margin, this was set as a hard length limit for production reasons. For smaller overall specimen lengths such as the ASTM D3039 recommended 250 mm, the transition curvature from tab to gauge regions would have become too aggressive when still aiming for the required $\frac{w_{gauge}}{w_{tab}}$-ratio. This would have further amplified the induced shear stresses, which this specimen geometry design exercise aimed to minimise. Finally as recommended by De Baerre et al. [83], for each geometry a 5 mm long straight section was kept in front of the tabs before the start of any transition section. This ensures minimum interaction of the induced transition shear stresses with the natural stress concentration region directly in front of the tabs.

Furthermore, for the initial evaluation of the three geometrical concepts shown in Figure 5.3, common gauge and tab widths were set at 15 and 20 mm respectively. This gave a $\frac{w_{gauge}}{w_{tab}}$ ratio of 0.75 and allowed for a focussed comparison on the effect of the transition shapes concepts alone.

5.5.5. FEA geometry evaluation

For the initial finite element analysis, the specimen were simplified to a 2D shell meshed with S4 fully-integrated conventional shell elements. As the main purpose of the model was to evaluate the shear stresses induced by the transition curvatures, the complex out-of-plane compression loading due to the clamping pressure was not considered. The complexity of accurately modelling the tab stress concentration, including clamp geometry and glue interface layer was considered out of the scope of this comparative evaluation, and was instead accounted for by the assumed minimal gauge/tab width ratio as per Equation 5.1. Therefore, the model only contained the 10 mm of tapered tab length sticking out of the clamps as a change in local laminate, which accounts for the the local jump in in-plane stiffnesses and contraction.

To represent the constrainment of the tab clamping, the bottom clamp edge nodes were considered fully constrained and the top/pulling clamp edge rigidly coupled to a reference node. This reference node itself was constrained to only vertical displacement, to which the load was applied to create a symmetric loading case. In reality the 0/90 laminate in the between the $\pm 45^{\circ}$ tabs and glue interface will still have some, albeit small, degree of lateral contraction. Therefore, this constrainment set-up is considered as a conservative worst-case.

For each of the three geometry types, 5-10 iterations were analysed where parameters such as taper angle, constant gauge section length and curvature radii were varied between. For a valid comparison between iterations, a load was applied to each one with a magnitude such that the minimum central gauge section experiences a net 100 MPa tensile stress. To simplify the comparison of these results and the discussion that would lead to a geometry concept selection, only the considered best iteration for each of the three geometry types will be discussed here. The FEA results for the larger set of iterations are given for future reference in Appendix A instead.

To start of with the comparison, Figure 5.4 shows the distinct S_{12} shear stress distributions over the normalised clamp-to-clamp lengths of each of the three concepts' best iteration. Each of the plots is marked with their corresponding geometry type A, B or C.

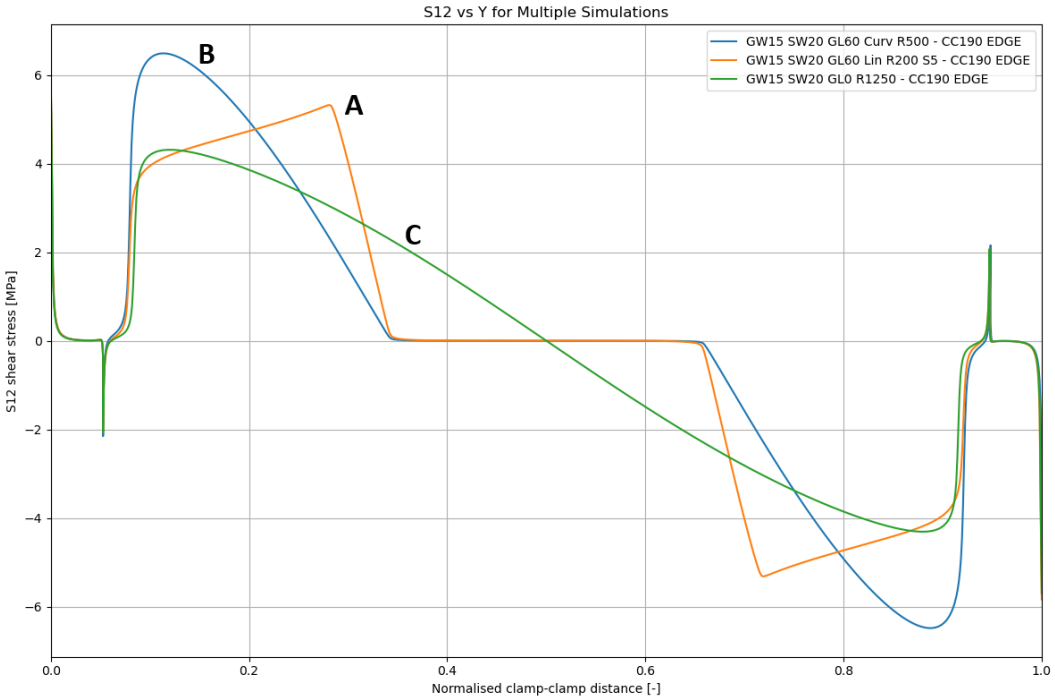

Figure 5.4: Maximum S_{12} shear stresses along clamp-to-clamp distance comparison between optimised iterations of type A, B and C dogbone geometries for 15 mm gauge width and 20 mm tab width.

As clearly shown in the above figure, each of the three geometry types has a distinct shear stress profile over the specimen length. Overall, the peak shear stress in geometry type C with the continuous curvature is shown to be lowest at about 4.1 MPa. Geometry type B with the curved transitions but otherwise straight gauge section shows the largest peak at 6.3 MPa, albeit at a very similar location to type C. These peaks so close towards the tabs highlights the importance of the constant 5 mm segment in front of the tabs as suggested by De Baerre et al. [83]. Geometry type A on the other hand with the linear transition has a peak shear stress between that of the alternatives, however this peak occurs much closer towards the constant gauge section. Unlike the continuously curved geometry of C, both A and B do naturally not have any induced shear stresses in their constant width gauge section.

However, based on solely a shear stress evaluation like that of Figure 5.4 it may appear that the geometry selection be of a trade-off between minimising the peak shear strain versus the net shear stress in the central gauge region. However, the current author considered it most critical to instead evaluate the interaction that these shown shear stress profiles have with the net section tensile stresses and how this effects the most likely location of damage initiation. Therefore, Figure 5.5 instead shows the Tsai-Wu failure index value along both the critical specimen outer edges (full lines) and the specimen centre lines (dashed lines).

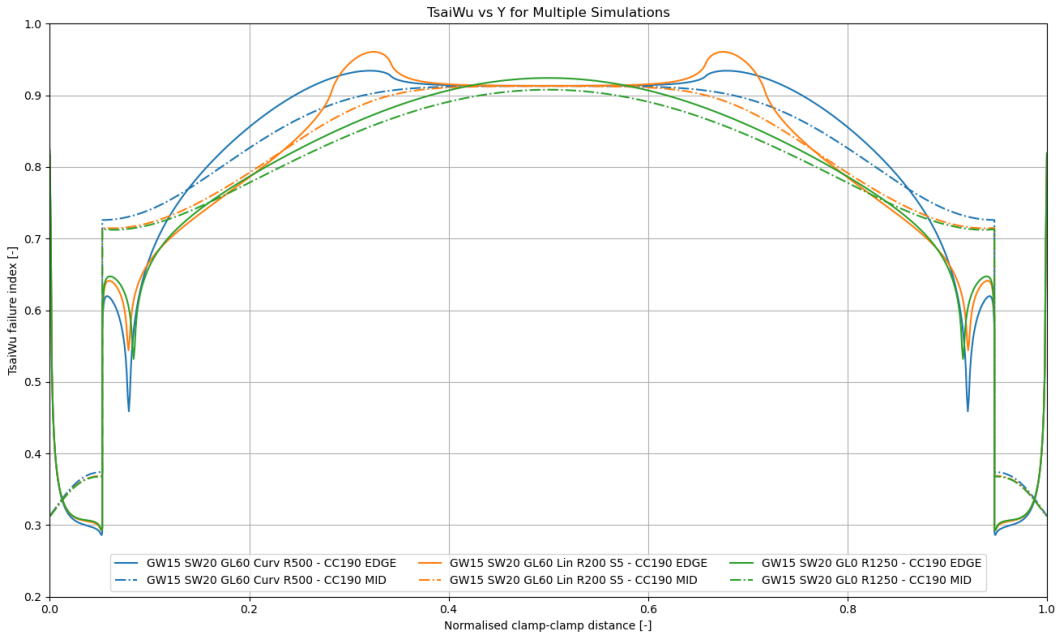

Figure 5.5: Maximum Tsai-Wu failure index along clamp-to-clamp distance comparison between optimised iterations of type A, B and C dogbone geometries for 15 mm gauge width and 20 mm tab width.

Such expression in terms of failure index indeed shows that for the geometries A and B with constant gauge section, there is a clear interaction between the net section tensile and the induced shear stresses. Despite the tensile stresses being largest in the constant width gauge section and there being no shear stresses in this section either, the overall failure index still shows two distinct failure peaks outside of this constant gauge section. This means that with such geometry, it is most likely that fatigue damage in the current 0/90 unidirectional-based laminate will first initiate and potentially further propagate in the transition region where this failure index finds itself at a maximum. The current author firmly believes that this negates the original purpose of maintaining a constant gauge section for uniform stress, if the likelihood is ultimately high that the critical fatigue damage still forms such this transition region.

For geometry type C on the other hand, the failure index clearly peaks right at the centre of the specimen where the width is at its minimum. Unlike the alternatives, this failure index value also drops much quicker moving away from this centre. So, despite a small but consistent shear stress remaining present in the central specimen region, the FEA results for geometry type C gave a much better confidence towards consistent central failure. This was considered critical for both the repeatability and consistency of failure mechanisms between stress levels and R-ratios, as well as having a clear region of the specimen to focus the DIC-based strain measurements on with good confidence of also capturing the failure in that region. There wont be a purely constant gauge section width, but within the central 50 mm the cross sectional area would only vary by about 3%.

5.5.6. Final dogbone geometry

Based on the results and discussion in subsection 5.5.5, a constant curvature geometry of type C shown in Figure 5.3 was selected as most favourable for the outlined testing objectives. It minimises both the absolute magnitude of shear stresses in the specimen, as well as its overall influence on the damage initiation stress and location.

With this general shape concept chosen, a final selection happened with respect to the minimum gauge section width. So far, the shown results have all been on a fixed 15 mm minimum gauge width. Based on further iterations, it was ultimately decided to increase this minimum width to 18 mm with a corresponding tab width of 25 mm. The primary reason for this was to increase the volume of material under load and thus also magnitude of the energy dissipation measurement. On top of this, a slightly smaller gauge/tab width ratio (0.72 vs 0.75) would further improve the ratio of Tsai-Wu failure index at

the specimen's central gauge section compared to right in front of the tabs. Finally, such larger width also gave an increased surface area for improved DIC correlation.

Therefore, the final monotonic tensile and fatigue testing specimen geometry for this thesis' experiments consisted of an 18 mm minimum width, 25 mm tab width, 290 mm overall length and a curvature with a maximum radius of 900 mm. These dimensions together with those of the tabs discussed in subsection 5.5.1 are shown in the drawing of Figure 5.6.

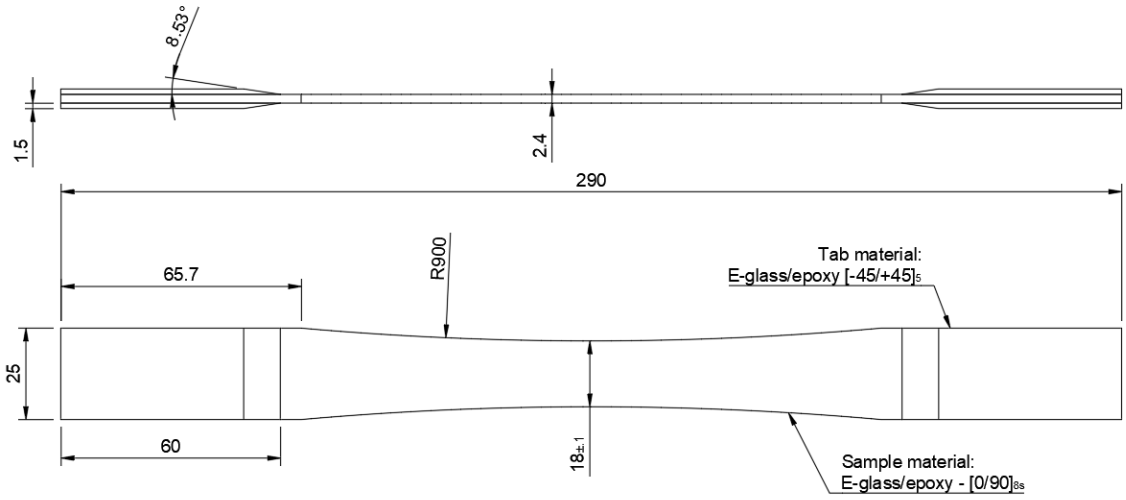

Figure 5.6: Final iteration dimensions of the tensile and fatigue specimen geometry.

For this final geometry, the shear stress and Tsai-Wu failure index distributions are given by figures 5.7 and 5.8 respectively. For good engineering practices, Figure 5.9 also provides the mesh convergence for this final geometry.

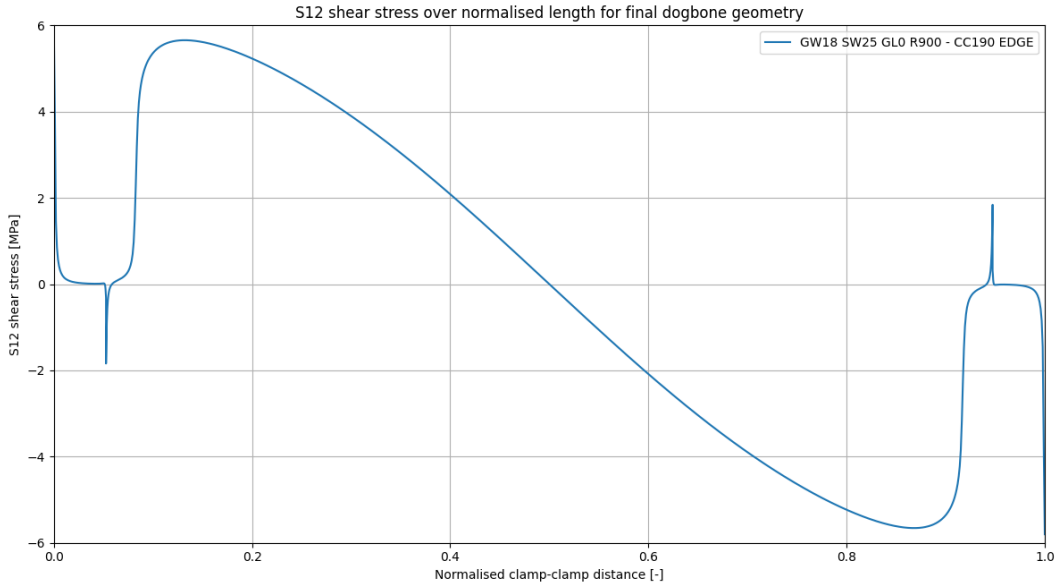

Figure 5.7: Maximum τ_{12} shear stresses along clamp-to-clamp distance for the final selected geometry.

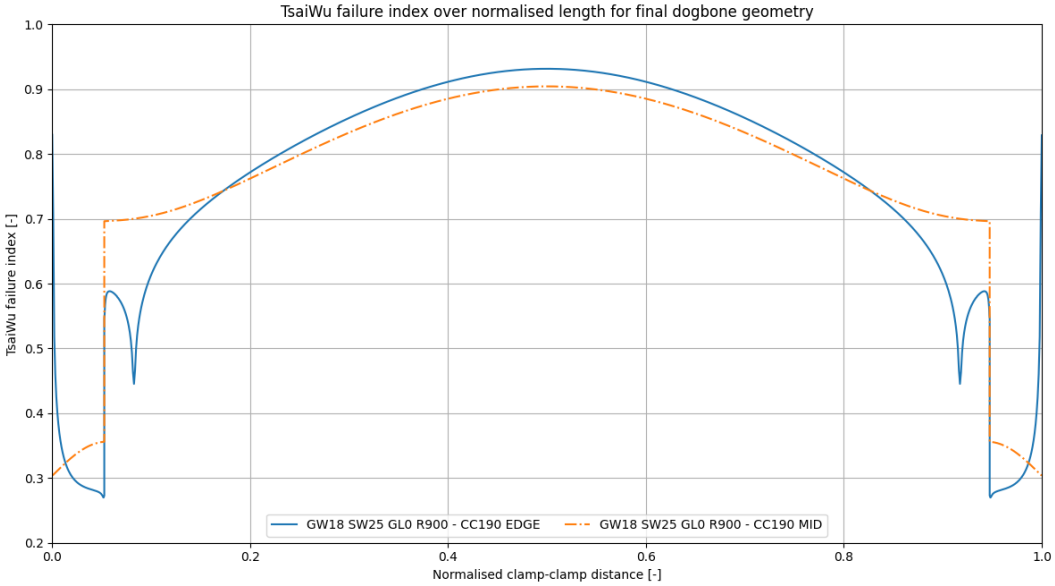

Figure 5.8: Maximum Tsai-Wu failure index along clamp-to-clamp distance for the final selected geometry.

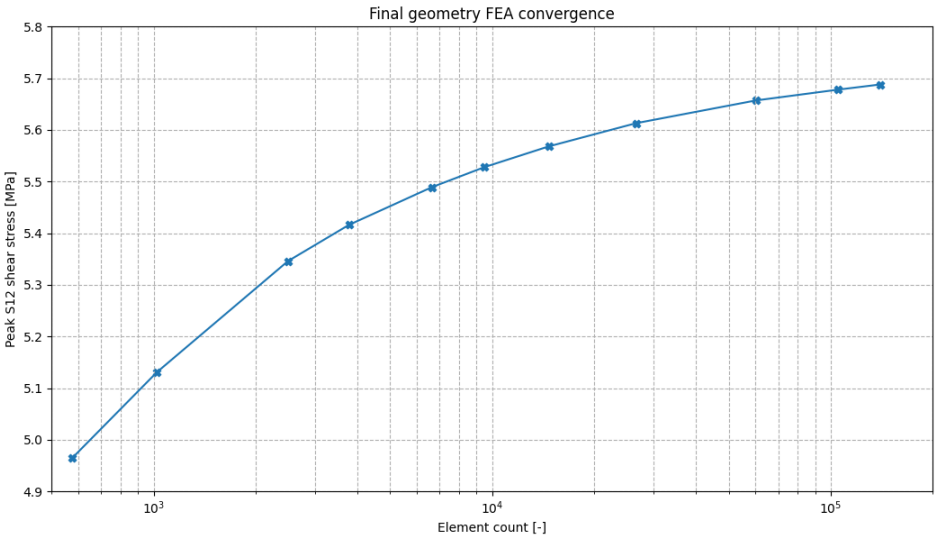

Figure 5.9: Maximum S_{12} shear stress based mesh convergence for the final selected specimen geometry.

5.6. Produced specimen overview

A total of 25 specimen were produced according to the design shown in Figure 5.6 for monotonic tensile and fatigue testing purposes. The detailed step-by-step overview of the complete specimen production proses is given in Appendix B. For continuation of this current chapter, the key production process steps are summarised as follows:

- For the main body of the specimen, a 600 x 600 mm $[0/90]_{4s}$ E-glass/epoxy laminate plate was produced from the base unidirectional prepreg material. Two further plates of 210 x 620 mm were laminated with a layup of $[-45/+45]_5$ and $[+45/-45]_5$ for left and right hand side tabs respectively.
- These laminate plates were oven-cured under full vacuum for 12 hours at 80$^\circ C$ after with an additional 2 hour post-cure at 120$^\circ C$ was performed to maximise the glass transition temperature and thus minimise the matrix' temperature sensitivity.

- Once cured, the rectangular tab and specimen outer profiles were water diamond saw cut on a Compcut ACS 600 CNC composite cutting machine.
- The 8.5° tapers were ground on all tabs using a specially designed taper grinding jig to ensure consistency.
- From the pre-cut rectangular specimen strips, the final specimen geometries were machined by the Tu Delft's Dienst Electrische en Mechanische Ontwikkeling (DEMO) workshop according to the drawing of Figure 5.6. To prevent edge delamination, this machining was done using specialised composite compression end mills. Unlike regular metal cutting milling bits, these are designed to compress the composite layers against each other during cutting and thus prevent the initiation of edge delaminations.
- Before tab bonding, all gluing surfaces were sanded to 300 grit and cleaned throughoughly with isopropanol. All tab bonding was done using Loctite AE 3430 two-component adhesive. To aid a consistent adhesive interface thickness, 0.2 mm diameter glass beads were applied. To enhance the overlap shear strength and increase the hot-strength, all adhesive tab bonds were cured for 6 hours at 40°C.
- The gauge sections of all specimen were painted matte-white onto which a matte black speckle pattern was applied for the purpose of DIC.

To conclude this section Table 5.8 gives an overview of the produced specimen dimensions as well as their testing allocation.

Table 5.8: Produced specimen allocation and dimensions.

Specimen ID	Minimum width [mm]	Avg. thickness [mm]	Length [mm]	Allocation
M-1	18.21	2.52	290	Monotonic tensile
M-2	18.22	2.53	290	Monotonic tensile
M-3	18.19	2.51	290	Monotonic tensile
M-4	18.24	2.52	290	Monotonic tensile
F-1	18.23	2.51	290	Fatigue testing - R0.1
F-2	18.22	2.54	290	Fatigue testing - R0.1
F-3	18.23	2.55	290	Fatigue testing - R0.1
F-4	18.24	2.55	290	Fatigue testing - R0.1
F-5	18.23	2.53	290	Fatigue testing - R0.1
F-6	18.21	2.52	290	Fatigue testing - R0.1
F-7	18.22	2.55	290	Fatigue testing - R0.1
F-8	18.23	2.54	290	Fatigue testing - R0.1
F-9	18.15	2.55	290	Fatigue testing - R0.1
F-10	18.17	2.57	290	Fatigue testing - R0.1
F-11	18.17	2.56	290	Fatigue testing - R0.1
F-12	18.16	2.53	290	Fatigue testing - R0.1
F-13	18.20	2.53	290	Fatigue testing - R0.1
F-14	18.21	2.51	290	Fatigue testing - R0.3
F-15	18.21	2.51	290	Fatigue testing - R0.3
F-16	18.15	2.53	290	Fatigue testing - R0.3
F-17	18.18	2.51	290	Fatigue testing - R0.3
F-18	18.12	2.52	290	Fatigue testing - R0.3
F-19	18.11	2.53	290	Fatigue testing - R0.3
F-20	18.22	2.53	290	Fatigue testing - R0.3
F-21	18.14	2.52	290	Fatigue testing - R0.3

5.7. Fatigue loading parameter evaluation

As discussed in section 5.1, a key part of the testing objectives was to perform the fatigue tests at the various stress level and R-ratio combinations at comparable strain rates as opposed to the standard practice of a fixed 5-10 Hz frequency like suggested by ASTM D3479 [5], [39]. As concluded in subsection 2.5.5 of the literature study, the current author promotes the view that fatigue testing parameters should be chosen such as to minimise the side-effects of frequency, strain rates or time at peak load depending on the objectives of the study. With a particular focus on damping characteristics and energy dissipation, for this thesis this meant stepping away from such standard fixed frequencies and optimising instead in favour of consistent viscoelastic material behaviour under equivalent strain rates.

5.7.1. Frequency selection method

Ideally, the discussion at the start of this section would imply not only selecting a starting frequency to hit an initial strain rate target, but to also continuously vary and update the loading frequency throughout a test to retain this strain rate despite the progressive loss of laminate stiffness. However, unfortunately most standard servo-hydraulic fatigue machine controllers, including the MTS machines available in the Delft Aerospace Composites and Materials Lab (DASML), do not easily allow such continuously varying frequency testing control schemes. Therefore, an alternative middle-ground was considered in the fatigue experiments for this thesis. Here, the loading frequency within a single test was kept constant. However, between the different tested fatigue stresses and R-ratios this frequency was adapted such that the predicted average strain rate throughout the test would remain close to the original target. Thus, to calculate the required testing frequency for each stress level and R-Ratio combination, Equation 5.2 was used.

$$f = \frac{\dot{\epsilon}_{target} \cdot E_{avg}}{2(1-R) \cdot \sigma_{max}} \tag{5.2}$$

Here, the average laminate stiffness was calculated as $E_{avg} \approx \frac{\sigma_{max}}{\epsilon_{max}}$ based on the equivalent rate monotonic tensile stress-strain response. Initially, this was estimated using the Puck-based simulation of Figure 5.2 for rough parameter determination. These frequency values were then later updated to their final value before testing based on the performed dynamic monotonic tensile test results.

Figure 5.10 shows how the predicted average strain rate following the above described approach compares to that if a constant frequency of 5 Hz would have been selected instead. In addition to this, the expected average strain rates are shown of an alternative constant loading or stress rate approach, such as originally followed by Movahedi-Rad et al. [41] whilst gathering the original data analysed in chapter 4. This latter method is in principle quite similar, but does not account for differences in average laminate stiffnesses.

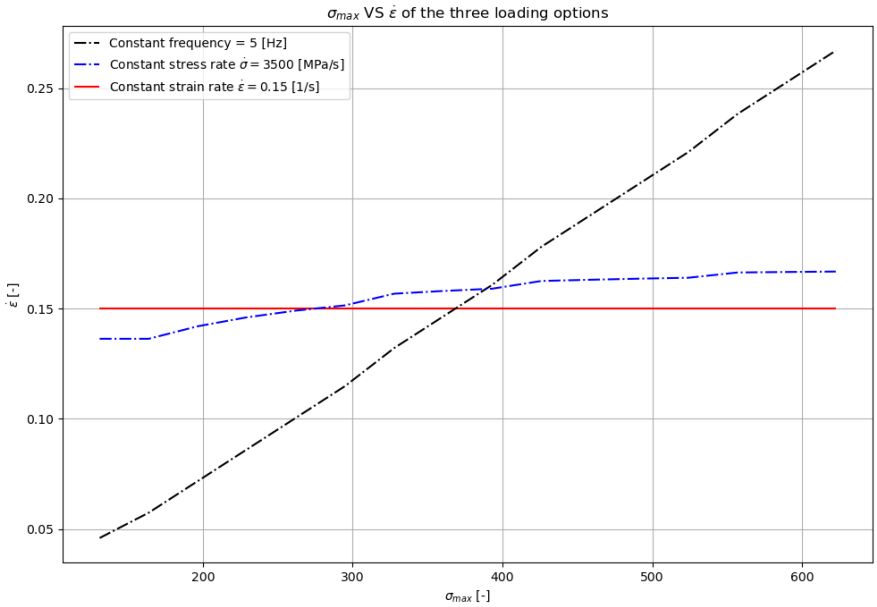

Figure 5.10: Comparison of strain rates for constant frequency, constant stress rate and constant strain rate conditions.

This clearly shows how for a fixed 5 Hz frequency the strain rates on a 200 to 600 MPa stress range would vary quite significantly with with about a factor 3 difference between the extremes. Compared to the current approach, a constant loading rate remains much closer, with the difference effectively being only the result of the additional dynamic tensile stress-strain based stiffness compensation.

5.7.2. Target strain rate and R-ratio selection

To select at which target average strain rate and R-ratios the fatigue tests would be performed, Equation 5.2 was used to evaluate feasibility and practicality of the required frequencies and piston speeds for a number of combinations. This gave the frequency vs maximum stress plots for the three R-ratios of 0.1, 0.3 and 0.5 shown in Figure 5.11.

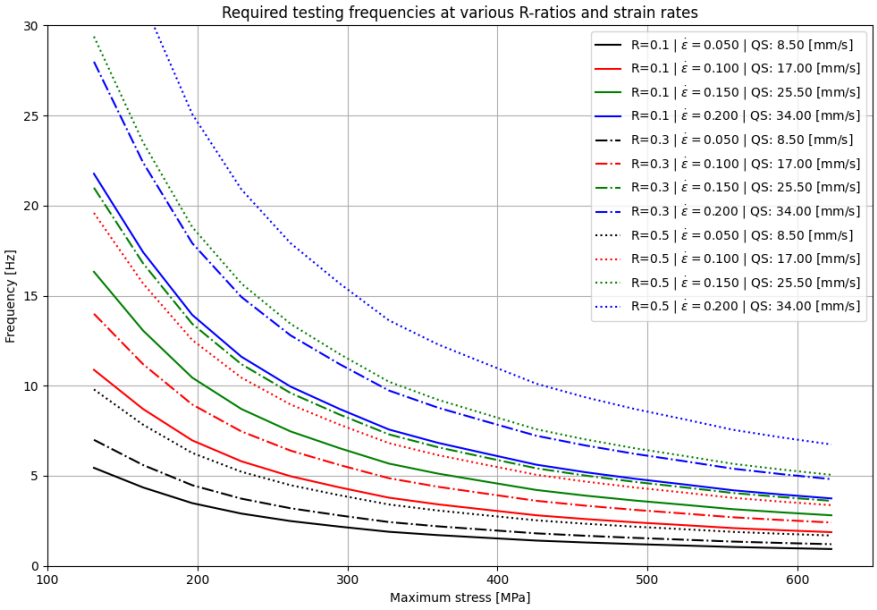

Figure 5.11: Required testing frequency vs maximum stress for constant strain rates at $R = 0.1, 0.3$ and 0.5.

For evaluation of the results shown in Figure 5.11, maximum stresses ranging from 0.45 to 0.9 of the laminate ultimate strength were considered reasonable initial targets for the fatigue tests. This equated to maximum stresses between 295 and 590 MPa. Selecting which constant average cycle strain rate to test on was a trade-off between keeping the peak piston velocities within reasonable limits w.r.t. the machine capability, accurate hysteresis loop reconstruction at fixed sampling rate, as well as on the other hand not too low frequencies such that the experiment duration time drastically increases. With this in mind, based on Figure 5.11 an average strain rate of 0.15 $1/s$ at stress ratios of 0.1 and 0.3 were deemed most appropriate targets. Furthermore, for the overall specimen length of 290 mm and 190 mm clamp-to-clamp length, this would correspond to just over 44 mm/s peak piston velocity, which together with the DASML mechanical testing staff was deemed as high, but still an achievable target.

5.7.3. Effect of chosen parameters on heating rate

As was discussed in subsection 2.5.1, the primary justification given in glass-fibre composite fatigue literature on the common choice of a fixed 5 Hz frequency is with regards to minimising excessive hysteresis caused self-heating at the higher stress levels [5], [38]. To ensure such excessive heating would not dominate the fatigue measurements at the chosen frequencies with respect to such recommended and known conservative 5 Hz standard, Figure 5.12 below was created. This gives a comparison between the rates of applied strain energy per second for both constant 5 Hz frequency and constant average strain rate testing methods.

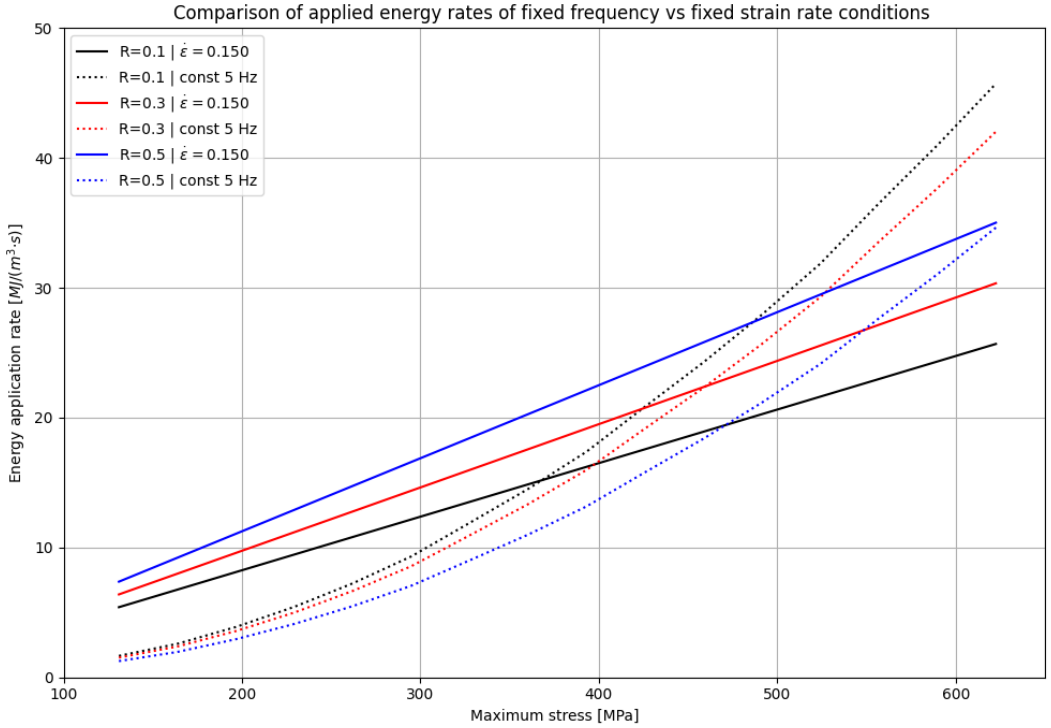

Figure 5.12: Comparison of applied energy rate for constant frequency, constant stress rate and constant strain rate conditions.

For the constant 0.15 $1/s$ strain rate at varying frequency, this plot shows that at $R = 0.1$, stresses above 370 MPa result in lower strain energy input per second than if they would be tested at the standard 5 Hz. Thus compared to results in literature where tests were performed at the standard 5 Hz frequency for glass/epoxy laminates, excessive internal heating at the higher stress values was expected to remain limited in this study [5], [80], [89], [90]. At the higher stress ratio of $R = 0.3$ however, this cross-over would be somewhat later at around 460 MPa.

5.7.4. Effect of chosen parameters on creep

To finally conclude this section on fatigue testing parameter section, the Figure 5.13 shows that for the followed approach the criteria of time at load following Equation 2.6 actually decreases for increasing R-ratio. This meant that combined with the fibre-dominance of the chosen laminate, creep was expected to not play a significant factor in the comparison of results obtained at $R = 0.1$ and $R = 0.3$.

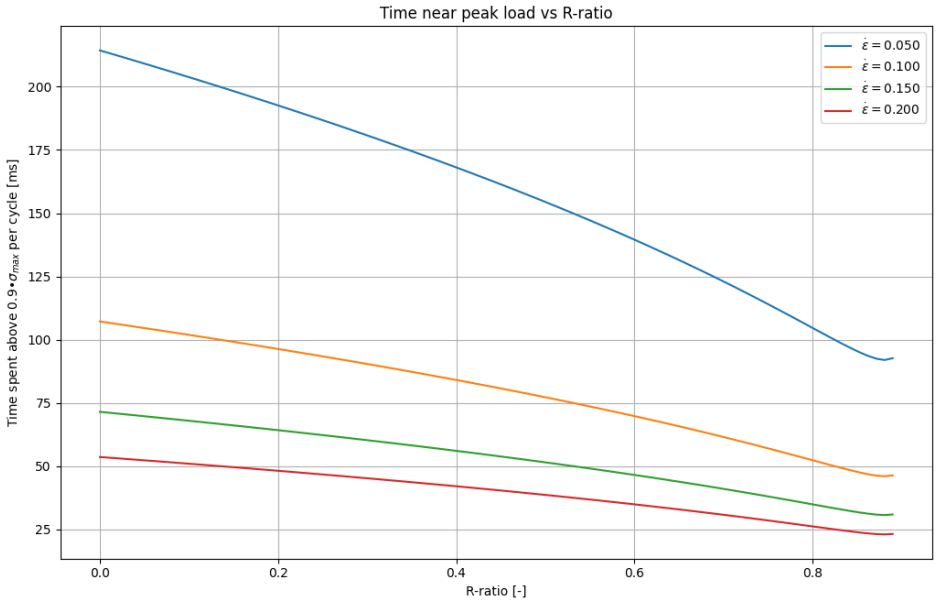

Figure 5.13: Time spent above 90% of σ_{max} per cycle vs R-ratio for four constant strain rate conditions.

5.8. Tensile and fatigue testing experimental set-up and procedure

This section finally covers the experimental set-up and procedures of both monotonic tensile and fatigue testing. Both experiment types were performed using the same 100 kN servo-hydraulic test bench and high speed Digital Image Correlation (DIC) set-up. Figure 5.14 gives an overview of how this equipment and its set-up as well as the dogbone specimen clamping looked like.

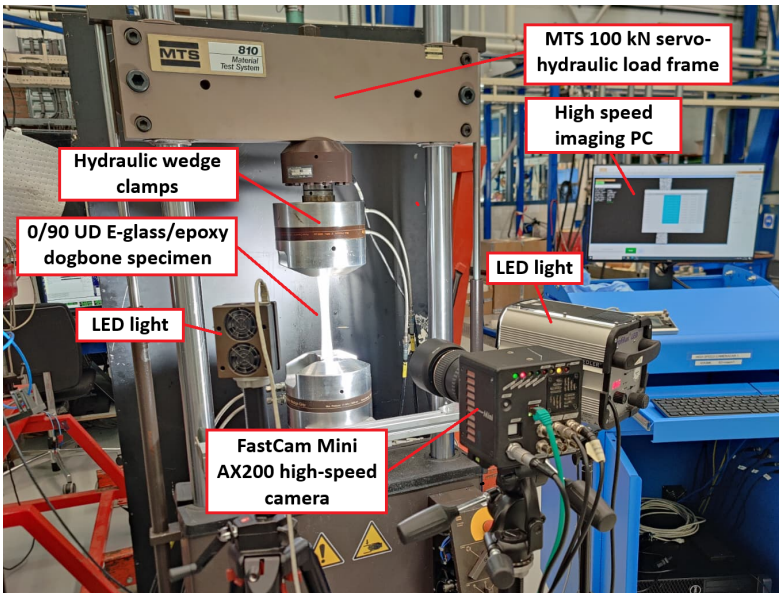

Figure 5.14: Experimental set-up used for high-rate monotonic tensile and fatigue testing.

5.8.1. Testing equipment

As shown in Figure 5.14, for both monotonic tensile and fatigue tests a 100 kN MTS servo-hydraulic test machine was used, equipped with hydraulic actuate wedge grips. To measure the local strain in the damage concentrating central zone of the dogbone specimen, a high-speed DIC set-up was used. This included a Fastcam Mini AX200 high speed camera with a 1 megapixel imaging resolution up to 6400 FPS. These DIC strain measurements were set up as a so called 'virtual extensometer', of which the image processing and incorporation with the MTS force-displacement data logger will be discussed in more detail in chapter 6. Because of the non-constant geometry of the dogbone specimen the piston displacement data on its own would not results in a good strain measurement to determine local fatigue strain in the concentrated central specimen region. By evaluating the local strain on the specimen rather than the average strain as calculated from the piston displacement, the local damage formation could thus be more accurately captured as well as removing inherent machine and grip compliance from the overall strain readings. The main reason for using DIC over alternative options such as a physical extensometer was the high risk of damaging such contact based strain measurement device upon the explosive final failure characteristic of the fibre-dominated laminates tested.

Finally, a FLIR A665SC infrared camera was used to measure the extent of the self-heating of the specimen as result of the hysteresis energy dissipation. Unfortunately, due to high demand on this infrared camera and only one unit being available in the DASML mechanical test lab, such temperature measurements could only be taken for a limited number of fatigue tests.

5.8.2. Monotonic tensile test procedure

As was shown by the specimen allocation in Table 5.8, 4 out of the total 25 produced dogbone specimen were reserved for monotonic tensile testing. This included one reference quasi-static test at a low rate of 5 mm/min. This was followed up by 3 dynamic tensile tests performed at the fatigue target strain rate of 0.15 $\frac{1}{s}$. As was shown in Figure 5.11 this was equivalent to 25.5 mm/s or 1530 mm/min. This was thus a factor 305 larger than the quasi-static reference test.

All tests were performed at equal clamping pressure of 100 bar. For each test a DIC reference image was taken under unloaded conditions. All tests were started from a 0.3 kN preload. For the high-rate tests, a DIC images were captured at 500 FPS and the force-displacement data logged at 512 Hz.

The results by high-rate tensile tests were used as input to update the preliminary stress vs frequency plot of Figure 5.11, however the final fatigue frequencies ultimately remained very similar to the original prediction. The stiffness, ultimate strengths and failure strains obtained at both high and low rates would be used to compare to fatigue measurements. Such as inclusion of tensile strengths into the S-N curve and allowed for the comparison of dynamic and fatigue failure strains.

5.8.3. Fatigue testing procedure

After performing the monotonic tensile tests, the remaining 21 specimen were split up into two batches. The first 13 specimen were exclusively tested at an R-ratio of 0.1, which formed the main baseline dataset. The other 8 specimen were all tested under an R-ratio of 0.3, where to maximise the evaluation of the results only maximum stresses were used that had also been tested on the $R = 0.1$ baseline dataset.

For practical reasons fatigue tests were not performed well beyond 1 million cycles due to testing time limitations. Directly experimentally reaching the HCFS likely in between 1 and 10 million cycles would have would have consumed an unfeasible amount of testing time for ultimately only one or two data points. This is also one of the current limitations in fatigue testing where such direct measurements of very high cycle fatigue life are time and cost intensive. This is why alternative methods such as thermography based or the current proposed loss factor based high cycle fatigue strength estimation methods are very powerful from practical testing and engineering perspective. Therefore, instead of focussing solely on the high to very high cycle fatigue range, focus was put on obtaining a well-balanced dataset across the multiple decades of fatigue life between 10 and 10^6 cycles to failure. Due to the power-law nature of S-N curve, but also the TDE vs N_f and TDE vs σ_{max} trends, gathering data well spread over these different factors of 10 of fatigue life resulted in an overall better capability of trend fitting and data interpolation. The tested R-ratio and maximum stress combinations with corresponding loading frequencies, clamping pressures etc. are shown in Table 5.9.

For all fatigue tests, continuous force-displacement measurements were taken at sampling rates that resulted in at least 20-30 data points per cycle. This ensured that the stress-strain hysteresis loops could be accurately reconstructed in the data post-processing. As high speed DIC imaging at multiple hundred frames per second for a full test duration is unfeasible from a data size and storage perspective, DIC measurements were instead taken at discrete intervals. Each DIC recording aimed to capture about 5-10 cycles. Depending on estimated fatigue life, the DIC trigger interval was adjusted. Here, the aim was to obtain at least 15 recordings per test as to have a sufficient amount of data to confidently interpolate. Most tests however had 20-30 or even more. To automate the DIC capturing process and ensure synchronisation with the MTS cyclic data, a digital trigger signal was sent out by the MTS controller to the HS camera upon which it automatically started the recording.

Typically for tests all performed at a fixed 5-10 Hz frequency, the PID controller of the servo-hydraulic test machine would be tuned for this fixed frequency. However, as for these experiments the frequencies were varied between tests, this would not be applicable. Therefore instead, the initial force controlled PID tune was performed at the mid-range frequency. On top of this a PVC adaptive compensator was used that would continuously self-update the initial PID tuning based on the current stiffness.

Table 5.9: Overview of fatigue testing parameters.

ID	σ_{max} [MPa]	R [-]	f [Hz]	P_{min} [kN]	P_{max} [kN]	P_{clamps} [bar]	Sampling [Hz]	DIC interval [cycles]
F-1	500	0.1	3.2	2.29	22.90	83	78	150
F-2	400	0.1	4.25	1.85	18.46	83	102	150
F-3	450	0.1	3.63	2.08	20.80	83	102	150
F-4	350	0.1	5.05	1.63	16.30	83	102	1000
F-5	325	0.1	5.52	1.50	15.02	90	128	1500
F-6	310	0.1	5.86	1.423	14.23	90	128	5000
F-7	375	0.1	4.61	1.74	17.40	93	128	1000
F-8	425	0.1	3.92	1.96	19.64	93	102	250
F-9	520	0.1	3.03	2.41	24.08	103	102	N/A
F-10	530	0.1	2.95	2.47	24.65	110	102	N/A
F-11	600	0.1	2.46	2.79	27.90	124	102	N/A
F-12	640	0.1	2.24	2.94	29.40	124	102	N/A
F-13	660	0.1	2.14	3.04	30.35	124	102	N/A
F-14	500	0.3	4.10	6.86	22.85	110	102	200
F-15	450	0.3	4.67	6.17	20.57	97	128	250
F-16	375	0.3	5.90	5.17	17.22	97	128	5000
F-17	600	0.3	3.15	8.21	27.35	124	128	N/A
F-18	530	0.3	3.79	7.25	24.15	110	128	N/A
F-19	640	0.3	2.88	8.80	29.32	124	128	N/A
F-20	350	0.3	6.44	4.85	16.15	90	146	5000
F-21	325	0.3	7.08	4.46	14.86	90	170	5000

5.9. Dynamic mechanical analysis

Last but not least, dynamic mechanical analysis tests were performed on the used E-glass/BT080-epoxy composite material using a TA Instruments RSA-G2 solids analyser at the DASML physics lab, as shown in Figure 5.15 below. Following the objectives described in section 5.1, the goal of these tests was to measure the pristine laminates loss factor at very low stresses. Like first shown in the preliminary analysis, these measurements would then later be used to compare to the loss factor values derived in fatigue with the goal of evaluating the proposed energy based R-ratio correction factors and to establish a high cycle fatigue strength estimate. Furthermore, these tests served as an opportunity to evaluate the temperature sensitivity of the viscoelastic characteristics of the material.

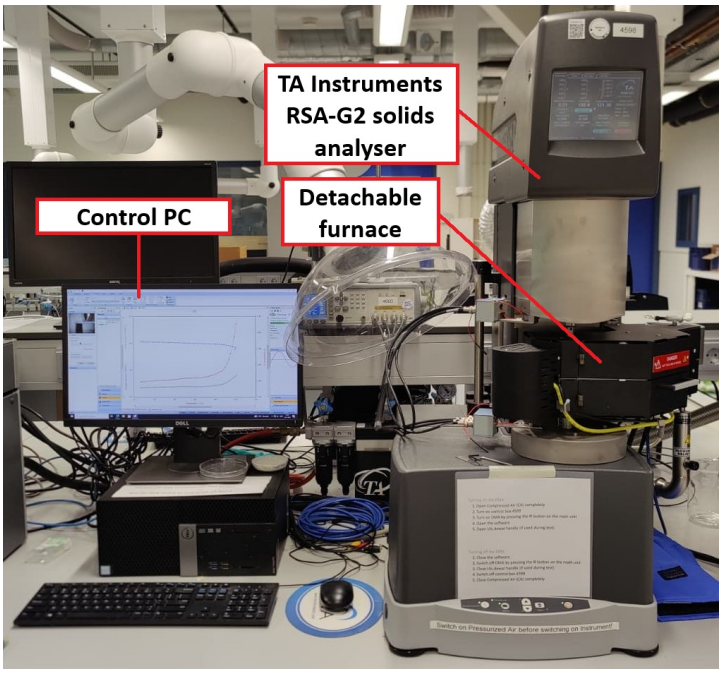

Figure 5.15: TA Instruments RSA-G2 solids analyser used for the DMA measurements.

Dynamic mechanical analysers are very low load and sensitive machines, which can only apply small forces on specimen. The RSA-G2 as used for these experiments is considered as quite a high-load capability DMA machine, however still it has a maximum load limit of only 35N. For stiff materials such fibre-reinforced polymer composites, such a low load limit eliminates the ability to directly perform dynamic mechanical analysis in a tensile load case. Therefore, for these material types such DMA tests are restricted to a bending mode.

However, a bending load case inherently induces a non-constant stress-strain through the thickness of the specimen. For unidirectional composite laminates like the 0/90 E-glass/epoxy in question here, a direct test of a sample with this layup would thus result a disproportionately large contribution of the outer $0°$-layers to the overall loss factor compared to a uniform tensile case. Therefore, the viscoelastic loss factor of the $0°$ and $90°$ directions had to be tested independently and results later combined following a similar approach to Equation 3.14.

For these independent direction DMA tests, two different bending set-ups were used. Namely a 3-point bending setup with a 40 mm span, as well as a so called dual-cantilever bending (DCB) with a 38 mm span. The latter here should not be confused with a the similarly named doula-cantilever beam test. Both of these bending set-ups are shown for reference in Figure 5.16. The main advantage of the DCB tooling is that unlike a 3-point bending case, load cycles with an effective test R-ratios of $R = -1$ can be directly applied due to the clamping at both the span ends as well as the central load applicator. This way, the results of these DCB tests did not have to be any further compensated for R-ratio to be comparable with the R-ratio corrected loss factor values derived in fatigue.

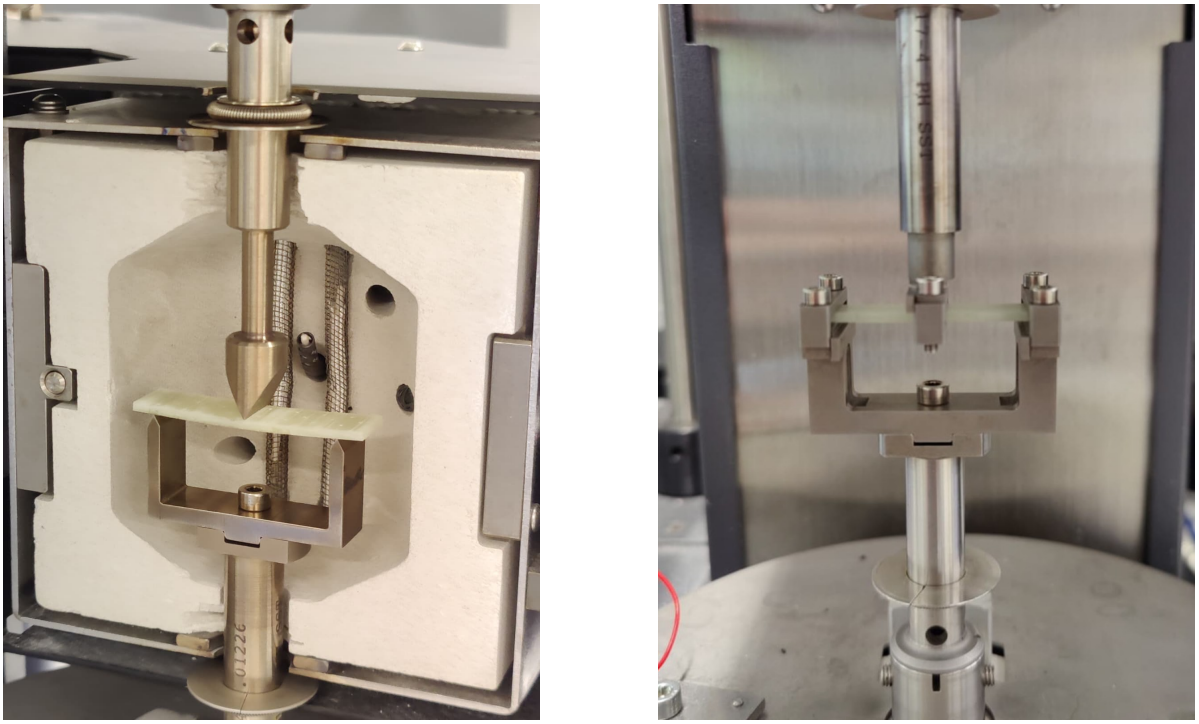

(a) 3-Point bending tooling on the TA Instruments RSA-G2.

(b) DCB tooling on the TA Instruments RSA-G2.

Figure 5.16: Two used DMA bending set-ups: a) 3-Point Bending (3PB), b) Dual Cantilever Bending (DCB).

Although the load case itself is inherently different between 3-point bending and such dual-cantilever bending, the RSA-G2 solids analyser directly compensates its loss factor measurement for this different load case. The requirement by the manufacturer here however is that the DCB span over specimen thickness ratio should be greater than 10. For fibre-reinforced composite specimen, the manufacturer furthermore recommends a minimum sample width of 10 mm to limit any edge effects. Additionally, for an acceptable measurement the strain amplitude must remain within linear viscoelastic region of the material, for which the ASTM D7028 standard for DMA testing of polymer matrix composites [91] recommends a maximum strain limit of 0.1%. Finally, both 0° and 90° specimen shall be loaded to the same peak strain value.

With all these consideration in mind as well as the relative stiffness difference between the 0° and 90° laminate orientations, for the 0° degree specimen a 10 mm width was chosen, whilst for the 90° specimen this was increased to 12 mm. Both specimen types were produced to the same thickness of 1.85 mm. For the DCB tests, this gave a span to thickness ratio of 20.5, which is well over the minimum required value of 10.

However, a known issue regarding the DMA testing of stiff but lightweight material such continuous fibre-reinforced polymer composite is the occurrence of resonance [25]. This often limits the frequencies at which the samples can be tested, which also showed itself to be the case in the DMA tests performed for this thesis. Based on initial exploratory tests, the 3-point bending measurements were restricted to maximum frequency of 10 Hz before getting into a resonance band. Hence in this configuration, DMA measurements were taken at 5 and 10 Hz only. In the DCB mode, higher frequencies up to 25 Hz could be tested. Hence in this last mode, measurements were taken at 5, 10 and 25 Hz. All tests aimed for peak strain of strain of 0.1%.

Then finally, all DMA tests were done as temperature sweeps from 25/30$^\circ C$ up to 160$^\circ C$. As mentioned at the start of this section, this gave information on not only the loss factor at room temperature, but also its temperature sensitivity and furthermore allowed later selection of the most representative temperature for comparison to the fatigue dataset.

6

Data Processing

The following chapter on data processing acts as a bridge between the experiment design and execution covered in chapter 5 and the final results that will be presented in the upcoming chapter 7. The data processing steps undertaken to go from raw test data to analysis results is summarised by Figure 6.1. Section 6.1 will first cover the DIC data processing approach and validation of the self-developed pipeline with implementation of the open-source μDIC correlator. Section 6.2 then covers the integration of this these local DIC measurements with the global strains. Section 6.3 summarises the methods and formulations used to establish the primary fatigue analysis metrics within the current modified linear viscoelastic fatigue analysis framework. Finally, section 6.4 briefly covers the post-processing of the DMA test results.

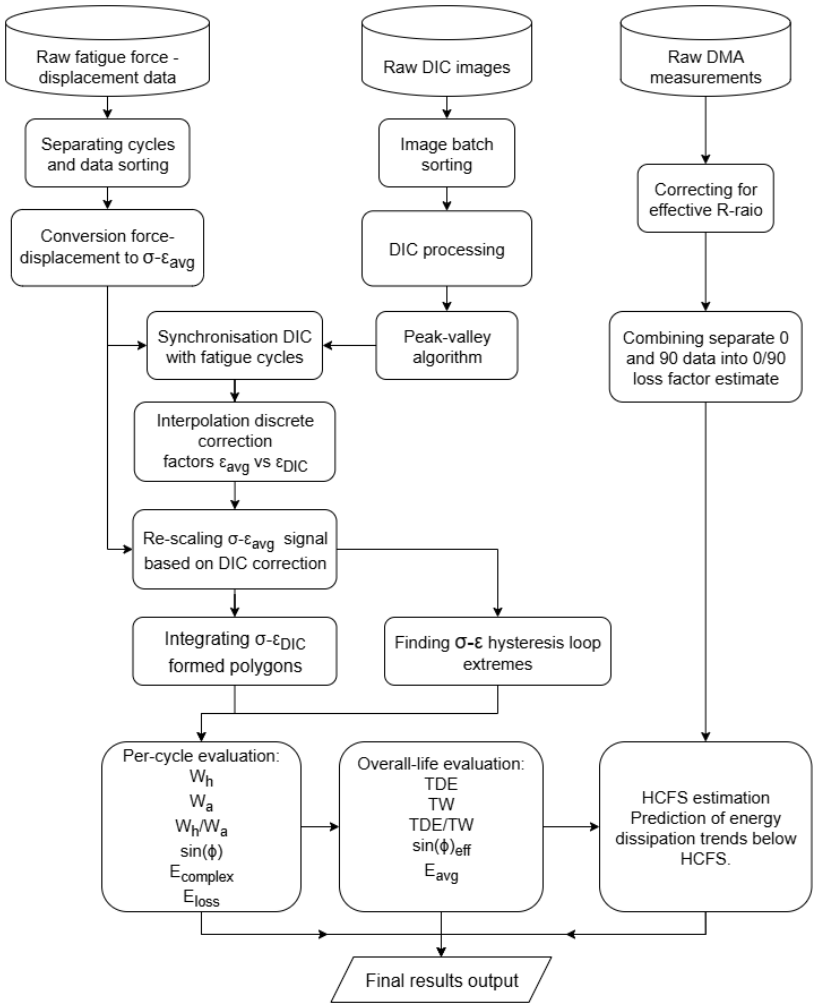

Figure 6.1: Flowchart representing the flow of data and processing steps.

6.1. DIC processing

As was discussed in subsection 5.8.3 of the previous chapter and also shown in the flowchart of Figure 6.1, ultimately the hysteresis strain measurements of the fatigue tests were based on the local high-speed DIC strain analysis of the central specimen section. To obtain such measurements, high-speed images of multiple full cycles at a time were taken at fixed cycle intervals, triggered by a counter on the MTS servo-hydraulic test machine controller. For each of such high-speed DIC recordings, a frame rate of 250 FPS was used, with the total image count per recording varying mostly between 400 and 500 images.

For all of the 21 performed fatigue tests together, this accumulated a total of 770 Gb worth of DIC images. With such a large amount of data to process, the use of semi-manual licensed DIC processing software such as 2D-VIC (most commonly used by the ASM department) would not have been feasible within the time constraints of this project. The available licences of this 2D-VIC software are very limited and were therefore also naturally in high demand for other research projects. To circumvent this and drastically speed up the DIC analysis by automation of processes, a custom DIC processing scheme was self-developed in the Python programming language. This was built around the open-source DIC correlator package by Olufsen et al. [92], called μDIC.

A first overview of the steps included in this DIC processing scheme, as well as how the μDIC correlator package integrates with this is shown in the flowchart of Figure 6.2 below. Further details on the individual processing blocks shown here will be given in subsection 6.1.1, followed by a validation process in subsection 6.1.2.

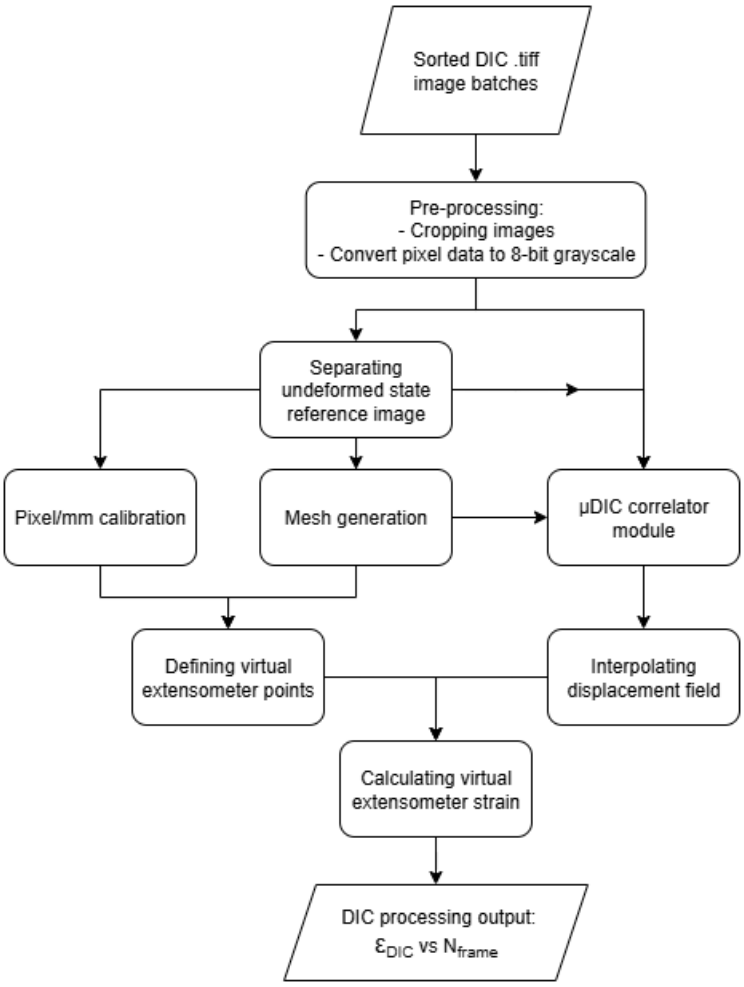

Figure 6.2: Flowchart representing the DIC processing procedures.

6.1.1. μDIC implementation

As shown in the flowchart of Figure 6.2, the DIC processing started with the high-speed images sorted in chronological order into their respective recording batches. These images were then first reduced in size by cropping away most of the non-informative background portions. Then, the pixel data of these original tiff images were converted into 8-bit grayscale.

As the strain measurements were all based on the deformation relative to the undeformed state of the specimen, the fist image taken in every fatigue tests where the specimen was still fully unloaded was isolated and stored separately to be used as strain reference. Al subsequent DIC image correlation would be performed relative to this initial reference. Furthermore, on this reference image the pixel to mm calibration was performed using the known minimum widths of specimen as well as the DIC meshes being generated. Then all sequential grayscale data was passed onto the iterative solver of the μDIC correlator. The output of this module was a displacement field for each image, which consisted of the displacement vector at the centroid of each mesh element.

The DIC analysis was based on the principle of a so called 'virtual extensometer', meaning that the strains measured were the average over a specified line segment drawn in the undeformed DIC mesh. Here, a 45 mm virtual gauge length was used, which roughly equalled 2.5 times the minimum width. This was centred on the specimen geometry, where the cross-section was at its smallest. By interpolating the discrete displacement field outputs by the μDIC correlator, the extension of this virtual extensometer line was calculated. From this, the final strain output for each DIC image followed by simple comparison to the original undeformed length of 45 mm.

For each sorted recording batch, the output of the DIC processing scheme was the virtual extensometer strain measurement vs the image/frame count. An example of this for the first recording of test F-21 at 325 MPa and an R-ratio of 0.3 is shown in Figure 6.3 below.

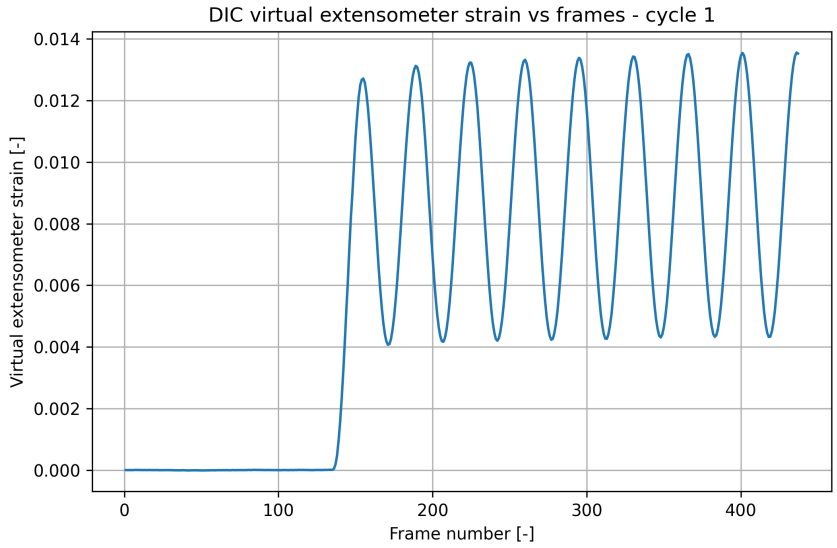

Figure 6.3: Example of the DIC processing scheme output for first recording of test F-21 at R0.3 325 MPa.

6.1.2. Validation using 2D-VIC

To ensure that both the open-source μDIC correlator as well as its implementation resulted in accurate and reliable DIC strain measurements, the first high-speed DIC recording of each test was also manually processed using the licenced 2D-VIC software by Correlated Solutions. These measurements were considered as validation reference, to which the measurements obtained through the implementation discussed in subsection 6.1.1 would be compared. Figure 6.4 shows these validation results, which expresses the errors in the maximum cycle strain values of the own DIC processing scheme relative to the 2D-VIC output.

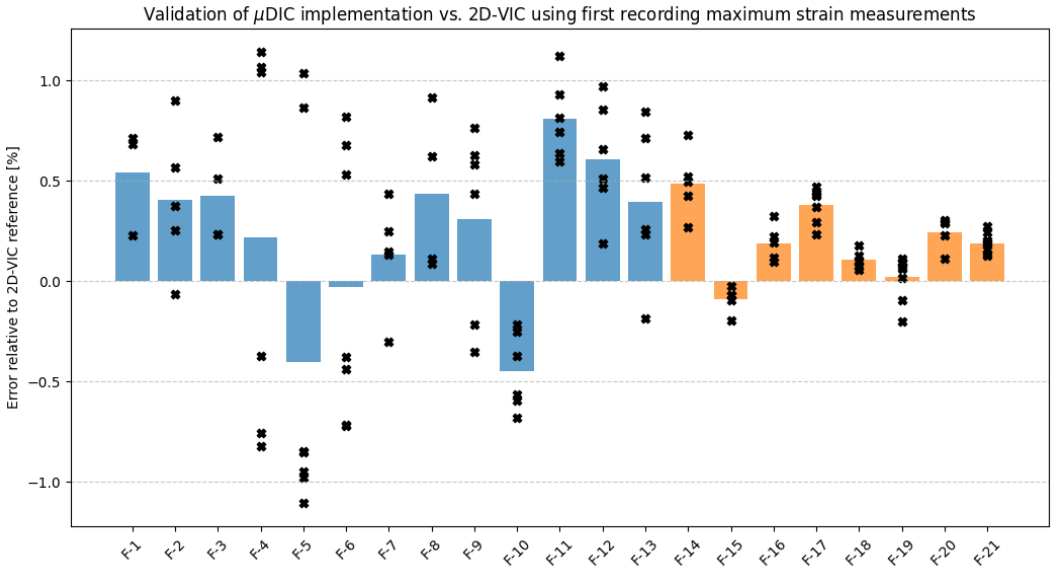

Figure 6.4: μDIC implementation relative error w.r.t. 2D-VIC for first DIC batch of each test.

As the above figure shows, the relative error of the current DIC approach with respect to the 2D-VIC output remains mostly within $\pm 1\%$. This gave good confidence in generated strain dataset. Interestingly the relative error becomes smaller and more consistent for the $R = 0.3$ tests as shown in orange. The reason for this is believed to be a more consistent and slightly finer speckle pattern that was applied on these specimen after gaining more experience following the first $R = 0.1$ batch.

6.2. DIC-based strain correction

Due to the DIC strain measurements only being taken at discrete cycle intervals and at sampling rates that did not match those of the force-displacement data logging by the servo-hydraulic test machine, the full cyclic DIC strain output as shown in the example of Figure 6.3 could not directly be matched with the force measurement signal. Therefore instead, a peak-valley algorithm was applied to the DIC analysis output to find the maximum and minimum strain value of each measured cycle.

The high-speed camera recordings were triggered by the servo-hydraulic test machine controller, which was furthermore set up to also leave a time-stamp in the force-displacement output file. Therefore, these maximum and minimum strain measurements of these DIC cycles could be straightforwardly synchronised with the test's force-displacement data. For such cycles where both DIC measured and displacement based average maximum and minimum strain values were available, their relative scaling factors could be calculated. Figures 6.5 and 6.6 show examples of these DIC over average strain scaling factors look like over the normalised life for the maximum and minimum strains of test F-21.

These figures show that the average strains are always higher than the local DIC measurement, which is to be expected due to the stacking of compliances in the piston displacement measurement. Furthermore, these ratios are not constant throughout the fatigue life as damage propagates and localises. However, the general trend or shape in the data is the same for minimum and maximum strains.

Figures such as 6.5 and 6.6 then gave continuous strain correction functions which were used adapt and re-scale all the displacement-based average specimen strain data to the actual local strains in the central 45 mm of the specimen. In the case of the F-21 test examples shown here, a best fit 4th order polynomial function was used. The same process was followed for the reaming tests.

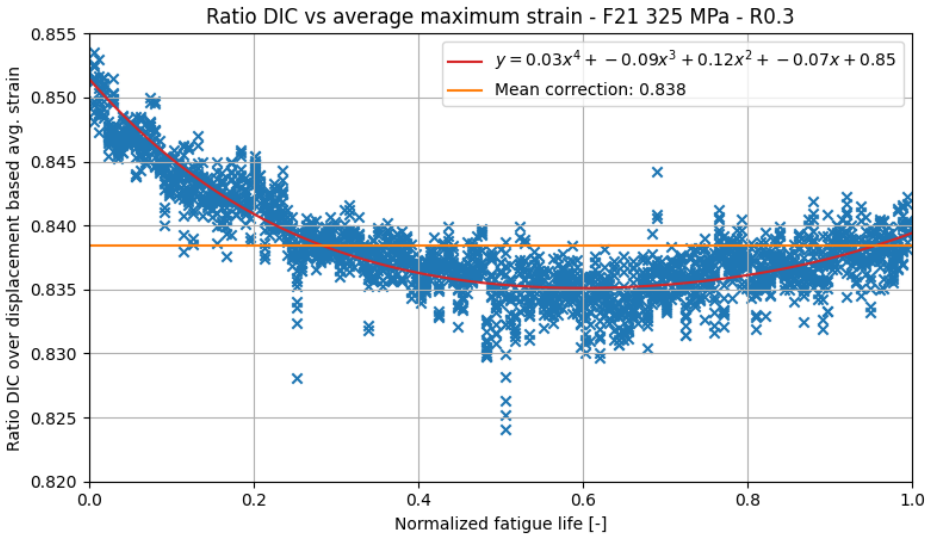

Figure 6.5: Example of DIC-based maximum strain correction function for test F21 at R0.3 325 MPa.

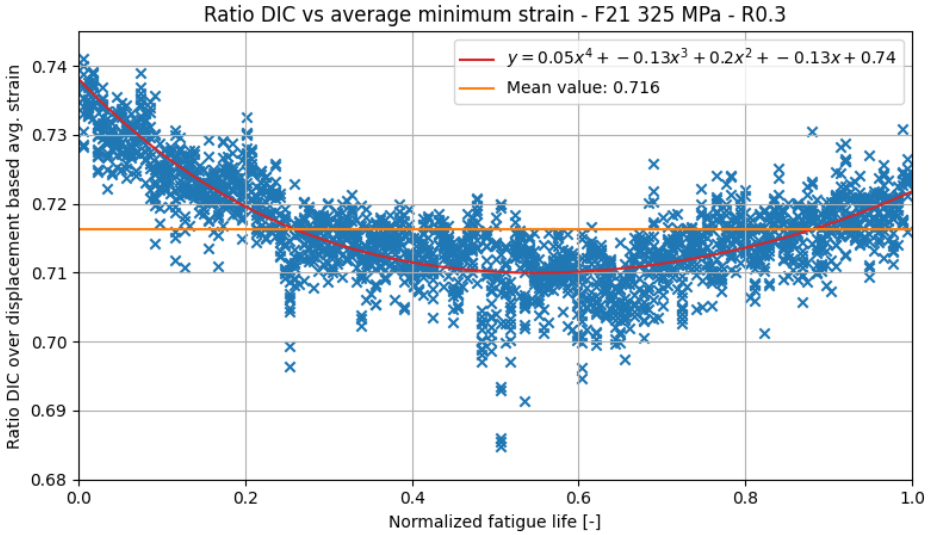

Figure 6.6: Example of DIC-based minimum strain correction function for test F21 at R0.3 325 MPa.

Using such interpolated strain correction functions as those shown in the figures above, all displacement based strain data points $\epsilon_{avg,i}$ that make up a measured fatigue cycle could be converted to its estimated local strain $\epsilon_{corrected,i}$ following Equation 6.1.

$$\epsilon_{corrected,i} = \epsilon_{DIC,min} + \frac{(\epsilon_{avg,i} - \epsilon_{avg,min})\,(\epsilon_{DIC,max} - \epsilon_{DIC,min})}{\epsilon_{avg,max} - \epsilon_{avg,min}} \tag{6.1}$$

Here, $\epsilon_{avg,max}$ and $\epsilon_{avg,min}$ are the original minimum and maximum strain values based on the initial displacement. $\epsilon_{DIC,min}$ and $\epsilon_{DIC,max}$ on the other hand are the DIC based strain extremes of the cycle following from the established interpolation functions.

6.3. Calculation of fatigue metrics

This section aims to provide the reader with an overview of the calculations that formed the primary modified linear viscoelastic fatigue analysis metrics. Some of the formulations shown in this section have been introduced or discussed before throughout chapters 3 and 4. However, for completeness and easy reference these will be shown here again.

6.3.1. Definition of stress

To be most consistent with the DIC virtual extensometer strain over a central length of 45 mm, a matching definition of stress was used that averaged the stress value over this same 45 mm region. Using this definition, each fatigue force data point as output by the servo-hydraulic testing machine data logger was converted to a stress value through Equation 6.2.

$$\sigma_i = \frac{P_i}{A_{central,avg}} \tag{6.2}$$

Here, P_i was the force measurement and $A_{central,avg}$ is the average cross-sectional area in the central 45 mm virtual gauge section. The values for this average cross-sectional area were based on the width and thickness measurements of the specimen as they were reported in Table 5.8, combined with the known 900 mm radius curvature or the specimen edges.

6.3.2. Hysteresis dissipated energy

Having obtained representative stress-strain hysteresis data for each fatigue cycle following the DIC based strain re-scaling and stress definition of subsection 6.3.1, the energy dissipation could be calculated. Here it was recognised that the stress-strain data points of each cycle effectively form a closed ordered polygon. Therefore, the hysteresis dissipated energy was calculated using the so called 'shoelace formula' [93], which is adapted here in Equation 6.3 to represent the current stress-strain data.

$$W_h = \frac{1}{2}\sum_{i=1}^{n}(\epsilon_i\sigma_{i+1} - \sigma_i\epsilon_{i+1}) \tag{6.3}$$

Here, n is the number of stress-strain points measured for each loop and thus a function of data sampling rate. To furthermore ensure a fully closed hysteresis loop, the last data point is connected back to the first and therefore $(\epsilon_{n+1}, \sigma_{n+1}) = (\epsilon_1, \sigma_1)$.

The total dissipated energy over the whole fatigue life was then simply determined by summation of the individual cyclic dissipation values, as formulated by Equation 6.4.

$$TDE = \sum_{i=1}^{N_f} W_{h_i} \tag{6.4}$$

6.3.3. Complex modulus

As initially introduced in section 3.1, the complex (or dynamic) laminate modulus of each cycle $|E_i^*|$ was defined as the average stress-strain slope between the two extremes of the hysteresis loop. For wide elliptical hysteresis loops such as seen for pure viscoelastic polymers, the tips of the extreme tips of the hysteresis loops are not directly the maximum and minimum stress-strain values. Typically for such cases, one would first do a principle component analysis to find the major axis of the elliptical loop and then the extremes closest to this principle direction vector. However, for the current stiff composite material, the hysteresis loops are naturally quite stretched and thin as result of the comparatively low viscoelastic loss factor. Therefore, it was considered a justified simplification with minimal error to directly take the overall extreme stress and strain as the hysteresis loop tips. The complex modulus was then calculated following Equation 6.5.

$$|E_i^*| = \frac{\sigma_{max,i} - \sigma_{min,i}}{\epsilon_{max,i} - \epsilon_{min,i}} \tag{6.5}$$

6.3.4. Applied energy per cycle

The applied energy or work done per cycle for R-ratios between 0 and 1 were calculated using Equation 6.6 as originally introduced in subsection 3.5.2.

$$W_a = \frac{\sigma_{max}^2}{2 \cdot |E^*|} - \frac{\sigma_{min}^2}{2 \cdot |E^*|} \tag{6.6}$$

Similar to the total dissipated energy, the total work done over the whole fatigue life was a simple summation of the applied energy in each cycle.

$$TW = \sum_{i=1}^{N_f} W_{a_i} \tag{6.7}$$

6.3.5. Viscoelastic loss factor

Both formulations for cyclic and effective loss factors already introduced and used in chapter 4, however their formulations are still added here for consistency and to provide the full overview of the data processing steps. Cyclic viscoelastic loss factor was calculated based on the cyclic dissipation ratio $\frac{W_h}{W_a}$ and an inverted R-ratio energy correction factor as given by Equation 3.37.

$$\sin(\phi) = \frac{1}{\pi} \frac{W_h}{W_a} \left(\frac{1+R}{1-R} \right)^2 \quad \text{for } 0 \leq R \leq 1 \tag{3.37}$$

In a very similar manner, the effective loss factor describing the energy weighted average loss factor over the whole fatigue life was then calculated based on the total dissipated over total work ratio.

$$\sin(\phi_{eff}) = \frac{1}{\pi} \frac{TDE}{TW} \left(\frac{1+R}{1-R} \right)^2 \tag{4.3}$$

6.4. DMA data processing

DMA measurements were performed in 3-point bending and dual-cantilever bending. As originally discussed in subsection 4.4.1 of the preliminary analysis, DMA tests performed in 3-point bending inherently have a positive R-ratio. In order for such measurement to be made comparable to the modified linear viscoelastic loss factor definition, this 3-point bending R-ratio needed to be corrected for. This was done using Equation 4.2 again.

$$\sin(\phi) = \frac{\sin(\phi_{DMA})}{2} \frac{1+R_{DMA}}{1-R_{DMA}} \quad \text{for } 0 \leq R \leq 1 \tag{4.2}$$

Then finally, to obtain a loss factor estimate for the complete 0/90 laminate, the measured loss factor values of each pair of 0° and 90° tests under the same loading conditions were combined using Equation 6.8 following a similar relationship proposed by Murayama [94].

$$\sin(\phi_{[0/90]}) = \frac{V_0 \sin(\phi_0) E_0 + V_{90} \sin(\phi_{90}) E_{90}}{V_0 E_0 + V_{90} E_{90}} \tag{6.8}$$

Here, V_x represents the relative volume fraction of the each of these two fibre orientations, E_x the DMA measured laminate stiffness along that direction and finally $\sin(\phi_x)$ the R-ratio corrected loss factor measurement for each of the two principle directions.

7
Results

This chapter presents the results of the monotonic tensile, tensile–tensile fatigue, and dynamic mechanical analysis tests performed on the $[0/90]_{4s}$ UD E-glass/BT080-epoxy fibre-reinforced polymer composite specimen, following the experimental procedures described in chapter 5 and the data processing outlined in chapter 6. The results are organised according to the sequence of analysis steps undertaken. Where appropriate, comparisons are made and critical intermediate interpretations are provided to support the presentation of the complete dataset. A more comprehensive discussion of the implications and significance of these findings is reserved for chapter 8.

The chapter begins with section 7.1, presenting the results of the monotonic tensile tests at quasi-static and fatigue-equivalent dynamic strain rates. This is followed by a general overview of the fatigue behaviour in section 7.2, which includes the measured stress–life relations, stiffness degradation trends, as well as the fatigue failure strains. Building on this, section 7.3 reports the progression of cyclic energy dissipation and cyclic loss factor values across the fatigue lives, while section 7.4 integrates these per-cycle measurements into the total dissipated energies. The focus then shifts in section 7.5 to the pristine material dynamic mechanical analysis, whose loss factor results are subsequently combined with the fatigue data in section 7.6 to show the effective loss factor trends and its potential for a viscoelastic damping based high-cycle fatigue strength prediction. In section 7.7, the overall observed results are then finally combined and extended to a fatigue life prediction, using part of the dataset as input and the remainder for validation.

7.1. Monotonic tensile tests

Monotonic tensile test were performed on the same dogbone geometry specimen as the later discussed fatigue tests. One reference test was performed at a near quasi-static displacement rate of 5 mm/min. A further three tensile tests were done at the estimated fatigue equivalent displacement rate of 25.5 mm/s, a factor 306 times faster than the reference case.

The DIC-based stress-strain responses measured in these tests are given by Figure 7.1. The resulting laminate tensile properties are summarised in Table 7.1 below.

Table 7.1: Overview measured laminate tensile properties.

Specimen ID	Displacement rate	Initial modulus [GPa]	Ultimate strength [MPa]	Failure strain [%]	Note
M-1	5 mm/min	29.54	574.5	3.02	N/A
M-2	25.5 mm/s	30.77	719.5	3.41	N/A
M-3	25.5 mm/s	28.99	705.8	3.70	N/A
M-4	25.5 mm/s	26.81	605.2	3.33	Specimen missalignment

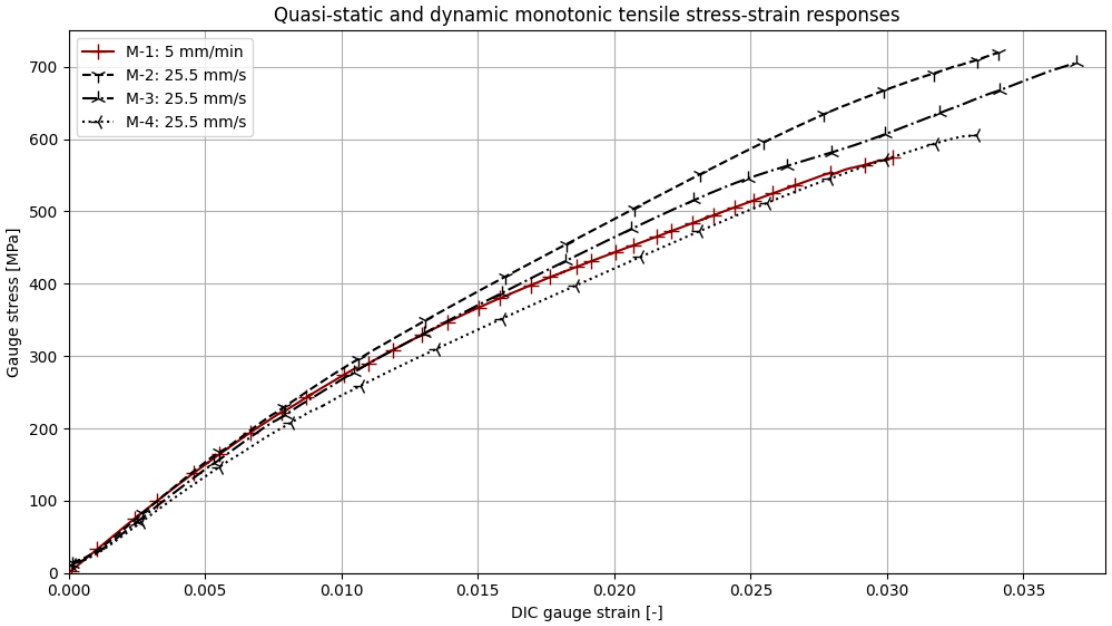

Figure 7.1: Monotonic tensile test results at quasi-static 5 mm/min and dynamic 25.5 mm/s displacement rates.

As the note in Table 7.1 suggests and is also visible from the stress-strain response of Figure 7.1, the M-4 high-rate test has both lower initial modulus and ultimate strength compared to the other high rate results. The reason for this is believed to be a misalignment of the specimen with respect to the loading direction. Therefore, the results from the M-4 tests were not further included in any results or analysis.

Excluding this M-4 test, Table 7.1 shows that between the 5 mm/min quasi-static and the 25.5 mm/s high-rate tests the materials ultimate strength increased with 23-25%. The failure stain furthermore increased by 13-20%. This confirmed the strong strain rate sensitivity of the this material.

7.2. Overview of general fatigue performance

This section provides a more general overview of the measured fatigue performance of the $[0/90]_{4s}$ UD E-glass/BT080-epoxy composite specimen. The results are presented in terms of the stress–life (S–N) relations, stiffness degradation trends and the fatigue failure strain versus fatigue stress response. These more generic fatigue characteristics first establish a baseline description of the material's performance before addressing the more specific energy dissipation and viscoelastic loss factor measurement results in the subsequent sections.

First, the tables 7.2 and 7.3 below provide a summary of the applied stresses, cycles to failure and failure strain for the $R = 0.3$ and $R = 0.1$ fatigue tests respectively. An overview of the failed fatigue specimen is provided in Appendix C.

Table 7.2: Overview of maximum stress, average gauge stress, cycles to failure and failure strains for the $R = 0.3$ fatigue tests.

Test ID	σ_{max} [MPa]	$\sigma_{gauge,avg}$ [MPa]	N_f [cycles]	ϵ_{fail} [%]
F-14	500	491.60	2373	2.51
F-15	450	442.62	26902	2.30
F-16	375	368.84	87666	1.99
F-17	600	580.25	15	3.04
F-18	530	522.50	492	2.64
F-19	640	624.02	11	3.14
F-20	350	344.65	273444	1.77
F-21	325	319.79	869642	1.72

Table 7.3: Overview of maximum stress, average gauge stress, cycles to failure and failure strains for the $R = 0.1$ fatigue tests.

Test ID	σ_{max} [MPa]	$\sigma_{gauge,avg}$ [MPa]	N_f [cycles]	ϵ_{fail} [%]
F-1	500	493.84	1782	2.75
F-2	400	391.83	24922	2.20
F-3	450	439.86	5021	2.44
F-4	350	347.12	98468	1.90
F-5	325	320.21	257172	1.88
F-6	310	304.88	473133	1.89
F-7	375	368.39	27060	2.11
F-8	425	416.99	14820	2.41
F-9	520	511.83	187	2.67
F-10	530	517.49	1061	2.79
F-11	600	585.81	28	3.35
F-12	640	629.53	81	3.32
F-13	660	646.87	13	3.15

7.2.1. Stress-life curves

The S-N curve based on the average cyclic maximum stress in the central DIC gauge section of the specimen is presented in Figure 7.2 below.

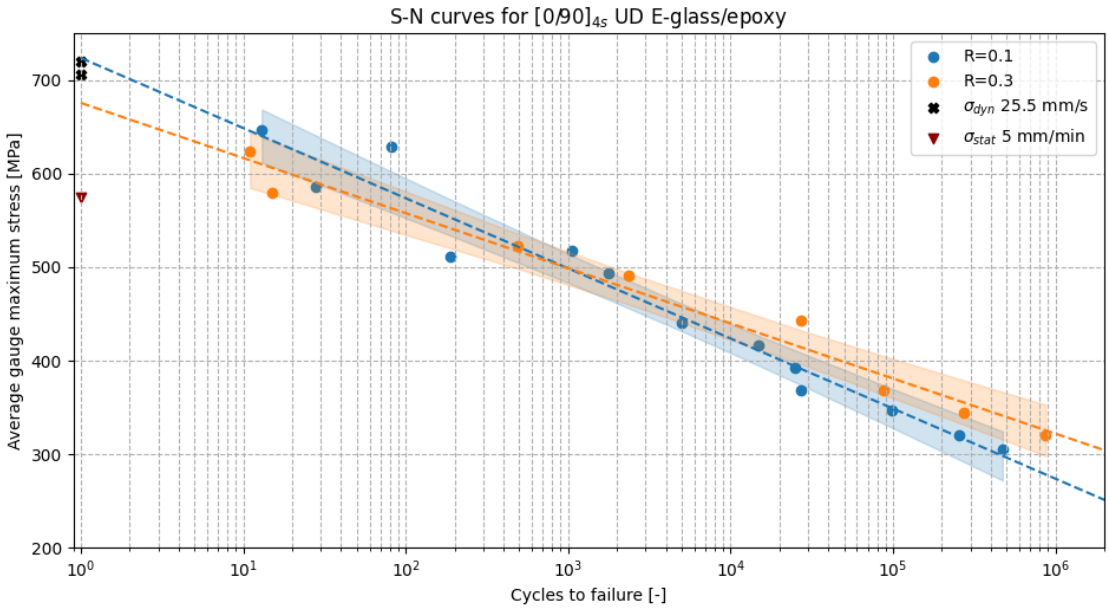

Figure 7.2: Maximum stress vs fatigue life ($S - N$) curves for the performed fatigue tests at $R = 0.1$ and $R = 0.3$.

Here, the blue and orange markers represent the $R = 0.1$ and $R = 0.3$ data respectively. The dashed lines show the power-law fits describing the S-N curves around their respective 95% percent confidence intervals.

As Figure 7.2 illustrates, the performed fatigue tests covered a wide fatigue life range of 5 decades, with the minimum cycles to failure at just over 10^1 cycles whilst the maximum goes up to 10^6. In the low cycle fatigue range of $10^1 - 10^3$ cycles, the S-N data of both tested R-ratios show considerable scatter at these high stresses. In the intermediate to high cycle fatigue range of $10^3 - 10^6$, their respective power-law fits diverge, with the larger fatigue lives being measured at the higher R-ratio of 0.3.

Furthermore, Figure 7.2 also shows how unlike the quasi-static, the laminate strength measured at the equivalent fatigue strain rate aligns itself well with the extrapolations of the fatigue data to a single cycle to failure.

In addition to the maximum stress representation, the fatigue results are also expressed in terms of average gauge stress amplitude versus cycles to failure, as shown in Figure 7.3. Expressing the S-N results in terms of stress amplitude shows the separation between the $R = 0.1$ and $R = 0.3$ datasets more clearly.

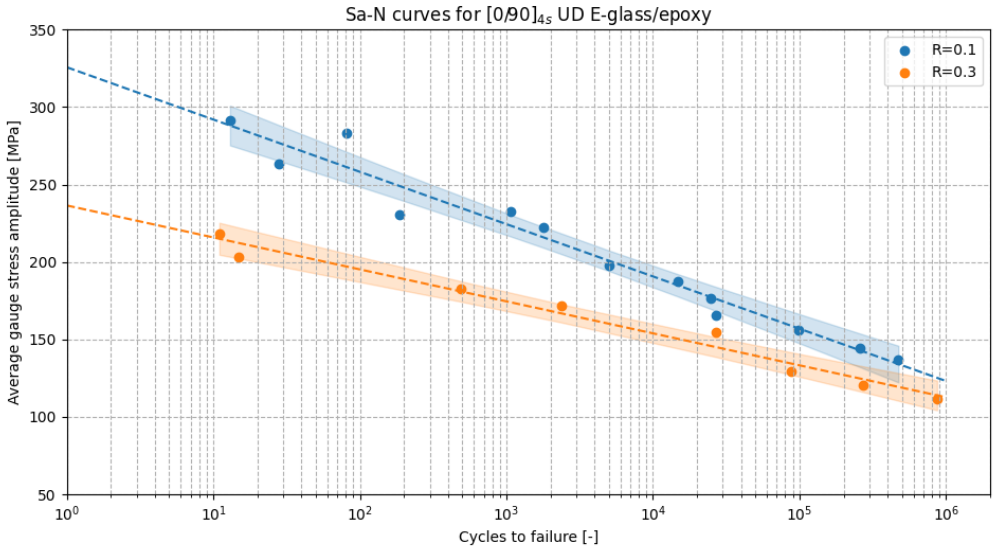

Figure 7.3: Stress amplitude vs fatigue life ($S_a - N$) curves for the performed fatigue tests at $R = 0.1$ and $R = 0.3$.

7.2.2. Stiffness degradation

Stiffness degradation was a key factor in the laminate selection process, as the test objectives aimed for a stabilised degradation that minimised the relative differences in strain rate and complex modulus between test. This behaviour enabled the changes in the viscoelastic damping characteristics to be more clearly isolated. Figure 7.4 below presents the measured stiffness degradation over the normalised fatigue lives, expressed in terms of the complex modulus $|E^*|$.

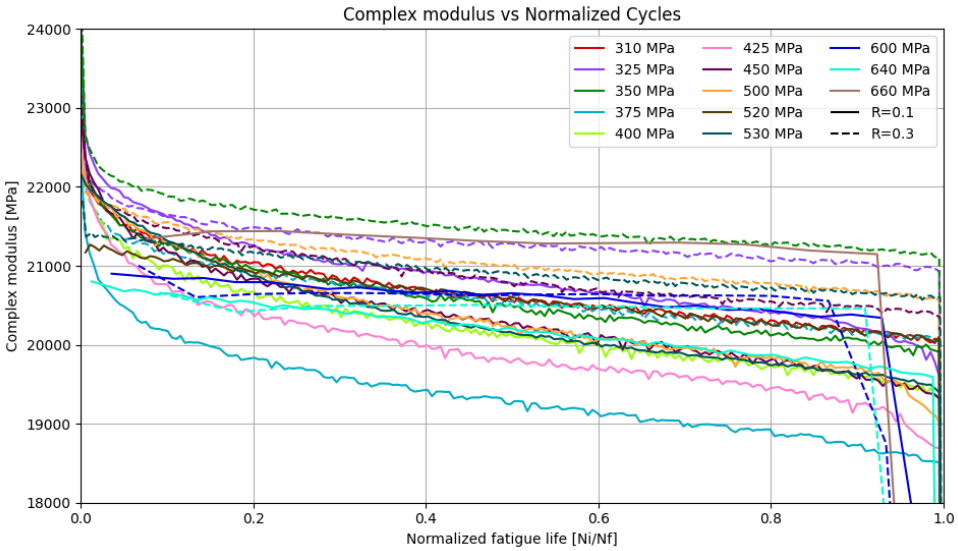

Figure 7.4: Complex modulus degradations over normalised fatigue lives for $R = 0.1$ (solid) and $R = 0.3$ (dashed) tests.

As shown in Figure 7.4, the complex moduli experience sharp reductions during the initial cycles. Within the first 20% of fatigue life, this rate of stiffness loss decreases, after which all tests show a stable and almost constant degradation up to failure.

The average pristine modulus of the two valid equivalent-rate tensile tests was 29.88 GPa. During fatigue loading, the specimens retained complex moduli between 21.5 and 19 GPa, corresponding to approximately 72–64% of its assumed pristine value. At lower applied stresses, the relative stiffness loss was smaller. Furthermore, the $R = 0.3$ tests generally exhibited slightly less degradation than its $R = 0.1$ counterparts.

To highlight the small differences in overall complex moduli, Figure 7.5 compares the average complex moduli $|E^*_{\text{avg}}|$ measured over each fatigue life against the maximum applied stress. Here, the spread of these average values show no systematic positive or negative trend with the maximum stress level. The consequent mean moduli of both R-ratio datasets ultimately differ by only 1.4% relative to the pristine modulus. This confirmed that the overall stiffness response remained well consistent across the dataset.

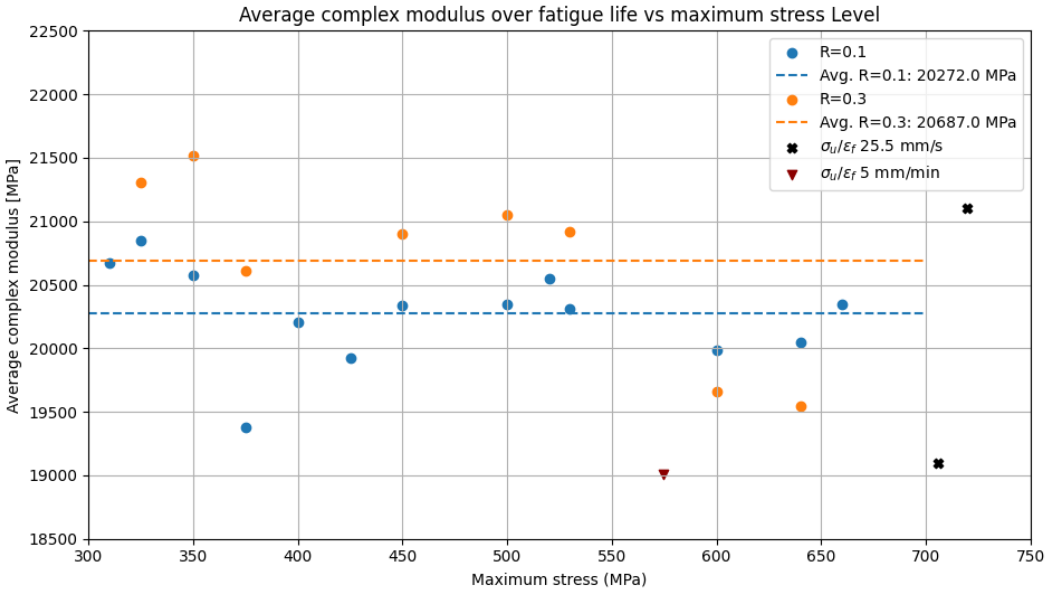

Figure 7.5: Comparison of fatigue life average complex moduli across the tested maximum stresses and R-ratios.

Finally, in Figure 7.5 also the effective moduli at failure ($\frac{\sigma_{ult}}{\epsilon_f}$) based on the tensile tests of Figure 7.1 were added for reference. These tended to fall generally within the same range as the fatigue test average complex moduli.

7.2.3. Strain rate variance

By being proportional to the inverse of the stiffness degradation, the strain rate evolutions over the normalised fatigue lives followed similar overall trends to those observed in Figure 7.4. The target strain rate for the fatigue tests was 0.15 s^{-1}. As shown in Figure 7.6, the measured values remained between approximately 0.13 and 0.16 s^{-1} for most tests, indicating that equivalent strain rate conditions were reasonably well maintained.

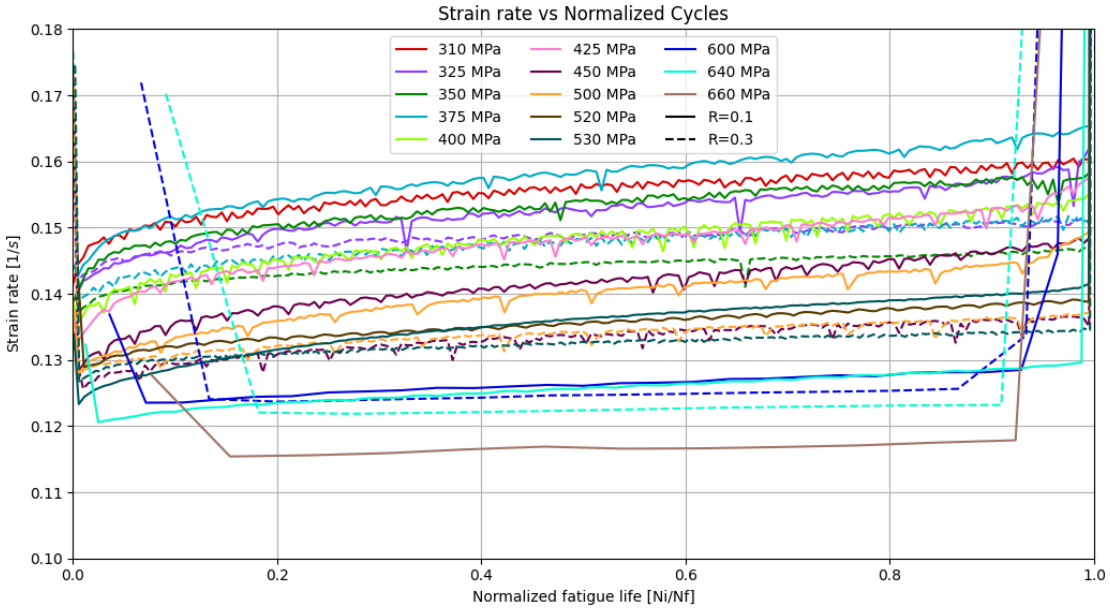

Figure 7.6: Average cycle strain rate over normalised fatigue lives for $R = 0.1$ (solid) and $R = 0.3$ (dashed) fatigue tests.

7.2.4. Fatigue failure strain

Figure 7.7 shows the fatigue failure strains plotted against the cyclic maximum stresses for both $R = 0.1$ and $R = 0.3$ datasets. Each dataset is represented by a linear fit with their 95% confidence bands shown. The results reveal two approximately parallel trends, with the $R = 0.3$ failure strains being consistently less than those measured at $R = 0.1$. Both trends extrapolate reasonably well to the equivalent high-rate monotonic tensile failure stress-strain measurements. Additionally, even the quasi-static tensile result falls within the range spanned by the fatigue data.

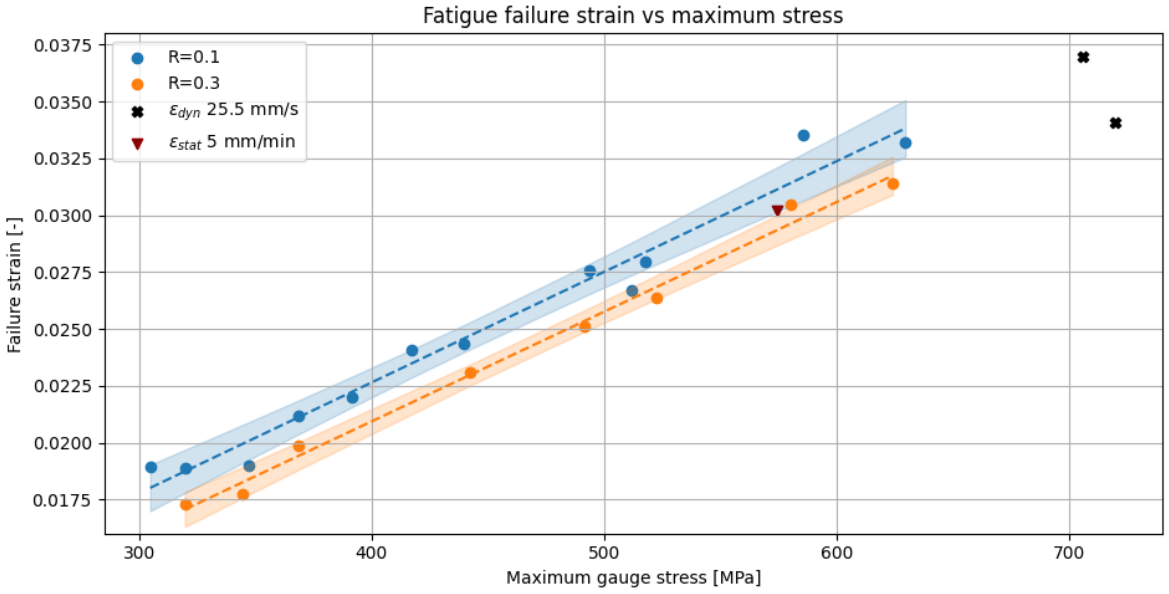

Figure 7.7: Fatigue failure strains vs cyclic maximum gauge stress.

Interestingly, the vertical shift in strain between the shown trends at the two R-ratios can be expressed through the strain energy based factor of $(1 - R^2)$. This term originates from the definition of total work (TW) as first defined in Equation 3.39 of chapter 3 and reflects the ratio of the amount of work done on the material in a cycle over the maximum strain potential stored at the peak of the cycle ($\frac{W_a}{W}$). Normalising the failure strain measurements by this factor of $(1 - R^2)$ effectively collapses the distinct $R = 0.1$ and $R = 0.3$ trends onto a single unified relation with maximum stress representative of equivalent loadcases at $R = 0$, as illustrated in Figure 7.8.

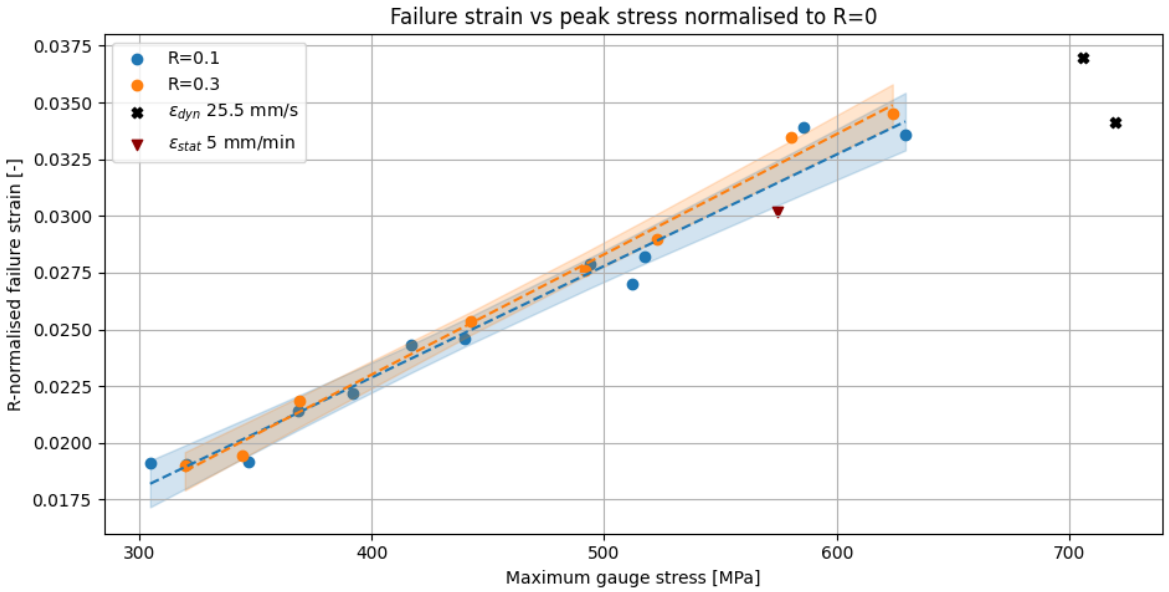

Figure 7.8: Fatigue failure strains vs cyclic maximum gauge stress collapsed to an equivalent $R = 0$ case.

7.3. Hysteresis dissipation and loss factor progression

Since the changing viscoelastic damping characteristics of the fatigue loaded composite laminate are central to the present work, this section gives the experimental results related to the hysteresis heating, cyclic dissipated energy and the derived progression of the viscoelastic loss factor through the fatigue lives.

7.3.1. Hysteresis heating localisation

To first off verify that the hysteresis heating and thus the viscoelastic damping was well confined to the central region of the specimen where the DIC strains were measured, infrared thermal images were taken of during a limited number of fatigue tests. Figure 7.9 shows two of such representative infrared images of the dogbone specimen specimen under cyclic loading. These show that the heating is clearly concentrated in the central narrow section, corresponding to the same gauge region of the current stress definition and strain measurements. This confirms that both peak viscoelastic dissipation and mechanical strain data originated from the same localised region on the designed dogbone specimen.

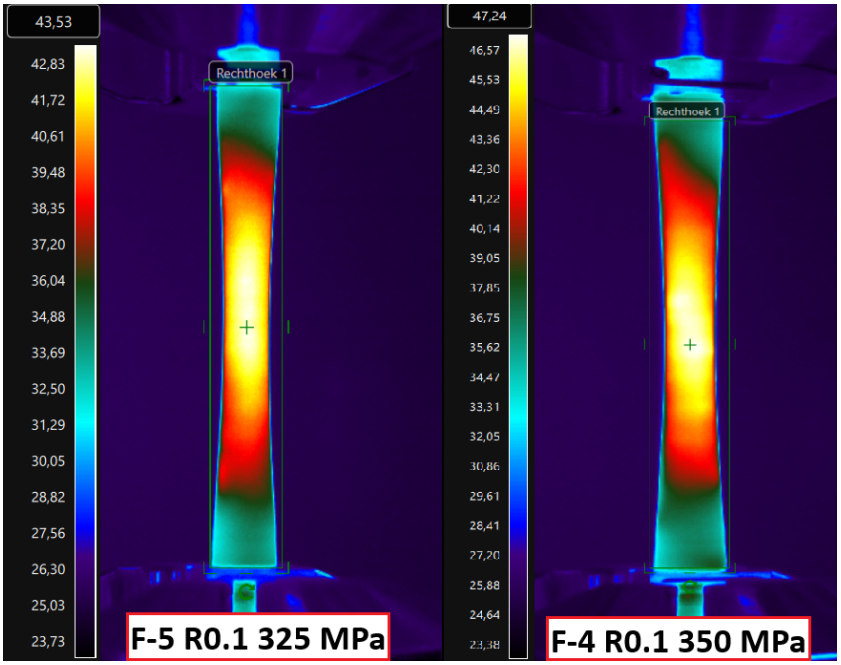

Figure 7.9: Infrared temperature measurements during tests F-4 and F-5.

7.3.2. Cyclic dissipated energy, W_h

The amount of energy dissipated per cycle W_h, obtained by the integration of the enclosed area by the hysteresis loops, is presented in Figure 7.10. This includes results for both $R = 0.1$ (solid) and $R = 0.3$ (dashed) as progression over the normalised fatigue lives. However, it must be noted that data from tests at stresses of 600 MPa and higher were excluded from this current figure for clarity. For reference, these high-stress results will be provided in Appendix C instead.

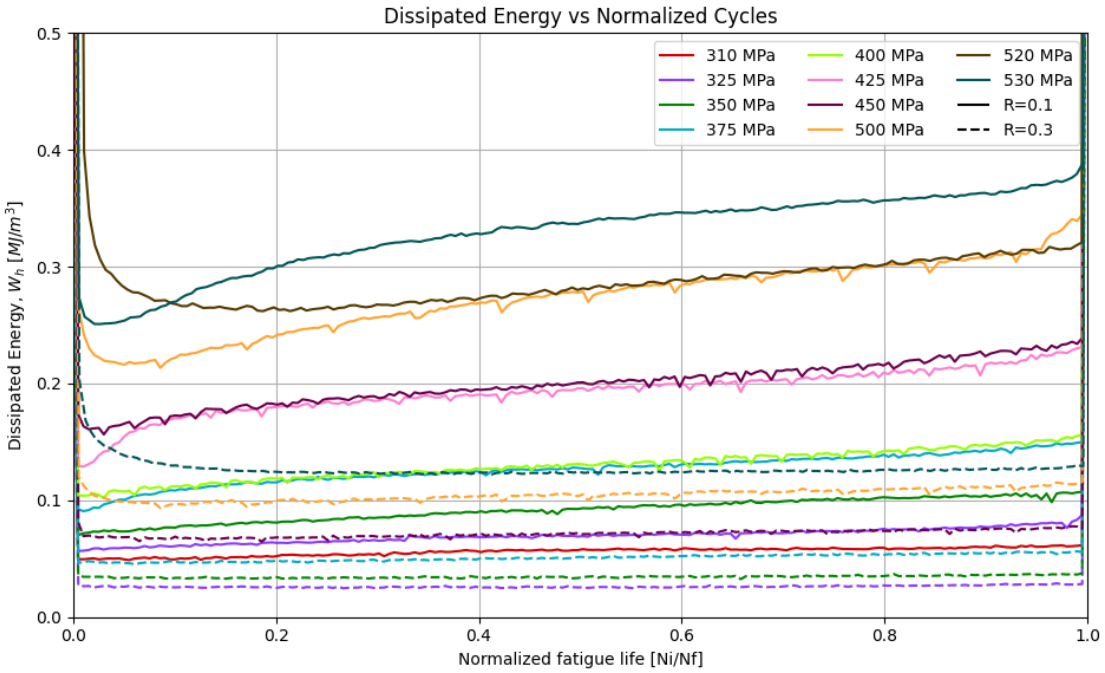

Figure 7.10: Hysteresis energy dissipation W_h over the normalised fatigue lives for $R = 0.1$ (solid) and $R = 0.3$ (dashed) tests.

From Figure 7.10 it is evident that all tests exhibit large amount of energy dissipation in the first cycle(s), consistent with the almost instantaneous initial stiffness reduction that was observed in Figure 7.4. During the experiments, this early stage was often accompanied by audible cracking or 'pinging' sounds, suggesting the onset of matrix damage in the 90° plies. After these initial cycles, the dissipation per cycle stabilises quickly at lower stresses, particularly for $R = 0.3$, and then increases only slightly over the remainder of fatigue life. At higher stresses however, this stabilisation is less pronounced and the dissipation shows a more progressive increase throughout the specimen's fatigue life. A second sharp dissipation spike is consistently seen at the end of life, reflecting the sudden final failure and the consequent near instantaneous release of strain energy from the highly loaded 0° layers.

Such a sequence of dissipation is further illustrated in Figure 7.11, which shows an example of an arrangement of hysteresis loops from specimen F-2 tested at 400 MPa and $R = 0.1$. Here, the hysteresis loop width of the first cycle is notably much wider than those that make up the bulk of the fatigue life. This matches the high initial energy dissipation upon the damage initiation in the first cycle. After this, the hysteresis width remains reasonably stable until the end of life, when again a final large release of strain energy is concentrated in one cycle, matching the final dissipation spike of Figure 7.10. For most tests this final failure occurred in a single cycle, however for some (predominantly at $R = 0.3$) this process was spread over the last two cycles.

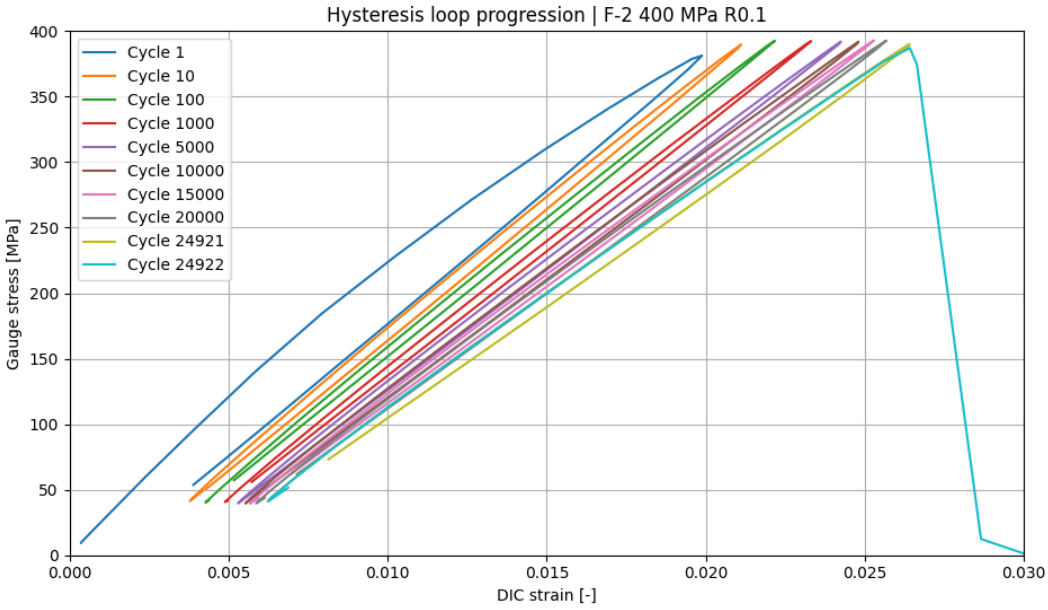

Figure 7.11: Example of hysteresis loop shape change throughout fatigue life for F-2 at 400 MPa $R = 0.1$.

7.3.3. Viscoelastic loss factor progression

The modified viscoelastic loss factors per cycle, calculated from the dissipated energy, the applied energy, and the R-ratio correction factors defined in this work, are shown in Figure 7.12.

All tests exhibit a pronounced spike in the first cycle(s), consistent with the initiation stage already seen in the cyclic energy dissipation results. At lower stress levels, the loss factor rapidly returns to a lower value from which it rises only gradually during fatigue life. With increasing stress, both the absolute value of the loss factor and its growth over life become larger. A distinction is also visible between the two R-ratios. Namely, for $R = 0.3$, the recovery from the initiation spike tends to take longer (about 20% of life), whereas at $R = 0.1$ the loss factor first recovers faster, but begins to grow again afterwards in a similar manner as seen in the preliminary analysis of chapter 4. Beyond this initial phase however, the loss factor trends at the two R-ratios generally converge and evolve near parallel for the remainder of fatigue life.

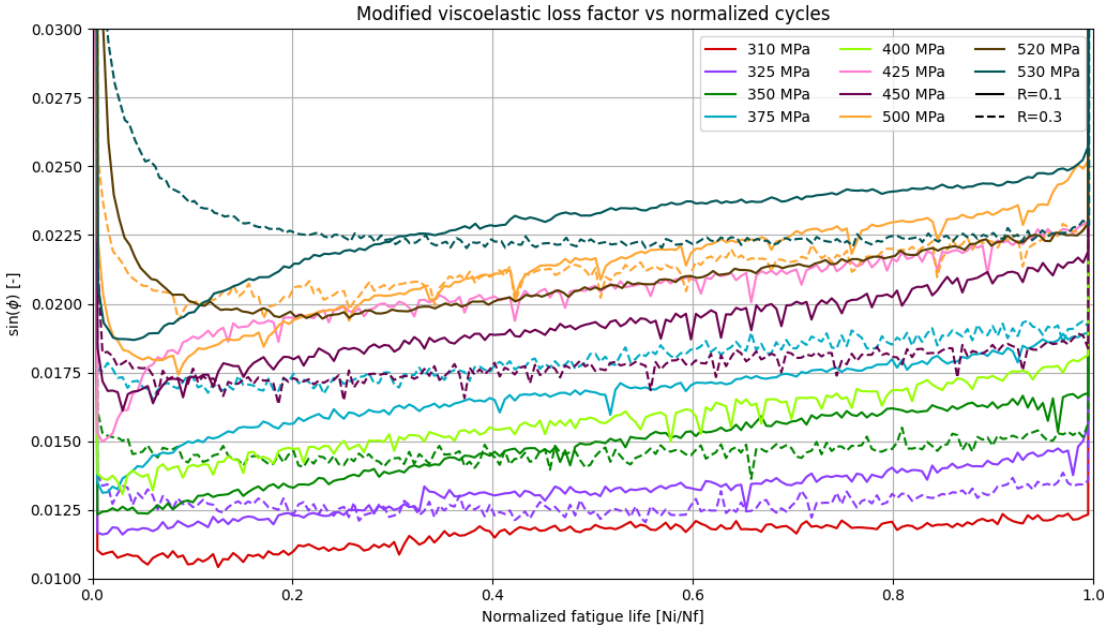

Figure 7.12: Modified viscoelastic loss factor $\sin(\phi_i)$ progression over normalised fatigue lives for intermediate to low stresses at $R = 0.1$ (solid) and $R = 0.3$ (dashed).

7.4. Total and critical dissipated energies

The total dissipated energy (TDE) was originally interpreted as the sum of all strain energy dissipated within a fatigue test. However, the results of the previous section, in particular Figure 7.10 and Figure 7.11, demonstrate a clear distinction between the cyclic hysteresis energy dissipated up to the point of the initiation of final failure and the rather large strain energy release associated with final failure itself. Moreover, this final failure contribution is not a constant quantity as tests at higher stresses release more strain energy upon failure than those at lower stresses.

The latter of this is illustrated in Figure 7.13, which compares failed specimens tested at 350, 450, and 650 MPa at a stress-ratio of $R = 0.3$. Although the failure locations are similar, the extent of final damage varies decidedly with stress level, ranging from mostly clear fibre fracture at 350 MPa with limited delamination to much more explosive failure along side extensive delamination propagation along the entire specimen length at 650 MPa. This indicates that the total dissipated energy, if defined to include final failure dissipation, does not provide a consistent basis for the comparison of a critical energy dissipation level that ultimately induces the final fatigue failure of the material. Particularly for the short fatigue lives at the high stress levels, any variation final failure dissipation has a considerable effect on the overall fatigue life dissipated energy total.

Therefore, an alternative definition is considered here: the *Critical Dissipated Energy (CDE)*. This critical dissipated energy is then defined as the sum of all hysteresis energy dissipation up to the initiation of final failure, excluding the large strain energy release of the final (catastrophic) failure itself. This distinction allows the damping and dissipation behaviour during the fatigue life to be considered independent of the variable final failure mechanisms.

When such critical dissipated energies for the $R = 0.1$ and $R = 0.3$ fatigue data are plotted against the maximum stress, then Figure 7.14 shows that the 95% confidence intervals of these respective log-linear trends overlap up to stresses of approximately 530 MPa. This corresponds to a wide range between low-cycle (10^2) to high-cycle (10^6) fatigue. This observation of largely overlapping confidence intervals of the critical dissipated energies at these two R-ratios indicates the independence of this critically accumulated dissipation term from the input energy and mean stress effects caused by the R-ratio. The concept of the CDE-stress trend as an R-ratio independent failure criteria will be explored further in the fatigue life prediction results of section 7.7.

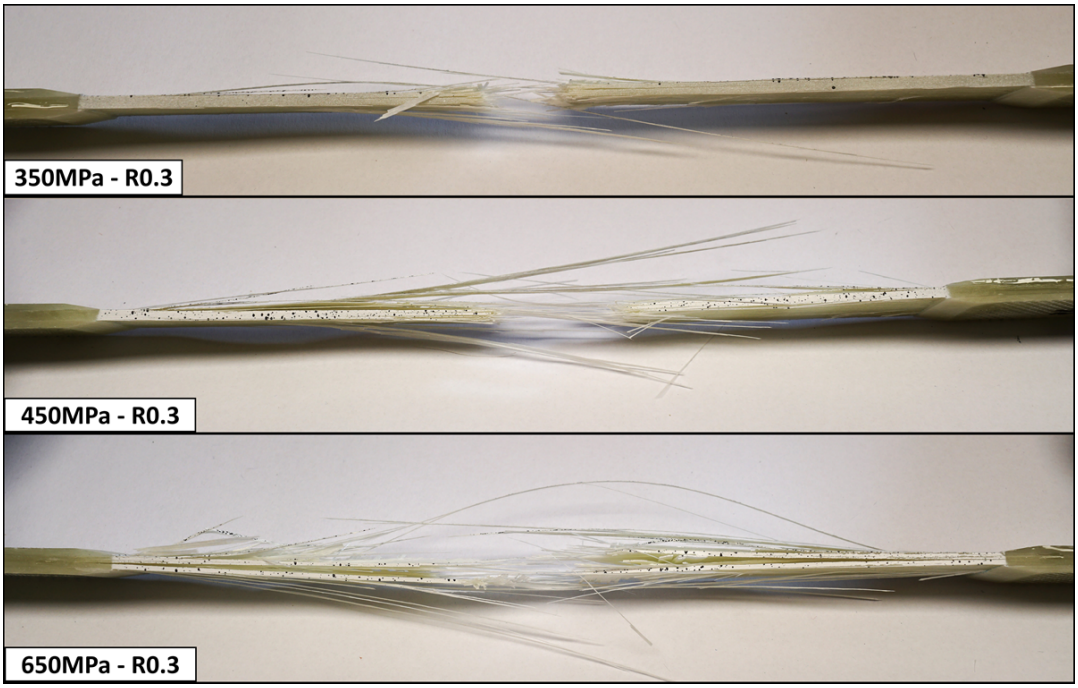

Figure 7.13: Comparison of final failure damage at increasing maximum fatigue stress (350, 450 and 650 MPa) at $R = 0.3$.

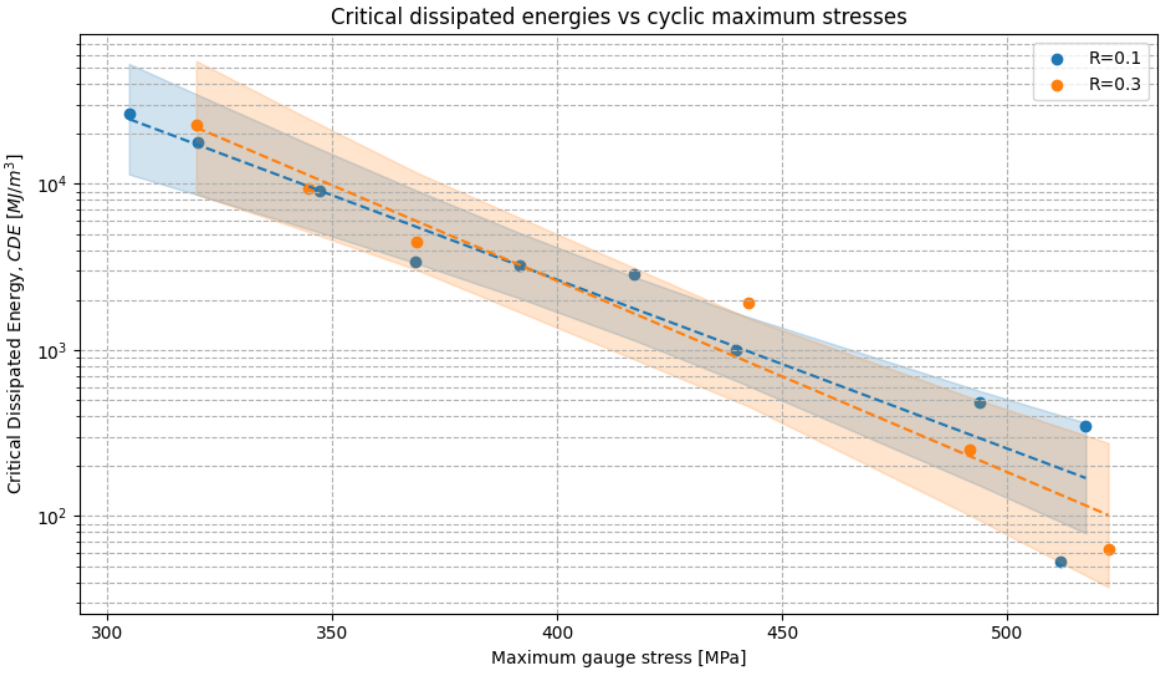

Figure 7.14: Log-linear critical dissipated energy (CDE) vs σ_{max} curves for $R = 0.1$ and $R = 0.3$ fatigue datasets, including overlapping 95% confidence intervals.

7.5. Dynamic mechanical analysis

Five sets of matching $0°$ and $90°$ orientation UD E-glass/BT080 DMA tests were successfully performed, with the main limiting factor on successful loading parameters being the inherent resonance sensitivity as explained earlier in section 5.9. The successfully used DMA test parameters are summarised in Table 7.4, including the type of bending mode, loading frequency, minimum and maximum cyclic strains, R-ratio and finally the applied DMA R-ratio correction factors based on Equation 4.2. Measurements performed on individual $0°$ and $90°$ oriented specimens were combined following the approach outlined in section 6.4, which ultimately led to the storage modulus and loss factor vs temperature plots of Figure 7.15.

Table 7.4: Overview of critical dynamic mechanical analysis testing parameters.

Test ID	Mode	Frequency $[Hz]$	ϵ_{max} $[\%]$	ϵ_{min} $[\%]$	R-ratio $[-]$	Applied correction factor $[-]$
DMA-1	3PB	5	0.1	0.01	0.1	0.611
DMA-2	3PB	10	0.1	0.03	0.3	0.929
DMA-3	DCB	5	0.1	-0.1	-1	N/A
DMA-4	DCB	10	0.1	-0.1	-1	N/A
DMA-5	DCB	25	0.1	-0.1	-1	N/A

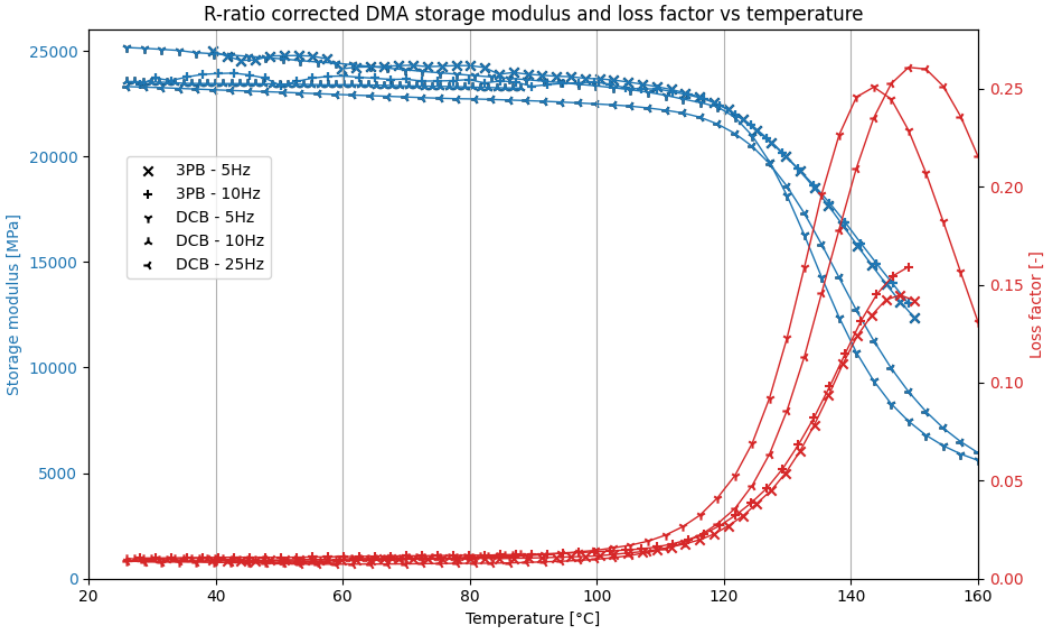

Figure 7.15: DMA measured storage modulus and loss factor vs temperature for the 3PB and DCB mode tests.

From Figure 7.15 a glass transition temperature of approximately $124°C$ was identified using the approach dictated by ASTM D7028 [91]. However, such conventional full-range loss factor representation as typically reported in literature [68], [69], is not practical for the current application. Therefore instead, Figure 7.16 provides a zoomed-in view of the loss factor over a reduced, but for the current results more appropriate, temperature range.

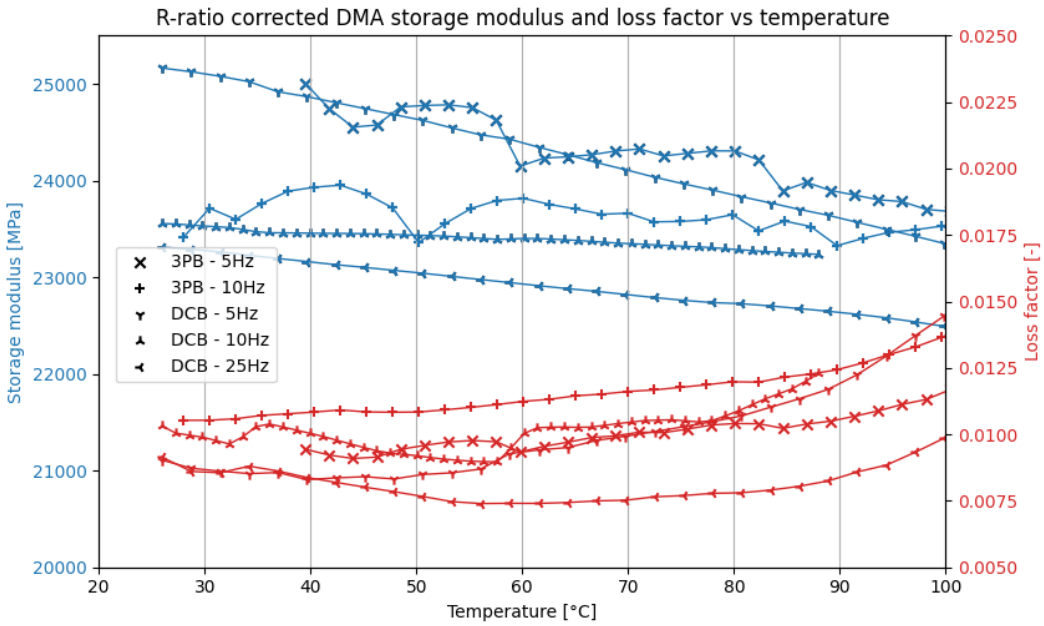

Figure 7.16: Reduced DMA measured storage modulus and loss factor vs temperature plot, focussed on the more representative $25 - 100°C$ temperature range.

The more focussed results of Figure 7.16 illustrate that although there is still a fair amount of spread, the R-ratio corrected 3-point bending DMA loss factor values align reasonably well with the direct $R = -1$ measurements in dual-cantilever bending. Furthermore, no consistent trend is observed with increasing frequencies. This either indicates that the strain rate differences between these tests were insufficient to have a major effect or the scatter in the data is larger than the rate or bending mode sensitivity.

Overall, the loss factor values appear to be little effected by temperature up to $80°C$. This suggests that temperature effects on the viscoelastic properties of this laminate and thus its energy dissipation remained small or negligible. Therefore, no temperature compensation terms were believed to be required in any of the analysed results. So, for use in the following sections, a representative loss factor value of 0.0097 ± 0.0012 was taken from Figure 7.16, based on the average and variation of measurements at a slightly elevated temperature of $40°C$.

7.6. Effective loss factor and HCFS

With the DMA based pristine material viscoelastic loss factor measurements, these results can now be related to the effective loss factors. This was defined as the energy-weighted average of the individual cycle loss factors over the fatigue life. To remain consistent with the short discussion on critical vs total dissipated energies of section 7.4, these derived effective loss factor values did not include the varying energy releases at under final failure. The resulting effective loss factors per test are plotted against their maximum stress in Figure 7.17, which also includes the pristine material DMA reference range as determined section 7.5. This figure shows how most interestingly, the effective loss factor vs maximum stress data at both $R = 0.1$ and $R = 0.3$ naturally collapse to what appears as a single linear trend, thus independent of the R-ratio.

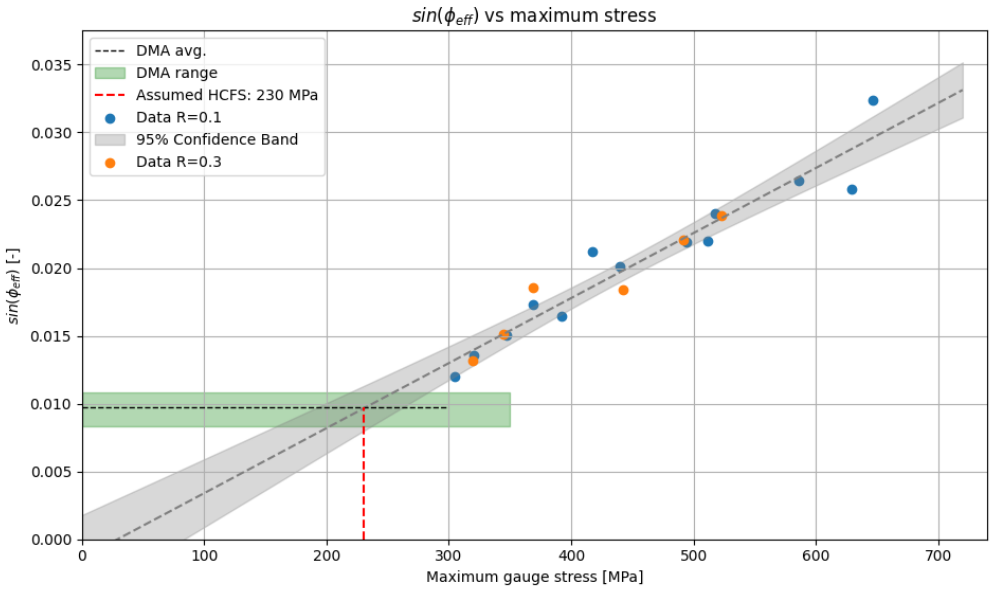

Figure 7.17: Effective loss factors $\sin(\phi_{eff})$ vs maximum cyclic gauge stress and their intersection with the DMA measured loss factors for HCFS estimation.

Consistent with the preliminary analysis of chapter 4, the intersection of the $\sin(\phi_{\text{eff}})$–σ_{max} trend with the DMA-derived loss factor provides an estimate of the high cycle fatigue strength (HCFS). For the current fatigue dataset and the average of the DMA measurements, this approach gives a HCFS of 230 ± 30 MPa, accounting for the width of the 95% confidence interval of the linear extrapolation.

To further examine the validity of this HCFS estimate, Figure 7.18 shows the energy dissipated in the first cycle of each test plotted against its maximum stress. For both R-ratios, the this data follows again a linear trend that intersect the pure DMA-based predicted dissipation curves at approximately 250 MPa. This suggests that around this 250 MPa maximum stress, the dissipation in the first fatigue cycle will start to diverge from what otherwise would be the continued predicted dissipation based on the DMA loss factor. This sudden increase in first-cycle dissipation aligns closely with DMA-based HCFS estimate and would be the confirmation of a dominant damage mechanism activating around the predicted HCFS stress level.

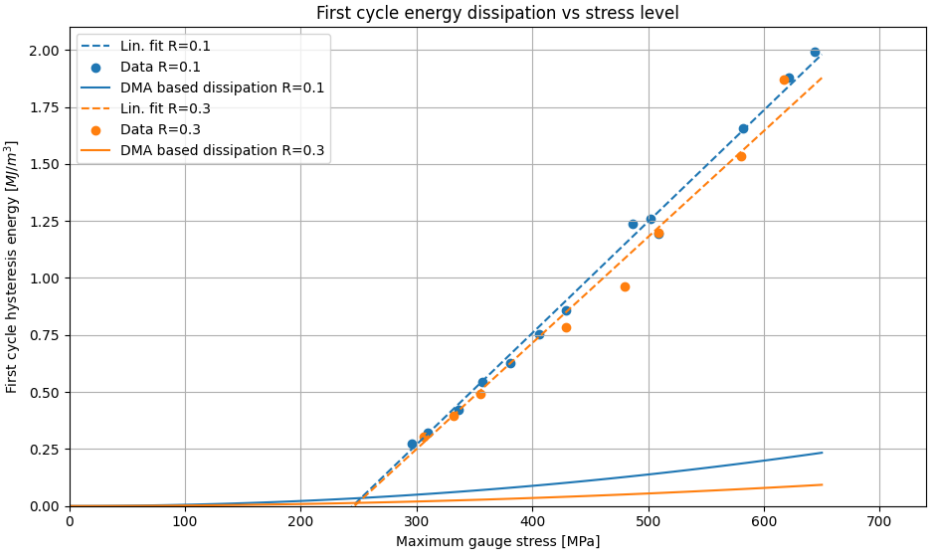

Figure 7.18: Energy dissipation of the first cycle in each fatigue test vs the maximum cyclic gauge stress.

Finally, Figure 7.19 combines the constant DMA reference with the linear $\sin(\phi_{\text{eff}})$–σ_{max} relation to predict the energy dissipation rate as a function of maximum stress for both R-ratios. Similarly to what was shown in section 4.5 of the preliminary analysis on the literature based $\pm 45°$ woven glass/epoxy fatigue dataset, such DMA and effective loss factor trend based dissipation rate plot aims to reconstruct the equivalent dual-linear thermography trend as well reported and accepted method for determining the HCFS. Here, Figure 7.19 shows that assuming linear heat conduction and convection, the measured infrared temperature changes ΔT are in good agreement with the predicted heating rate curves, further confirming the consistency and close relation of the current DMA and effective loss factor based HCFS estimation approach relative to the common infrared thermography method.

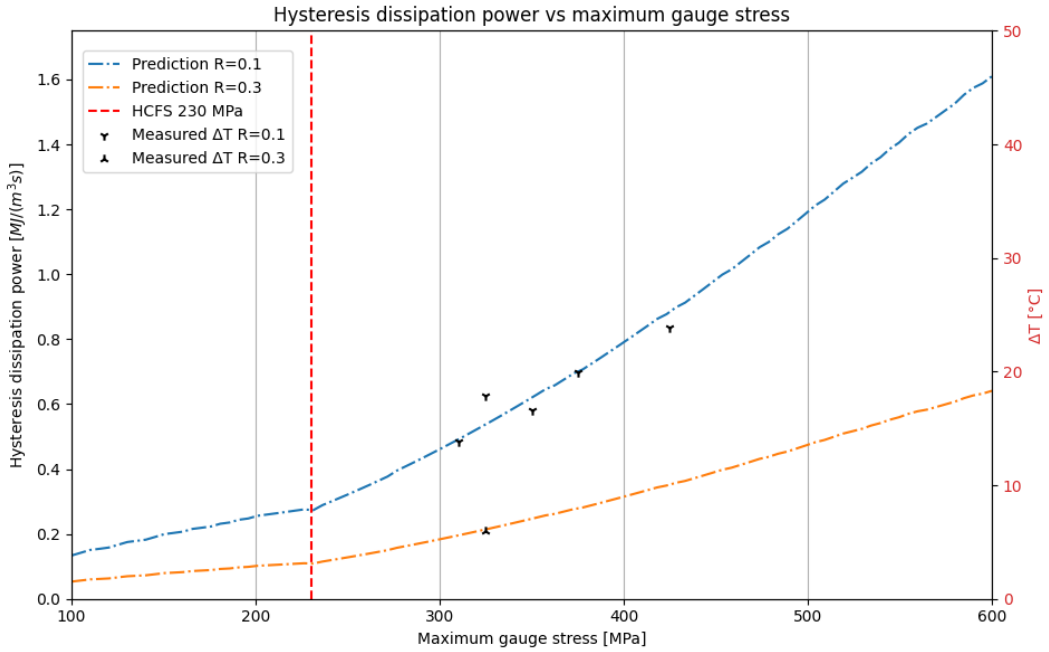

Figure 7.19: Comparison of DMA and $\sin(\phi_{eff})$ based dissipation rate prediction $\dot{W}_h$ and stabilised infrared temperature measurements.

7.7. Fatigue life predictions

In section 7.4, it was observed that the 95% confidence intervals of CDE vs σ_{max} log-linear trends of the $R = 0.1$ and $R = 0.3$ datasets largely overlapped, indicating a likely independent CDE–σ_{max} trend with respect to the R-ratio. Such a fixed relationship was also hypothesised in the literature study and subsequently used in chapter 3 as condition to formulate the modified linear viscoelastic loss factor based fatigue life prediction of Equation 3.46 in section 3.8.

$$N_{f_{R_2}} = N_{f_{R_1}} \cdot \frac{\left(\frac{1-R_1}{1+R_1}\right)^2}{\left(\frac{1-R_2}{1+R_2}\right)^2} \frac{(1-R_1^2)}{(1-R_2^2)} \frac{|E^*|_{avg,R_2}}{|E^*|_{avg,R_1}} \frac{\sin(\phi_{eff})_{R_1}}{\sin(\phi_{eff})_{R_2}} \tag{3.46}$$

As shown in subsection 7.2.2, the mean complex moduli of both R-ratio datasets differed by only 1.4% relative to the pristine high-rate tensile modulus. This therefore suggest that in the case of this fibre dominated cross-ply laminate under equivalent strain rates, it is fair to assume that:

$$\frac{|E^*|_{avg,R_2}}{|E^*|_{avg,R_1}} \approx 1$$

Furthermore, section 7.6 demonstrated that for this $[0/90]_{4s}$ UD E-glass/BT080-epoxy composite material at similar strain rates and consistent failure, the effective loss factor trends collapsed to a single $\sin(\phi_{eff})$–σ_{max} relation independent of R-ratio. Hence, from this it furthermore follows that:

$$\frac{\sin(\phi_{eff})_{R_1}}{\sin(\phi_{eff})_{R_2}} \approx 1$$

With these simplifications, Equation 3.46 reduces to Equation 7.1, which is a pure energy based R-ratio correction scaling factor to predict the cycles to failure at one R-ratio to the equivalent life at a different R-ratio for an equal cycle maximum stress.

$$N_{f_{R_2}} = N_{f_{R_1}} \cdot \frac{\left(\frac{1-R_1}{1+R_1}\right)^2}{\left(\frac{1-R_2}{1+R_2}\right)^2} \frac{(1-R_1^2)}{(1-R_2^2)} \tag{7.1}$$

To evaluate this, Figure 7.20 below gives the power-law trends between the critical dissipated energy CDE and the cycles to failure N_f for both measured R-ratio datasets. As seen in this figure, these two trends appear as close parallels.

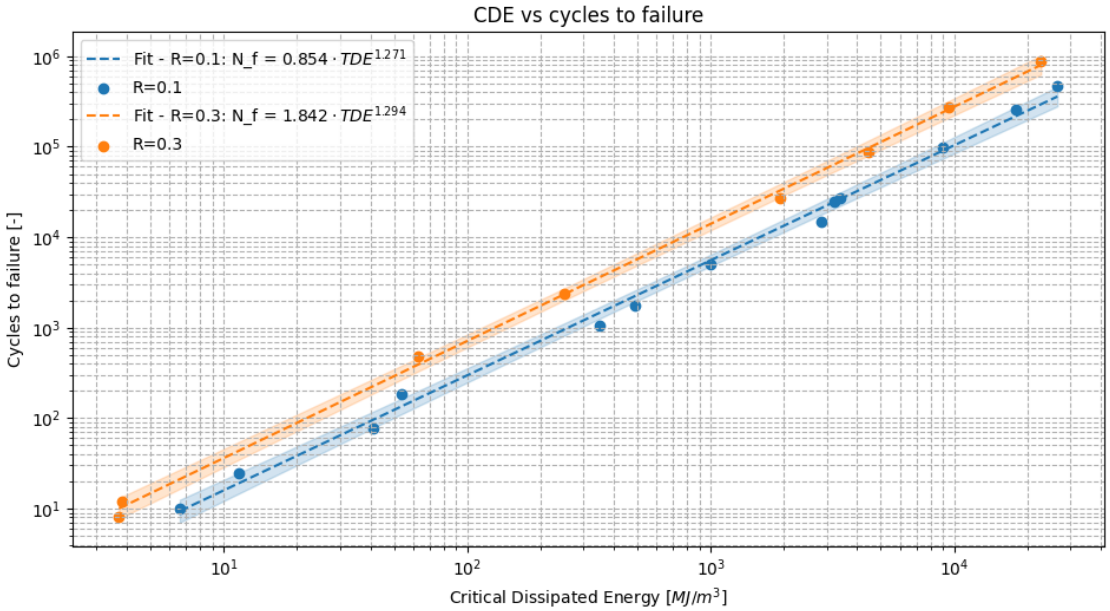

Figure 7.20: Critical dissipated energy (CDE) vs cycles to failure (N_f) for the $R = 0.1$ and $R = 0.3$ fatigue datasets.

Then, Equation 7.1 was used to normalises both datasets to an equivalent $R = -1$ load case. As shown in Figure 7.21, the otherwise distinct CDE vs N_f trends then collapse onto a single 'master' power-law curve, further supporting the proposed energy-based R-ratio scaling.

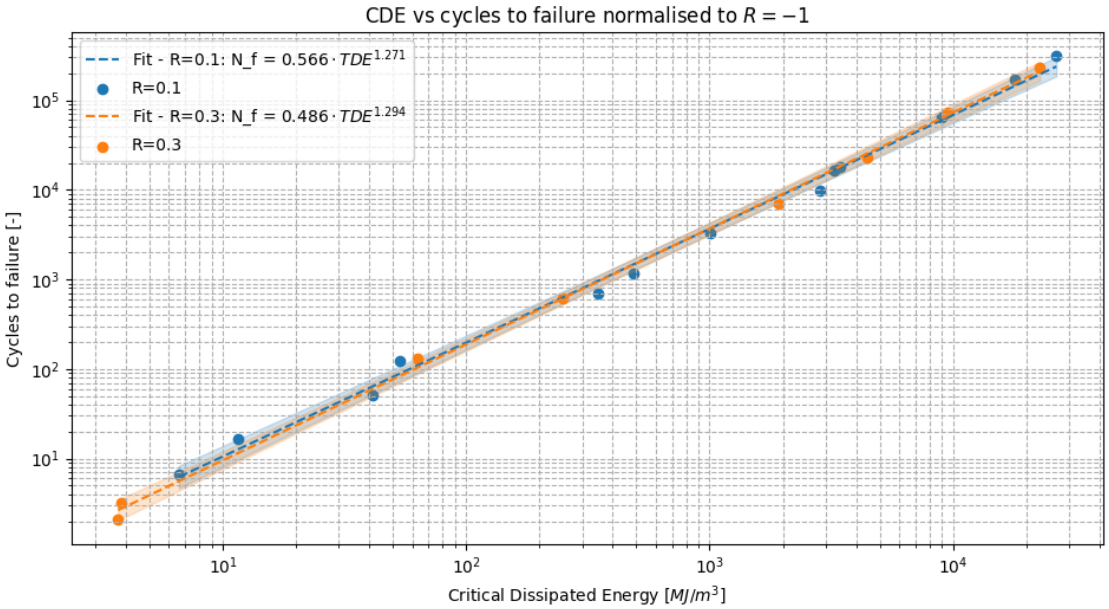

Figure 7.21: R-ratio normalised critical dissipated energy (CDE) vs cycles to failure (N_f) for the $R = 0.1$ and $R = 0.3$ fatigue datasets.

This collapsed trend of Figure 7.21 gave confidence in the fatigue life scaling of Equation 7.1 and was therefore used to generate Figure 7.22, showing the predicted S_a–N curves. Here, the $R = 0.1$ dataset was used as model input (using its $|E^*_{avg}|$, CDE–σ_{max}, and $\sin(\phi_{eff})$ trends) and predictions were made for the alternative stress ratios of $R = 0, R = 0.3$ and $R = 0.5$.

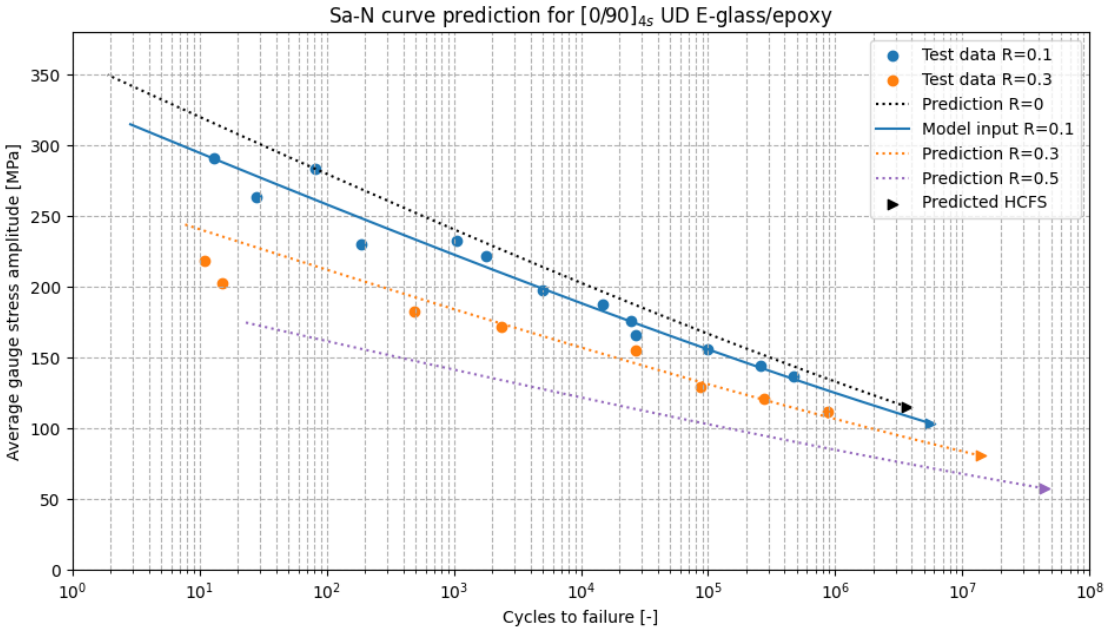

Figure 7.22: Predicted stress amplitude vs fatigue life ($S_a - N$) curves using the $R = 0.1$ dataset as model input and $R = 0.3$ as validation data.

These predictions based on solely the $R = 0.1$ data was validated against the tested $R = 0.3$ dataset, which gave a root-mean-square error (RMSE) of 0.51 decades over the full tested fatigue life range. However, when excluding the two very high-stress points with $N_f \leq 15$ cycles, the prediction error is reduced significantly to an RMSE of 0.22 decades. Within this low- to high-cycle fatigue life range, the predictions therefore fall within a reasonable factor of 1.6 of the actual measured cycles to failure. This further highlights the predictive capability of the current modified linear viscoelastic framework based on only a limited input dataset. Furthermore, the triangular markers in Figure 7.22 indicate the stress amplitudes at which the DMA-based HCFS estimated of the previous section is reached. Below this corresponding stress amplitude, the S_a–N curve is expected to gradually flatten towards infinite life.

8

Discussion

The aim of this chapter is to further interpret and discuss the meaning of the experimental findings, as well as the implications and limitations of the performed work. This chapter is structured with a focus towards being able to provide clear final answers to the main research question and its sub-components in the upcoming conclusions of chapter 9. The discussion in this chapter will therefore follow roughly the order of the research sub-questions, each addressing a particular aspect of the performed analysis and results by the current modified viscoelastic energy-based framework for composite fatigue.

8.1. Evaluation of changing loss factors throughout fatigue life

In the preliminary $\pm 45^{\circ}$ woven glass/epoxy fatigue dataset by Movahedi-Rad et al. [15], the derived loss factor values in the first cycles were observed to start close to the assumed pristine DMA reference value based on measurements on similar material by Karvanis et al. [68]. This suggested that in the first few cycles of each test, damage in the laminate in the form of matrix cracks and fibre-matrix disbonds remained limited and was seen as supporting evidence of the considered R-ratio energy correction and its ability to relate fatigue-based loss factor terms to those alternatively measured through DMA.

During the further progression of the initiation phase however, the loss factor for all tests rose sharply. This behaviour reflected a faster degradation of the laminate complex modulus compared to the dissipation related loss modulus. At the lower cyclic maximum stress, the loss factor then stabilised at a nearly constant level for the majority of the remaining fatigue life. From a damping perspective, this suggests that an equilibrium had been reached between the continuing reduction of complex modulus and a proportional reduction in the viscous loss modulus as the matrix also carried and dissipated a smaller overall portion of the applied strain energy. So, despite slowly increasing damage in the laminate under these lower stress levels, the viscoelastic loss factor would not increase much throughout this stabilised phase.

At higher stresses however, this stabilisation gave way to a continuous increase in loss factor throughout life, presumably driven by the ever growing frictional contributions offsetting the above mentioned balance as also identified as one of the primary damping mechanisms in the literature study review of work by Chandra et al. [13] and Tang et al. [24]. This then manifested in the measurements of continuously rising loss moduli despite the ongoing decline of the complex modulus. As the viscoelastic loss factor is defined as the ratio between these moduli, this explains the observed overall progressive loss factor growth.

The subsequent tested $0/90$ dataset showed both a contrast and agreement with this behaviour. In these tests, the first cycle began with a high dissipation and consequent large loss factor, reflecting the immediate initiation of damage in the 90° plies and its growth towards the 0-90 ply interfaces. This is believed to be the cause of the large and sudden corresponding release of strain energy within the first few cycles. Over the next 10-20% of the fatigue lives, the loss factor in all tests dropped sharply, after which it either similarly stabilised at low stresses or continued following a steady growth at higher stresses. Such stabilisation of the loss factor for most of the fatigue life at low stresses again signified a balance between the degradation rates of loss and complex moduli as well as friction contributions in the laminate.

A further trend was observed when comparing $R = 0.1$ and $R = 0.3$ in the $0/90$ laminate dataset. Despite differences in initiation and early propagation stages, the loss factors at similar maximum stress levels for these two distinct stress ratios tended to converge in the second half of their fatigue life. At $R = 0.1$ the recovery from the initiation phase occurred more rapidly, whereas at $R = 0.3$ this was slower. Ultimately however, both conditions approached similar loss factor levels. This suggests that while initiation is sensitive to R–ratio, the subsequent damage evolution and saturation would be governed primarily by the maximum stress. This then drives the accumulated loss of laminate stiffness and rise in internal friction and is reflected in the long-term damping response identified by the loss factor.

As hypothesised in the literature study, the evaluation of the loss factor throughout fatigue life thus provides an arguably more descriptive representation of damage evolution than considering stiffness degradation or dissipated energy in isolation. Here, the loss factor measurements derived from the currently proposed modified linear viscoelastic theory directly reflected the combined effects of complex modulus degradation, viscous loss modulus changes and friction-driven damping. As highlighted in the preliminary analysis, this made the loss factor trends more distinctive and conclusive compared to the raw stiffness or dissipation data alone. Moreover, with the proposed R-ratio correction, the loss factor formulation also enables direct comparison of fatigue damage progression across different stress ratios. Because applied and dissipated energies are inherently offset at varying R-ratios, such comparisons would otherwise be obscured.

8.2. Effective loss factor, DMA correlation and HCFS estimates

This section discusses the broader implications of the effective loss factor results, with particular focus on their relation to DMA measurements, high cycle fatigue strength estimates and established thermography methods. For clarity, this discussion is structured into several sub-topics.

8.2.1. Observed effective loss factor trend and R-ratio collapse

The effective loss factors, defined as the energy–weighted averages of the per-cycle loss factor values over the fatigue life, were found to exhibit a strong near-linear dependence on the cyclic maximum stress for both reference $\pm 45^\circ$ and experimental $0/90$ laminate datasets. A particularly notable result for the $0/90$ laminate fatigue experiments was that the $\sin(\phi_{eff})$ vs σ_{max} data points collapsed onto a single linear trend shared between both $R = 0.1$ and $R = 0.3$ tests. This would further indicate that the effective loss factor in the fatigue life of such fibre dominated laminate is governed primarily by the maximum stress, the associated damage mechanisms and its corresponding levels of caused internal friction, rather than by pure R–ratio based input energy effects. Such observation would be in line with the previous discussion of section 8.1 on the progression of the per-cycle loss factor, where also there this characteristic damping parameter was shown to remain closely matched between the R-ratios for a large portion of the fatigue lives.

Such linear relation may be related to observations by Broughton et al. [95], who performed both monotonic tensile and fatigue tests on UD-based $0/90$ cross-ply glass/epoxy laminates. They evaluated the damage density with both optical and acoustic measurement methods and in their results showed a mostly linear trend between applied stress and measured density. This would be consistent with the current observation on the linear trends of effective loss factor with the cyclic maximum stress, with the reasoning that a dominant factor controlling such trend is the amount of internal friction in the laminate cased by a particular type and density of fatigue damage.

However, it remained of particular interest how both the reference $\pm 45^\circ$ and experimentally tested $0/90$ laminates revealed an apparently similar near-linear stress–dependent trend of the effective loss factor, despite relying on different underlying damage mechanisms. In the $0/90$ laminate, the near-constant average complex modulus between tests implied that the effective trend was almost entirely driven by the increase of the weighed average loss modulus with maximum stress. In contrast, for the $\pm 45^\circ$ laminate both distinct variances in complex and loss moduli were observed across tests, yet still an overall similar $\sin(\phi_{eff})$ behaviour was found. However, based on the current results and no alternative R-ratios for the $\pm 45^\circ$ data having been available, the observed R-ratio independence of the $\sin(\phi_{eff})$–σ_{max} measurements on the $0/90$ laminate cannot yet be universally extended to other more matrix-dominated laminates. Here it remains unknown how the R-ratio impacts the relative change of both average loss and complex moduli, whose ratio ultimately make up the loss factor.

8.2.2. Relation to DMA measurements and HCFS estimate

As discussed in subsection 2.6.2 of the literature study, authors such as La Rosa and Risitano [64], Montesano et al. [65] and Colombo et al. [67] have all related the high cycle fatigue strength in fibre-reinforced polymer composites to the stress level at which a pronounced infliction point shows in the slope of the infrared thermography measured average or stabilised temperatures. Beyond this stress level, the energy dissipation rates were shown to rapidly increase, resulting from the onset of a significant rise in internal damping. This in turn produces the classical dual-linear thermography plots. The inflection point between the two distinct dissipation regimes was then associated with the initiation of a critical damage mechanism or critical damage density, which from that stress level onward would dominate the intermediate to high cycle fatigue life [65]–[67].

Below such HCFS however, Han et al. [8] suggested that the dissipation behaviour is dominated by purely the viscoelastic characteristics of the material itself. At the end of the literature study, it was therefore hypothesised that within the context of a consistent linear viscoelastic loss factor definition, dynamic mechanical analysis measurements on pristine material samples (representing the pure viscoelastic dissipation) could be compared to equivalent measurements in fatigue. The high cycle fatigue strength would then correspond to the point of divergence of the fatigue data from this DMA reference. This hypothesis was first based on the total dissipation ratio (TDE/TW), but throughout the theory developed in chapter 3 and the preliminary analysis of chapter 4, it became clear that the newly established effective loss factor trend with stress posed a more suitable metric to identify this HCFS diversion point.

Applied to the reference $\pm 45^{\circ}$ dataset by Movahedi-Rad et al. [15] and using the DMA loss factor estimate derived from the tests by Karvanis et al. [68], this new method resulted in a high cycle fatigue strength estimate between 43 and 45 MPa, corresponding to a fatigue life between 10^6 and 10^7 cycles. Although exact comparisons to alternative tests in literature remain difficult due to differences in material, loading conditions and environmental factors, the estimated HCFS on this dataset aligned reasonably well with similar woven $\pm 45^{\circ}$ glass/epoxy fatigue data reported in literature, such as the endurance limit of 45-50 MPa by Liang et al. [71] and the HCFS estimate of 37 MPa by Colombo et al. [67] using the thermography method.

For the experimental $0/90$ datasets tested in this thesis, the average loss factor obtained from DMA tests on the pristine material intersected the effective loss factor curves measured in fatigue at a maximum stress level of 230 ± 30 MPa, with the ± 30 MPa margin accounting for the width of the 95% confidence interval of the linear extrapolation. For the $R = 0.1$ and $R = 0.3$ tests, this resulted in estimated fatigue life run-outs beyond $3.8 \cdot 10^6$ and $3.6 \cdot 10^7$ cycles respectively. Like the HCFS estimate on the reference $\pm 45^{\circ}$ dataset, these cycles to failure ranges match the general $10^6 - 10^7$ fatigue limits typically assumed in literature as described by Montesano et al. [65].

Furthermore, when comparing again to fatigue measurements by Broughton et al. [95], their S-N curve on $0/90$ glass/epoxy cross-ply at $R = 0.1$ suggested a $10^6 - 10^7$ cycle endurance limit between around 30 to 40 percent of the materials ultimate strength at a fatigue-equivalent loading rate. For the material tested in this thesis with an average high-rate strength of 712 MPa, this would equate to an endurance limit estimate between 214 and 285 MPa, which matches the current predicted HCFS of 230 ± 30 MPa reasonably well. Nevertheless, such comparisons must be treated critically due to inevitable variances in material, fibre volume fraction and loading conditions, as well as dogbone geometry differences between Broughton et al. and this current work. Therefore, the most direct confirmation of the HCFS prediction on the $0/90$ material tested for this thesis comes from the matching sudden increase of first cycle strain energy dissipation at around 250 MPa maximum stress, as was shown in Figure 7.18 of chapter 7. This indicated that indeed around the DMA and effectively loss factor based inflection point, a critical damage mechanism activates that already shows its direct effect in the damage formation in the first cycle. Together, these agreements and references to literature lend confidence to the applicability of the energy–based correction factors introduced into the viscoelastic framework as well as the framework's ability to predict a high cycle fatigue strength based on measurable and physical material damping principles.

As both the $\pm 45^\circ$ and $0/90$ laminates produced justifiable HCFS estimates through this approach, it demonstrates the robustness of the method across substantially different laminate configurations, dominant damage mechanisms and levels of matrix dependence. The results therefore suggest that the direct comparison of fatigue-derived effective loss factors with pristine DMA reference values, as enabled by the current modified viscoelastic analysis framework, is a valuable and within current knowledge generally applicable method. The particular strength of the proposed HCFS determination lies in its inherent observed linearities, which allow the construction of the dual-domain trend with only limited fatigue data.

8.2.3. Post-HCFS damping divergence and acting damage mechanisms

According to Bensadoun et al. [96], fatigue failure of $0/90$ UD cross-ply laminates is not driven by transverse cracks in the 90° plies alone, but ultimately by delaminations formed between the 90° and 0° layers. As also discussed in the literature study, Talreja et al. [22] described the cross-ply damage progression as starting with fibre–matrix debonding and transverse cracking in the 90° plies, which then accumulate until they reach a critical length or density. At that stage, cracks propagate to the ply interfaces and initiate delaminations. Reduced load transfer between plies then promotes fibre–matrix debonding and fibre breakage in the main load-carrying 0° plies.

The current results are consistent with such a “delayed” onset of the critical failure mechanism. The finite element analysis of the selected specimen dogbone geometry in chapter 5 suggested that the first damage in the 90° plies would initiate at around 107 MPa maximum stress. However, neither the DMA-based HCFS estimate nor the first-cycle dissipation divergence indicated a significant change in damping behaviour at this lower stress level. A likely explanation is that such early transverse matrix cracks open and close in the loading direction without generating any slip and thus have a minimal effect on internal friction. Their contribution to damping therefore remains small, with the degradation of complex modulus and viscous loss modulus occurring in a relatively balanced fashion as discussed for the low stress loss factor stabilisation in section 8.1. Therefore, the overall loss factor is not substantially altered by these transverse cracks, at least not beyond the variance in the DMA measurements themselves.

By contrast, when delaminations or 0° ply fibre–matrix debonds form at higher cyclic stresses, presumably around the identified 230 MPa HCFS, slip occurs between surfaces along the loading direction. This frictional energy dissipation then disrupts the balance between loss modulus and complex modulus. This is believed to be the main mechanism behind the observed divergence of the fatigue loss factor from the DMA baseline at the HCFS, marking the activation of the critical failure mechanism that ultimately governs the intermediate to high cycle fatigue life.

8.2.4. Similarities and improvements compared to infrared thermography

Within the current framework, the effective loss factor measured during fatigue tests could be directly related to the average hysteresis energy dissipated per cycle. Combined with the known cyclic frequency, this enabled a straightforward calculation of the average energy dissipation rate. Under the assumption of linear heat conduction and convection, such $\sin(\phi_{eff})$–σ_{max} derived dissipation rates allowed direct comparison to infrared temperature trends and thermography method results reported in literature.

These generated dissipation rate plots exhibited the same characteristic behaviour as typical for infrared thermography, with a distinct dual-linear trend and an inflection point at the estimated HCFS. Consistent with the reasoning of Han et al. [8], the initial slope represents a regime dominated by viscoelastic damping and was fully captured here by the DMA measurements on the pristine material. At higher stresses, the transition to a steeper slope reflects the activation of damage-induced frictional mechanisms, consistent with thermography literature and the previous sections of this discussion.

For the experimental $0/90$ dataset, the predicted dissipation rate trend shown in Figure 7.19 also aligned well with the few stabilised infrared temperature measurements taken during tests. This strengthens the interpretation that the effective loss factor trend with maximum cyclic stress represents the underlying change in damping characteristics that ultimately dictates thermal dissipation and thus governs thermography-based observations. Here, the current $\sin(\phi_{eff})$–σ_{max} description is considered to provide the physical basis for the infrared thermography method. Whereas thermography implies changes

in damping characteristics indirectly from temperature measurements, the current method quantifies it in a more direct manner as a change in the effective viscoelastic loss factor. In this way, the modified linear viscoelastic framework thus complements this established approach by grounding it in a measurable and physically interpretable changing material property.

8.3. Application of TDE and CDE and their dependence on R-ratio

This section discusses the role of accumulated energy dissipation measures in the current fatigue results, with focus on the distinction between total dissipated energy (TDE), critical dissipated energy (CDE) and their observed dependence on the stress ratio. The discussion then considers how these measures can be applied for fatigue life prediction.

8.3.1. Total vs critical dissipated energies

The total dissipated energy was originally interpreted as the sum of all strain energy dissipated during a fatigue test and considered in the literature study as a potential energy-based fatigue failure criterion. This was supported in the work of Movahedi-Rad et al. [41], [57], [60], who proposed that the power-law relation between accumulated hysteresis energy to failure and maximum cyclic stress follows a fixed trend, independent of R-ratio. However, direct experimental evidence for this assumption has remained scarce, both in the work of these authors and more generally in the composite fatigue literature.

In this thesis, both the $\pm 45^\circ$ woven glass/epoxy preliminary reference data as well as the tested $0/90$ UD glass/epoxy cross ply were shown to follow a negative log-linear trend of TDE with the cyclic maximum stress. Meaning that at low stresses, exponentially more total energy is dissipated. However, the experimental results also demonstrated that an alternative accumulated energy measurement, the critical dissipated energy defined as the hysteresis energy accumulated up to the onset of final failure, provides a more consistent energy-based failure criterion for the fibre-dominated $0/90$ cross-ply laminate. This alternative definition separates the accumulation of cyclic hysteresis energy during fatigue life from the variable final strain energy release associated with the final failure mechanisms. Here, at increasing maximum cyclic stresses, more explosive final failures were observed with increased amounts of delamination in the last few cycles. The associated energy dissipated within these final cycles therefore skews the TDE comparison across fatigue stress levels and R-ratios.

Although improved, particularly at the higher stresses, some scatter remains in the CDE-σ_{max} data due to material, loading and external variances. However, the 95% confidence intervals of the log-linear fits for the $R = 0.1$ and $R = 0.3$ tests were found to overlap over a wide fatigue life range of 10^2–10^6 cycles. For the tested fibre-dominated laminate, this supports the concept of a fixed dissipation-based fatigue criterion as proposed by Movahedi-Rad et al., but with the refinement of considering CDE up to final failure initiation rather than the TDE.

Within the broader energy dissipation framework, such CDE criterion combined with the energy-weighted effective loss factor trend and its DMA-based HCFS intersection provides a rounded, physically based foundation for fatigue analysis. The ability of this framework to perform fatigue life predictions will be further discussed in subsection 8.3.2.

8.3.2. Ability to perform fatigue life predictions

The predictive capability of the modified viscoelastic framework relies on the validity of the CDE–σ_{max} relation being approximately independent of R-ratio. This assumption, justified in subsection 8.3.1, allowed the S–N curve at a reference stress ratio to be scaled to another using the method introduced in section 3.8. This method consisted of scaling the observed fatigue lives using the ratios of energy-based correction factors, cyclic to maximum strain energies, average laminate stiffnesses over the fatigue life and finally that of the effective loss factors.

For the tested fibre-dominated $0/90$ cross-ply, these scaling relations simplified considerably. The average complex modulus was found to be essentially constant across stress levels and insensitive to the stress ratio, with only a 1.4% variance relative to monotonic results. Similarly, as discussed in subsection 8.2.1, the effective loss factor trends for $R = 0.1$ and $R = 0.3$ collapsed onto a single curve. Together, these observations justified the assumptions $\frac{|E^*|_{avg,R_2}}{|E^*|_{avg,R_1}} \approx 1$ and $\frac{\sin(\phi_{eff})_{R_1}}{\sin(\phi_{eff})_{R_2}} \approx 1$, reducing the fatigue life scaling to a pure R-ratio term.

A strong power-law relation was observed between CDE and N_f. For the two tested stress ratios, these curves ran in parallel and were separated by a constant scaling, which matched that predicted by the reduced fatigue life scaling term as described above. This simplified R-ratio term therefore enabled both distinct CDE and N_f datasets to collapse onto a single representative $R = -1$ equivalent curve. This provided direct evidence of the predictive capability of the framework when stiffness and effective loss factor ratios remain constant or can be estimated reliably.

Predictions made using only the $R = 0.1$ dataset as input reproduced the measured $R = 0.3$ results with a root-mean-square error of 0.22 decades between 10^2 and 10^6 cycles. This corresponds to a deviation within a factor of about 1.6 of the actual fatigue lives, which is a reasonable level of accuracy given the typical scatter in composite fatigue experiments and limited quantity of fatigue tests performed. Together with the DMA-based HCFS estimate, this highlights the ability of the method presented in this thesis to provide fatigue life predictions from a limited input dataset.

At the same time, the applicability of the simplifications to Equation 3.46 is likely limited to fibre-dominated laminates. In more matrix-dominated materials, such as the preliminary $\pm 45°$ dataset, the terms $\frac{|E^*|_{avg,R_2}}{|E^*|_{avg,R_1}}$ and $\frac{\sin(\phi_{eff})_{R_1}}{\sin(\phi_{eff})_{R_2}}$ are expected to vary more distinctly with the maximum stress and particularly with R-ratio. In these cases, the general predictive relation of Equation 3.46 should still hold on physical grounds, but additional functions would be needed to capture this stress ratio dependence of both $|E^*|_{avg}$ and $\sin(\phi_{eff})$ before the method can be applied to reliably predict the behaviour at untested stress ratios.

8.4. TDE/TW-ratio and its hypothesised two-domain trend

The initial hypothesis of a fixed total dissipated energy over total work ratio (TDE/TW) by Alderliesten and Movahedi-Rad [10] as a potential characteristic property of fibre-reinforced composites was a driving factor for the start of this thesis work. However, the literature study already indicated that there is sufficient evidence to suggest that such a total dissipation ratio is not a material constant and instead depends on both the applied maximum stress and the stress ratio. This was linked to changing viscoelastic material characteristics, from which the thesis objective followed to adapt linear viscoelastic theory to consistently define such energy dissipation and dissipation ratio terms as functions of the underlying viscoelastic damping properties.

Using the modified linear viscoelastic analysis approach that followed, the TDE/TW-ratio was shown in chapter 3 to be expressed as a direct function of the newly established effective loss factor and R-ratio energy scaling terms. This implies that the TDE/TW-ratio mirrors the two-domain behaviour of $\sin(\phi)_{eff}$ vs. σ_{max} as already covered in detail in subsection 8.2.1. Below the identified HCFS, hysteresis dissipation is thus believed to be governed by the viscoelasticity of the pristine material, where the TDE/TW-ratio remains approximately constant. Above the HCFS however, damage-induced frictional mechanisms dominate, leading to the TDE/TW-ratio following the linear increase of $\sin(\phi_{eff})$ with σ_{max}. This confirms the later revised hypothesised two-domain trend but also clarifies that the ratio is not universally constant.

The original constant hypothesis therefore only retain partial validity in the very high-cycle regime below HCFS at assumed constant viscoelastic damping, although even there TDE/TW remains directly dependent on stress ratio. At higher R-ratios, the TDE/TW-ratio was shown to be lower, meaning that a smaller portion of the total applied work is lost as dissipated energy. This behaviour is consistent with the typically longer fatigue lifetimes observed for higher R-ratios.

Finally, in line with the earlier discussion of TDE vs. CDE, a more meaningful expression for fibre-dominated laminates is given by the ratio of critical dissipated energy to critical work (CDE/CW). By excluding the variable energy release of final fracture, this definition better reflects the cumulative dissipation associated with damage progression up to the onset of final failure and provides a more consistent basis for fatigue analysis.

8.5. Fatigue failure strains

The relationship between maximum cyclic stress and failure strain revealed clear linear trends for both $R = 0.1$ and $R = 0.3$ in the experimental $0/90$ fatigue data. Failure strains at $R = 0.3$ were systematically lower than those at $R = 0.1$. However, when normalised by $(1 - R^2)$ the σ_{max}–ϵ_f data from both stress ratios collapsed onto a single linear relation representative of an equivalent $R = 0$ load case. This collapsed trend aligned with the monotonic tensile strength and strain-to-failure values measured at comparable loading rates. Notably, even the low-rate monotonic tensile test at 5 mm/min fell at the edge of the 95% confidence intervals of this collapsed data.

These observations indicate that the fatigue failure strain in the tested laminate depends linearly on the cycle maximum stress and also scales with the factor $(1 - R^2)$. This term, originating from the definition of applied energy in chapter 3, reflects the ratio of the work done per cycle to the maximum strain energy potential at peak load. For any reasonable stress ratio of interest, the corresponding fatigue failure strain could then be estimated by scaling with the $(1 - R^2)$ energy ratio. When combined with effective loss factor trends and DMA-based HCFS estimates, this approach would further reduce reliance on extensive fatigue testing and provide a basis for quick failure strain engineering estimates.

At the same time, these findings must be contextualised within the specific experimental conditions. The material, specimen geometry, and strain rate were deliberately selected to produce a consistent material strength, damage type and damage location, which likely contributed to the clarity of the observed trends. In laminates or geometries prone to multiple failure mechanisms, the collapse and linearities observed failure strains may not hold. This highlights both the importance of strain rate control and the careful design of specimen geometry to expose such underlying behaviour that might otherwise be left uncovered by strength and failure mode variances.

8.6. Limitations of the current work

The findings of this thesis provide a consistent proof of concept for the modified linear viscoelastic approach. However, a number of limitations of the current work limit these current results from broader generalisation. These limitations concern theoretical and experimental assumptions, as well as pointing towards areas where further testing and validation will be required.

8.6.1. Experimental validation of HCFS

Direct experimental validation of the high cycle fatigue strength was not achieved. The performed fatigue tests were limited to a maximum length of about 10^6 cycles due to constraints in duration of the experimental phase of this thesis as well as consecutive machine availability. If aimed to directly perform fatigue tests to failure at stresses down to and below the predicted HCFS, this would have required individual tests at week-long durations. This limitation is common in the literature, where few studies report in detail the very high cycle fatigue life of specimen. Hence the active efforts in composite fatigue research to establish alternative means of predicting the high cycle fatigue behaviour of the materials, such as the aim of this study.

The HCFS estimates in this thesis should therefore be regarded as indirect, derived from DMA reference loss factor measurements. Nevertheless, these estimates were grounded in multiple lines of evidence. Together, these still lend confidence in the HCFS evaluation method proposed in this thesis, despite the absence of direct experimental validation.

8.6.2. Creep effects

This thesis assumed that for continuous fibre-dominated composite laminates, pure cyclic hysteresis strain and creep strain build-up could be treated as independent. This implied that creep would not occur within a cycle, but could be seen as separate effect between cycles. This allowed for the direct application of the complex modulus based linear viscoelastic theory on the now closed stress-strain hysteresis loops, which formed the basis of the method proposed in this thesis.

For the chosen fibre-dominated cross-ply thermoset composite this was a reasonable approximation, since creep sensitivity was low and no significant creep strain accumulation was observed. However, this assumption may not hold for more creep-prone matrix-dominated composite laminates. In such cases, additional terms describing creep-sensitive energy dissipation would need to be incorporated.

8.6.3. Temperature sensitivity

Temperature effects were consciously minimised by using a fibre-dominated laminate and a reasonably high glass transition temperature epoxy matrix system, post cured for a maximum T_g. The DMA experiments on this material confirmed that stiffness and loss factor values remained largely insensitive to temperature up to about 80°C, which justified neglecting thermal corrections in this study. For more temperature-sensitive materials however, explicit compensation for hysteresis heating generated temperatures would likely be required, or alternatively a form of active specimen cooling to keep the viscoelastic characteristics of the material controlled. Thus, while thermal effects were not a concern in this particular study, the general applicability of the method further depends on material temperature sensitivity and on how reliably such effects can be characterised or compensated for.

8.6.4. Negative R-ratios

The scope of this thesis was deliberately limited to the tensile–tensile fatigue regime. Nevertheless, the formulation of the R-ratio correction terms in chapter 3 also produced expressions for $-1 \leq R < 0$. These have not been experimentally evaluated in the present work. The fundamental aim of these correction terms was to modify the viscoelastic dissipation description in such a way as to create a physically consistent definition of the loss factor, regardless of the applied R-ratio in fatigue tests. In practice, all corrections were defined relative to the assumed theoretically correct linear viscoelastic case of a fully reversed cycle at $R = -1$, given the direct application in literature to mostly vibrational damping. As a result, all fatigue-derived loss factor values in this thesis are effectively projected to an equivalent $R = -1$ load cycle.

This projection proved valuable for the tensile–tensile fatigue analysis, enabling clear comparisons across stress levels and stress ratios. Moreover, DMA tests performed at $R = -1$ were found to agree well with positive R-ratio bending DMA results once corrected with the proposed terms, suggesting that compressive and tensile viscoelastic dissipation remain broadly similar under the small strains of the linear viscoelastic regime ($\epsilon < 0.1\%$). However, direct application of the method to fatigue tests at $R < 0$ remains unproven and must be treated with caution. In practice, compressive fatigue introduces mechanisms such as microbuckling that are absent in tension–tension loading, leading to different damage progression and frictional damping behaviour. It is therefore uncertain whether experimentally measured $R = -1$ fatigue data would align with the projected values from positive R-ratios. This limitation applies both to the absolute loss factor values and to the $R = -1$ 'collapsed' trends observed for CDE vs N_f. While the framework provides a mathematical description to project fatigue data to $R = -1$, its physical equivalence to compressive fatigue loading remains to be demonstrated.

8.6.5. DMA testing mode

Dynamic mechanical analysers are inherently sensitive and low-load instruments, capable of applying only small forces to a specimen. For stiff materials such as fibre-reinforced polymer composites, these load limits prevent the ability to perform direct tensile DMA tests. As a result, DMA measurements on these materials are restricted to bending modes, such as the three-point or dual-cantilever bending configurations used for this thesis. As long as one stays within the linear viscoelastic regime of the material, the effects of the non-constant stress-strain through the thickness remain small and accountable.

However, DMA testing in bending does mean that for a multi-direction composite laminate, the layers further away from the neutral axis contribute to the stiffness and loss factor measurements disproportionally compared to a uniform tensile case. To avoid this, separate DMA tests were performed on unidirectional 0° and 90° specimen, of which the results were later combined to estimate the pristine loss factor of the full cross-ply laminate. While this approach was reasonable for the current $[0/90]_{4s}$ configuration, it does neglect interlaminar shear and friction damping effects between the layers. These are believed to become increasingly important in composite layups containing numerous off-axis plies.

This known limitation was one of the reasons for selecting a relatively simple $0/90$ cross-ply as the experimental focus. For more complex laminates, such as triaxial or quasi-isotropic, the current bending mode DMA approach may not provide accurate enough pristine loss factor estimates if interlaminar damping effects do play a significant role. Therefore, to extend the the broader applicability of the HCFS prediction method of this thesis, further development of tensile-based DMA testing methods for composites would be highly beneficial.

8.6.6. Specimen geometry and loading rate effects

The dogbone geometry used in this thesis was designed to promote consistent, centralised failure and thereby limit scatter between tests. This choice was critical for ensuring that the loss factor measurements at varying stress levels and R-ratios were directly comparable and could be linked to an overall consistent critical damage mechanism, such that the direct effects of these changes in cyclic maximum stress and R-ratio could be isolated as best as possible. If multiple competing failure mechanisms were active, the observed loss factor trends would likely have been less distinct. This underlines the importance of geometry selection in fatigue studies. In addition to this, fibre-reinforced polymer composite strength and viscoelastic response are known to be sensitive to strain rate, as discussed extensively in the literature study. The strain rate and testing frequencies in this thesis' experimental work were furthermore deliberately chosen to remain as consistent as possible.

Therefore, this dependence on the exact specimen geometry and strain rate combination means that the reported S-N curves, HCFS estimates and failure strain values cannot be regarded as universal fatigue response of the material nor are they directly transferable to alternative geometries or general engineering applications. This does however remain a more general problem typically faced in composite fatigue analysis.

8.6.7. DIC strain measurement approach

Stress–strain loops in this thesis were reconstructed by combining global force–displacement signals with local strain measurements obtained through high-speed DIC. This approach captured the local cyclic strains accurately and ensured synchronisation of the stress-strain data by re-scaling of the displacement based average strain. However, this does mean that the phase lag between the stress and corrected strain signals remained governed by the global force-displacement measurement. Therefore, the viscoelastic phase lag could not be fully localised and the less-damaged regions outside of the DIC zone will have slightly effected the derived hysteresis dissipation values.

However, infrared thermal imaging confirmed that both heat generation and damage were strongly localised within the DIC measurement region. This suggests that any averaging of the phase lag over the specimen remained limited. Most importantly, the same DIC-based method was applied consistently across all tests, ensuring reliable relative comparisons between datasets. While this measurement approach is judged as adequate for this proof-of-concept type study, it may not remain universally valid for other material systems or geometries where damage and heat localisation is less distinct. In those cases, one would want to take direct contact based local strain measurements, such as the use of extensometers. For this thesis however, an extensometer could not be used due to the explosive nature of the final failure and the associated risk of equipment damage.

9
Conclusions

This thesis set out to contribute to the currently ongoing research efforts with the goal of reducing the dependence on extensive and time consuming fibre-reinforced composite fatigue testing. This broader work is based on the recognised potential of improved consistency and predictive capabilities of strain energy dissipation trends over the typical empirical-phenomenological stress-life fatigue expressions. To pursue this, the approach was taken in this thesis to describe and model the cyclic and total strain energy dissipation trends observed in the fatigue of fibre-reinforced polymer composites from a viscoelastic analysis perspective. The main research question guiding this work was:

How can linear viscoelastic theory be adapted to define a consistent energy dissipation formulation for fibre-reinforced polymer composites under tensile–tensile fatigue, and how can these be used in conjunction with a critical dissipated energy criterion to predict fatigue lives across varying stress levels and R-ratios?

To address this question, a modified viscoelastic framework was developed and evaluated through both literature reference data and a dedicated experimental programme on a $[0/90]_{4s}$ cross-ply laminate. Complementary DMA and monotonic tensile tests enabled direct comparison between fatigue and non-fatigue data. This combined dataset formed the basis for evaluating failure strains, damping characteristics, high-cycle fatigue strength estimates and fatigue life predictions within the proposed modified viscoelastic framework.

This chapter first summarises the findings for each of the six research sub-questions in section 9.1 before returning to the main research question for a final conclusion in section 9.2.

9.1. Answers to sub-questions

To address the main research question, six supporting sub-questions were formulated. The following section aims to provide clear final answers to each, based on the theoretical and experimental findings of this thesis.

How can the applied and dissipated strain energies per cycle as well the TDE/TW ratio be defined as explicit functions of viscoelastic loss factor, R-ratio and laminate stiffness whilst being consistent with classic linear viscoelastic theory?

A complex modulus formulation of linear viscoelasticity was adopted for its simplicity and reliance on a single descriptive parameter, the loss factor $\sin(\phi)$. To apply it in fatigue, cyclic hysteresis and creep strains were treated as independent, giving closed stress–strain hysteresis loops. Identified limitations restricting the theory to fully reversed cycles were overcome by introducing energy-based R–ratio correction terms, which compensated for R-ratio discrepancies in applied energy. This yielded explicit expressions for cyclic and total dissipated energies and their ratios as functions of maximum stress, laminate stiffness, $\sin(\phi)$, and the R–ratio correction terms.

How does the viscoelastic loss factor progress during fatigue life for different cyclic maximum stresses and R-ratios and how can be this be related to the occurring damping and damage mechanisms?

The per-cycle evaluation of the loss factor revealed clear patterns in both the reference $\pm 45^\circ$ and experimental $0/90$ laminates. In both cases, a rapid increase marked the initiation phase, though with different characteristics: the $\pm 45^\circ$ laminate showed a steep logarithmic rise, while the $0/90$ laminate exhibited a high instantaneous dissipation linked with the onset of transverse cracking towards the ply interfaces. At lower stresses, both laminates reached a stabilised regime, with the loss factor remaining nearly constant through most of life despite ongoing stiffness degradation. This reflected a balance between complex modulus reduction and proportional decreases in matrix viscous contribution. At higher stresses, stabilisation gave way to continuous growth in loss factor, driven by increasing frictional dissipation from matrix cracking, delaminations and fibre–matrix debonds. These progressions allowed damage initiation and propagation to be distinguished more clearly than through stiffness or dissipated energy trends alone.

For the $0/90$ laminate, initiation behaviour was influenced by R–ratio, but trends at $R = 0.1$ and $R = 0.3$ converged later in life, showing that maximum stress governs the long-term damping response. When taken over the whole fatigue life, the effective loss factor collapsed onto a linear trend with maximum stress, independent of R. The $\pm 45^\circ$ laminate showed a similar apparent linearity despite different balances of complex and loss modulus changes, but without multi–R-ratio data the R-ratio independence observed for the $0/90$ laminate cannot yet be universally extended to such matrix-dominated laminate.

How do viscoelastic loss factors measured via dynamic mechanical analysis compare to the (weighted) average loss factors obtained from fatigue tests, and what does this imply about the viscoelastic damping-based high cycle fatigue limit?

For both the reference $\pm 45^\circ$ and the tested $0/90$ laminates, the effective loss factors measured in fatigue increased linearly with maximum stress and could be directly compared to pristine material references obtained through DMA. The intersections of the R-ratio corrected fatigue and DMA data provided high cycle fatigue strength (HCFS) estimates of 43–45 MPa for the reference $\pm 45^\circ$ woven glass/epoxy and 230 ± 30 MPa for the $0/90$ UD cross-ply, both consistent with the typical $10^6 - 10^7$ cycle endurance limit. These indirect HCFS predictions aligned well with literature and the $0/90$ estimate was further supported by a matching divergence in first-cycle dissipation near 250 MPa, lending confidence to the method despite the absence of direct very high-cycle fatigue testing.

How is the total dissipated energy (TDE) vs maximum stress (σ_{max}) relation effected by the R-ratio, and how can these be combined with loss factor trends to predict the fatigue lives at alternative maximum stresses and R-ratios?

The total dissipated energy (TDE) showed a negative log–linear relation with σ_{max} in both the $\pm 45^\circ$ and $0/90$ datasets, but its scatter at higher stresses was strongly influenced by the variable strain energy release of final failure. Defining the critical dissipated energy (CDE) as the accumulated hysteresis dissipation up to the onset of final failure proved to be a more consistent criteria, particularly for the fibre-dominated $0/90$ laminate. Furthermore, this CDE–σ_{max} relation was found to be approximately independent of R-ratio, with overlapping 95% confidence intervals at $R = 0.1$ and $R = 0.3$ across the large spread fatigue lives of 10^2–10^6 cycles.

This R-ratio independence of the CDE–σ_{max} relation enabled the predictive use of the modified viscoelastic framework. The approach scaled the S–N curve from a reference R-ratio to another using ratios of cyclic to maximum strain energies, average laminate stiffness and effective loss factors. For the fibre-dominated $0/90$ laminate, both average stiffness and effective loss factor trends were effectively independent of R, simplifying the scaling to a pure energy-based R-ratio term. Using only the $R = 0.1$ dataset as input, predictions for $R = 0.3$ achieved good accuracy, with a root-mean-square error of 0.22 decades in fatigue life. This demonstrated how CDE, combined with loss factor trends, can form the basis of a physically grounded fatigue life prediction method. However, extending this framework to more matrix-sensitive systems would require the development of additional functions to describe stiffness and loss factor evolution across R-ratios, which was beyond the scope of this study.

How do the DMA- and fatigue-derived loss factors relate to the corresponding TDE/TW ratios, and do these relations support the hypothesized two-domain trend of TDE/TW vs σ_{max}?

Within the modified linear viscoelastic framework, the TDE/TW-ratio was expressed as a direct function of the effective loss factor and the R–ratio correction terms. This linked the TDE/TW-ratio to the effective loss factor and DMA measurements that form the two-domain characteristic trend of $\sin(\phi_{eff})$ vs. σ_{max} established in this thesis. From this it follows that below the HCFS, the TDE/TW-ratio is governed by the pristine viscoelastic behaviour measured in DMA and therefore remains approximately constant. Above the HCFS, the TDE/TW-ratio follows the linear increase of $\sin(\phi_{eff})$ with σ_{max}. The ratio furthermore remained explicitly dependent on R-ratio, with higher R values giving lower TDE/TW. At the same time, separating the variable strain energy release of final failure led to the alternative definition of the critical dissipated energy over critical work ratio (CDE/CW), which like the TDE vs. CDE discussion, reduced scatter at higher stresses and provided a more consistent basis for fatigue analysis.

How do the fatigue failure strains correlate with cyclic maximum stress, R-ratio, and total work done?

The fatigue failure strains of the $0/90$ laminate showed a linear correlation with σ_{max} for both tested R–ratios and generally aligned with monotonic tensile failure strains at equivalent loading rates. Furthermore, failure strains measured at $R = 0.3$ were systematically lower than those observed at $R = 0.1$. When normalised by $(1 - R^2)$ this σ_{max}–ϵ_f data from both stress ratios collapsed onto a single linear relation representative of an equivalent $R = 0$ load case. This term reflects the ratio of the work done per cycle to the maximum strain energy potential at peak load. At the same time, this correlation is expected to be sensitive to laminate configuration, geometry and strain rate and may not extend to cases where multiple competing failure mechanisms are active.

9.2. Main research question and overall conclusion

The main research question asked how linear viscoelastic theory could be adapted to define a consistent energy-based description of cyclic dissipation in fibre-reinforced polymer composites under tensile–tensile fatigue, and how this could be combined with a critical dissipated energy criterion to predict fatigue lives across stress levels and R–ratios.

This thesis addressed this by extending complex modulus viscoelastic theory with energy-based R–ratio correction terms, enabling dissipated energies and dissipation ratios to be expressed consistently across stress ratios. Within this framework, the viscoelastic loss factor emerged as the fundamental parameter linking stress, damping and damage. Its progression through fatigue life captured both initiation and propagation phases more clearly than stiffness or energy trends alone, while its life-averaged form of the effective loss factor provided a robust linear dependence on maximum stress. Direct comparison with DMA data allowed estimation of the high-cycle fatigue strength (HCFS), yielding values of 43–45 MPa for a woven $\pm 45^\circ$ laminate and about 230 ± 30 MPa for the $0/90$ cross-ply, consistent with typical endurance limits and other dissipation metrics. In parallel, defining the critical dissipated energy (CDE) as dissipation accumulated up to the onset of final failure established a consistent, R–independent fatigue criterion. Together, these elements formed a physically grounded framework capable of predicting fatigue lives across stress ratios, with predictions at $R = 0.3$ based only on limited $R = 0.1$ data achieving an root-mean-square error of 0.22 decades over a wide life range of $10^2 - 10^6$ cycles.

The implications of this thesis are both scientific and practical. Scientifically, the work identifies the loss factor as the central characteristic property of changing damping behaviour and its direct link to damage formation, while also providing the an underlying viscoelastic principle that connects to alternative predictive methods such as infrared thermography. Practically, the framework shows that with DMA reference data and a limited fatigue experiments, it is possible to estimate a HCFS, compare behaviour across R–ratios, and predict fatigue lives. While further validation across laminate types, matrix systems and very high-cycle regimes is required, this thesis demonstrates that an energy-based viscoelastic analysis approach can provide both improved understanding and practical predictive capability for fibre-reinforced polymer composite fatigue.

10 Recommendations

This thesis has demonstrated the potential of a modified linear viscoelastic framework for analysing and predicting fatigue behaviour of fibre-reinforced polymer composites. However, the work was scoped as a proof-of-concept and thus plenty opportunities remain further progress on this work. The following recommendations aim to highlight a number of primary identified opportunities for expanding, refining, and validating the considered linear viscoelastic analysis approach in future research.

Recommendations

1. **Validation across more laminate configurations.** To generalise the framework and identify its edge cases, the work should be expanded to additional laminate configurations while keeping the material system constant (e.g. the glass/epoxy UD system tested here). Initial focus is recommended to be on cross-ply, quasi-isotropic, and $\pm 45^\circ$ laminates. This forms a natural increasing order of matrix dominance. For each configuration, a limited but well-spread dataset of an initial approximately 6–10 fatigue tests covering 10^2–10^6 cycles at each of two to three R-ratios ($R = 0.1$, 0.3, 0.5) would already provide high value. Particular interest lies in validating the assumed linearity of the effective loss factor with stress and whether this trend consistently collapses across R-ratios. A similar evaluation should be performed for the generalisation of the CDE vs. σ_{max} R-independence. Together, these would provide a broader assessment of the applicability of the method proposed in this thesis.
2. **Very high-cycle fatigue regime.** The current work could not directly experimentally verify the predicted HCFS, nor the assumption of a constant DMA-based loss factor below this limit. A dedicated experimental study targeting the damping characteristics in the very high cycle fatigue regime would therefore be valuable. Such tests should aim to explicitly verify the DMA-based HCFS predictions, assess whether the loss factor indeed approaches this pristine DMA reference at these long lives and finally establish how TDE or CDE criteria change below the onset of the critical damage mechanisms. It is hypothesised that TDE or CDE vs. σ_{max} relations will also show an inflection at the HCFS.
3. **Temperature effects.** Once a more generalised understanding of the method has been established at room temperature, the sensitivity of effective loss factor trends to temperature would be valuable to investigate. Starting again with a fibre-dominated laminate, tests at cooled (sub-zero) and elevated temperature conditions could allow deviations in fatigue-based loss factor behaviour to be linked to DMA or monotonic tensile temperature sensitivities. Such work could potentially form a basis for corrective scaling or shifting factors that enable fatigue predictions under alternative thermal conditions from a single room-temperature reference dataset. Parallel evaluation of CDE and monotonic strength across these temperatures would be required. This recommendation has the aim of extending the current framework beyond maximum stress and R-ratio predictions to also include temperature effects.

4. **Alternative DMA-like testing in tension.** Current DMA equipment is not optimised for stiff fibre-reinforced composite materials, limiting tests to bending modes with inherent drawbacks. Developing a dedicated tensile-based DMA-like methodology for composite specimens is therefore recommended. This could potentially be achieved using small specimens on a lower load rating servo-hydraulic test machine equipped with high-speed data logging, enabling direct determination of the viscoelastic loss factor from the phase lag angle between the force and displacement signals. Such a setup would offer greater freedom to further explore the linear viscoelastic region and loss factor changes at low-stress damage states. The main challenge will be overcoming signal-to-noise ratios, but progress here would remove a critical barrier to broader application of the current HCFS estimation method.
5. **Specimen geometry and strain rate guidelines.** The current work showed that specimen geometry and strain rate strongly influence both monotonic tensile as well as fatigue characteristics. Current testing standards however provide limited guidance on geometry optimisation or frequency selection, resulting in large variability across studies. It is therefore recommended to establish a more standardised approach to specimen design, strain rate and frequency selection selection as well as documentation of these decisions. Such more unified selection approach and particularly documentation could aid to improve compatibility between studies and maximise the re-evaluation of existing datasets using new analysis methods.
6. **Creep contributions.** This study assumed creep and cyclic hysteresis strains could be treated as independent and that creep effects were negligible for the fibre-dominated laminate tested. For matrix-dominated laminates, particularly at higher R-ratios, this assumption will not universally hold. Future work should therefore investigate how creep can be systematically incorporated into the current work. A promising direction is the introduction of creep dissipation predictions as suggested by Movahedi-Rad et al. [55]. This could potentially extend the applicability of the viscoelastic fatigue analysis framework to a wider range of composite systems and loading conditions.
7. **Improved local dissipation and loss factor measurements.** In this study, high-speed DIC provided local strain measurements, but loss factor evaluation remained partially influenced by less stressed specimen regions. This introduced a degree of averaging in the measurements. For more accurate determination of loss factors and HCFS estimates, directly integrated methods for local strain and local damping measurements with the force signal are recommended. This may involve alternative specimen designs, new measurement approaches or a different data synchronisation strategy of high-speed DIC. Such improved synchronisation of local strain and global force signals would directly enhance the quality of the local loss factor measurement and thus the accuracy of the analysis method.
8. **Extension to thermoplastic composites.** While the current framework was demonstrated on a thermoset matrix system, industrial applications are increasingly shifting toward thermoplastic matrices. These introduce additional phenomena such as viscoplastic dissipation (matrix yielding), which are rarely observed in thermosets. As a result, damping behaviour may be influenced not only by frictional damage mechanisms but also by matrix plasticity. Thermoplastics are furthermore more sensitive to temperature and creep, which strengthens the case for extending the recommendations above on thermal and creep effects. Initial studies should therefore evaluate whether the effective loss factor trends and energy-based fatigue criteria established in this thesis remain valid and where additional terms should be introduced to compensate for increased viscoplastic, creep and thermal sensitivities.

Together, these recommendations outline a path for further validating, extending and refining the proposed viscoelastic fatigue analysis framework, with the ultimate aim of enabling more reliable and efficient fatigue characterisation of fibre-reinforced polymer composites.

References

[1] J. Bhangale, "Fatigue analysis of wind turbine blade materials using a continuum damage mechanics framework," Doctoral Thesis, Dept. of Aerospace Engineering, Delft Univ. of Technology, Delft, 2021. DOI: 10.4233/uuid:7ea21785-c7ec-49db-85c4-d2e2f6ce6e9b.

[2] K. H. Boller, "Fatigue fundamentals for composite materials," in *Composite Materials: Testing and Design*, S. Yurenka, Ed. West Conshohocken: ASTM International, 1969, pp. 217–235. DOI: 10.1520/STP49819S.

[3] G. Grimes, "Structural design significance of tension-tension fatigue data on composites," in *Composite materials, testing and design: 4th conference*, Philadelphia, 1977. DOI: https://doi.org/10.1520/STP617-EB.

[4] M. Salkind, "Fatigue of composites," in *Composite Materials: Testing and Design (Second Conference)*, H. Corten, Ed. West Conshohocken: ASTM International, 1972, pp. 143–169. DOI: 10.1520/STP27745S.

[5] A. P. Vassilopoulos, "The history of fiber-reinforced polymer composite laminate fatigue," *International Journal of Fatigue*, vol. 134, p. 105 512, May 2020. DOI: 10.1016/j.ijfatigue.2020.105512.

[6] A. Wöhler, "Über die festigkeitsversuche mit eisen und stahl," *Zeitschrift für Bauwesen*, vol. 20, pp. 73–106, 1870.

[7] B. P. Haigh, "Experiments on the fatigue of brasses," *Journal of the Institute of Metals*, vol. 18, pp. 55–86, 1917.

[8] Y. Han, F. Wu, and Y. Lian, "Fatigue life prediction of composite laminates based on energy conservation and damage entropy accumulation," *International Journal of Fatigue*, vol. 199, p. 109 088, Oct. 2025. DOI: 10.1016/j.ijfatigue.2025.109088.

[9] C. Sillero Illanes *et al.*, "Transition to sustainability in the european union aviation system," European Commission, JRC136536, Oct. 2024.

[10] R. Alderliesten, *Private communication*, Total dissipated over total applied energy ratio hypothesis discussion, Dec. 2024.

[11] M. O. Cadavid *et al.*, "Experimental studies of stiffness degradation and dissipated energy in glass fibre reinforced polymer composite under fatigue loading," *Polymers and Polymer Composites*, vol. 25, no. 6, pp. 435–446, Jul. 2017. DOI: 10.1177/096739111702500602.

[12] P. Michal *et al.*, "The impact of internal structure changes on the damping properties of 3d-printed composite material," *Applied Sciences*, vol. 14, no. 13, p. 5701, Jun. 2024. DOI: 10.3390/app14135701.

[13] R. Chandra, S. Singh, and K. Gupta, "Damping studies in fiber-reinforced composites – a review," *Composite Structures*, vol. 46, no. 1, pp. 41–51, Sep. 1999. DOI: 10.1016/S0263-8223(99)00041-0.

[14] Y. Han *et al.*, "Nonlinear viscoelastic mechanical behavior and fatigue hysteresis loops modeling of composite laminates," *Engineering Fracture Mechanics*, vol. 306, p. 110 233, Aug. 2024. DOI: 10.1016/j.engfracmech.2024.110233.

[15] A. V. Movahedi-Rad, T. Keller, and A. P. Vassilopoulos, "Modeling of fatigue behavior based on interaction between time- and cyclic-dependent mechanical properties," *Composites Part A: Applied Science and Manufacturing*, vol. 124, p. 105 469, Sep. 2019. DOI: 10.1016/j.compositesa.2019.05.037.

[16] S. V. Panin *et al.*, "Estimating low- and high-cyclic fatigue of polyimide-CF-PTFE composite through variation of mechanical hysteresis loops," *Materials*, vol. 15, no. 13, p. 4656, Jul. 2022. DOI: 10.3390/ma15134656.

[17] H. Koruk and S. Rajagopal, “A comprehensive review on the viscoelastic parameters used for engineering materials, including soft materials, and the relationships between different damping parameters,” *Sensors*, vol. 24, no. 18, p. 6137, Sep. 2024. DOI: 10.3390/s24186137.

[18] H. El Kadi and F. Ellyin, “Effect of stress ratio on the fatigue of unidirectional glass fibre/epoxy composite laminae,” *Composites*, vol. 25, no. 10, pp. 917–924, Nov. 1994. DOI: 10.1016/0010-4361(94)90107-4.

[19] J. A. Epaarachchi and P. D. Clausen, “An empirical model for fatigue behavior prediction of glass fibre-reinforced plastic composites for various stress ratios and test frequencies,” *Composites Part A: Applied Science and Manufacturing*, vol. 34, no. 4, pp. 313–326, Apr. 2003. DOI: 10.1016/S1359-835X(03)00052-6.

[20] A. A. Bogdanov, S. V. Panin, and P. V. Kosmachev, “Fatigue damage assessment and lifetime prediction of short fiber reinforced polymer composites—a review,” *Journal of Composites Science*, vol. 7, no. 12, p. 484, Nov. 2023. DOI: 10.3390/jcs7120484.

[21] A. V. Movahedi-Rad, T. Keller, and A. P. Vassilopoulos, “Interrupted tension-tension fatigue behavior of angle-ply GFRP composite laminates,” *International Journal of Fatigue*, vol. 113, pp. 377–388, Aug. 2018. DOI: 10.1016/j.ijfatigue.2018.05.001.

[22] R. Talreja, “Fatigue of composite materials: Damage mechanisms and fatigue-life diagrams,” *Proceedings of the Royal Society of London. A. Mathematical and Physical Sciences*, vol. 378, no. 1775, pp. 461–475, 1981. DOI: 10.1098/rspa.1981.0163.

[23] G. R. Ahmadzadeh and A. Varvani-Farahani, “Ratcheting assessment of GFRP composites in low-cycle fatigue domain,” *Applied Composite Materials*, vol. 21, no. 3, pp. 417–428, Jun. 2014. DOI: 10.1007/s10443-013-9341-8.

[24] X. Tang and X. Yan, “A review on the damping properties of fiber reinforced polymer composites,” *Journal of Industrial Textiles*, vol. 49, no. 6, pp. 693–721, Jan. 2020. DOI: 10.1177/1528083718795914.

[25] A. Treviso *et al.*, “Damping in composite materials: Properties and models,” *Composites Part B: Engineering*, vol. 78, pp. 144–152, Sep. 2015. DOI: 10.1016/j.compositesb.2015.03.081.

[26] S. Keusch and R. Haessler, “Influence of surface treatment of glass fibres on the dynamic mechanical properties of epoxy resin composites,” *Composites Part A: Applied Science and Manufacturing*, vol. 30, no. 8, pp. 997–1002, Aug. 1999. DOI: 10.1016/S1359-835X(99)00007-X.

[27] D. J. Nelson and J. W. Hancock, “Interfacial slip and damping in fibre reinforced composites,” *Journal of Materials Science*, vol. 13, no. 11, pp. 2429–2440, Nov. 1978. DOI: 10.1007/BF00808058.

[28] J. Kenny and M. Marchetti, “Elasto-plastic behavior of thermoplastic composite laminates under cyclic loading,” *Composite Structures*, vol. 32, no. 1, pp. 375–382, Jan. 1995. DOI: 10.1016/0263-8223(95)00052-6.

[29] E. K. Gamstedt and R. Talreja, “Fatigue damage mechanisms in unidirectional carbon-fibre-reinforced plastics,” *Journal of Materials Science*, vol. 34, no. 11, pp. 2535–2546, 1999. DOI: 10.1023/A:1004684228765.

[30] R. Talreja, “Physical modelling of failure in composites,” *Philosophical Transactions of the Royal Society A: Mathematical, Physical and Engineering Sciences*, vol. 374, no. 2071, p. 20 150 280, Jul. 2016. DOI: 10.1098/rsta.2015.0280.

[31] R. Pipes, “Fatigue of composite materials,” in *Composite Materials Series*, K. Reifsnider, Ed., vol. 4, Blacksburg: Elsevier, 1991, pp. 1–519.

[32] B. Zhang *et al.*, “Research on damping performance and strength of the composite laminate,” *Scientific Reports*, vol. 11, no. 1, p. 18 281, Sep. 2021. DOI: 10.1038/s41598-021-97933-w.

[33] K. M. Mini *et al.*, “Effect of fibre volume fraction on fatigue behaviour of glass fibre reinforced composite,” *Fatigue & Fracture of Engineering Materials & Structures*, vol. 35, no. 12, pp. 1160–1166, Dec. 2012. DOI: 10.1111/j.1460-2695.2012.01709.x.

[34] D. Flore and K. Wegener, “Influence of fibre volume fraction and temperature on fatigue life of glass fibre reinforced plastics,” *AIMS Materials Science*, vol. 3, no. 3, pp. 770–795, 2016. DOI: 10.3934/matersci.2016.3.770.

[35] U. Mortensen *et al.*, “The impact of the fiber volume fraction on the fatigue performance of glass fiber composites,” *Composites Part A: Applied Science and Manufacturing*, vol. 169, p. 107 493, Jun. 2023. DOI: 10.1016/j.compositesa.2023.107493.

[36] K. Reifsnider, “Fatigue behavior of composite materials,” *International Journal of Fracture*, vol. 16, no. 6, pp. 563–583, Dec. 1980. DOI: 10.1007/BF02265218.

[37] I. Daniel, B. Werner, and J. Fenner, “Strain-rate-dependent failure criteria for composites,” *Composites Science and Technology*, vol. 71, no. 3, pp. 357–364, Feb. 2011. DOI: 10.1016/j.compscitech.2010.11.028.

[38] A. D’Amore, A. Califano, and L. Grassia, “Modelling the loading rate effects on the fatigue response of composite materials under constant and variable frequency loadings,” *International Journal of Fatigue*, vol. 150, p. 106 338, Sep. 2021. DOI: 10.1016/j.ijfatigue.2021.106338.

[39] *Test method for tension-tension fatigue of polymer matrix composite materials*, D3479/D3479M-19, ASTM International, 2023.

[40] B. Fazlali, S. V. Lomov, and Y. Swolfs, “Reducing stress concentrations in static and fatigue tensile tests on unidirectional composite materials: A review,” *Composites Part B: Engineering*, vol. 273, p. 111 215, Mar. 2024. DOI: 10.1016/j.compositesb.2024.111215.

[41] A. V. Movahedi-Rad, T. Keller, and A. P. Vassilopoulos, “Fatigue damage in angle-ply GFRP laminates under tension-tension fatigue,” *International Journal of Fatigue*, vol. 109, pp. 60–69, Apr. 2018. DOI: 10.1016/j.ijfatigue.2017.12.015.

[42] D. Perreux and E. Joseph, “The effect of frequency on the fatigue performance of filament-wound pipes under biaxial loading: Experimental results and damage model,” *Composites Science and Technology*, vol. 57, no. 3, pp. 353–364, Jan. 1997. DOI: 10.1016/S0266-3538(96)00155-8.

[43] M. Crowther, R. Wyatt, and M. Phillips, “Creep-fatigue interactions in glass fibre/polyester composites,” *Composites Science and Technology*, vol. 36, no. 3, pp. 191–210, Jan. 1989. DOI: 10.1016/0266-3538(89)90020-1.

[44] C. Saff, “Effect of load frequency and lay-up on fatigue life of composites,” in *Long-Term Behavior of Composites*, T. O’Brien, Ed. West Conshohocken: ASTM International, 1983, pp. 78–91. DOI: 10.1520/STP31817S.

[45] M. Eftekhari and A. Fatemi, “On the strengthening effect of increasing cycling frequency on fatigue behavior of some polymers and their composites: Experiments and modeling,” *International Journal of Fatigue*, vol. 87, pp. 153–166, Jun. 2016, ISSN: 01421123. DOI: 10.1016/j.ijfatigue.2016.01.014.

[46] I. De Baere *et al.*, “On the tension–tension fatigue behaviour of a carbon reinforced thermoplastic part i: Limitations of the ASTM d3039/d3479 standard,” *Polymer Testing*, vol. 30, no. 6, pp. 625–632, Sep. 2011. DOI: 10.1016/j.polymertesting.2011.05.004.

[47] G. C. Jacob *et al.*, “Strain rate effects on the mechanical properties of polymer composite materials,” *Journal of Applied Polymer Science*, vol. 94, no. 1, pp. 296–301, Sep. 2004. DOI: 10.1002/app.20901.

[48] S. Barré, T. Chotard, and M. Benzeggagh, “Comparative study of strain rate effects on mechanical properties of glass fibre-reinforced thermoset matrix composite,” *Composites Part A: Applied Science and Manufacturing*, vol. 27, no. 12, pp. 1169–1181, 1996. DOI: 10.1016/1359-835X(96)00075-9.

[49] J. Kwon *et al.*, “Evaluation of the effect of the strain rate on the tensile properties of carbon–epoxy composite laminates,” *Journal of Composite Materials*, vol. 51, no. 22, pp. 3197–3210, Sep. 2017. DOI: 10.1177/0021998316683439.

[50] J. Harding and L. M. Welsh, “A tensile testing technique for fibre-reinforced composites at impact rates of strain,” *Journal of Materials Science*, vol. 18, no. 6, pp. 1810–1826, Jun. 1983. DOI: 10.1007/BF00542078.

[51] H. Hahn and R. Kim, “Proof testing of composite materials,” *Journal of Composite Materials*, vol. 9, no. 3, pp. 297–311, Jul. 1975. DOI: 10.1177/002199837500900308.

[52] S. Lee, T. Nguyen, and T.-j. Chuang, “Model of fatigue damage in strain-rate-sensitive composite materials,” *Journal of Materials Research*, vol. 18, no. 1, pp. 77–80, Jan. 2003. DOI: 10.1557/jmr.2003.0011.

[53] L. Ma *et al.*, “Review of strain rate effects of fiber-reinforced polymer composites,” *Polymers*, vol. 13, no. 17, p. 2839, Aug. 2021. DOI: 10.3390/polym13172839.

[54] M. Rueppel *et al.*, “Damping of carbon fibre and flax fibre angle-ply composite laminates,” *Composites Science and Technology*, vol. 146, pp. 1–9, Jul. 2017. DOI: 10.1016/j.compscitech.2017.04.011.

[55] A. V. Movahedi-Rad, L. Liu, and T. Keller, “A novel fatigue life prediction methodology based on energy dissipation in viscoelastic materials, synergistic effects of stress level, stress ratio, and temperature,” *International Journal of Fatigue*, vol. 184, p. 108 296, Jul. 2024. DOI: 10.1016/j.ijfatigue.2024.108296.

[56] A. Bledzki and J. Gassan, “The accumulated dissipated energy of composites under fatigue loadings,” *Science and Engineering of Composite Materials*, vol. 8, pp. 99–106, Apr. 1999. DOI: 10.1515/SECM.1999.8.2.99.

[57] A. V. Movahedi-Rad, G. Eslami, and T. Keller, “A novel fatigue life prediction methodology based on energy dissipation in viscoelastic materials,” *International Journal of Fatigue*, vol. 152, p. 106 457, Nov. 2021. DOI: 10.1016/j.ijfatigue.2021.106457.

[58] F. Ellyin and H. El-Kadi, “A fatigue failure criterion for fiber reinforced composite laminae,” *Composite Structures*, vol. 15, no. 1, pp. 61–74, Jan. 1990. DOI: 10.1016/0263-8223(90)90081-O.

[59] S. Mandegarian and F. Taheri-Behrooz, “A general energy based fatigue failure criterion for the carbon epoxy composites,” *Composite Structures*, vol. 235, p. 111 804, Mar. 2020. DOI: 10.1016/j.compstruct.2019.111804.

[60] A. V. Movahedi-Rad and T. Keller, “A novel methodology of predicting temperature and rate effects on tensile properties of viscoelastic materials,” *International Journal of Non-Linear Mechanics*, vol. 159, p. 104 613, Mar. 2024. DOI: 10.1016/j.ijnonlinmec.2023.104613.

[61] H. Hahn and R. Kim, “Fatigue behavior of composite laminate,” *Journal of Composite Materials*, vol. 10, no. 2, pp. 156–180, Apr. 1976. DOI: 10.1177/002199837601000205.

[62] S. Khoshmanesh, S. Watson, and D. Zarouchas, “The effect of the fatigue damage accumulation process on the damping and stiffness properties of adhesively bonded composite structures,” *Composite Structures*, vol. 287, p. 115 328, May 2022. DOI: 10.1016/j.compstruct.2022.115328.

[63] S. Mandegarian, S. S. Samareh-Mousavi, and F. Taheri-Behrooz, “Experimental investigation on in-plane shear fatigue failure criteria of ± 45° angle-ply carbon epoxy composite,” *International Journal of Fatigue*, vol. 160, p. 106 873, Jul. 2022. DOI: 10.1016/j.ijfatigue.2022.106873.

[64] G. La Rosa and A. Risitano, “Thermographic methodology for rapid determination of the fatigue limit of materials and mechanical components,” *International Journal of Fatigue*, vol. 22, no. 1, pp. 65–73, Jan. 2000. DOI: 10.1016/S0142-1123(99)00088-2.

[65] J. Montesano, Z. Fawaz, and H. Bougherara, “Use of infrared thermography to investigate the fatigue behavior of a carbon fiber reinforced polymer composite,” *Composite Structures*, vol. 97, pp. 76–83, Mar. 2013. DOI: 10.1016/j.compstruct.2012.09.046.

[66] A. Premanand, M. Rienks, and F. Balle, “Accelerated estimation of the very high cycle fatigue strength and life of polymer composites under ultrasonic cyclic three-point bending,” *Materials & Design*, vol. 240, p. 112 872, Apr. 2024. DOI: 10.1016/j.matdes.2024.112872.

[67] C. Colombo *et al.*, “Fatigue behaviour of a GFRP laminate by thermographic measurements,” *Procedia Engineering*, vol. 10, pp. 3518–3527, 2011. DOI: 10.1016/j.proeng.2011.04.579.

[68] K. Karvanis *et al.*, “Preparation and dynamic mechanical analysis of glass or carbon fiber/polymer composites,” *IOP Conference Series: Materials Science and Engineering*, vol. 362, p. 012 005, May 2018. DOI: 10.1088/1757-899X/362/1/012005.

[69] Z. Guo *et al.*, “A new temperature-dependent modulus model of glass/epoxy composite at elevated temperatures,” *Journal of Composite Materials*, vol. 47, no. 26, pp. 3303–3310, Dec. 2013. DOI: 10.1177/0021998312464080.

[70] J. Cortazar-Noguerol *et al.*, “Preload influence on the dynamic properties of a polyurethane elastomeric foam,” *Polymers*, vol. 16, no. 13, p. 1844, Jun. 2024. DOI: 10.3390/polym16131844.

[71] S. Liang, P. Gning, and L. Guillaumat, “A comparative study of fatigue behaviour of flax/epoxy and glass/epoxy composites,” *Composites Science and Technology*, vol. 72, no. 5, pp. 535–543, Mar. 2012. DOI: 10.1016/j.compscitech.2012.01.011.

[72] Y. Adde, “Stress analysis of rotating composite solid disc,” *International Journal of Aeronautical Science & Aerospace Research*, pp. 205–209, Aug. 2019. DOI: 10.19070/2470-4415-1900025.

[73] B. Icten *et al.*, “Low temperature effect on impact response of quasi-isotropic glass/epoxy laminated plates,” *Composite Structures*, vol. 91, pp. 318–323, Dec. 2009. DOI: 10.1016/j.compstruct.2009.05.010.

[74] B. Fadhil, “Effect of plies stacking sequence of e-glass/epoxy composite material on its damage behavior under impact loading,” *Journal of pure and applied sciences*, vol. 21, Jan. 2009.

[75] E. Karlus, R. Himte, and R. Rathore, “Optimisation of mono parabolic leaf spring,” *International Journal of Advances in Engineering & Technology*, vol. 7, pp. 283–291, Mar. 2014.

[76] C. Kassapoglou, *Design and Analysis of Composite Structures: With Applications to Aerospace Structures*, 1st ed. New York: John Wiley & Sons, Incorporated, 2010.

[77] M. Knops and A. Puck, *Analysis of failure in fiber polymer laminates: the theory of Alfred Puck*. Berlin: Springer, 2008.

[78] C. McCarthy, M. McCarthy, and V. Lawlor, “Progressive damage analysis of multi-bolt composite joints with variable bolt–hole clearances,” *Composites Part B: Engineering*, vol. 36, no. 4, pp. 290–305, Jun. 2005. DOI: 10.1016/j.compositesb.2004.11.003.

[79] P. P. Camanho and F. L. Matthews, “A progressive damage model for mechanically fastened joints in composite laminates,” *Journal of Composite Materials*, vol. 33, no. 24, pp. 2248–2280, Dec. 1999. DOI: 10.1177/002199839903302402.

[80] P. A. Carraro, M. Simonetto, and M. Quaresimin, “Fatigue damage evolution in glass/epoxy cross-ply laminates under spectrum loadings,” *Composites Part A: Applied Science and Manufacturing*, vol. 173, p. 107 680, Oct. 2023. DOI: 10.1016/j.compositesa.2023.107680.

[81] *Test method for tensile properties of polymer matrix composite materials*, D3039/D3039M-14, ASTM International, 2014.

[82] I. De Baere, W. Van Paepegem, and J. Degrieck, “On the design of end tabs for quasi□static and fatigue testing of fibre□reinforced composites,” *Polymer Composites*, vol. 30, no. 4, pp. 381–390, Apr. 2009. DOI: 10.1002/pc.20564.

[83] I. De Baere *et al.*, “On the tension–tension fatigue behaviour of a carbon reinforced thermoplastic part II: Evaluation of a dumbbell-shaped specimen,” *Polymer Testing*, vol. 30, no. 6, pp. 663–672, Sep. 2011. DOI: 10.1016/j.polymertesting.2011.05.005.

[84] F. Pagano *et al.*, “Numerical and experimental approach for improving quasi-static and fatigue testing of a unidirectional CFRP composite laminate,” *Procedia Engineering*, vol. 213, pp. 804–815, 2018. DOI: 10.1016/j.proeng.2018.02.076.

[85] J. Yoo *et al.*, “Tensile properties of CFRP manufactured by resin transfer molding considering stacking sequences at various strain rates,” *Journal of Composite Materials*, vol. 53, no. 14, pp. 2015–2030, Jun. 2019. DOI: 10.1177/0021998318816441.

[86] *Technical data sheet LOCTITE® EA 3430*, Henkel Loctite Corp. [Online]. Available: https://datasheets.tdx.henkel.com/LOCTITE-EA-3430-en_GL.pdf (visited on 03/16/2025).

[87] V. Perruchoud, *Private communication*, Discussion on recommended specimen geometry, Mar. 2025.

[88] *Test method for tensile properties of plastics*, D638-14, ASTM International, 2022.

[89] A. Rotem, “Load frequency effect on the fatigue strength of isotropic laminates,” *Composites Science and Technology*, vol. 46, no. 2, pp. 129–138, 1993. DOI: 10.1016/0266-3538(93)90168-G.

[90] J. Mandell and U. Meier, “Effects of stress ratio, frequency, and loading time on the tensile fatigue of glass-reinforced epoxy,” in *Long-Term Behavior of Composites*, T. O’Brien, Ed. West Conshohocken: ASTM International, 1983, pp. 55–77. DOI: 10.1520/STP31816S.

[91] *Test method for glass transition temperature of polymer matrix composites by dynamic mechanical analysis (DMA)*, D7028-07, ASTM International, 2015.

[92] S. N. Olufsen, M. E. Andersen, and E. Fagerholt, “MDIC: An open-source toolkit for digital image correlation,” *SoftwareX*, vol. 11, p. 100 391, Jan. 2020, ISSN: 23527110. DOI: 10.1016/j.softx.2019.100391.

[93] W. Lim, “Shoelace formula: Connecting the area of a polygon and vector cross product,” *Mathematics Teacher*, vol. 110, pp. 631–636, Apr. 2017. DOI: 10.5951/mathteacher.110.8.0631.

[94] T. Murayama, *Dynamic mechanical analysis of polymeric material*, 2nd ed. Amsterdam: Elsevier Scientific Publishing Company, 1982.

[95] W. R. Broughton and M. J. Lodeiro, “Fatigue testing of composite laminates,” National Physical Laboratory, Teddington, NPL Report CMMT(A) 252, Oct. 2000.

[96] F. Bensadoun *et al.*, “Fatigue behaviour assessment of flax–epoxy composites,” *Composites Part A: Applied Science and Manufacturing*, vol. 82, pp. 253–266, Mar. 2016. DOI: 10.1016/j.compositesa.2015.11.003.

A

Additional specimen geometry FEA results

In chapter 5 the specimen design process and corresponding FEA study were discussed. In this main body chapter, for the comparison between the three considered geometry types of Figure 5.3, only the results for the considered best iteration of each type for a fixed 15/20 gauge-tab width ratio were shown. Numerous more iterations were performed as an initial exploratory optimisation exercise, which when plotted against each other per geometry type indicate how the shear stress distribution and Tsai-Wu failure indices change with some of the geometrical variables. This appendix will not discuss the effects of these geometrical changes in detail, but will provide some additional FEA results available as reference for those undertaking a similar specimen optimisation process.

This appendix is therefore structured in three parts, each providing additional FEA results per geometry type (A, B and C). Here, type A consisted of a constant gauge section with linear (tapered) transitions to the tabbed region. Type B also contained a constant gauge section, but with a curved transition. Last but not least, the geometry type C as ultimately used in for this thesis consisted of a continuous curvature without constant section. For each geometry type, the shear stress distributions along the normalised length of the specimen and their corresponding distribution of Tsai-Wu failure indices will be shown. All of these additional results are for an applied net gauge section tensile stress of 100 MPa.

A.1. Geometry type A

The figures A.1 and A.2 show the additional FEA results for geometry type A with the following naming convention: GWxx indicates the gauge width; SWxx gives the tab width; GLxx represents the gauge length; Lin Rxxx gives the transition radius from the linear taper to the gauge section and finally CCxxx indicates the clamp-to-clamp distance as measure of the specimen length.

These figures show that the shear stress distribution on the type A geometry is very sensitive to transition radius and consequent angle of the tapered section. For increasing radii, the shear stress peak is reduced but simultaneously brought closer to the centre of the specimen. Here it interacts more with the net section gauge stresses, which is furthermore reflected in the Tsai-Wu failure indices of Figure A.2.

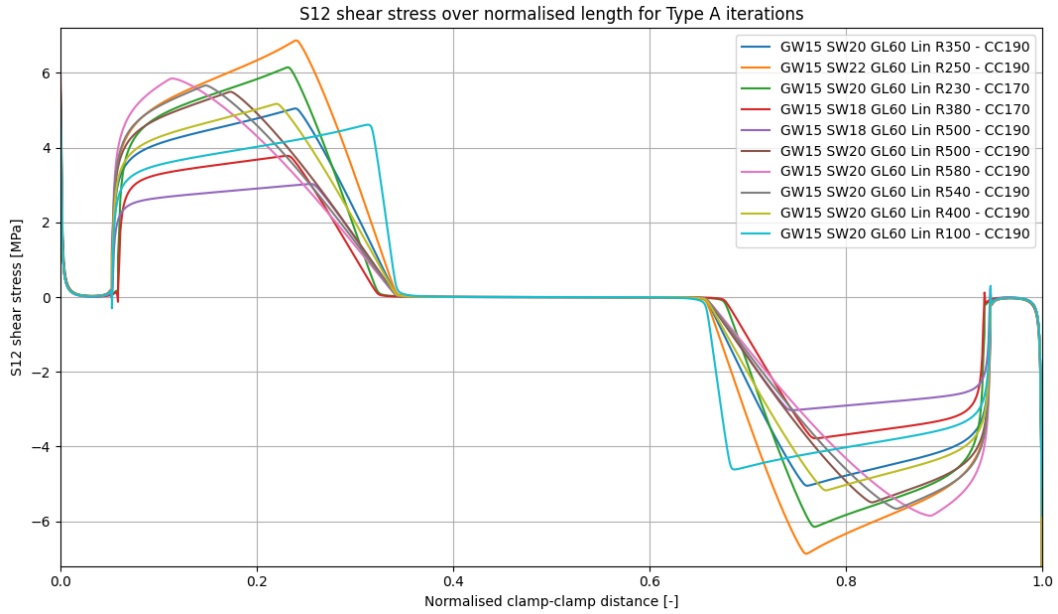

Figure A.1: Maximum S_{12} shear stresses along clamp-to-clamp distance comparison between iterations of type A dogbone geometries.

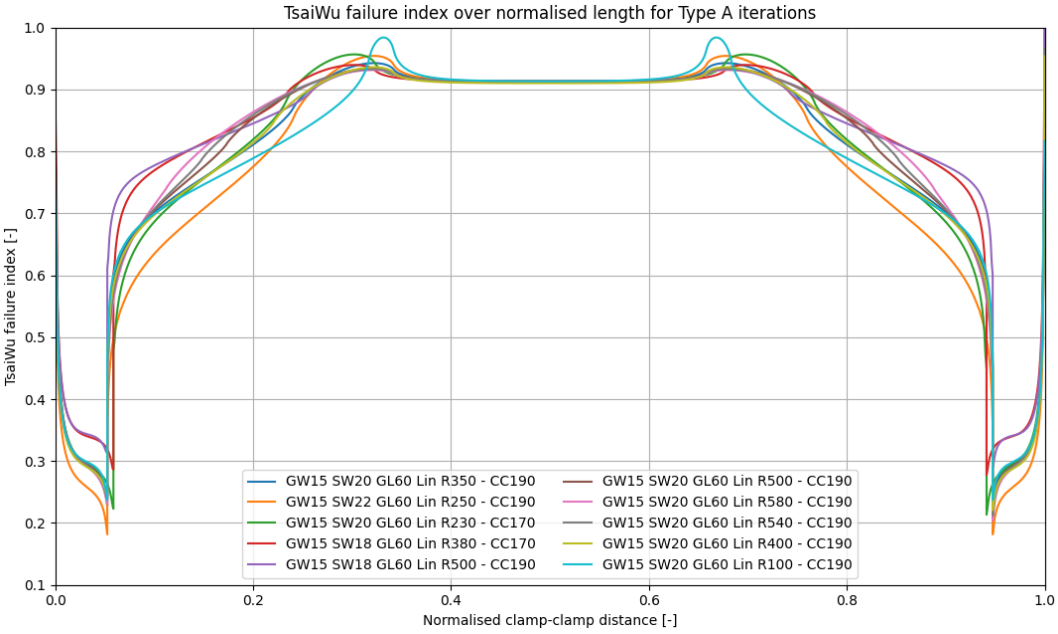

Figure A.2: Tsai-Wu failure indices along clamp-to-clamp distance comparison between iterations of type A dogbone geometries.

A.2. Geometry type B

The figures A.3 and A.4 show the additional FEA results for geometry type B. Here, Curv Rxxx represents the radius of the transition curvature.

In general, figures A.3 and A.4 indicate that as the gauge/tab width ratio decreases, the peak shear stresses rise. Furthermore, for a fixed gauge/tab width ratio decreasing the transition radius further increases the peak shear stress as well. Lastly, unlike type A, the location of the peak shear stress and peak failure index is reasonably insensitive to these geometry iterations. However, the magnitudes of peak shear stresses are considerably higher compared to type A as also discussed in chapter 5.

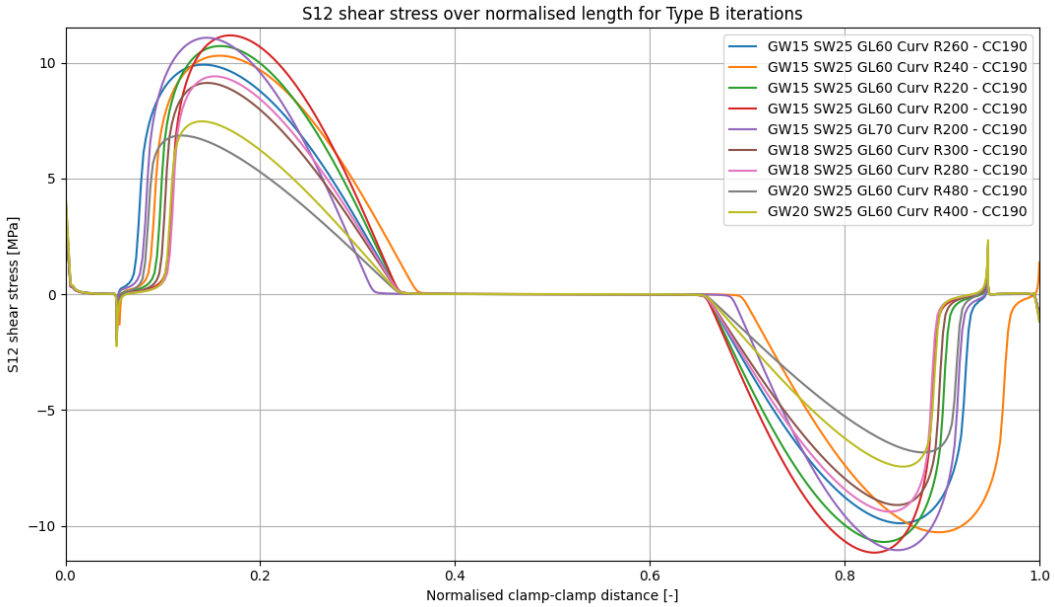

Figure A.3: Maximum S_{12} shear stresses along clamp-to-clamp distance comparison between iterations of type B dogbone geometries.

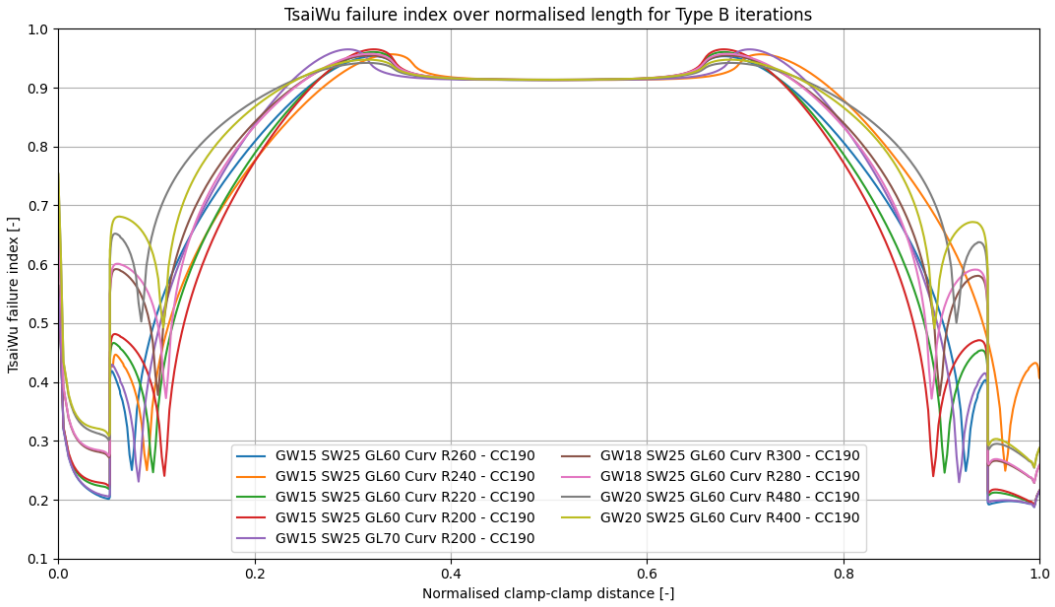

Figure A.4: Tsai-Wu failure indices along clamp-to-clamp distance comparison between iterations of type B dogbone geometries.

A.3. Geometry type C

Then finally, figures A.5 and A.6 show the two iterations on the continuous curvature type C geometry. These show the effect of changing gauge/tab width ratios and curvature radii, where the magnitude of shear stress appears to be much more effected than the overall failure indices.

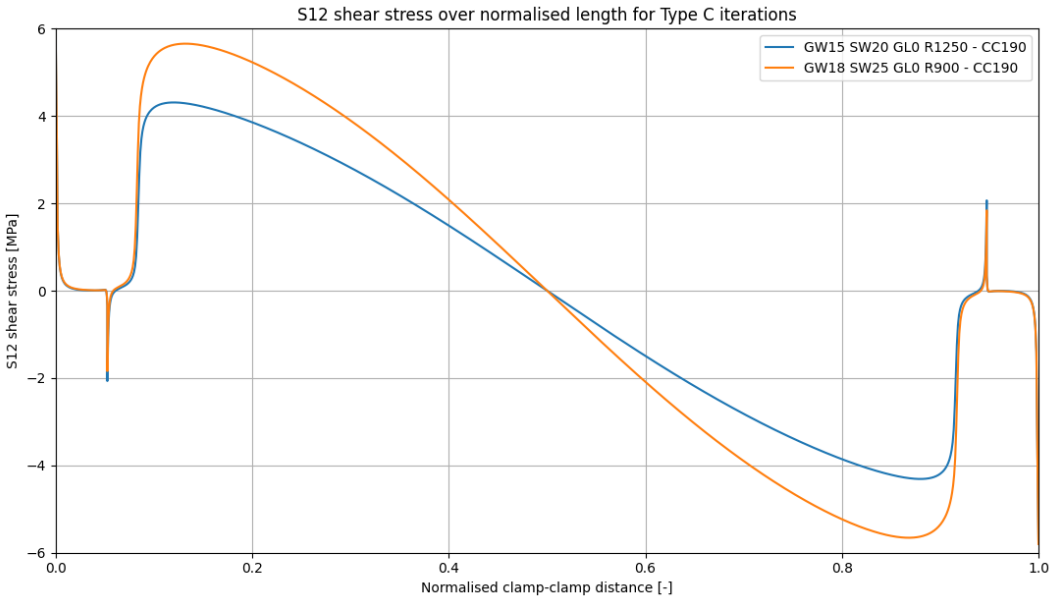

Figure A.5: Maximum S_{12} shear stresses along clamp-to-clamp distance comparison between iterations of type C dogbone geometries.

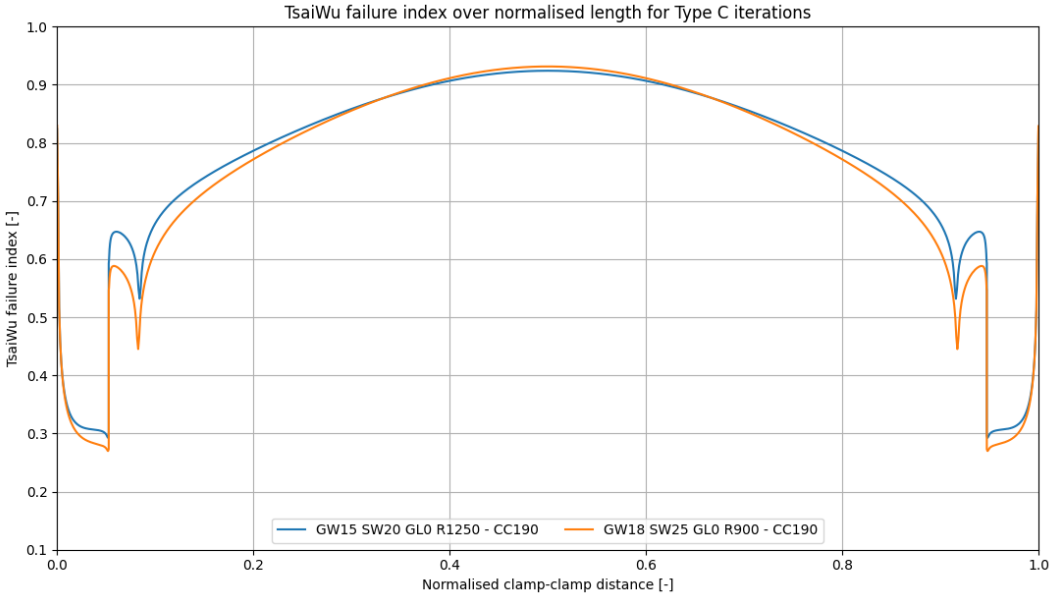

Figure A.6: Tsai-Wu failure indices along clamp-to-clamp distance comparison between iterations of type C dogbone geometries.

B

Specimen production overview

This appendix aims to provide a more detailed overview of the mains steps undertaken in the specimen production process than the initial short summary in the main body at section 5.6.

B.1. UD prepreg material

As also stated in the main body of this thesis, the material used for all specimen and tab material was an E-glass fibre and DeltaPreg BT-080 epoxy based UD prepreg. The details of which are given in Table B.1, below.

Table B.1: Glass fibre UD prepreg material details.

Material storage name	Deltapreg glass UD EGL-200-BT080-34 EF
Fibre type	E-glass
Matrix type	BT080 OoA epoxy based resin system
Fibre areal weight	200
Resin content by weight	34%
Material responsible	Saullo G.P. Castro

The exact cured ply thickness of this material had not been tested yet at the time of the specimen production, nor did the manufacturer datasheet provide any estimates, therefore this was estimated using Equation B.1.

$$t_{cured} \approx \frac{GSM_f}{\rho_f \cdot V_f} \tag{B.1}$$

Here, the GSM_f is the areal weight of the UD glass fibres at 200 g/m^2. The fibre density was estimated at $\rho_f \approx 2.58\ g/cm^3$. V_f is the fibre volume fraction, which was further calculated using Equation B.2.

$$V_f = \frac{W_f/\rho_f}{W_f/\rho_f + W_m/\rho_m} \tag{B.2}$$

Using an epoxy resin density of $\rho_m \approx 1.3\ g/cm^3$ and the manufacturers 34% resin content by weight, the fibre volume fraction was calculated at $V_f \approx 0.494$. This then resulted in a predicted ply thickness of $t_{cured} \approx 0.157\ mm$. Later measured cured specimen thicknesses confirmed that this was indeed a reasonable estimate.

B.2. Cutting of prepreg material

As per recommendation of the prepreg manufacturer, the roll was taken out of the freezer and left to defrost for 6 hours before the sealed bag was opened. This minimised the condensation moisture absorption by the uncured prepreg.

For the main specimen material, 16 rectangular 600 x 600 mm plies were cut along the fibre direction. For the tabs, aimed to a nominal thickness of around 1.5-1.6 mm, 10 plies of 210 x 620 mm plies were cut at both $+45^{\circ}$ and -45°. Finally, for the DMA specimen with an aimed thickness of around 1.8 mm, 24 plies of 100 x 80 mm were cut to produce two 12-ply material plates. All cutting was performed on a GERBERcutter DCS located at the DASML composites lab. Overall this resulted in $\sim 10.5\ m^2$ of material usage, which equated to 17.5 linear meter of the 0.6 m wide roll.

To further minimise moisture absorption of the uncured prepreg material before laminating, all cut plies were stored in sealed bags and re-frozen until the morning of lamination. Here, before use all ply packages were left to defrost for a further two hours.

B.3. Material lamination and curing

All composite material for this thesis was laminated on a single large aluminium base plate. Before use, this plate was prepared by thorough scrubbing using Scotch-Brite pads to ensure a consistent and most importantly defect-free surface finish. After this, the aluminium base plate was cleaned multiple times using acetone. Then, three layers of Marbocoat release agent were applied with a 15 minute drying time between each coat.

After applying the first layer of each of the 5 laminate plates (1x fatigue specimen, 2x tabs and 2x DMA), a 3 minute debulk was performed to ensure proper adherence to the base plate and extract all air bubbles. Such debulks were then repeated every 4th laminated layer, with a 3 minute durations per ply laminated. Hence for a 4 ply interval this corresponded to 12 minute debulks. Debulking was done using perforated release film and a peel ply layer as air path.

As the prepreg material is specifically for out-of-autoclave curing, also a perforated release film (Wrightlon 7300, $T_{max} = 121^{\circ}C$) was used for curing to minimise trapped air and voids. To prevent excessive resin extraction through these perforations, only a single a layer of light-weight peel ply (Stitch ply A (Nylon), $T_{max} = 232^{\circ}C$) was used as curing air path. This furthermore had the benefit of leaving a smoother surface finish on the non-tooling side of the cured laminates. Finally, a standard vacuum bag (Wrightlon 5400, $T_{max} = 177^{\circ}C$) was used with seal tape applied directly onto the base plate. Figure B.1 shows the consumables and vacuum bag arrangement.

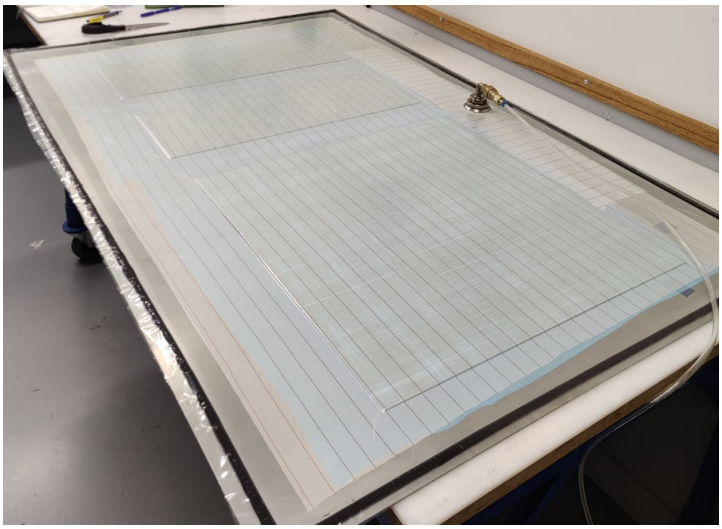

Figure B.1: Laminated specimen and tab material plates vacuum bagged ready for curing.

Before curing, a vacuum drop test was performed with a maximum allowed loss of 50 mbar over a 5 minute period. For the cure cycle itself, the manufacturer recommendation of 12 hours at 80$^{\circ}C$ was followed. To maximise the cured material's thermal stability glass transition temperature, this initial cure was followed up by a 120$^{\circ}C$ post-cure step with a 1 hour duration. The full cure cycle used, including ramp up and cooling rates, is given by Table B.2.

Table B.2: Recommended curing cycle for laminates up to 5 mm thickness.

Step	Specification	Duration [hrs]
Initial ramp RT-80C	2°C/min	0.5
Dwell	80°C	12
Post-cure ramp 80-120C	0.33°C/min	2
Post-cure dwell	120°C	1
Cooldown 120-60C	-2°C/min	0.7
Total curing time		16-16.5

To minimise curing induced material variances, all material was cured in one go using the Votch 0952 large format oven at DASML.

B.4. Specimen cutting and machining

After the laminate plates were cured, the specimen strips and tabs were cut from the plates using the CompCut ACS 600 CNC diamond-bade water-cooled circular saw. The DMA sample strips (10 x 50 mm and 12 x 50 for 0° and 90° respectively) did not require any further post-processing after cutting. The fatigue and tensile dogbone specimen however were first cut to their rectangular outer dimensions (25 x 290 mm). These pre-cut specimen strips were then handed over to the Dienst Electrische en Mechanische Ontwikkeling (DEMO) workshop for machining of the final dogbone shape, as per the drawing shown in Figure 5.6 of the main body text. This machining operation was done using a specialised composite end mill with combined upwards and downwards facing flutes. When machining, these milling bits compress the layers together, preventing delamination on the machined edges.

Below, Figure B.3 shows how these pre-cut specimen laminate strips looked like. The following Figure B.3 shows the dogbone specimen after the CNC machining step.

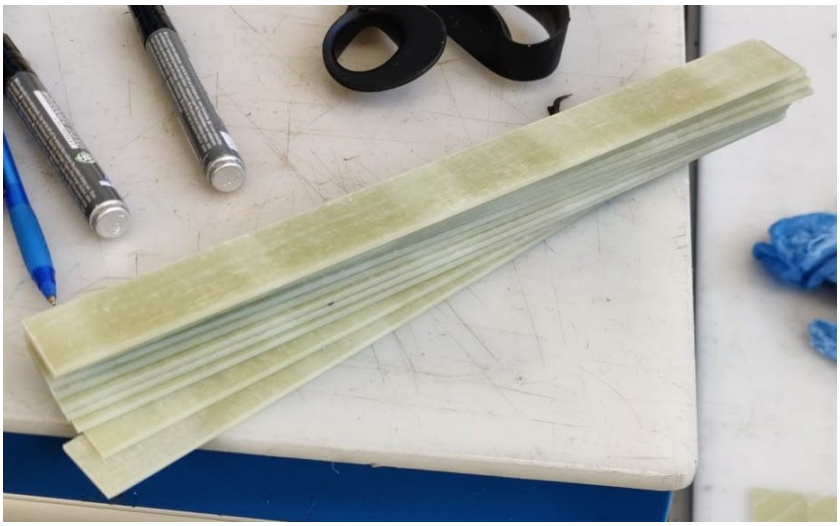

Figure B.2: Initial pre-cut $0/90$ specimen strips.

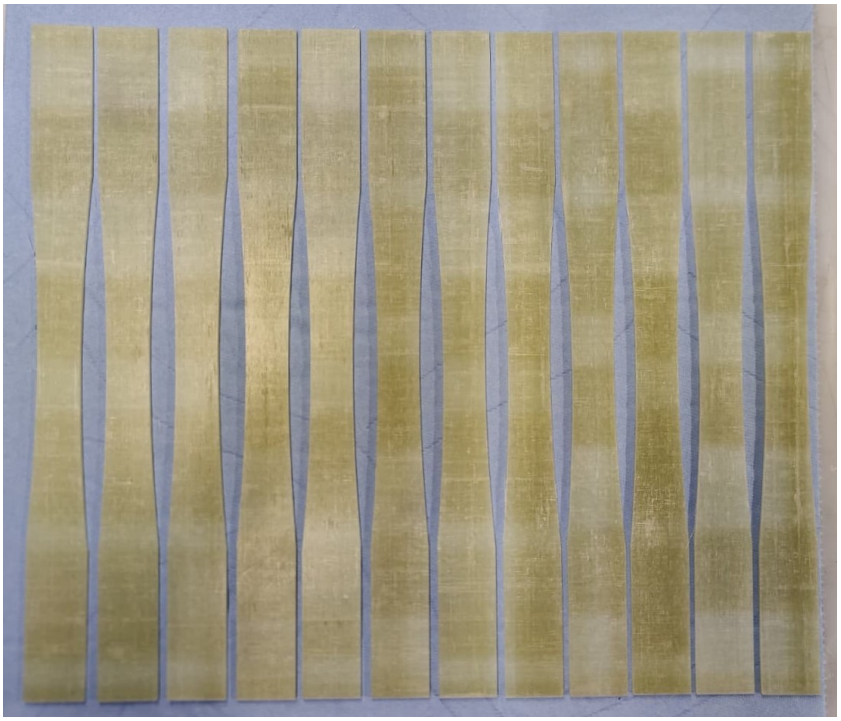

Figure B.3: Post-machined monotonic tensile and fatigue specimen.

B.5. Tab preparation and bonding

The tab material was also cut to size (25 x 260 mm) on the CompCut ACS 600. In order to produce consistent tap taper angles, a support jig was designed and 3D-printed. Figure B.4 shows how this jig was used in conjunction with a horizontal band saw to grind all tabs to a consistent 8.5° angle. Figure B.5 give an overview of how these glass/epoxy tabs looked post-tapering.

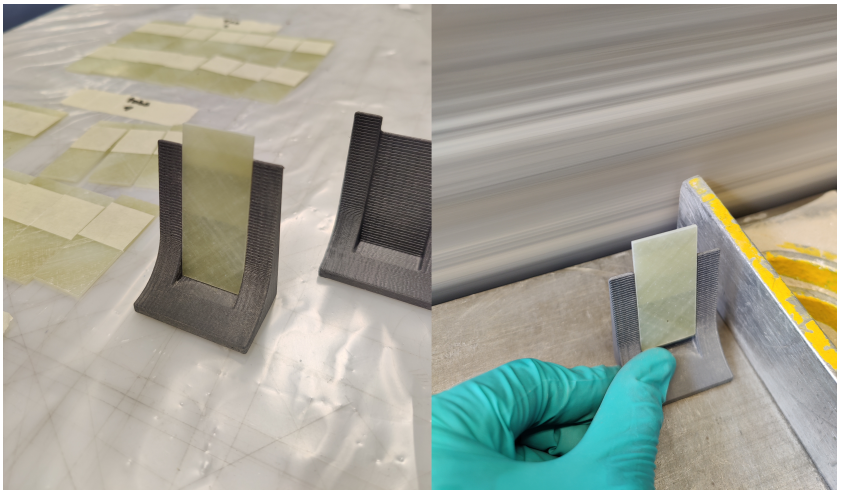

Figure B.4: 3D-printed tool for tapering of the composite tabs to a consistent angle.

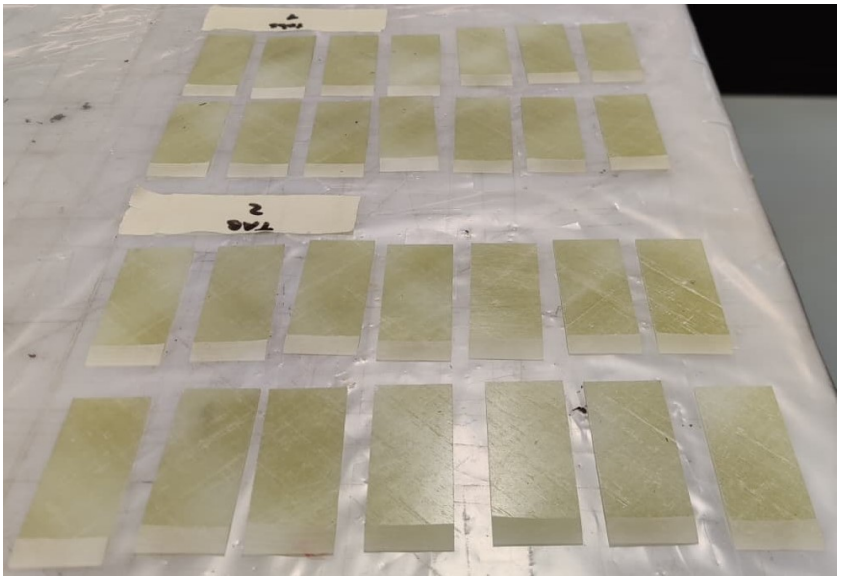

Figure B.5: Tapered $\pm 45^{\circ}$ glass/epoxy tabs ready for bonding.

For the bonding of the tabs to the dogbone specimen, Loctite AE 3430 two-component structural adhesive was used. This particular adhesive was selected for its good strength and low shear modulus, which aids in minimising tab-related stress concentrations. The bonding surfaces were prepared with 300 grid sandpaper and cleaned with isopropanol. Care was taken to not damage the surface finish of the dogbone specimen.

To ensure a consistent adhesive layer thickness, 200 μm glass beads were mixed in with the adhesive. Once the adhesive and tabs were applied, they were clamped in place with clips as also shown in Figure B.6. The specimen gauge sections were covered with flash-tape to prevent glue spillage. The adhesive was then cured at 40°C for 6 hours.

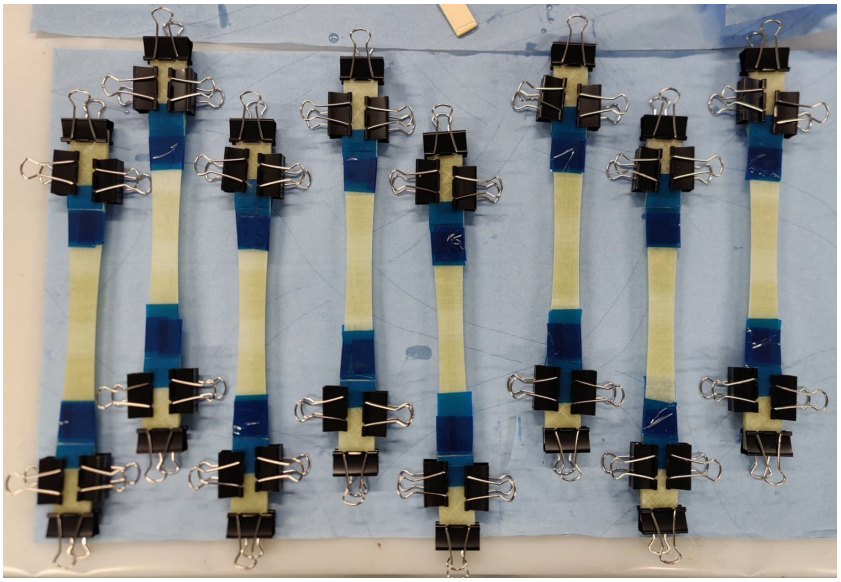

Figure B.6: Clamping arrangement for tab bonding.

B.6. DIC speckle pattern

The final step in the preparation of the monotonic tensile and fatigue dogbone specimen was the application of the DIC speckle patter. For this, first a matte white base coat was applied, followed by matte black speckles. These speckles were manually applied using a spray paint can. With consideration for the only 1 MPa high-speed camera resolution and the 'virtual extensometer' DIC use case, an intermediate size speckle pattern was aimed for.

Figure B.7 below shows how the final dogbone specimen looked like, with both the composite tabs as well as DIC speckle patterns applied.

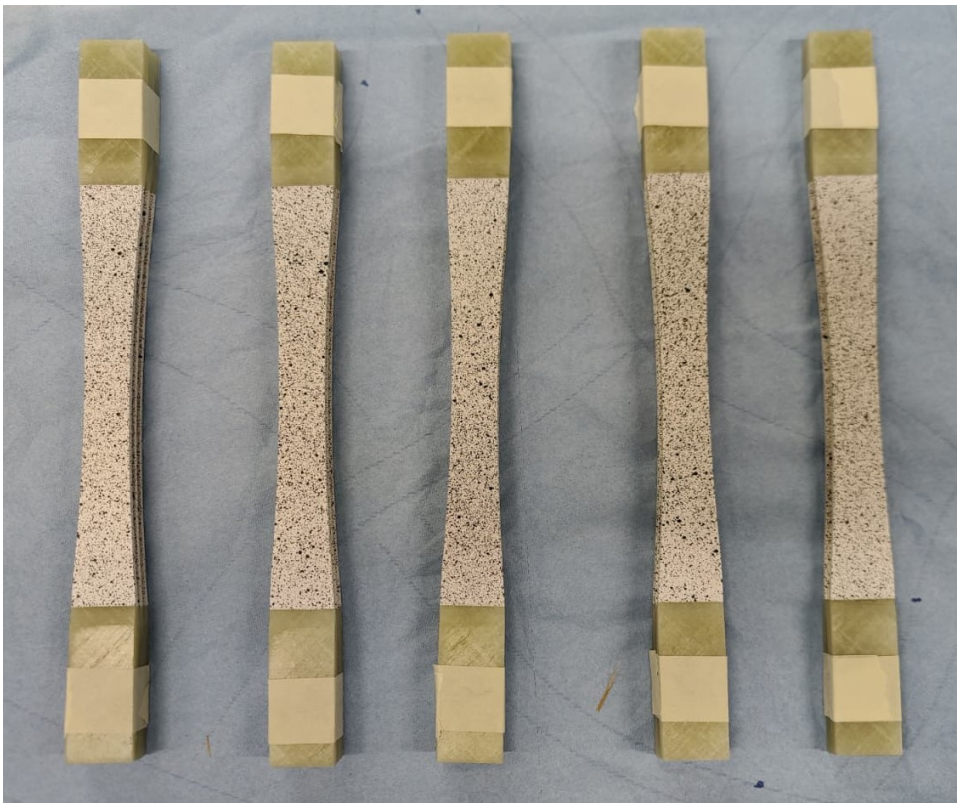

Figure B.7: Example of a number of testing-ready dogbone specimen including DIC speckle pattern.

B.7. Deltapreg BT080 datasheet

For completion and ease of reference, the prepreg manufacturers technical datasheet of the used BT-080 epoxy matrix system is attached over the next few pages of this appendix.

www.delta-tech.it

BT080

Out of autoclave, low temperature curable epoxy matrix

Introduction

BT080 resin system is characterized by low to medium minimum viscosity and good flow control.

BT080 offers a versatile curing range from 80°C to 120°C.

BT080 is curable by vacuum assisted process.

BT080 is suitable mainly for large structures, such as marine applications.

Key Features

BT080 epoxy resin offers 80°C out of autoclave processing.

Main features are:

- Maximum achievable DMA Tg of 140°C
- Processing by out of autoclave vacuum bag curing, also by autoclave curing
- Good flow for high areal weight UD, appropriate for large structures
- Low exothermal enthalpy for thick section
- High compressive properties
- Recommended cure from 80 to 120°C
- Out life of 60 days at 20°C

BT080 Resin Matrix Properties

Chemical nature	Low activation temperature thermoset epoxy system
Cure temperature	From 80° to 120°C
Density of cured net resin	1,22 g/cm^3
Dynamic viscosity	Low to medium viscosity system

The following chart shows the rheological behaviour of BT080.

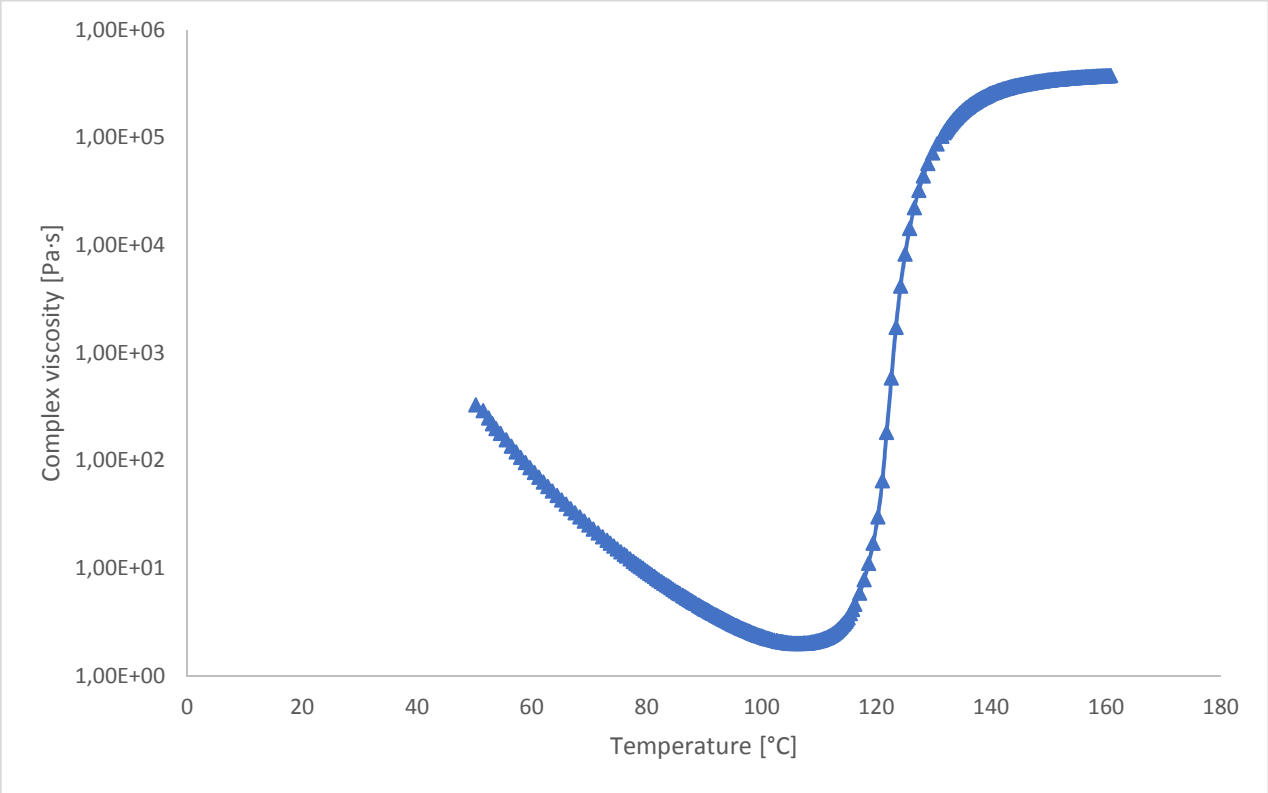

Figure 1: Dynamic Viscosity profile for BT080 resin (constant heating rate 2°C/min)

Thermal Performance of BT080 laminates

The following table indicates the typical glass transition temperature (Tg) developed by **BT080** laminates.

Cure Cycle and post cure	Tg (°C)
12 hours @ 80°C	130°C Maximum
12 hours @80°C + post cure 1 hour @ 120°C	140°C Maximum

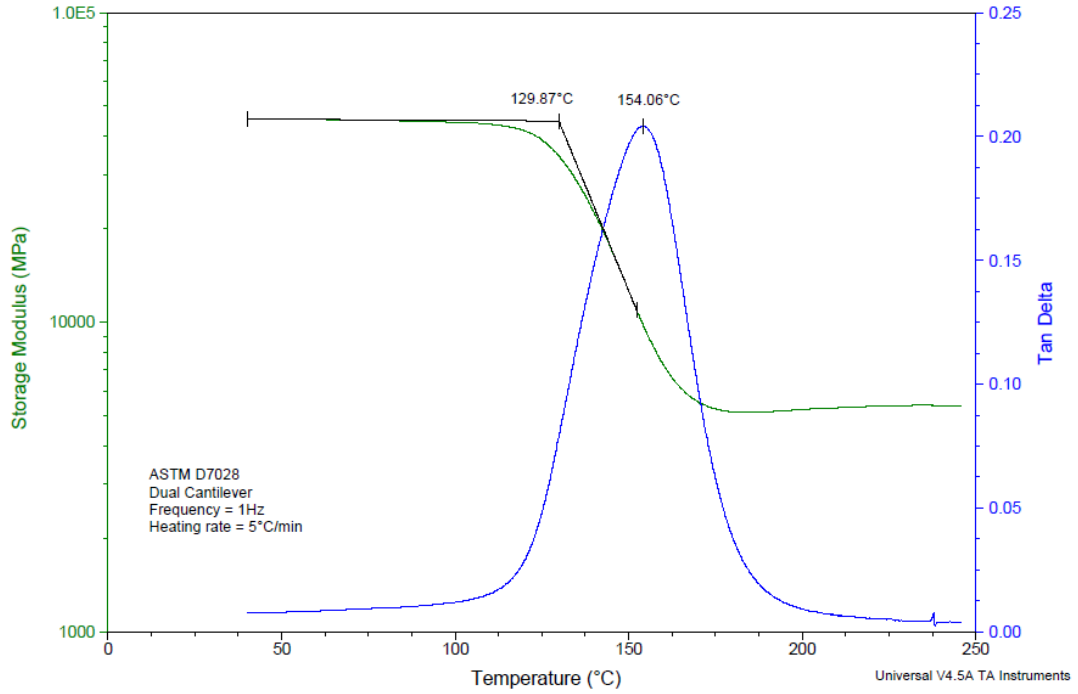

Figure 2: DMA Tg for T700-300-BT080-33% Unidirectional Prepreg Cured for 12 hour at 80°C

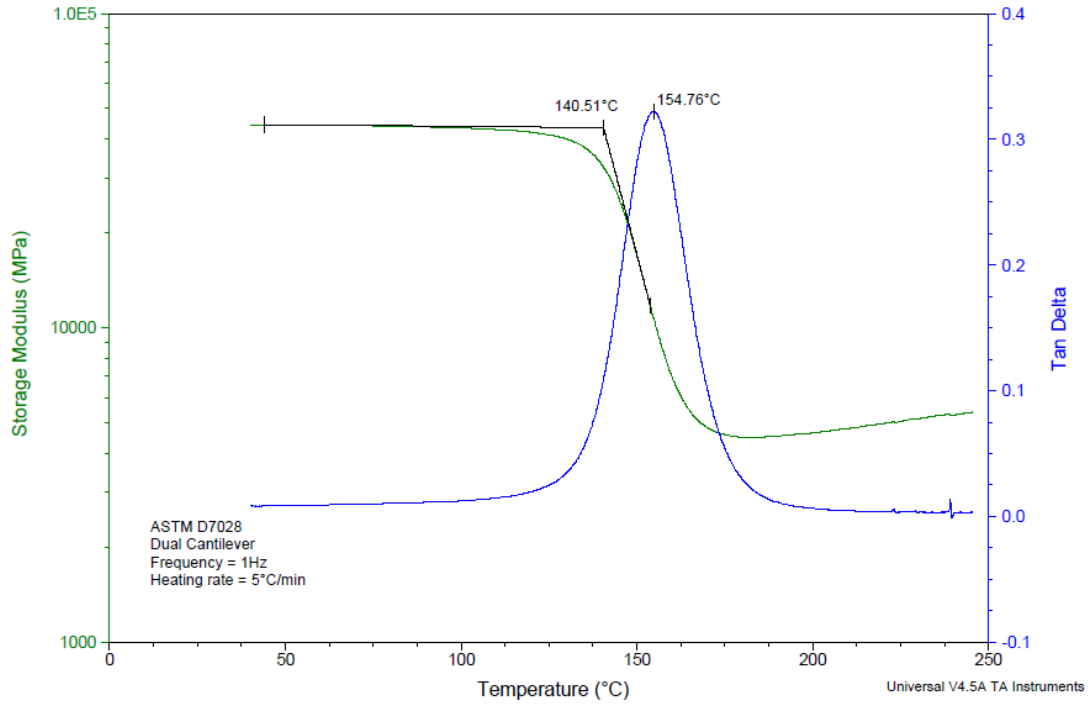

Figure 3: DMA Tg for T700-300-BT080-33% Unidirectional Prepreg Cured for 12 hours at 80°C + post cure 1h at 120°C.

Note: The Tangent Modulus Intercept Tg value has been measured by DMA, according ASTM D7028.

Mechanical Properties of Carbon Fibre Reinforced Laminates

In the below **Table 1** there are reported some indicative averaged mechanical characteristics of **BT080** carbon fibre laminates reinforced with a 300gsm High Strength 12k (T700S) unidirectional reinforcement at 33%rw. The laminates were cured Out of Autoclave 12h @ 80°C.

Table 1

Mechanical Tests	Test Method	RT
		T700S-300
Tensile Strength (0°) [MPa]	ASTM D 3039	2850
Tensile Modulus (0°) [GPa]	ASTM D 3039	128
Compression Strength (0°) [MPa]	ASTM D 6641	1200
	ASTM D 695	1400
Compression Modulus (0°) [GPa]	ASTM D 6641	122
	ASTM D 695	123
ILSS [MPa]	ASTM D 2344	85

Recommended Cure Cycles for BT080 products

BT080 is curable out of autoclave by only vacuum bag.
The recommended cure cycle is **12 hours at 80°C**. We do not recommend curing BT080 resin system at temperatures below 80°C.
The system can however be cured for shorter time at higher temperatures. A cure of 1 hr at 120°C has been used for validating mechanical properties, alternative cure cycle can be developed (including faster ramps and/or intermediate dwells) but mechanical and thermal properties should be checked and validated prior to be used in the manufacture of composite structures.

Oven Vacuum Bag Curing Cycles

The following are recommended cycles:

Low temperature cycle: 12h @ 80°C

Middle temperature cycle: 1h @ 120°C

The above cure cycles use an initial heating ramp-rate of 1 to 3°C/min from room temperature to the cure temperature. Ramp rate below 1°C/min should be discussed with Delta Tech Technical Support team.

Post-Cure Options after Initial Cure

If maximum Tg is required then postcuring can be applied. The free-standing postcure cycle is:

- Heat the part at 2°C/ minute ramp rate to the initial cure temperature of 80°C
- Slow the ramp rate.
- Heat the part at 0.3°C/min (20°C/Hour) to 120°C
- Dwell at 120°C for 60 minutes.
- Cool the part at 2°C/min.

Processing Guidelines

Important notice: Prepregs rolls must be stored in a freezer at -18°C when not being used. Thaw the prepreg to room temperature before removing the roll from the protective bag of polyethylene. This may typically take six (6) hours. This will prevent the uncured prepreg product from absorbing moisture from the air, as this can affect the quality of the final part. After using the roll of prepreg it is recommended to seal the roll in the protective bag before replacing it in the freezer.

Prepreg Lay Up and Laminating

1. Prepreg: Pay particular attention to conform the prepreg plies to the geometry of the released mould when laminating, especially in corners of small radius of curvature.
2. A perforated release film must be used to have a direct contact with the breather during the cure process. This is a good process to minimize the level of voids inside the final part.
3. Breather (non-woven polyester). Make sure the breather covers the entire part and reaches all the vacuum valves. A lightweight breather is recommended.
4. Vacuum bag. Use a generous quantity of high temperature bagging film to cover the part. Make sure the bag can fill all corners of the part with excess film, and there is no bridging of the film which could cause a bag burst in the autoclave.
5. Make sure the vacuum in the bag is to a high level, typically 980 mbar. Check the vacuum tightness of the bag before curing, by removing the vacuum pump for at least 5 minutes. The loss of vacuum pressure should not be greater than 50 mbar.

For further information, please contact Delta-Tech's Technical Service Department.

Exothermic Reaction

BT080 is a low reactivity epoxy system that allows the manufacture of thick laminates when cured under specific and controlled conditions. **However it is a reactive resin formulation which can undergo excessive exothermic heating during the initial curing process if the correct curing procedures are not followed. Care must be taken to use the heating rates and dwell temperatures in the recommended cure cycles. The risk of exotherm increases with laminate thickness and increasing cure temperature. If laminates are greater than 5 mm in thickness, please contact our technical department for confirmation of the correct cure cycle.**

Available Products/Prepregs

BT080 resin can be impregnated with a wide range of fibre reinforcements, such as woven and unidirectional tapes of high strength and high modulus carbon fibre with a range of fibre weights per square metre.

Prepreg Storage

Out life: 60 days @ 20°C
Shelf life: 12 months @ -18°C

Handling Precaution

When handling uncured resins and fibrous materials precaution should be considered. It is recommended to use suitable personnel protective equipment (minimum clean protective gloves) in order to protect the operators and avoid contamination of the components.

C

Additional experimental results

This final appendix provides some final additional experimental results and figures that related to the results presented in chapter 7, but were not directly covered.

C.1. Failed specimen overview

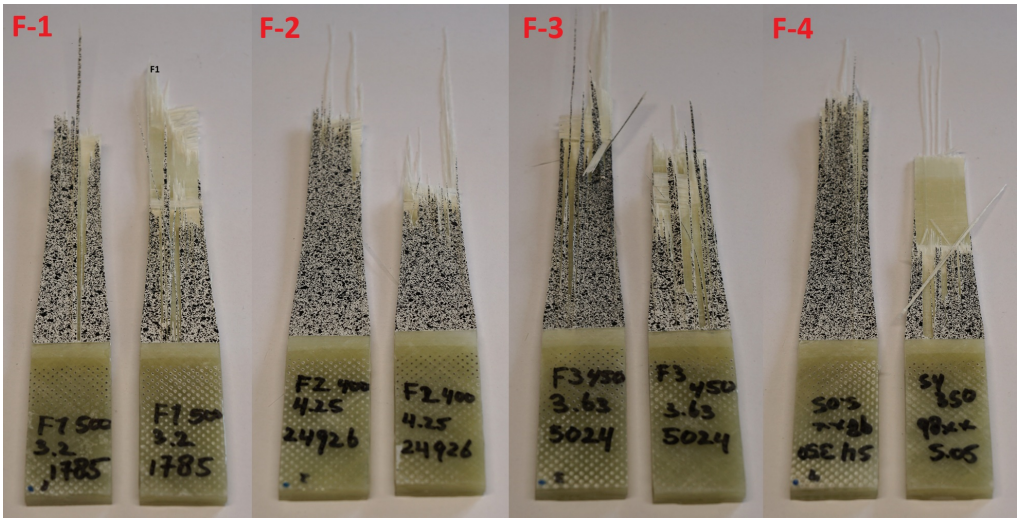

Figure C.1: Overview of failed specimen: Part A (F-1 to F-4).

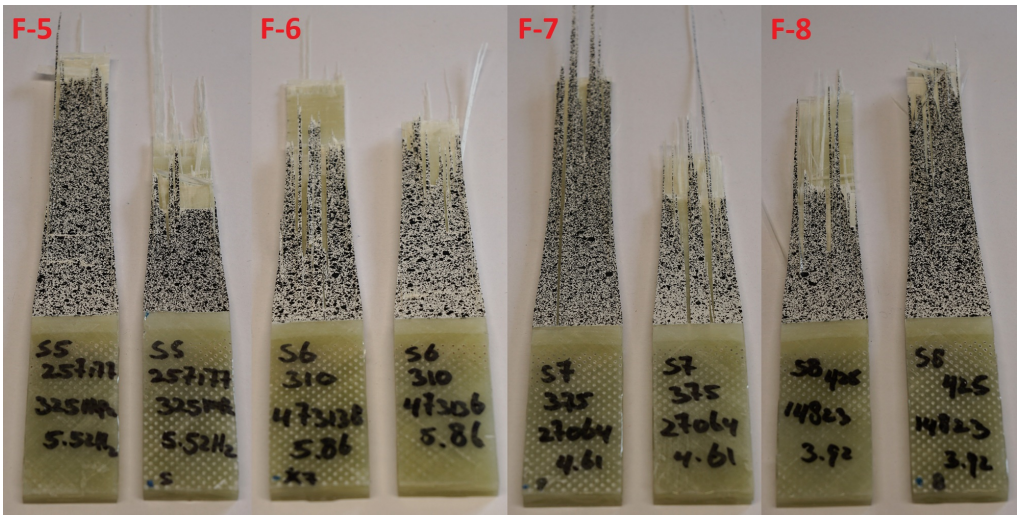

Figure C.2: Overview of failed specimen: Part B (F-5 to F-8).

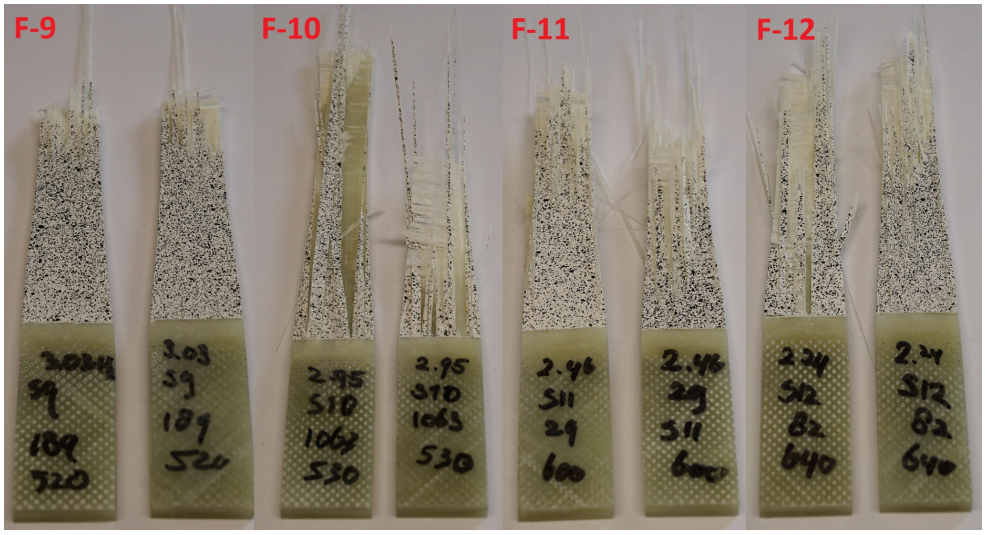

Figure C.3: Overview of failed specimen: Part C (F-9 to F-12).

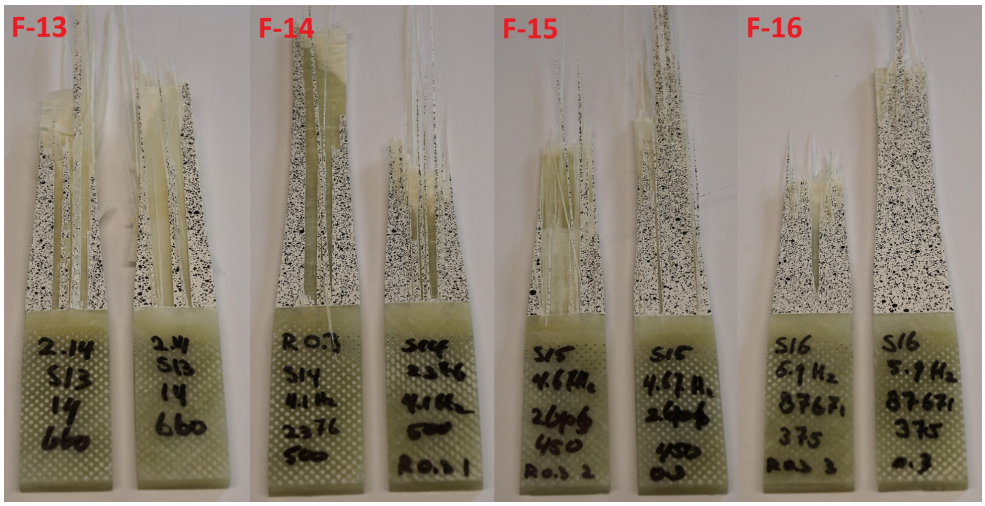

Figure C.4: Overview of failed specimen: Part D (F-13 to F-16).

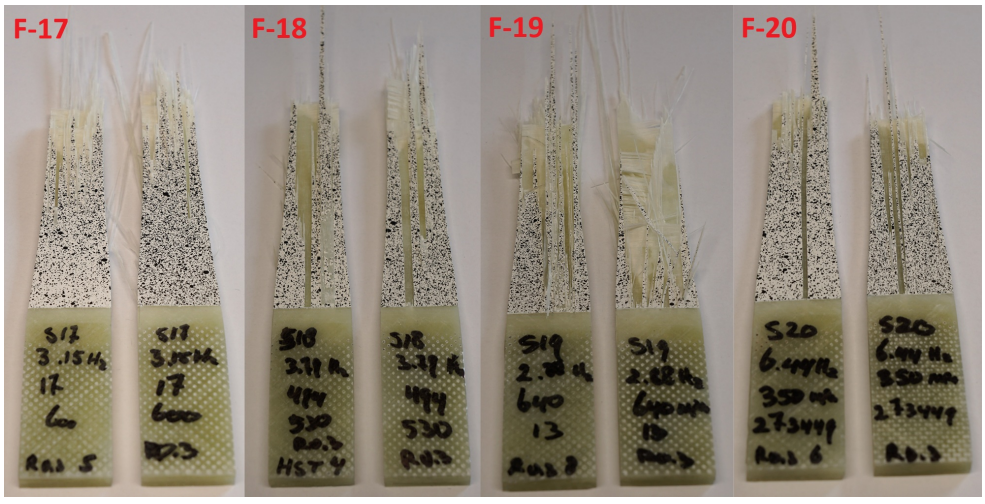

Figure C.5: Overview of failed specimen: Part E (F-17 to F-20).

C.2. High stress level dissipation plots

For clarity of the graphs, the W_h and $\sin(\phi)$ vs normalised fatigue life trends presented in section 7.3 did not include the highest stress levels ($\sigma_{max} \geq 600$ MPa) with fatigue lives of only a few tens of cycles. Therefore these are presented in this appendix instead in figures C.6 and C.7 respectively.

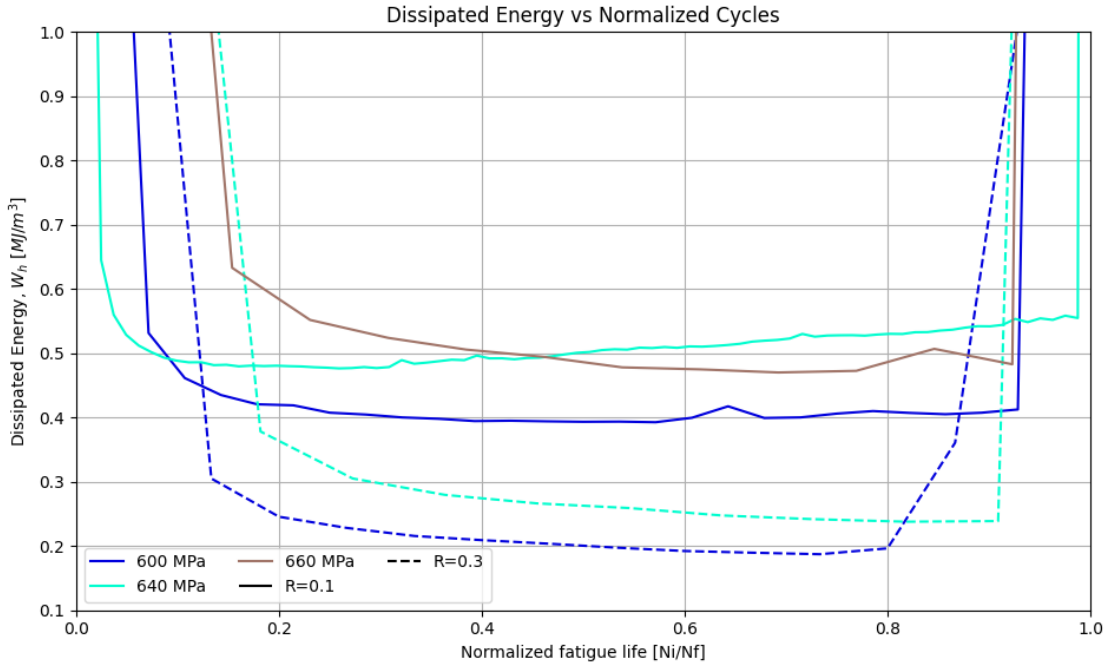

Figure C.6: Hysteresis energy dissipation W_h over the normalised fatigue lives for high stresses ($\sigma_{max} \geq 600$ MPa) at $R = 0.1$ (solid) and $R = 0.3$ (dashed).

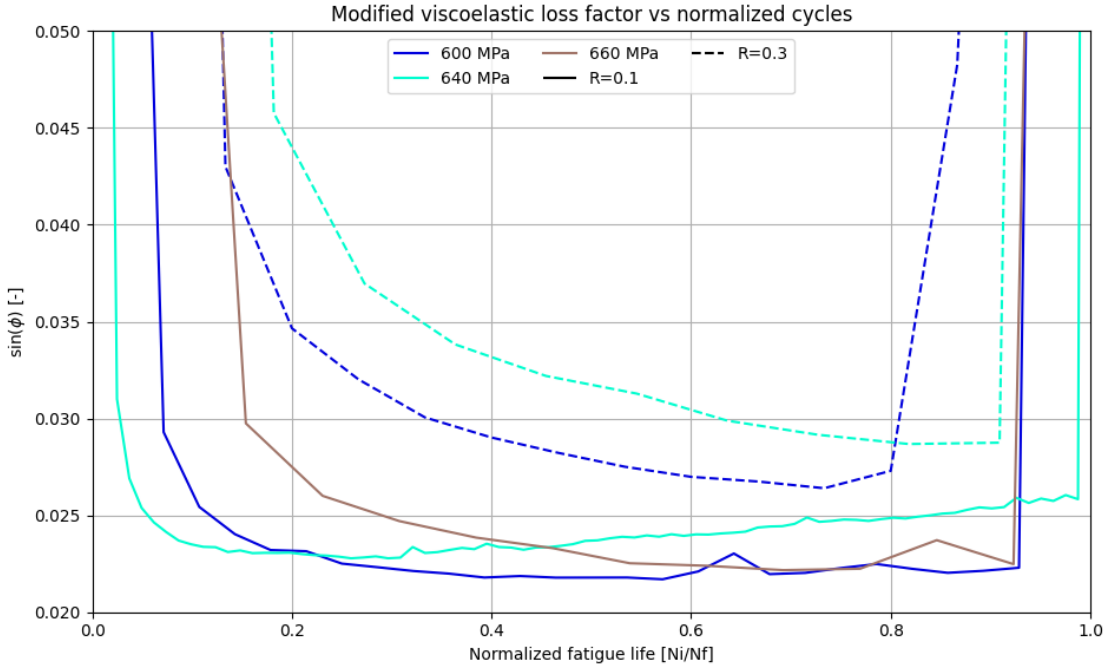

Figure C.7: Modified viscoelastic loss factor $\sin(\phi_i)$ progression over normalised fatigue lives for high stresses ($\sigma_{max} \geq 600$ MPa) at $R = 0.1$ (solid) and $R = 0.3$ (dashed).

C.3. Cyclic dissipation ratios

Figure C.8 below shows the progression of the cyclic dissipation ratios ($\frac{W_h}{W_a}$) over the normalised fatigue lives. In the main results of chapter 7, the focus was put in the viscoelastic loss factor $\sin(\phi)$ as the more descriptive parameter to evaluate. Figure C.8 however still serves a purpose to highlight that without the R-ratio corrective terms that link the cyclic dissipation ratio to the loss factor, a sole evaluation of $\frac{W_h}{W_a}$ is tampered by the inherent energy offset between R-ratios as demonstrated in this figure.

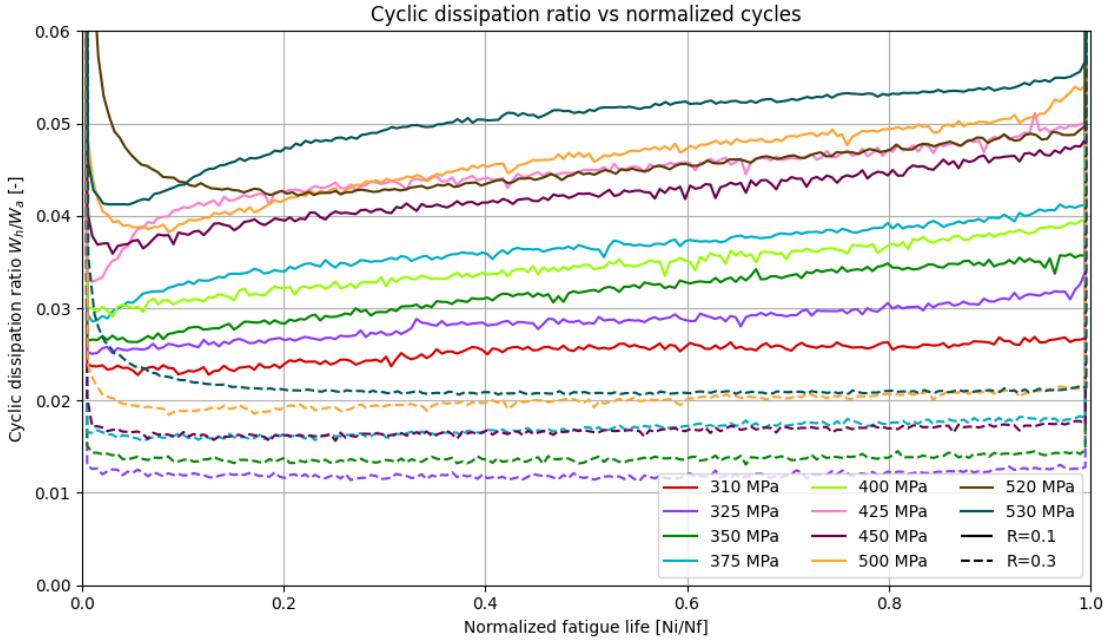

Figure C.8: Cyclic dissipation ratios $\frac{W_h}{W_a}$ over normalised fatigue lives at $R = 0.1$ (solid) and $R = 0.3$ (dashed).